



University
of Glasgow

Ngo, Duc The (2010) *Lorentz TEM characterisation of magnetic and physical structure of nanostructure magnetic thin films*. PhD thesis.

<http://theses.gla.ac.uk/1841/>

Copyright and moral rights for this thesis are retained by the author

A copy can be downloaded for personal non-commercial research or study, without prior permission or charge

This thesis cannot be reproduced or quoted extensively from without first obtaining permission in writing from the Author

The content must not be changed in any way or sold commercially in any format or medium without the formal permission of the Author

When referring to this work, full bibliographic details including the author, title, awarding institution and date of the thesis must be given

LORENTZ TEM CHARACTERISATION OF
MAGNETIC AND PHYSICAL STRUCTURE OF
NANOSTRUCTURE MAGNETIC THIN FILMS

Duc-The Ngo, M.Sc.



*Submitted in fulfilment of the requirements for
the Degree of Doctor of Philosophy*

*Department of Physics and Astronomy
Faculty of Physical Sciences
University of Glasgow*

Abstract

The work presented in this thesis is an investigation which aims to quantitatively characterise the physical microstructure, magnetic structure and micromagnetic behaviour of nanostructured thin films for magnetic recording and spintronics application. The nanostructures in the present work involve continuous and patterned thin films.

Chapters 1, 2, and 3 present the overview backgrounds directly relevant to the work. **Chapter 4** focuses on vortex structure in magnetic nanodots. The results confirm that the behaviour of the vortex can be modified by changing the edge geometry of the dots. It is demonstrated a practical method to determine the out-of-plane component of the vortex core with high accuracy and speed. Additionally in-plane curling magnetisation of the vortex is also mapped by reconstructing the electron phase using the transport-of-intensity equation. However this method is susceptible to spurious low spatial frequency and this aspect is explored to show limitations of the method. **Chapter 5** deals with the characterisation of magnetic structure in nanoconstrictions intended to trap domain walls (DWs) in the nanoconstrictions. A structure was fabricated with two micron-sized pads as the sources for creation of DWs. A DW can be driven to be pinned at the nanoconstriction resulting in a change of magnetoresistance due to the contribution of the DW to the resistance of the device. The magnetisation configuration around the constriction is studied during the reversal process. It is apparent that that understanding the magnetisation rotation around the constriction and into the pads is the key to the magnetoresistance measurements and the DW resistance is part of this process. Evidences of DW compression at the nanoconstriction were noted. In **Chapter 6** the investigation of the physical structure and micromagnetism of CoIr film is described. A hexagonal crystal structure with a [0001] texture normal to the film plane was characterised. Weak anisotropy is observed in the film denoted by a complex reversal on the hard axis due to incoherent rotation of magnetic moments. The film exhibits typical soft magnetic behaviour it merits compared to other soft materials are discussed in light of the results obtained here. **Chapter 7** concludes with a discussion of the outcomes of the present thesis. Additionally possible directions for future research in topics discussed in this thesis are proposed.

Contents

1	Magnetism, magnetic materials and their applications	1
1.1	Introduction	1
1.2	Ferromagnetism and ferromagnetic materials	3
1.3	Micromagnetic energy terms and micromagnetic simulation	4
1.3.1	Exchange energy	4
1.3.2	Anisotropy energy	5
1.3.3	Magnetostatic energy	7
1.3.4	Zeeman energy	8
1.3.5	Magnetostrictive energy	9
1.3.6	Total energy	9
1.3.7	Micromagnetic simulation	9
1.4	Magnetic domains and domain walls	11
1.4.1	Domain configurations	12
1.4.2	Domain wall configurations	13
1.4.3	The magnetic vortex	15
1.5	Hysteresis loop and magnetisation reversal	17
1.6	Magnetoresistance and spintronics	19
1.6.1	Anisotropic magnetoresistance	19
1.6.2	Giant magnetoresistance	20
1.6.3	Domain wall resistance	21
1.6.4	Spintronics	22
1.7	Magnetic recording media and soft underlayer	22
1.7.1	Magnetic recording media	22
1.7.2	Soft underlayer in perpendicular recording media	23

2	Instrumentation and fabrication techniques	31
2.1	Introduction	31
2.2	Substrates for fabrication	32
2.3	Thin film deposition	33
2.3.1	Thermal evaporation	33
2.3.2	Sputtering technique	34
2.4	Electron beam lithography	35
2.4.1	Lithography and electron beam lithography	35
2.4.2	Resist and spinning resist	37
2.4.3	Design, layout and beam writer	38
2.4.4	Resist development	40
2.5	Focused ion beam	40
3	Instrumentation and characterisation techniques	45
3.1	Introduction	45
3.2	Transmission electron microscopy	45
3.2.1	Conventional transmission electron microscopy (CTEM)	46
3.2.2	Scanning transmission electron microscopy (STEM)	48
3.3	Physical microstructure characterisation by TEM	49
3.3.1	Electron-specimens interaction	49
3.3.2	Electron diffraction	50
3.3.3	Dark-field and bright-field imaging	53
3.3.4	High-resolution TEM	55
3.3.5	FEI Tecnai T20 and TF20	56
3.4	Magnetic imaging in TEM	57
3.4.1	Lorentz microscopy	57
3.4.2	Fresnel imaging	60
3.4.3	Differential phase contrast (DPC)	62
3.4.4	Philips CM20 TEM/STEM	66
3.4.5	Magnetisation ripple in Lorentz image	67
3.5	Summary	69

4 Fresnel imaging of magnetic vortex in permalloy nanodots	72
4.1 Objective and motivation	72
4.2 Influence of edge geometry on the micromagnetic behaviour of the vortex in permalloy dots	75
4.2.1 Micromagnetic simulation results	76
4.2.2 Experimental observation	82
4.3 Determination of vortex core polarity using off-axis Fresnel imaging . .	86
4.3.1 Method description	86
4.3.2 Evidence of vortex polarity	88
4.3.3 Justification of the method	95
4.3.4 Discussion	99
4.4 Mapping magnetic structure in a magnetic vortex by phase reconstruction	101
4.4.1 Transport-of-intensity equation	101
4.4.2 Low-spatial frequency noise in reconstructed phase	105
4.5 Summary	112
5 Magnetic configuration in nanoconstrictions	116
5.1 Objective and Motivation	116
5.2 Structure for research	117
5.3 Micromagnetic behaviour of the structures	118
5.4 Magnetic configuration in the nanoconstrictions	122
5.5 Rotation of the magnetic induction	132
5.6 Electrical transport in the structures	135
5.7 Summary	137
6 Microstructure and magnetisation reversals of CoIr/Ru multilayer film for SUL	139
6.1 Objective and motivation	139
6.2 Physical microstructure of CoIr/Ru film	141
6.2.1 Crystal structure	141
6.2.2 Plan view grain structure	144
6.2.3 Cross-sectional microstructure	147
6.2.4 Texture determination	149

6.3	Micromagnetic behaviour	151
6.3.1	Reversal process on easy axis	151
6.3.2	Reversal process on hard axis	153
6.3.3	Formation and suppression of 360° walls	154
6.4	Magnetic ripple characterisation	156
6.5	Discussions	158
6.6	Summary	159
7	Conclusions and Future works	162
7.1	Conclusions	162
7.2	Future works	164

List of Figures

1.1	The magnetic moment in an atom is contributed by the magnetic moments of orbital motion (\mathbf{L}) and the spin motion \mathbf{S} of the electron. . . .	1
1.2	The alignment of the magnetic moments in a) paramagnetic, b) ferromagnetic, c) antiferromagnetic and d) ferrimagnetic materials.	2
1.3	The shape anisotropy energy is greatly affected by the shape of the specimen and is dependant on the size of the demagnetising field: (a) has lower magnetostatic energy than (b). From a magnetostatic point of view, (a) shows a preferred orientation.	7
1.4	The magnetic field generated by a field source at the point P: due to surface magnetic charge and volume magnetic charge from a point \mathbf{r}'	8
1.5	Larmor precession with damping of the magnetic moment in external applied field: (a) precessional motion without damping, (b) gyro-precessional motion with damping.	10
1.6	Discretisation of a 2D domain into FD cells of side, Δ , in which the micromagnetic equations are satisfied. The red outline denotes the boundary of a particle.	11
1.7	Variation of domain structure in a square thin film element: a) single-domain cubic, b) multi-domain state with large magnetostatic energy, c) magnetocrystalline anisotropy, d) anisotropic flux closure, e) single-domain shape-anisotropic state in a rectangular element, f) S-state in the rectangular.	12
1.8	Plan view schematic illustrations of Bloch-type wall (a), Néel-type wall (b), cross-tie wall (c), 360° wall loop (d) and linear 360° wall (e). Film plane is xy.	14

1.9	Phase diagram of permalloy film showing energy density of Néel wall, Bloch wall and cross-tie wall as a function of film thickness [25].	15
1.10	Spin configuration in a magnetic vortex (a): the in-plane magnetisation curls around the vortex core (counter clockwise chirality) whereas the magnetisation points perpendicularly to the wall plane at the centre of the core (b, c) to create the polarity.	16
1.11	An experimental phase diagram of transformation from vortex state to single domain state in permalloy nanodots. The figure is redrawn from ref. [28]: dark dots denote the single-domain state, circular dots denote the vortex structure and the solid line shows a lower bound to the theoretical phase boundary between the vortex state (above the boundary) and the single-domain state (below the boundary).	16
1.12	Hysteresis loops of the 600 nm diameter, 20 nm thick $Ni_{80}Fe_{20}$ circular element with perpendicular edge shape, and magnetic structure at various states: (0): demagnetised state, (1) before annihilation of vortex, (2) remanent and (3) after vortex nucleation.	18
1.13	Two recording methods in magnetic recording hard disk: longitudinal recording (a) and perpendicular recording (b) (from Hitachi Global Storage Technology).	23
1.14	The cross-sectional stack of a perpendicular recording medium (a) and writing process in perpendicular magnetic recording (b) with mutual mirror configuration for closing magnetic circuit.	24
2.1	Front, back and cross-section (a) schematic diagrams of a single Si_3N_4 membrane, and a block of 2×2 membrane wafer used for thin film deposition and electron beam lithography (b) [2].	32
2.2	Schematic diagram of a resistive thermal evaporation system (redrawn from PhD thesis of Shabbir A. Bashir (1998), King's College London).	33
2.3	Schematic diagram of a DC sputtering system (photo from ETA Film Technology Inc. (Taiwan)).	34
2.4	Schematic diagram of the Vistec VB6 UHR EWF beamwriter used for electron beam lithography [2].	36

2.5	Block diagram of two patterning techniques: a) lift off, b) etching etch- niques.	37
2.6	File processing required before patterning can begin: designed by L-edit software in PC, transferred to CATS computer for fracturing, and finally sent to control computer for writing the pattern [2].	39
2.7	The different profiles achieved with (a) a single layer of resist, (b) resist soaked in chlorobenzene and (c) a bilayer of electron sensitive resist [2].	40
2.8	Photograph of a gallium liquid metal ion source (a), schematic of ion column in the FIB (b) and dual beam system (c) [11].	41
3.1	(a) The structure of a transmission electron microscope (from University of Delaware, US) and (b) simplified ray diagram for image formation in a CTEM [3].	47
3.2	Principle schematics of a scanning transmission electron microscope (from M.E. Müller, Imaging nature across dimensions): the electron beam is focused as a fine probed by condenser lens and aperture; and scanned as a raster on the specimen by deflection coil. The transmitted beam is collected by HAADF detector (high angle deflected beam), bright field (BF) detector (low angle deflected beam) and EELS detector for chem- ical analysis.	48
3.3	Various electron-specimen interactions produce forward and backscat- tered electrons as well as a large number of secondary signals (a) (copied from William and Carter book [2]), a Fresnel image of a permalloy dot showing contrast of magnetic vortex (b) denoted by the variation of the intensity (c).	49
3.4	Electron diffraction on crystal lattice: (a) two incident waves reflecting on (hkl) planes are in-phase when their path difference is equal to an integer number of wavelengths, and (b) principle of electron diffraction in the TEM.	51
3.5	The Ewald sphere of reflection to construct the diffraction spot from reciprocal space.	52

3.6	Electron diffraction patterns obtained by a) single crystal specimen, b) polycrystalline specimen, c) textured-polycrystalline sample and d) amorphous sample [12].	53
3.7	Principle of bright-field and dark-field imaging: a) bright-field image, b) dark-field image and c) centred dark-field image.	54
3.8	An example of bright-field (BF) and dark-field (DF) (by selecting (10 $\bar{1}0$) diffraction ring) plan-view images of the Co ₈₀ Ir ₂₀ /Ru multilayer film.	55
3.9	An example of HRTEM micrograph of cross-sectional specimen of Co ₈₀ Ir ₂₀ /Ru multilayer film.	56
3.10	Deflection of the electrons due to Lorentz force when passing through a thin magnetic film.	57
3.11	Lorentz image formation in CTEM. This picture is re-drawn from Chapman (1984) [16].	58
3.12	Principle of defocused Fresnel image (a) and mechanism of intensity profile in terms of phase shift (b) in a patterned thin film with an inclusion of amplitude contrast.	60
3.13	Fresnel images of (a) 20 nm thick Ni ₈₀ Fe ₂₀ showing the domain walls on magnetic ripple background; (b) a 20 nm thick Ni ₈₀ Fe ₂₀ sub-micron dot showing a magnetic vortex at the centre contributed by curling magnetisation and strong edge contrast mainly by electrostatic phase shift.	62
3.14	Principle of the DPC technique: a) probe scanning on the specimen, b) construction of a DPC system and c) probe image on the detector.	63
3.15	Low magnification scanning (LMS) and high magnification scanning (HMS) DPC.	65
3.16	Modifications in the Phillips CM20: (a) an eight-segment detector for DPC, (b) modified objective lens.	66
3.17	Generating a magnetic field parallel to the specimen plane by tilting the specimen.	67
3.18	(a) Schematic representation of longitudinal and transverse magnetisation ripple configurations; (b) ray diagram of electron traversing a film displaying ripple (b). The pictures are redrawn from Leaver (1968) [27].	68

4.1	Four possible states of a magnetic vortex: (a,b) counter-clockwise chirality with up/down polarities, (b,c) clockwise chirality with up/down polarities.	72
4.2	Magnetic configuration of the simulated 600 nm - diameter $\text{Ni}_{80}\text{Fe}_{20}$ with thickness of 20 nm: M_x , M_y , M_z components of the vortex core (a,b,c) as the grey scale images, the profiles of the in-plane and out-of-plane component around the vortex core (d) and spin pattern of vortex (e). The colour in frame (e) illustrates the variation of the horizontal component of the in-plane magnetisation.	73
4.3	Multilayer-mesh is used to define the slope of the edge: (a) perpendicular edge ($\theta = 90^\circ$), (b) $\theta = 30^\circ$, (c) $\theta = 45^\circ$, (d) $\theta = 60^\circ$, (e) $\theta = 75^\circ$	76
4.4	OOMMF simulation result of formation of vortex state (a) in 600-nm-diameter and correspondent Fresnel image at 200 μm defocus (b). Cell size in this case is $2.5 \times 2.5 \times 2.5 \text{ nm}^3$	77
4.5	Simulated Fresnel images for the dots with 90° edge (a) and 45° edge (b) at demagnetised state; and line profiles of Fresnel images through the vortex (c,d). Frames (e,f) illustrate the electrostatic phases for two cases.	78
4.6	Simulated hysteresis loop (a) and magnetisation configuration (0-5) of the 90° -edge dot.	79
4.7	Simulated hysteresis loop (a) and magnetisation configuration (0-5) of the 45° -edge dot.	80
4.8	Magnetisation components, M_x (a), M_y (b), M_z (c) before vortex nucleation (+136 Oe) as the grey scale images of the 45° -edge dot. Frame (d) shows the line profile of the M_z image measured through the reversed domains, frame (e) shows the spin pattern from OOMMF simulation. Frames (f,g,h,i) show the similar result for the dot with a straight edge at -30 Oe.	81
4.9	Hysteresis loop characteristics (annihilation field, H_a , nucleation field, H_n) of the magnetic vortex as the functions of the edge angle. The discontinuous square and circular dots show experimental results.	82

4.10 (I): Fresnel images of the 600 nm diameter dot in initial magnetisation process: (a) 0 Oe, (b) 68 Oe, (c) 150 Oe compared with Fresnel images and spin patterns obtained by simulation at corresponding states for the dot with 45° edge. (II): Fresnel images of the 600 nm diameter dot demagnetising process: (d) - +200 Oe, (e) - +80 Oe, (f) - 0 Oe compared with Fresnel images and spin patterns obtained by simulation at corresponding states for the dot with 45° edge.	83
4.11 Experimental (a) and simulated Fresnel images of the 45° -edge $\text{Ni}_{80}\text{Fe}_{20}$ dot at the state before nucleation of the vortex. Frame (c) shows the simulated spin pattern. The detailed magnetic structure of this state was shown previously in Fig. 4.8	84
4.12 SEM image (a) of $\text{Ni}_{80}\text{Fe}_{20}$ dot array for experiment; (b) TEM cross-section image of a dot in specimen series fabricated with the dose of $2500 \mu\text{Ccm}^{-2}$, and (c) TEM images of cross-section showing edge geometries 45° ; and (d) other specimen series fabricated with the dose of $2000 \mu\text{Ccm}^{-2}$ showing a 60° edge slope.	85
4.13 Tilted Fresnel images to determine the vortex polarity. Contribution of polarity projection to Fresnel images is enhanced by obtaining a difference image of two symmetrically tilted Fresnel images.	87
4.14 Simulated Fresnel images of a 20 nm thick permalloy dot with 600 nm diameter at $\pm 30^\circ$ tilted angles (a,b), and difference image (c) at $250 \mu\text{m}$ defocus. Line profiles of contrast of the images are shown in frame (d) in comparing with contrast of the vortex in untilted Fresnel image. The inset a contrast-enhanced selected area of white-black contrast of difference image.	89
4.15 A comparison of tilted Fresnel images and difference image in three cases: (a,b,c) a normal magnetic vortex with in-plane curling magnetisation and out-of-plane core; (d,e,f) a curling magnetisation without out-of-plane core; (g,h,i) a structure with only out-of-plane core. Defocus value in this case is $250 \mu\text{m}$	90

4.16	Experimental Fresnel images at $\pm 30^\circ$ tilted (a,b) and difference image (c) at $250 \pm 20 \mu m$ defocus. The plot in frame (d) compares experimental and simulated contrast profiles with 5-lines averaging; frame (e) illustrates another difference image for an opposite polarity.	92
4.17	The contrast (a) and the width (b) of the polarity as a function of the defocus value. The simulation results are denoted by the red (convergent core), brown (divergent core) dots and the experimental data are denoted by the green dots.	93
4.18	Tilted Fresnel images (a,b) and difference image (c) for the case of divergent vortex case. Frame (d) illustrates line-trace profile of contrast and frame (e) shows a simulated difference image in the same condition ($\Delta f = 250 \mu m$).	94
4.19	Un-tilted Fresnel image (a) of the dot recorded at $\Delta f = 250 \mu m$ and (b) the level of signal variation measured from a 5-line profile near the vortex core.	94
4.20	Experimental Fresnel images at $250 \mu m$ defocus, $\pm 30^\circ$ tilted (a,b). Difference image is obtained when frame (1) is fixed, frame (2) moves out of cross-correlated position a number of pixels on two orthogonal axes.	95
4.21	Simulated difference images at various positions of selected frame when it is displaced on the tilt axis for the vortex structures with up/down polarity and without an out-of-plane core. Frames (a,b) show the contrast at various displaced positions (a) and the variation of polarity contrast as a function of number of pixels displaced (b). Defocus value in this case is $250 \mu m$	97
4.22	Simulated difference images at various positions of selected frame when it is displaced on the axis normal to the tilt axis for the vortex structure with down/up polarity and without out-of-plane polarity. The variation of polarity contrast (a) and rotated angle (b) as a function of displacement position are included. Defocus value in this case is $250 \mu m$	98

4.23	Experimental difference images at various positions of selected frame when it is displaced on x axis (a), y axis (b). Plots (c, d) provide the contrast of polarity on the the x and y axes, respectively, plot (e) shows the rotated angle of black-white contrast as a function of pixel number. Defocus value here is $250 \pm 20 \mu m$	100
4.24	Principle of TIE considered as the propagation of the plane wave through a transparent specimen (a) and application of the TIE to recover the phase from the Fresnel images (b).	102
4.25	An example of phase reconstruction using the TIE from Fresnel images with a comparison between experiment (a-d) and simulation (e-h) for 20 nm thick, 600 nm diameter $Ni_{80}Fe_{20}$ nanodot taken at $140 \mu m$ defocus.	103
4.26	The reconstructed phases recovered: from experimental inputs (a), from simulated inputs (b) and their corresponding line profiles (c,d). The blue dash lines denote the lines to measure the profiles.	104
4.27	Difference image of the free space (a) taken at $\pm 100 \mu m$, corresponding reconstructed (b); and line profiles of the difference image (c) and reconstructed image (d) with vertical scale in radians [29].	105
4.28	Simulated (a) and experimental (b) Fresnel images of a holey carbon film taken at defocus value of $+160 \mu m$ in field free mode in the TEM. Frames (c,d) shows the edge profiles of the holey carbon film in simulation (c) and experiment (d) measured from in-focus images (un-defocused images).	106
4.29	Transfer function ($T(k)$) and derivative of the transfer function $T'(k)$ with respect to spatial frequency k . From this plot, the linear limit for the Fresnel image is determined as the point at which two curves start to deviate (k_{L2}).	107
4.30	Reconstructed phases of the holey carbon film: (a) simulated, (b) experimental results taken at a defocus value of $160 \mu m$, and line profiles measured near the edge of the hole (c,d).	108
4.31	Simulated (a) and experimental (c) TIE reconstructed phase of holey carbon film and their line profile (c, d, e), taken at $80 \mu m$ defocus and image size of 256×256 pixels.	109

4.32	Filtering effect in the TIE solution using Fourier transform algorithm. The white noise spectrum from the vacuum is shown in the top trace. The TIE in effect is a filter in k space with a factor of $1/k^2$ as seen in the green linetrace. The resulting filtered white noise spectrum shows that the low frequencies have been significantly enhanced in the red linetrace. The arrows illustrate displacement of the plots.	110
4.33	Experimental TIE reconstructed phase from holey carbon film taken at defocus value of $80 \mu m$ from images with the size of 256×256 pixels (a) and line profile from phase (b). Frames (c) and (d) are the results for TIE phase reconstructed from images with the size of 512×512 pixels.	111
5.1	SEM micrograph of a ‘H-shape’ structure with two micrometer size pads (an elliptical pad and an elongated pad), connected by a $200 \times 280 \text{ nm}^2$ constriction (a). Frame (b) defines the geometrical dimension of the constriction with the width, w and the height, h	117
5.2	Fresnel images of the structure with a $200 \times 280 \text{ nm}^2$ nanoconstriction during demagnetisation at various magnetic field: (a): +20 Oe, (b): 0.0 Oe, (c): -3.6 Oe, (d): -4.1 Oe, (e): -9.0 Oe, (f): -11.0 Oe, (g): -20 Oe, and corresponding hysteresis loop measured by MOKE at the Durham University [2].	119
5.3	Schematic diagrams of the magnetisation configuration in the pads shown in Fig. 5.2: (a) corresponds to elliptical pad in Fig. 5.2(c), and (b) elongated pad in Fig. 5.2(e), respectively.	119
5.4	A pair of DPC images (a,) of the structure with a constriction size $200 \times 280 \text{ nm}^2$ at domain wall nucleation state (Fig. 5.2(d)) mapped along two orthogonal directions. White arrows denote the mapping directions. . .	120
5.5	Constriction height dependence of field characteristics of the structures with constriction dimension $300 \times h \text{ nm}^2$ ($h = 300 \div 900 \text{ nm}$): H_N : magnetic field to nucleate a single DW in the elliptical pad, H_{AP-P} field for propagating DW from the constriction at which the structure was switched to antiparallel state.	121

5.6	DPC images for the structure with $200 \times 280 \text{ nm}^2$ showing a domain wall nucleating in the elliptical pad: (a) experiment, (b) simulation, (c) 20-lines profiles of induction measured normal to the wall, (d) induction profile and its derivative to determine the wall width. Flux lines of the magnetic induction in the sample are shown in frame (e). The black arrow denotes the mapping direction.	123
5.7	DPC images for the structure with $200 \times 280 \text{ nm}^2$ constriction at remanent state: experiment (a) and simulation (b); (c) 20-lines induction profiles in the structure, (d) out-of-plane magnetisation curl component; and (e) simulated induction flux. The black arrow denotes the mapping direction; the region between the dash lines in frame (d) is the constriction area.	124
5.8	DPC images for the structure with $200 \times 280 \text{ nm}^2$ constriction at domain wall nucleation state: experiment (a,b) and simulation (c,d). Frames (e,f) show the induction profiles measured along the constriction height from DPC images that was averaging out over 20 pixels: (e) horizontal mapping, (f) vertical mapping. The white arrows denote the mapping directions.	126
5.9	(a) High-mag. scanning DPC image and (b) 20-line profiles of the induction measured along the constriction for the structure with a $200 \times 280 \text{ nm}^2$ constriction at domain wall nucleation state. The blue line and the white arrows show the line to measure the profile and the mapping direction, respectively.	127
5.10	(a) Simulated DPC image and (b) 20-line profiles of the induction measured at various positions for the structure with $200 \times 280 \text{ nm}^2$ constriction at domain wall nucleation state: (1) along the constriction, (2-4) various positions cross the wall in the elliptical pad.	127
5.11	The out-of-plane magnetisation curl (a) simulated induction flux calculated from electron phase (b) and (c) magnetisation configuration at domain wall nucleation state for the structure with a $200 \times 280 \text{ nm}^2$ constriction. Frame (c) illustrates a higher density of the flux lines around the constriction.	128

5.12	(a) SEM micrograph of the H-shape patterned structure, (b) SEMPA images of induction distribution measured in the constriction, (c) induction profile measured in antiparallel state and (d) two-wall profile. These results are redrawn from ref. [10] as a comparison.	129
5.13	DPC images for the structure with $200 \times 280 \text{ nm}^2$ constriction at antiparallel state: experiment (a) and simulation (b); simulated magnetisation curl in the structure (c), flux lines of the induction (d) and 20-line profiles measured along the constriction (e) with a comparison with profile in remanent state. The black arrow denotes the mapping direction. . .	130
5.14	Schematics of magnetic configuration in the structures during the magnetisation reversal at various states: (a) parallel-remanent state, (b) antiparallel with domain wall nucleation state, (c) antiparallel state, and (d) switched-parallel state.	131
5.15	The angle of magnetic induction in the constriction is defined as the angle θ with the cosine of θ can be determined from DPC images. . . .	132
5.16	An example of determination of the induction angle, θ from two DPC image (a,b). The blue lines denote the 30-line-averaging profile of the induction shown in frames (c,d). The arrows show the mapping directions.	133
5.17	Induction angle as a function of applied field during reversal process calculated for the structure with a constriction of $200 \times 280 \text{ nm}^2$	134
5.18	Rotation of the magnetic induction in the constriction during reversal process. The magnetic induction is denoted by the red arrows.	134
5.19	The AMR hysteresis loops for the structure with $200 \times 280 \text{ nm}^2$ constriction. The arrows illustrate the direction of the magnetic field variation.	136
6.1	Cross-section stacks of the multilayer film system used in the research.	141
6.2	SAED patterns of plane-view specimen: (a) un-tilted sample (beam normal to the film) and (b) 30° tilted sample. The inset shows a doublet ring resulted from two crystals. Frames (c,d) shows calculated diffraction rings of CoIr (red rings) and Ru (blue rings) layers (a).	142
6.3	Indexing the diffraction rings from SAED patterns for outer rings system (CoIr).	143

6.4	Crystallography plane of hexagonal crystal structure [11].	144
6.5	(a) A $(10\bar{1}0)$ dark field image, (b) respect threshold image for counting the grains and (c) grain distribution of the plan-view film.	145
6.6	(a) Plan-view bright-field TEM micrograph reveal nanostructure of the film and a system of Moiré fringes and (b) mechanism of Moiré fringes formation [10].	146
6.7	Schematic of TEM cross-section sample preparation by conventional method (from Craig Brownlie PhD thesis [14]): (a-e): mechanical process to obtain thin 3 mm discs, (f) mechanical polishing, (g) ion milling to obtained thin-foil specimen.	147
6.8	Bright-field (a), dark-field (b) TEM micrographs and SAED pattern (c) of two cross-sections of the CoIr/Ru film. Frame (d) shows HRTEM micrograph of cross-section. The inset shows Fourier transform of cross-sectional specimen.	148
6.9	Schematic of SAED pattern formation in textured sample with untilted sample (a), 30° tilted sample (b) and correspondent SAED patterns (c,d).150	
6.10	Fresnel images in a hysteresis sequence on the easy axis in plane of the film. The insets shows the Fourier transform of Fresnel images.	152
6.11	Fresnel images in a hysteresis sequence on the hard axis in plane of the film. The inset shows a Fourier transform of the Fresnel image at maximum applied field.	153
6.12	Fresnel image of CoIr film as magnetised on the easy axis at negative field of -28 Oe in which a 360° wall is observed (a) and the 360° walls annihilation field as a function of angle between applied field and the easy axis (b).	155
6.13	Calculation of ripple wavelength from Fresnel image using Fourier transform.	156
6.14	The magnetisation ripple wavelength, λ (a) and inverse wavelength square (λ^{-2}) (b) as the function of applied field during reversal process on the easy axis.	157

List of Tables

4.1	Hysteresis loop characteristics of experimental patterned dots with various edge slopes modified by changing electron dose. This results were also plotted in Fig. 4.9.	86
5.1	The width of induction variation, δ_{90} at remanent state; δ_2 at the domain wall nucleation state in various geometries of the constriction.	129
5.2	Comparison of induction angle (in degree) for the structures with the smallest ($200 \times 280 \text{ nm}^2$) and largest ($300 \times 900 \text{ nm}^2$) constrictions at certain states. The number in \pm here shows the variation of the magnetic induction direction rather than error.	135
6.1	Comparison of magnetic characteristics of the $\text{Co}_{80}\text{Ir}_{20}$ film with other magnetic thin films for SUL.	143
6.2	Comparison of magnetic characteristics of the $\text{Co}_{80}\text{Ir}_{20}$ film with other magnetic thin films for SUL.	158

Acknowledgements

There years in Glasgow is an important time of my life. I would like to thank all people for the time working in the Solid State Physics group. First of all, I wish to express my deep gratitude to my supervisors: Dr. Stephen McVitie, Prof. John Chapman and Dr. Ian MacLaren for excellent help, tuition and guidance from them. In Vietnamese culture, there is an idiom said that ‘*Nothing can be succeed without the help of your teacher*’. I spend this idiom for my supervisors with all great gratitude.

Secondly, I would like to thank all the staff members and postgraduate students in the Solid State Physics, Department of Physics and Astronomy, James Watt Nanofabrication Centre. My special thanks are due to Professors Alan Craven, Dr. Damien McGrouther for all of their help for my work. I am also grateful for the support from the support staffs: Sam, Brian, Billy, Colin and Lucy. Special thanks are due to the cooperations from Stoner Laboratory, University of Leeds with Dr. Christopher Marrows, Dr. Mark Hickey, Dr. Serban Lepadatu, Prof. Brian Hickey; and from the laboratory of Prof. Migaku Takahashi from Tohoku University (Japan) with Prof. Migaku Takahashi, Dr. Atsushi Hashimoto, Prof. Shin Saito. A big thank is due to my roommate M. Basith for his help in printing my thesis. I would like to express my thank to Engineering and Physical Sciences Research Council (EPSRC) and Overseas Research Student Award Scheme (ORSAS) for financial support.

From the bottom of my heart, I spend my special thanks to my family: my beloved wife Ngoc Lan, my parents, my sister and little nephew Bin, who have encouraged and supported me over three years of my research although they do not understand what my research is. They are my motivation and belief from which I can complete my research. A big thank is due to all of my friends for their encouragement.

Declaration

This thesis is a record of the work carried out by myself in the Solid State Physics Group, Department of Physics and Astronomy at the University of Glasgow during the period 2006-2010. The work described herein is my own with the exception of thin film deposition in chapter 6 for CoIr/Ru multilayer film, which was deposited by Dr. Atsushi Hashimoto at the Tohoku University (Japan) and in chapter 5 for Ni₈₁Fe₁₉ films by Dr. Serban Lepadatu at the University of Leeds; of anisotropic magnetoresistance measurement by Dr. Mark Hickey at the University of Leeds; MOKE measurement by Lara Bogart at Durham University in the UK in chapter 5. Some of the works in this thesis have been published at following conferences and journals:

1. S.McVitie and D.T. Ngo, **Quantitative measurements of phase using the transport of intensity equation**, presented at the Electron Microscopy and Analysis Group Conference, September, 2007, Glasgow, UK.
2. S.McVitie and D.T. Ngo, **Quantitative measurements of phase using the transport of intensity equation**, *Journal of Physics: Conference Series*. **126 (2008) 012041**.
3. Ngo D.T., S. McVitie, J. N. Chapman, A. Hashimoto, S. Saito, M. Takahashi, **Transmission electron microscopy investigation of CoIr/Ru multilayer film for soft magnetic underlayer in recording media**, presented at Joint European Magnetic Symposia, September 2008, Dublin, Ireland.
4. D.T. Ngo, D. McGrouther, S. McVitie, J.N. Chapman, M. Hickey, C. H. Marrows, **Lorentz microscopy characterisation of domain walls in nanoconstriction structures**, presented at Current Research In Magnetism (CRIM'08), December, 2008, London, UK.

This thesis has not previously been submitted for a higher degree.

List of Abbreviations

AC	alternative current
ADF	annular dark field
AFM	atomic force microscopy
AMR	anisotropic magnetoresistance
APF	aperture function
BELLE	beam writer exposure layout for lithographic engineers
BF	bright field
CATS	computer aided transcription system
CBED	convergent beam electron diffraction
CCD	charge-couple device
CMR	colossal magnetoresistance
CTEM	conventional transmission electron microscopy
DC	direct current
DF	dark field
DPC	differential phase contrast
DW	domain wall
DWR	domain wall resistance
EBL	electron beam lithography

EDX energy dispersive X-ray spectroscopy

EELS electron energy loss spectroscopy

EPSRC engineering and physical sciences research council

FIB focused ion beam

FT Fourier transform

FWHM full width at half maximum

GIF Gatan imaging filter

GMR giant magnetoresistance

HAADF high annular angle dark field

HDD hard disk drive

HMS high magnification scanning

HRTEM high-resolution transmission electron microscopy

IPA iso-propyl alcohol

JWNC James Watt nanofabrication centre

LLG Landau-Lifshitz-Gilbert

LMIS liquid metallic ion source

LMS low magnification scanning

LTEM Lorentz transmission electron microscopy

MFM magnetic force microscopy

MIBK methyl isobutyl ketone

MOKE magneto-optic Kerr effect

MRAM magnetoresistive random access memory

OOMMF objective oriented micromagnetic framework

PEEM	photoemission electron microscopy
PMMA	polymethyl methacrylate
RF	radio frequency
SAED	selected area electron diffraction
SEM	scanning electron microscopy
SEMPA	scanning electron microscopy with polarisation analysis
SP-STM	spin polarised scanning tunnelling microscopy
STEM	scanning electron microscopy
STM	scanning tunnelling microscopy
SUL	soft underlayer
TEM	transmission electron microscopy
TF	transfer function
TIE	transport-of-intensity equation
TMR	tunnel magnetoresistance
UV	ultra violet
WATE	wide adjacent track erasure
XMCD	X-ray magnetic circular dichroism
ZOLZ	zero-order Laue zone

Chapter 1

Magnetism, magnetic materials and their applications

1.1 Introduction

Magnetic materials and devices play important roles in engineering and technology. In solid state physics and materials science, magnetism is a subject of great interest, the magnetic properties of the materials can be exploited to produce electronic devices based on magnetism. The history of magnetism started a long time ago with use of magnets by ancient Chinese and Greeks from 700 B.C. Nowadays, it is easy to find applications magnetic materials in many industries, medicine as well as in the electronic devices. Recently, a great effort is being made in science and technology to create a new generation of electronic devices based on spintronics [1,2], in which both charge and spin of the electron are exploited. The Nobel prize in physics 2007 for A. Fert and P. Grünberg for the discovery of giant magnetoresistance [3,4] marked an important developing step of spintronics as well as magnetism and magnetic materials.

Magnetism in the matter originates essentially from atomic magnetic moment which is contributed by the orbital and spin motions of the electron (Fig. 1.1). The nu-

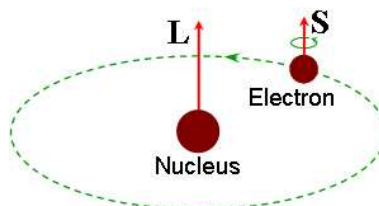


Figure 1.1: The magnetic moment in an atom is contributed by the magnetic moments of orbital motion (L) and the spin motion S of the electron.

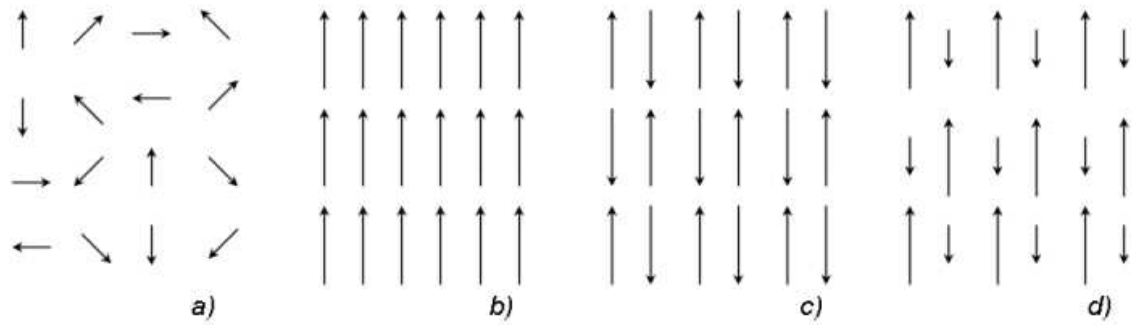


Figure 1.2: The alignment of the magnetic moments in a) paramagnetic, b) ferromagnetic, c) antiferromagnetic and d) ferrimagnetic materials.

clear magnetic moment is very small and hardly contributes to the atomic magnetic moment. The response of the atomic moment under the application of the external field causes the magnetism in the matter. In terms of the behaviour of the materials in a magnetic field and the magnetic moment alignment (Fig. 1.2), materials can be divided in to some categories: diamagnetic materials with no magnetic moment, paramagnetic materials with randomly oriented magnetic moments (e.g. O_2 , Al) - Fig. 1.2(a), ferromagnetic materials (Fig. 1.2(c)) with parallel orientation of magnetic moments, antiferromagnetic materials (Fig. 1.2c) compensated antiparallel orientation of magnetic moments in two sublattices, or not compensated antiparallel orientation of magnetic moments in ferrimagnetic materials (Fig. 1.2(d)). Among them, ferromagnetic materials and antiferromagnetic materials are considered as magnetically ordered materials. Diamagnetism is the property of an object which causes it to create an additional magnetic field in opposition of an externally applied field, thus resulting in a repulsive effect in accordance with Lenz's electromagnetic induction rule. Paramagnetism is a form of the magnetism that occurs only in the presence of an applied magnetic field. Paramagnetic materials are attracted to magnetic field hence have a relative magnetic permeability higher than 1. Antiferromagnetic materials consist of two antiparallel sub-lattices of magnetic moments so that the net magnetic moment is compensated to be zero. Generally ferromagnetic materials are the main material for most of magnetic applications although some magnetic systems (e.g. multi-layer devices) can be a combination of different kinds of magnetic materials.

The work in this thesis is focused on investigating the micromagnetic structure of ferromagnetic thin films and nanostructures. Namely, it can be summarised as:

- Imaging magnetic vortices in permalloy nanodots and characterising the vortex

behaviour using Fresnel imaging. The magnetic structure of the vortex (including polarity and in-plane curling magnetisation) was determined using Fresnel imaging.

- Controlling domain walls and investigating domain wall behaviour in NiFe thin film elements with nanoconstrictions for spintronic applications, quantitatively characterising wall structure using Lorentz TEM.
- Understanding the micromagnetic structure of soft magnetic CoIr thin film for soft magnetic underlayer (SUL) in perpendicular magnetic recording media.

This chapter will review briefly and basically relevant backgrounds for the research: ferromagnetic materials, magnetic domain and domain wall, magnetoresistance, etc.

1.2 Ferromagnetism and ferromagnetic materials

Ferromagnets have their own magnetisation below Curie temperature even without external field, this is called spontaneous magnetisation. At zero absolute temperature (0 K), the magnetic moments align parallel together to create the spontaneous magnetisation. For this purpose, there must be a strong interaction present between atoms/ions. In 1907, Weiss suggested an interaction by an internal molecular field, \mathbf{B}_m [5]:

$$\mathbf{B}_m = \lambda \mathbf{M} \tag{1.1}$$

where, the λ is the molecular field constant and \mathbf{M} is the magnetisation of the material. Each atomic moment is assumed to be acted on by this field, which is proportional to the magnetisation of its environment. If a parallel alignment of moments should appear locally at any place in the lattice, the molecular field will be produced which in turn will promote further alignment of the spins. The problem with this theory was that it is phenomenological, that it did not explain the origin of the field. Also, for typical ferromagnetic materials, the magnitude of the field is calculated to be on the order of 10^7 G, suggesting that an externally applied field would be insignificant in comparison and would not affect the system at all. This is clearly not the case. In 1928, Werner Heisenberg established a quantum mechanical theory [6] which allowed explanation of ferromagnetism in which the interaction can be assigned to a special ex-

change interaction between each atom and its nearest neighbours, caused by the overlap of the electron wave functions. Pauli's exclusion principle applied to fermions indicated that the total wave function for a quantum mechanical system must be antisymmetric. Hence, two electrons bound within the same orbital (symmetric space) must have opposite spin (antisymmetric space), whilst the case of electrons in different orbitals must have parallel spin. Therefore, the interaction responsible for ferromagnetic order is essentially electrostatic in nature and not a magnetic interaction as proposed by Weiss. From the Hamiltonian energy point of view, the interaction can be represented by the Heisenberg Hamiltonian:

$$H_{ij} = -2J\mathbf{s}_i\mathbf{s}_j \quad (1.2)$$

where, the H_{ij} is the exchange energy of two interacting electron spins (\mathbf{s}_i and \mathbf{s}_j), and J is the exchange integral, which is dependent on the material. Furthermore, the exchange interaction can also be used to describe antiferromagnetism. If the exchange integral in ferromagnets is positive, that causes a minimum energy for parallel spins, the antiferromagnets have a negative exchange integral resulting in a minimum energy when the spins are antiparallel.

1.3 Micromagnetic energy terms and micromagnetic simulation

The micromagnetic energy definition contributions allow determination of possible magnetic states of the ferromagnets. A stable state is reached when the micromagnetic energy is locally minimised. The different contributions to the total micromagnetic energy are now described.

1.3.1 Exchange energy

The exchange energy is the energy associated with the parallel alignment of the spin system. Heisenberg's model [6] suggested the origin of ferromagnetism was due to the exchange interaction when the wave functions of two neighbouring electrons overlap.

The energy in a ferromagnetic sample is given by:

$$E_{ex} = -2JS^2 \sum_{ij} \cos \psi_{ij} \quad (1.3)$$

where S is the magnitude of the spin, ψ_{ij} is the angle between spins i and j , and J is the exchange integral. Taking into account the three dimensional nature of crystals and integrating over a finite volume of the material (in the simple case for a cubic system), the exchange energy in the sample is written as:

$$E_{ex} = A \int_V [(\nabla\alpha)^2 + (\nabla\beta)^2 + (\nabla\gamma)^2] dV \quad (1.4)$$

here, α , β , γ are the direction cosines with respect to the crystal axes, and A is the exchange stiffness constant of the material, which is given by (for cubic system):

$$A = \frac{kJS^2}{a} \quad (1.5)$$

with k is a structure-dependent constant (1 for simple cubic, 2 for body centred cubic and 4 for face-centred cubic crystals) and a is the lattice parameter. For example, exchange stiffness constant for $\text{Ni}_{81}\text{Fe}_{19}$ alloy (permalloy) is $A = 13 \times 10^{-12} \text{ J/m}$ [7]. Normally, exchange energy is minimised in magnetic domains because of parallel alignment of the magnetic moments in the domains. However, in magnetic domain walls, the exchange energy becomes significant because the magnetic moments in the wall deviates from one direction to another one over the wall width.

1.3.2 Anisotropy energy

Anisotropy energy is related to the directional behaviour of the materials, in which the magnetisation properties depends on the measuring direction because the orientation of the magnetisation is influenced by the structure of the materials. There are two main types of anisotropy: magnetocrystalline and shape anisotropy (demagnetising energy).

Magnetocrystalline anisotropy

The magnetocrystalline anisotropy is caused by the spin-orbit interaction. The electron orbits are linked to the crystallographic structure, and the spin orbit interaction gives non-spherical charge distribution, that results in a preferred orientation direction of

magnetisation. The preferred directions for magnetisation are called the *easy axis* and the directions in which it is most difficult to align the magnetisation are called *hard axis*. Magnetocrystalline anisotropy is associated with the energy necessary to deflect the magnetic moment in a single crystal from the easy to the hard direction. For a hexagonal system, there is a uniaxial anisotropy with the energy given by [9]:

$$E_k = \int_V (K_1 \sin^2 \theta + K_2 \sin^4 \theta) dV \quad (1.6)$$

where, θ is the angle between the magnetisation and easy axis, K_1 , K_2 are first and second magnetocrystalline anisotropic constants, respectively. For example, $K_1 = 4.1 \times 10^5 \text{ J/m}^3$, $K_2 = 1.5 \times 10^5 \text{ J/m}^3$ for Co. If we use the direction cosines, eq. (1.6) becomes:

$$E_k = \int_V [K_1(1 - \gamma^2) + K_2(1 - \gamma^2)^2] dV \quad (1.7)$$

In the case of polycrystalline materials there is no overall preferred axis for magnetisation because the crystallites are randomly oriented. Instead, the anisotropy direction varies from crystallite to crystallite, i.e. local easy axes. A consequence of this variation is the formation of the magnetisation ripple which can be observed in Lorentz images of such films (chapter 3, section 3.4). Additionally, induced anisotropy can be created during or after growth process of the film using special treatment techniques. For example, using a seed layer to obtain a textured film or using a large magnetic field during annealing or deposition processes [9].

Shape anisotropy

The shape anisotropy is related to the magnetostatic effects of the system rather than the overlap of electron orbitals, however, it is specially important to the magnetic configurations of the thin films and objects with reduced dimensions. When a magnetic specimen is uniformly magnetised, the magnetic *free poles* are present at the surface of the specimen. Fig. 1.3 illustrates that the magnetostatic dipole interactions may produce magnetic anisotropy in an ellipsoid specimen magnetised along the long and short axes, it can be seen that free poles are separated by relatively long and short distances respectively.

Inside the specimen with ellipsoid shape (Fig. 1.3), the demagnetising field, H_d , is

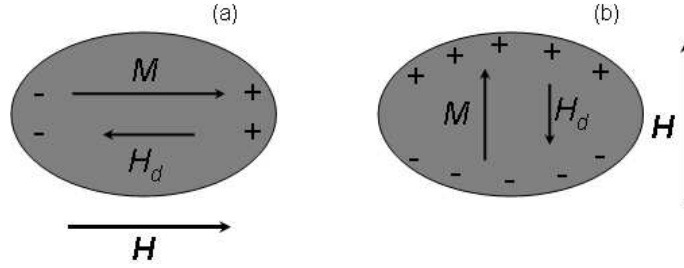


Figure 1.3: The shape anisotropy energy is greatly affected by the shape of the specimen and is dependant on the size of the demagnetising field: (a) has lower magnetostatic energy than (b). From a magnetostatic point of view, (a) shows a preferred orientation.

aligned oppositely to the direction of the magnetisation and the shape anisotropy energy will be given by [9]:

$$E_k = \int_V K_{eff} \sin^2 \theta dV \quad (1.8)$$

here,

$$K_{eff} = \frac{(N_b - N_a)M^2}{2} \quad (1.9)$$

where, θ is the angle between the long axis and the magnetisation direction, M is the magnetisation, and N_a , N_b are demagnetising factors in the long and the short axes, respectively. The demagnetising factors depends on the sample geometry and in 3D case, the demagnetising factors in three dimensions are given by:

$$N_a + N_b + N_c = 1 \text{ (in SI unit)} \quad (1.10)$$

In the above ellipsoid specimen, the cross section is circular, therefore, $N_b = N_c$. For example, a $Ni_{80}Fe_{20}$ ellipsoid particle with $a = 4 \mu m$, $b = c = 2 \mu m$, $M_s = 860 \times 10^3 \text{ A/m}$. Using the model in ref. [10], three demagnetising factors will be $N_a = 0.1735$, $N_b = N_c = 0.4132$, the effective anisotropy coefficient will be $K_{eff} = 7.4 \times 10^4 \text{ J.m}^{-3}$.

1.3.3 Magnetostatic energy

Magnetostatic energy effects arise from any magnetisation distribution which results from the build up of magnetic charge at the surface of a magnetic specimen and also from within a volume when the magnetisation distribution is discontinuous or divergent. As mentioned above, these poles generate a field which exists both inside (demagnetising field) and outside (stray field) the specimen, with H_d opposing the magnetisation.

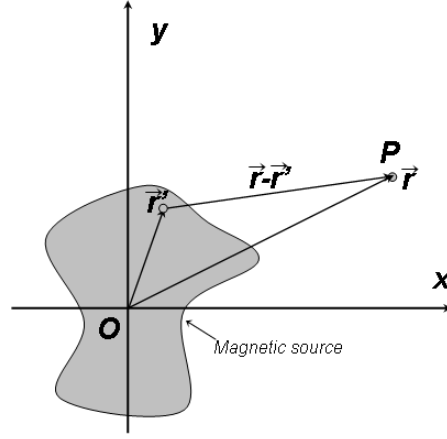


Figure 1.4: The magnetic field generated by a field source at the point P: due to surface magnetic charge and volume magnetic charge from a point \mathbf{r}' .

The magnetostatic energy in the SI unit will be given by:

$$E_d = -\frac{\mu_0}{2} \int_V \mathbf{M} \cdot \mathbf{H}_d dV \quad (1.11)$$

with μ_0 is the permeability of free space. The magnetostatic field, H_d at a point P at a position \mathbf{r} to the origin of the coordinate (O) originates from the surface (S) and the volume (V) charges (see Fig. 1.4), represented by [11]:

$$\mathbf{H}_d = \frac{-1}{4\pi} \int_V \frac{\nabla \cdot \mathbf{M}}{|\mathbf{r} - \mathbf{r}'|^2} dV' + \frac{1}{4\pi} \int_S \frac{\mathbf{M} \cdot \mathbf{n}}{|\mathbf{r} - \mathbf{r}'|^2} dS' \quad (1.12)$$

where \mathbf{r} is the position vector for the point at which the field from the magnetic charge is evaluated, \mathbf{r}' is the position of the differential magnetic charge. The magnetostatic energy of the specimen can be reduced by decreasing the amount of stray field generated at the edges or within the specimen. This can be achieved by the formation of the domain structure (section 1.4).

1.3.4 Zeeman energy

When the specimen is placed in an external field, the magnetic moments within the specimen will tend to align parallel to the applied field. The Zeeman energy takes into account the orientation of the magnetisation with respect to the applied field and given by [11]:

$$E_z = -\mu_0 \int_V \mathbf{M} \cdot \mathbf{H} dV \quad (1.13)$$

1.3.5 Magnetostrictive energy

Magnetostrictive energy is associated with materials in which the dimension of a ferromagnet is changed when subjected to an external magnetic field. Conversely, the magnetisation of the ferromagnet will be varied when it is exerted by a stress. As a result, the magnetostrictive energy term is written as [9]:

$$E_\lambda = \int_V \frac{3}{2} \lambda_s \sigma \sin^2 \alpha dV \quad (1.14)$$

where α is the angle between saturation magnetisation and the stress, σ . The λ_s is the saturation magnetostriction of the material, e.g. $\lambda_s = -0.2 \times 10^{-6}$ for $Ni_{81}Fe_{19}$ polycrystalline film [12].

The magnetostrictive energy is originated from spin-orbit interaction in ferromagnetic materials. The magnetostriction occurs when the electron cloud is not in spherically symmetric shape and has strong spin-orbit interaction. Under an applied magnetic field, the orbital moment tends to align with the field and distort the orbit. This effectively alters the position of the atom within the material and creates mechanical strain. The specimen either expands (positive magnetostriction) or contracts (negative magnetostriction) in the direction of the magnetisation.

1.3.6 Total energy

The total energy of a ferromagnetic specimen is the sum of the individual energy terms which are described above:

$$E_{total} = E_{ex} + E_k + E_d + E_z + E_\lambda \quad (1.15)$$

and the magnetic configuration (domain structure, which will be discussed in the next section) is a direct consequence of its local or global minimisation.

1.3.7 Micromagnetic simulation

Micromagnetic simulation is a useful method to model and interpret the magnetic state in magnetic objects. The output results of micromagnetic simulation will be used in chapter 4 to calculate Fresnel images of magnetic objects in Lorentz TEM. Therefore, micromagnetic simulation is required to create the input for image calculation. The

Chapter 1: Magnetism and magnetic material

Objective Oriented Micromagnetic Framework known as OOMMF package is a good choice for micromagnetic simulation. OOMMF is one of the most popular software for simulating the spin configuration of the small magnetic elements, developed by National Institute of Standard and Technology (NIST) [13].

The OOMMF works based on the micromagnetism by solving the Landau-Lifshitz-Gilbert (LLG) equation [15, 16] given by:

$$\frac{d\mathbf{M}}{dt} = -|\gamma|\mathbf{M} \times \mathbf{H}_{\text{eff}} - \frac{|\gamma|\alpha}{M_s}\mathbf{M} \times (\mathbf{M} \times \mathbf{H}_{\text{eff}}) \quad (1.16)$$

Where \mathbf{M} and \mathbf{H} are the magnetisation and external magnetic field, α is Gilbert damping constant and γ is the electron gyromagnetic ratio (not confused with directional cosine in 1.3.3). The first term arises from precession whereas the second one relates to the damping contribution as described in Fig. 1.5. The LLG equation is a differential equation describing the damped precessional motion of magnetisation \mathbf{M} under an application of the applied field.

OOMMF allows the distribution of the magnetic moments in a nano-sized ferromagnet with a particular size and shape to be determined, that is based on different energy contributions by using finite difference method. The finite difference method [14] is a numerical technique for finding approximate values of solutions of problems involving partial differential equations based on the idea of replacement of differential operators i.e. space, time etc. by finite difference (FD) operators. To perform this, a partial differential equation is converted to a system of algebraic equations which can be solved numerically by an iterative process. In the case of a magnetic element, the LLG equation is the main differential equation, and different energy contributions have to be approximated to their finite difference. The technique requires the use of a square

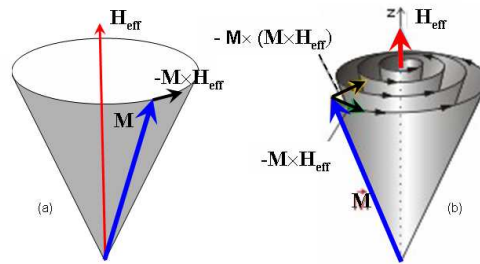


Figure 1.5: Larmor precession with damping of the magnetic moment in external applied field: (a) precessional motion without damping, (b) gyro-precessional motion with damping.

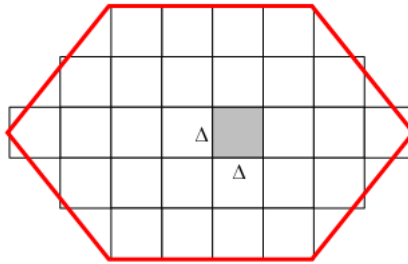


Figure 1.6: Discretisation of a 2D domain into FD cells of side, Δ , in which the micromagnetic equations are satisfied. The red outline denotes the boundary of a particle.

mesh (Fig. 1.6).

In the case of a magnetic element, the element is divided into cubic cells in which the magnetisation is uniform in each cell. The size of the cell is normally of the order of the ferromagnetic exchange-interaction length, L_{ex} of the material in the element (e.g. $L_{ex} = \sqrt{\frac{A}{2\mu_0 M_s^2}} \approx 4 \text{ nm}$ - for $\text{Ni}_{81}\text{Fe}_{19}$). It is important to note that if the cell size is much larger than the exchange-length, the results are unrealistic. In contrast, a too small cell size may take a long time of calculation. OOMMF then uses the Landau-Lifshitz-Gilbert equation to calculate the magnetisation at each field step. Starting from an initial state, the spins are adjusted to take into account the physical geometry and effective field before the total energy is estimated. The overall system is updated simultaneously with each time step and this procedure is repeated until the magnetisation is derived into an equilibrium state which is approached when the torque or dM/dt falls below a critical value. Alternatively, the control point is determined by a maximum iteration count or simulation time. Once the magnetisation has reached the equilibrium, the system is said to be converged. Because the external field is applied in a stepwise manner, this process has to be repeated with every perturbation. Finally, the simulation is completed with the hysteresis loops and domain structure of the object at each step [17].

1.4 Magnetic domains and domain walls

A ferromagnet may be divided into domains in order to minimise the micromagnetic energy. Therefore, understanding the magnetic domain configuration and domain wall structure is crucial for micromagnetic investigations.

1.4.1 Domain configurations

The concept of magnetic domains was firstly established by Weiss [5]. A magnetic domain is a region in which the magnetic moments align parallel. The existence of magnetic domains was indirectly confirmed at first by the detection of the Barkhausen jump [20] in the magnetisation curve, in which the reorientation of domains caused discrete changes in the magnetic induction within a ferromagnetic specimen which could be probed by a suitable amplification of the signal from a search coil wound around the specimen. The second confirmation, and the first direct visualisation was the observation of magnetic domain patterns on the surface of a ferromagnetic material by Bitter [21]. In the experiment, Bitter used a suspension solution made of the fine magnetic powder suspended in a carrier liquid which was spread on the surface of the specimen. The domain patterns were observed in the particle accumulations when viewed under an optical microscope.

The formation of the magnetic domains was subsequently explained in theory by Landau and Lifshitz [15, 16] and then developed by Kittel et al. [18]. Later micromagnetic theory established by William Fuller Brown Jr. in 1963 [22], explained the existence of domains as a consequence of the micromagnetic energy minimisation. For example, a breakup of the magnetisation into localised regions (magnetic domains) providing for

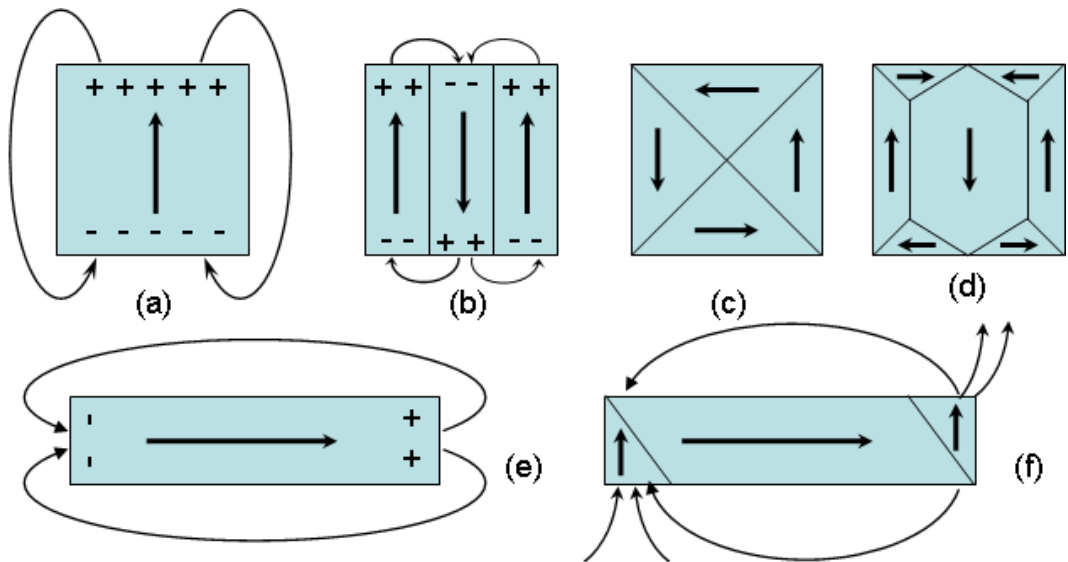


Figure 1.7: Variation of domain structure in a square thin film element: a) single-domain cubic, b) multi-domain state with large magnetostatic energy, c) magnetocrystalline anisotropy, d) anisotropic flux closure, e) single-domain shape-anisotropic state in a rectangular element, f) S-state in the rectangular.

flux closure at the ends of the specimen, reduces the magnetostatic energy. It is provided that the decrease in magnetostatic energy is greater than the energy necessary for forming domain walls then multi-domain patterns will arise. Some examples can be referred to Fig. 1.7: strong uniaxial anisotropy cubic square patterned film with large stray field (a), multidomain in uniaxial square to reduce stray field, and magnetostatic energy but increasing exchange energy (b), flux-closed square patterned soft magnetic thin film without stray field, no magnetostatic energy (c), weak uniaxial anisotropy with reduced magnetostatic energy (d), single-domain strong shape anisotropy with stray field and magnetostatic energy (e) and multi-domain shape anisotropy with reducing magnetostatic energy (f).

The configurations with non-global minimisation are called metastable states and are the local minimisation for the system. The configuration supported by a sample depends on the magnetisation history of the material as well as the strength and direction of the applied magnetic field. Applying a particular field will usually vary the configuration from one state to another.

1.4.2 Domain wall configurations

A magnetic domain wall is the boundary separating two magnetic domains. The existence of domain walls as the transitional regions between magnetic domains was firstly suggested by Bloch [23]. Within the wall, the magnetic moments of the specimen gradually rotate between two directions of the magnetisation in the domains. As the rotation occurs smoothly over many atoms, the domain wall width is a number of atomic spacing, $w = N.a$ (N is the number of atoms). However, because the walls introduce additional exchange, anisotropy, and magnetostatic energy into the system, their width will be an important parameter and dependent on an equilibrium state between the different energy terms.

As the magnetic moment in the wall is gradually rotated from one direction to another, an amount of exchange energy can be calculated, and as there are a number of magnetic moments away from the easy axis, the anisotropy energy is also included. The magnetostatic contribution is caused by the magnetic charges on two sides of the wall due to the divergence of the magnetisation. Hence, the competition between these additional energies will determine the width of the wall and the type of the wall. A

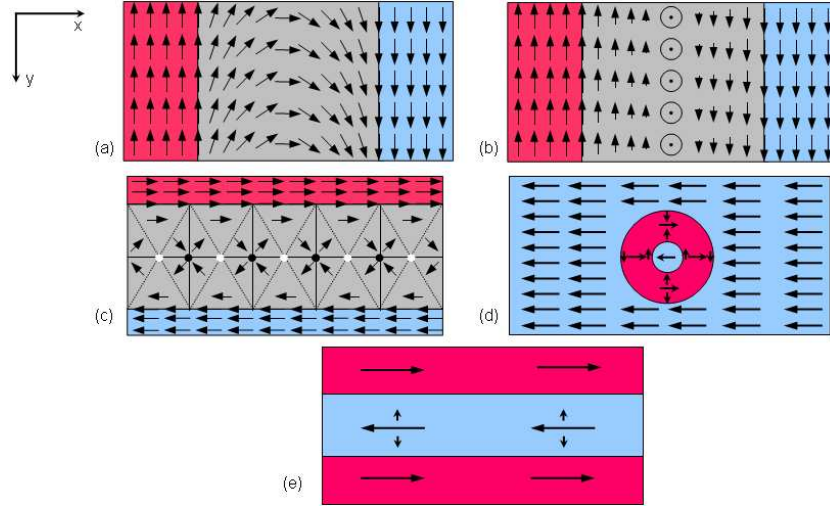


Figure 1.8: Plan view schematic illustrations of Bloch-type wall (a), Néel-type wall (b), cross-tie wall (c), 360° wall loop (d) and linear 360° wall (e). Film plane is xy .

magnetic domain wall is identified by its spin configuration and the angle through which the magnetic moments rotate in going from one domain to the next one. There are basically two types of domain wall: Bloch-type wall (a) and Néel-type wall (b) (Fig. 1.8). In the Néel wall, magnetic moments gradually rotate in plane of the film whereas in the Bloch wall, the magnetic moment rotation is out-of-plane. There is no divergence of the magnetisation for the Bloch wall. Hence, the Bloch walls are favourable in the thick film ($> 90 \text{ nm}$) in which the associated stray field is small. Taking into account the different energy terms, the width of a Bloch domain wall only depends on the exchange and magnetocrystalline anisotropy.

$$\delta_B = \pi \sqrt{\frac{A}{K_1}} \quad (1.17)$$

here, A and K_1 are the exchange constant and magnetocrystalline anisotropy constant of the material, respectively. For example, iron has $A = 8.3 \times 10^{-12} \text{ J.m}^{-1}$, $K_1 = 5 \times 10^4 \text{ J.m}^{-3}$ [24], therefore, it has a Bloch wall width $\delta_B \approx 40 \text{ nm}$.

Whereas, in the thin film, the out-of-plane magnetisation intersects the surface, free poles are created, therefore, the Bloch wall may become unfavorable. Instead the Néel wall structure occurs. The width of a Néel wall is dependent on the exchange energy, anisotropy energy and magnetostatic energy terms. It is notable that there are different definitions of the domain wall width. In the present thesis, the domain wall width is defined as the full width at maximum of the derivative of the induction distribution

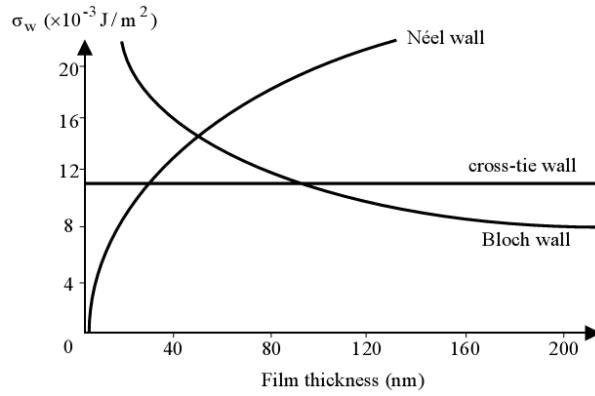


Figure 1.9: Phase diagram of permalloy film showing energy density of Néel wall, Bloch wall and cross-tie wall as a function of film thickness [25].

(see chapter 5, section 5.4). There have been a number of methods to determine the domain wall width e.g. Lorentz microscopy, SEMPA, X-ray microscopy, SP-SPM, etc. A calculated domain wall phase diagram of permalloy ($\text{Ni}_{80}\text{Fe}_{20}$) film [25], which describes the thickness dependence of wall energy density, σ_w , is illustrated in Fig. 1.9. It is noticed that besides the thickness of the film, magnetocrystalline anisotropy of the materials is also an important factor for Bloch-Néel walls transition. A variety of different domain wall configurations are possible by combining the basic Néel and Bloch type walls. These more complicated structures occur as the system tries to minimise the total energy. One common example is a cross-tie wall [26, 27] (Fig. 1.8(c)) which, from Fig. 1.9, is found in film thicknesses of between 30 and 90 nm for permalloy films. Other examples of complex domain wall configurations include 360° domain wall loops. These walls have been observed frequently in multilayer films [34–36] and appear in chapter 6 in the work on CoIr film.

The magnetisation on either side of the 360° wall lies in the same direction. Linear 360° walls (Fig. 1.8(e)) often form during reversal sequence in thin films due to the overlap of two low angle walls. The linear walls can join up to form 360° wall loops (Fig. 1.8(e)). The 360° walls are energetically unfavorable and can locally inhibit magnetisation reversal and so have a strong influence on the behaviours of magnetic thin films and elements.

1.4.3 The magnetic vortex

The magnetic vortex (or a vortex core) is a magnetic structure, which consists of an out-of-plane magnetisation (M_z - Figs. 1.10(b,c)) at its core and in-plane curling mag-

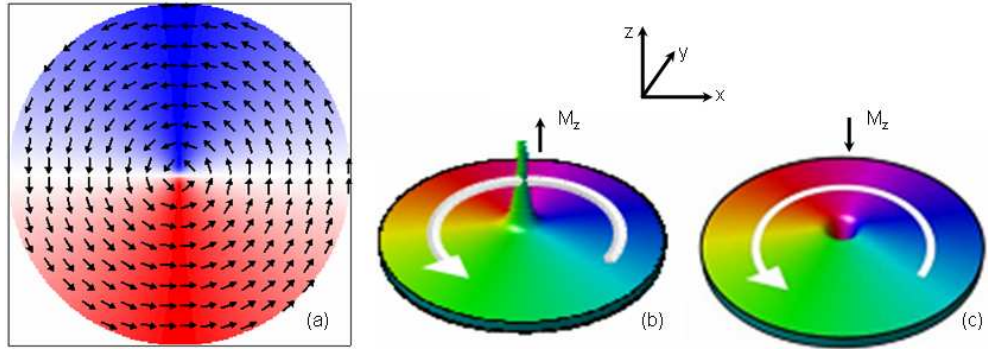


Figure 1.10: Spin configuration in a magnetic vortex (a): the in-plane magnetisation curls around the vortex core (counter clockwise chirality) whereas the magnetisation points perpendicularly to the wall plane at the centre of the core (b, c) to create the polarity.

netisation (M_x , M_y - Fig. 1.10(a)) around the vortex core. Magnetisation vortices are found frequently in ferromagnetic patterned film states which have a small amount of stray field. Hence, it could be remarked that the vortex wall is identified by the chirality (clockwise, or counter-clockwise) of in-plane magnetisation, and the polarity of the out-of-plane magnetisation (upward or downward). Figure 1.10 illustrates an example of spin configuration in a vortex wall with a counter clockwise chirality and two states of polarity. The formation of a magnetic vortex can be controlled by the geometry of the element e.g. in sub-micrometre circular, elliptical dots, square elements etc. Furthermore, the vortex structure may transform to single-domain state when the thickness and the diameter of the circular dot decrease as presented previously in Cow-

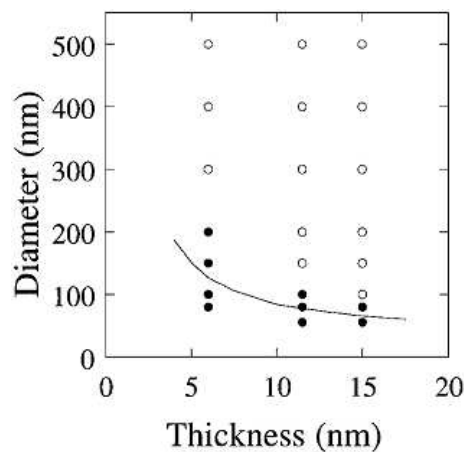


Figure 1.11: An experimental phase diagram of transformation from vortex state to single domain state in permalloy nanodots. The figure is redrawn from ref. [28]: dark dots denote the single-domain state, circular dots denote the vortex structure and the solid line shows a lower bound to the theoretical phase boundary between the vortex state (above the boundary) and the single-domain state (below the boundary).

burn et al. report [28] illustrated in Fig. 1.11. This showed that the vortex structure (circle dots in Fig. 1.11) only occurs in large diameter dots. The critical diameter to form the vortex structure increases with the thickness of the film.

Recently, some authors [29–31] have concentrated on controlling the switching properties of a vortex core by spin-polarised current. They indicate that a magnetic vortex with a given polarity should be a promising candidate for a memory cell in near-future non-volatile data-storage. Hence, determination of polarity of vortex will be crucial for both fundamental and application aspects. By using the magnetic force microscopy (MFM), the polarity of vortex core could be probed [31] but actually the MFM imaging tends to be slow and may perturb the magnetic state of the sample. Additionally X-ray Circular Dichroism (XMCD) has been used to detect the polarity of the vortex [32]. Recently, Junginger et al. [33] reported that it is possible to determine the polarity of vortex core with electron holography. Electron holography can provide the image with very high resolution but the experimental process involves reconstruction of the electron phase. In chapter 4, the study of determination of vortex polarity using simple Fresnel image in LTEM will be presented.

1.5 Hysteresis loop and magnetisation reversal

The magnetisation of ferromagnetic materials not only depends on the magnetic field, but also on the previous history of the magnetisation. This causes a behaviour named hysteresis phenomenon or hysteresis loop (Fig. 1.12). When a ferromagnet is placed into a magnetic field, a net magnetisation is induced in the field direction. Increasing the field gives rise to an increase of magnetisation to saturation state, M_s . When the magnetic field is removed, the magnetisation then drops to a non-zero value known as remanent magnetisation (so-called remanence), M_r . A field applied in the opposite direction will then decrease the magnetisation to zero at the negative field named coercivity or coercive field, H_c . Increasing the negative field saturates the magnetisation in the opposite direction. A similar process can be seen when the field is varied from negative saturation field to positive saturation field. The $M - H$ graph produced as the field is swept between positive and negative values is known as a hysteresis loop. This type of hysteresis loop is called a major loop since the magnetisation is driven

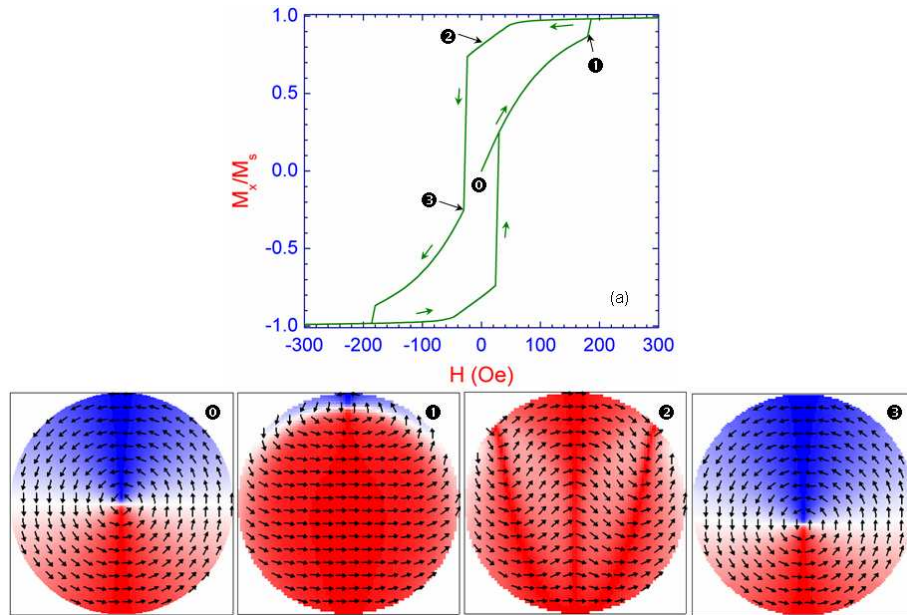


Figure 1.12: Hysteresis loops of the 600 nm diameter, 20 nm thick $Ni_{80}Fe_{20}$ circular element with perpendicular edge shape, and magnetic structure at various states: (0): demagnetised state, (1) before annihilation of vortex, (2) remanent and (3) after vortex nucleation.

between saturation in opposite directions. Cycling between smaller field values results in minor loops of which there can be an infinite number.

When an external field is applied, the magnetisation can change direction to align with the field in two different ways. One mechanism is coherent rotation. In this situation, the magnetic moments rotate smoothly from one direction to the other. This mechanism was firstly described by Stoner and Wohlfarth in 1948 with a model of small single-domain particles [37]. Although this model places a single domain constraint on the system, it can be used in a modified form to deal with more complicated problems [38]. However, in certain systems it may be favourable for reversal to occur through domain processes. This mechanism involves the nucleation of domains and domain walls, and subsequent domain wall motion. For example, considering a 20 nm thick $Ni_{80}Fe_{20}$ circular disk with diameter of 600 nm exhibiting initial vortex structure at the centre (Fig. 1.12) and a magnetic field is applied along x axis, the vortex core will move perpendicularly to the field to the top of the disk, causing the magnetic moments to align parallel to the field. This process is reversible up to a magnetic field, at which the vortex is annihilated (180 Oe). The magnetisation process is completed by an expulsion of vortex to saturate the disk.

From the hysteresis characteristics, the ferromagnetic materials can be divided into

two categories:

- **Hard magnetic materials:** These ferromagnets (e.g. $\text{Nd}_2\text{Fe}_{14}\text{B}$, CoPt), require a large applied field to be magnetised or demagnetised. Normally, a hard magnet has a large coercivity (because of high magnetocrystalline anisotropy). The hard magnets are used for permanent magnets, recording magnetic thin film, etc.
- **Soft magnetic materials:** A type of ferromagnetic material (e. g. NiFe , FeSi , FeSiB), which is easy to be magnetised and demagnetised. A soft magnet exhibits a small coercivity due to low magnetocrystalline anisotropy and may has a high saturation magnetisation and high permeability.

1.6 Magnetoresistance and spintronics

Magnetoresistance is the property by which some materials change their electrical resistance when an external magnetic field is applied to the sample. This effect was firstly discovered by William Thomson (commonly known as Lord Kelvin) in 1856 [39] in some ferromagnetic samples such as iron, nickel with a changing in resistance about 5% in several tens kG applied field. This effect was later called anisotropic magnetoresistance (AMR). Since then, however, other types of magnetoresistance have been discovered including giant (GMR) [3, 4], tunneling (TMR) [40, 41] and colossal magnetoresistance (CMR) [42], which have been shown to give larger effects. Nowadays, magnetoresistance is an important phenomenon in magnetism and spintronics.

1.6.1 Anisotropic magnetoresistance

The magnetoresistance observed in iron and nickel samples by Lord Kelvin was subsequently called anisotropic magnetoresistance (AMR) in 1951 by J. Smit [43]. The AMR is known as a dependence of the resistivity, ρ , on the angle, δ between the current density, \mathbf{J} and the magnetisation, \mathbf{M} . In a polycrystalline sample, the AMR effect is normally described as follows [44]:

$$\rho = \rho_{\perp} + (\rho_{\parallel} - \rho_{\perp}) \cos^2 \delta \quad (1.18)$$

with ρ_{\perp} and ρ_{\parallel} are the resistivity of the sample when $\mathbf{J} \perp \mathbf{M}$ and $\mathbf{J} \parallel \mathbf{M}$, respectively. AMR has been used for magnetic sensors and read heads in hard disks (later

substituted by giant magnetoresistive sensor). Recently, AMR is considered as a useful method to measure the domain wall resistance in nanostructures [45].

The mechanism of the anisotropic magnetoresistance in metallic films has been explained by spin-orbit interaction [43, 44]. When a current passes through a ferromagnetic sample, the conducting electron (s-state electron) is scattered by the electron spin in the sample including s and d electrons (e.g. 3d in ferromagnetic metals). The magnetoresistance in this situation is contributed by s-s and s-d scattering in which the s-d scattering is dominant. The s-d interaction (spin-orbit interaction), which makes the magnetisation align to a certain crystallographic direction, causes an anisotropic scattering mechanism. The symmetry of the wave functions is lowered by the spin-orbit interaction, which result in a resistance anisotropy [43].

1.6.2 Giant magnetoresistance

Giant magnetoresistance (*GMR*) is quantum mechanical magnetoresistance effect observed in multilayer films composed of alternating ferromagnetic and nonmagnetic layers and was first observed independently by two groups in 1988: in *Fe/Cr* superlattice by French group led by Albert Fert [3] and in *Fe/Cr/Fe* trilayer film by Peter Grunberg in Germany [4]. The discovery of GMR is commonly considered as the birth of spintronics, resulting in a Nobel Prize in Physics awarding for Fert and Grunberg in 2007. The term giant magnetoresistance was coined to describe this effect. This discovery led to the prospect of artificially engineering multilayered structures with complex magnetic structures, useful not only for understanding the physical nature of the materials but also for technological applications. Indeed, the magnetic thin films with GMR have already created plenty of applications such as for storing information in magnetic storage devices, magnetoresistive read heads, for magnetic random access memory (MRAM) etc. Furthermore, applications using hybrid magnetic/semiconductors structure, spin-switched devices based on transport of spin-polarised electrons across magnetic/nonmagnetic interface have been proposed and devised [47]. The origin of the GMR is a complex process and there have been several models to explain it e.g. mechanism of spin-dependent scattering of electrons [47] in which the resistance of the system depends on the relative orientation of magnetisation of the layers. When the electron passes through the system, it is scattered by the magnetisation of the

layers, causing a contribution into the resistance of the system. Such a contribution is independent on the orientation of the magnetisation in the layers. Low resistance is observed when magnetisations align parallel to each other whereas the resistance reaches maximum when the magnetisations are antiparallel.

1.6.3 Domain wall resistance

The studies of GMR usually involve multilayer structures, in which the process of interest typically occurs when an electron moves between layers of different composition (hence also different magnetisation either in direction or magnitude or both). A similar process is encountered when an electron passes through a domain wall in a chemically homogeneous material as can occur in a simple ferromagnetic wire or thin film. This is known as domain wall resistance.

Early results of domain wall resistance evidence were indirectly pointed out as early as the 1930s in Barkhausen jumps. The resistance jump of the sample was interpreted in terms of the AMR within the domains, rather than arising from the walls themselves. One of the most important pieces of evidence of domain wall resistance was concerned with the magnetoresistance of Fe whiskers [48, 49]. Particularly, the variation of the resistance on going to multi-domain state was very large at liquid helium temperature [49]. Some years later, some authors published reports on experiments on thin film samples. Okamoto et al. [50] reported both extraordinary Hall effect and the magnetoresistance of GdCo film and concluded that this system was closely related to the domain wall structure although no attempt to separate different possible mechanisms was made at this stage.

The domain wall resistance could be simply understood as due to the scattering of electrons from the magnetic moments in the wall because the magnetic moments in the wall deviate from domain to other domain. In recent years, the idea of an intrinsic domain wall resistance arising from spin-polarised current has been developed. Viret et al. [51] used a model of pseudo-Larmor precessions of electron spin around the rotating exchange field in a wall (semi-classical model of domain wall resistance) to explain small deviation from a pure AMR behaviour in magnetoresistance of Ni and Co films. The following year, Levy and Zhang [52] designed a fully quantum mechanical version of essentially this model. A fully worked-out model to describe the domain wall resistance

is being developed and domain wall resistance definition became specially importance in domain wall spintronics [53].

1.6.4 Spintronics

Spintronics (short for spin electronics), sometimes called magnetoelectronics, is the term given to microelectronic devices that function by exploiting the spin of electrons instead, or in addition to, the charge degree of freedom. For example, spin relaxation and spin transport in metals and semiconductors are of fundamental research interest not only for basic solid state physics issues, but also for the already demonstrated potential application in electronic technology. A well-known device that is already in use in industry as a read head and a memory-storage cell is the giant-magnetoresistive (GMR) sandwich structure which consists of alternating ferromagnetic and nonmagnetic metal layers. The configuration in this case involve two ferromagnetic layers separated each other by a non-magnetic layer deposited on the top of an antiferromagnetic layer. The magnetisation of the bottom ferromagnetic layer is pinned by the exchange-coupling with the antiferromagnetic layer. The magnetisation of the top ferromagnetic freely is reversed by the external field. Therefore the magnetoresistance of the device is only dependent on the orientation of the magnetisation of the top layer. This configuration is called spin-valve [2–4]. Spintronics research currently involves metallic ferromagnetic devices (based on GMR, TMR, DWR etc) and dilute magnetic semiconductors [1]. Among metallic ferromagnetic spintronics, there have been a number of devices based on controlling magnetic domain walls have been developed such as logic gates [54,55], race-track memory [56,57], or microwave excitation [58]. In such devices, the information bits are defined as the direction of the magnetisation [55], that is separated by a magnetic domain wall. The operation of the devices is utilised by controlling the propagation of the domain walls in the nanostructure.

1.7 Magnetic recording media and soft underlayer

1.7.1 Magnetic recording media

One of recent great efforts of the magnetism has been to develop the magnetic recording with high density and high processing speed. Since 1950s, hard disk drives (HDDs)

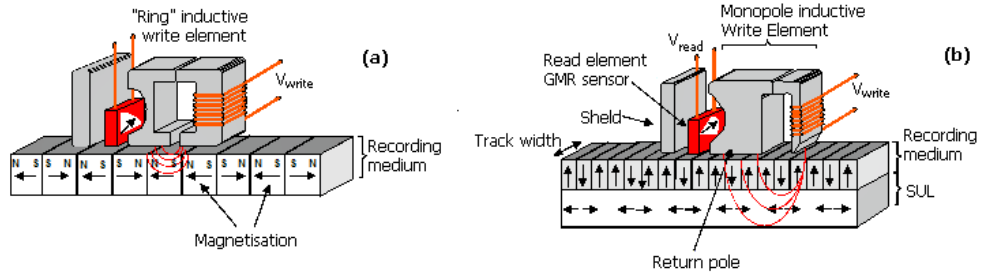


Figure 1.13: Two recording methods in magnetic recording hard disk: longitudinal recording (a) and perpendicular recording (b) (from Hitachi Global Storage Technology).

have been employed in computers when IBM introduced the random access method of accounting and control. The magnetic recording technology nowadays involves two methods in terms of alignment of magnetisation in hard magnetic storage layer (Fig. 1.13(a)). First way is called longitudinal recording in which the magnetisation of magnetic bit lies in plane of the recording medium. With continued growth in the areal recording density there is a risk of spontaneous demagnetisation of the bits due to thermal effects, this is known as the superparamagnetic effect and places a limit on the maximum achievable recording density [59]. An alternative approach is perpendicular recording in which the magnetisation points perpendicular to the plane of the recording medium (Fig. 1.13(b)). Aligning the bits in this manner takes less platter than what would have been required had they been placed longitudinally so they can be placed closer together on the platter, thus increasing the number of elements that can be stored in a given area [59].

1.7.2 Soft underlayer in perpendicular recording media

The main layers in a perpendicular recording medium are illustrated in Fig. 1.14. The information is stored in the hard magnetic layer (magnetic recording layer) of which a perpendicularly uniaxial anisotropy induced by an intermediate layer is required. The presence of the soft magnetic underlayer (SUL) is necessary as the SUL guides the magnetic flux from the write pole to the collector pole with low reluctance in order to close magnetic circuit during the writing process (Fig. 1.14(b)). Hence, the materials for SUL have high permeability, high saturation magnetisation and low coercivity [59]. Some typical SULs involve NiFe, CoFe, FeAlN, CoNbB, CoFeB, FeTaN, etc. The thickness of the SUL conventionally ranges between 100 and 400 nm. Note that, a thick

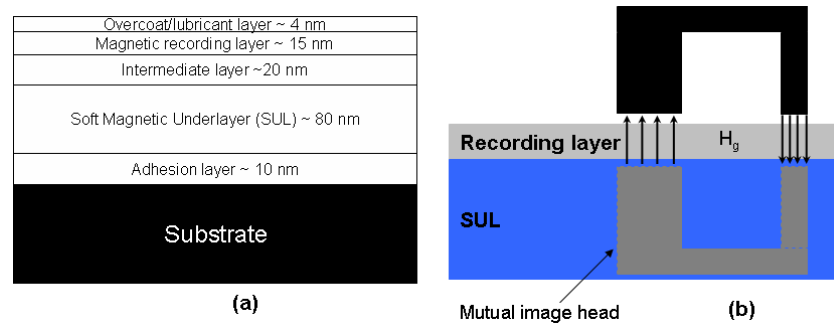


Figure 1.14: The cross-sectional stack of a perpendicular recording medium (a) and writing process in perpendicular magnetic recording (b) with mutual mirror configuration for closing magnetic circuit.

SUL may increase significantly the layer roughness, thus prohibiting the head flying close to the recording media however a thin SUL is not reliable because of the reduction of the writing ability [63, 64].

In the absence of a magnetic field, the SUL may form domains, e.g. stripe domains or 180° domains with Bloch-type domain walls. However, the formation of such domain walls will generate strong magnetic fields, which will contribute to strong noise during the reading process, named spike noise. The spike noise is made from a magnetic field created by the magnetic domain walls. The domain walls can affect the permeability of the soft magnetic layer locally. This permeability change gives the change of transfer function from the recording layer to the read head, and causes the variation of read signal around the domain walls.

Furthermore, thick SULs cause another technical problem called wide adjacent track erasure (WATE). The WATE phenomenon is a problem specific to a perpendicular magnetic recording medium, and is a phenomenon in which, when a signal is recorded in a particular track, signals are demagnetised over a broad area extending for several μm from the recorded track. The WATE occurs over a range of several micrometers in the off-track direction [59]. To suppress the spike noise, the formation of the single domain structure over the whole disk-shaped SUL stacked on or under an antiferromagnetic layer has been suggested in order to prevent the formation of Bloch walls [65]. To reduce the WATE, a multilayer SUL with magnetic moments aligned antiparallel by Ruderman-Kittel-Kasuya-Yoshida (RKKY) coupling is known to be effective [66] (RKKY refers to a coupling mechanism of nuclear magnetic moments or localised inner d or f shell electron spins in a metal by means of an interaction through the conduction

electrons). However, it seems to be a challenge to suppress both artefacts. Hence, the suppression of spike noise and WATE are important technical issues for the development of perpendicular recording technology [64].

The work in chapter 6 will concentrate on investigating the physical microstructure and micromagnetic behaviour in a CoIr film which is considered as one of the best SULs to overcome these issues [63, 64]. The WATE can be suppressed by realising wide distribution of magnetic flux around the return yoke, which can be achieved by reducing the local susceptibility of the SUL in the direction normal to the film plane. The spike noise is eliminated by forming the Néel walls instead of Bloch wall even in thick films above 100 nm. These are supported by a perpendicular negative anisotropy induced by c-plane texture normal to the film plane.

Bibliography

- [1] I. Zütic, J. Fabian, S. Das Sarma, *Rev. Mod. Phys.* **76** (2004) 323.
- [2] A. Fert, *Rev. Mod. Phys.* **80** (2008) 1517.
- [3] M. N. Baibich, J. M. Broto, A. Fert, F. Nguyen Van Dau, F. Petroff, P. Eitenne, g. Creuzet, A. Friederich, and J. Chazelas, *Phys. Rev. Lett.* **61** (1988) 2472.
- [4] G. Binasch, P. Grunberg, F. Saurenbach, and W. Zinn, *Phys. Rev. B* **39** (1989) 4828.
- [5] P. Weiss, *J. Phys. Theor. Appl.* **6** (1907) 661-690.
- [6] W. Heisenberg, *Z. Phys.* **49** (1928) 619-636.
- [7] M. C. Hickey, A. Atkinson, C. H. Marrows, B. J. Hickey, *J. Appl. Phys.* **103** (2008) 07D518.
- [8] B.D. Cullity, C.D. Graham, *Introduction to Magnetic Materials*, John Wiley (2008) ISBN: 0471477419.
- [9] P. R. Ohodnicki, K. Y. Goh, M. E. McHenry, K. Ziemer, Z. Chen, C. Vittoria, V. G. Harris, *J. Appl. Phys.* **103** (2008) 07E514.
- [10] J. A. Osborn, *Phys. Rev.* **67** (1945) 351.
- [11] D. C. Jiles, *Introduction to Magnetism and Magnetic Materials* 1st ed. Springer (1990) ISBN-10: 0412386402.
- [12] Y. K. Kim, T. J. Silva, *Appl. Phys. Lett.* **68** (1996) 2885.
- [13] <http://math.nist.gov/oommf/>

Chapter 1: Magnetism and magnetic material

- [14] K.W. Morton and D.F. Mayers, *Numerical Solution of Partial Differential Equations: An Introduction*, Cambridge University Press, (2005) 2nd ed. ISBN-10: 0521607930.
- [15] L. D. Landau, E. M. Lifshitz, *Phys. Z. Sowietunion* **8** (1935) 153.
- [16] T. L. Gilbert, *IEEE Trans. Magn.* **40** (2004) 3443-3449.
- [17] C. Brownlie, *A TEM Investigation of Controlled Magnetic Behaviour in Thin Ferromagnetic Films*, PhD thesis, University of Glasgow, 2007.
- [18] C. Kittel, *Rev. Mod. Phys.* **21** (1949) 541.
- [19] A. Hubert, R. Schafer, *Magnetic Domains: The Analysis of Magnetic Microstructure*, Springer, (1998), ISBN 3540641084.
- [20] H. Barkhausen, *Phys. Z.* **20** (1919) 401- 402.
- [21] F. Bitter, *Phys. Rev.* **38** (1931) 1903-1905.
- [22] Brown, William Fuller, Jr., *Micromagnetics*, (1963), Wiley.
- [23] F. Bloch, *Z. Phys.* **74** (1932) 295.
- [24] R. Skomski, J.M.D. Coeym, *Permanent magnetism*, Institute of Physics Publishing Ltd (1999) ISBN 07503 0478 2.
- [25] M. Prutton, *Thin ferromagnetic films*, Butterworth (1964).
- [26] E. E. Huber, Jr., D. O. Smith, and J. B. Goodenough, *J. Appl. Phys.* **29** (1958) 294.
- [27] N. Wiese, S. McVitie, J. N. Chapman, A. Capella-Kort, F. Otto, *Euro Phys. Lett.* **80** (2007) 57003.
- [28] R. P. Cowburn, D. K. Koltsov, A. O. Adeyeye, M. E. Welland, D. M. Tricker, *Phys. Rev. Lett.* **83** (1999) 1042.
- [29] S.-B. Choe, Y. Acremann, A. Scholl, A. Bauer, A. Doran, J. Stöhr, H. A. Padmore, *Science* **304** (2004) 420-422.

- [30] S-K. Kim, K-S. Lee, Y-S. Yu, Y-S. Choi, *Appl. Phys. Lett.* **92** (2008) 022509.
- [31] T. Shinjo, T. Okuno, R. Hassdorf, K. Shigeto, T. Ono, *Science* **289** (2000) 930-932.
- [32] K. W. Chou, A. Puzic, H. Stoll, D. Dolgos, G. Schultz, B. Van Waeyenberge, A. Vansteenkiste, T. Tylliszczak, G. Woltersdorf, C. H. Back, *Appl. Phys. Lett.* **90** (2005) 202505.
- [33] F. Junginger, M. Kläui, D. Backes, S. Krzyk, U. Rdiger, T. Kasama, R. E. Dunin-Borkowski, J.-M. Feinberg, R. J. Harrison, *Appl. Phys. Lett.* **92** (2008) 112502.
- [34] H. S. Cho, H. Fujiwara, *IEEE Trans. Magn.* **35** (1999) 3868-3870.
- [35] B. R. Craig, S. McVitie, J. N. Chapman, A. B. Johnston, and D. O. O'Donnell, *J. Appl. Phys.* **100** (2006) 053915.
- [36] M. Hehn, D. Lacour, F. Montaigne, J. Briones, R. Belkhou, S. El Moussaoui, F. Maccherozzi, N Rougemaille, *Appl. Phys. Lett.* **92** (2008) 072501.
- [37] E. E. Stoner, E. P. Wohlfarth, *Phil. Trans. Roy. Soc. A* **240** (1948) 599-642.
- [38] M. Labrune, J. C. S. Kools, A. Thiaville, *J. Magn. Magn. Mater.* **171** (1997) 1-15.
- [39] W. Thomson, *Proc. Roy. Soc.* **8** (1857) 546-550.
- [40] J. S. Moodera, Lisa R. Kinder, Terrilyn M. Wong, R. Meservey, *Phys. Rev. Lett.* **74** (1995) 3273-3276.
- [41] T. Miyazaki, N. Tezuka, *J. Magn. Magn. Mater.* **139** (1995) L231-L234.
- [42] S. Jin, T. H. Tiefel, M. McCormack, R. A. Fastnacht, R. Ramesh, L. H. Chen, *Science* **264** (1994) 413 - 415.
- [43] J. Smit, *Physica* **17** (1951) 612-627.
- [44] T. R. McGuire, R. I. Potter, *IEEE Trans. Magn.* **11** (1975) 1018-1038.
- [45] L. Thomas and S.S.P. Parkin, Current induced domain wall motion in magnetic nanowire, in *Handbook of Magnetism and Advanced Magnetic Materials*, Ed. by H.

Chapter 1: Magnetism and magnetic material

- Kronmüller and S. Parkin, Vol. 2: Micromagnetism* (2007) John Wiley & Sons, Ltd. ISBN: 978-0-470-02217-7.
- [46] M. Trushin, K. Výborný, P. Moraczewski, A. A. Kovalev, J. Schliemann, T. Jungwirth, *Phys. Rev. B* **80** (2009) 134405.
- [47] S. S. P. Parkin, *Annu. Rev. Mater. Sci.* **25** (1995) 357-388.
- [48] A. Isin, R. V. Coleman, *Phys. Rev.* **142** (1966) 372.
- [49] G. R. Taylor, A. Isin, R. V. Coleman, *Phys. Rev.* **165** (1968) 621.
- [50] K. Okamoto, T. Shirakawa, S. Matsushita, Y. Sakurai, S. Honda, T. Kusuda, *A.I.P. Conf. Proc.* **24** (1970) 113.
- [51] M. Viret, D. Vignoles, D. Cole, J. M. D. Coey, W. Allen, D. S. Daniel, J. F. Gregg, *Phys. Rev. B* **53** (1996) 8464.
- [52] P. M. Levy and S. Zhang, *Phys. Rev. Lett.* **75** (1997) 5110.
- [53] C.H. Marrow, *Adv. Phys.* **54** (2005) 585-713.
- [54] D. A. Allwood, Gang Xiong, M. D. Cooke, C. C. Faulkner, D. Atkinson, N. Vernier, and R. P. Cowburn, *Science* **296** (2002) 2003.
- [55] D. A. Allwood, G. Xiong, C. C. Faulkner, D. Atkinson, D. Petit, and R. P. Cowburn, *Science* **309** (2005) 1688.
- [56] S. S. P. Parkin, US Patent, 6834005 (2004).
- [57] S.S.P. Parkin, M. Hayashi, L. Thomas, *Science* **320** (2008) 5873.
- [58] L. Thomas, M. Hayashi, X. Jiang, R. Moriya, C. Rettner, S. S. P. Parkin, *Nature* **443** (2006) 197.
- [59] S. N. Piramanayagam, *J. Appl. Phys.* **102** (2007) 011301.
- [60] S. Iwasaki, K. Takemura, *IEEE Trans. Magn.* **11** (1975) 1173-1175.
- [61] S. Iwasaki, Y. Nakamura, K. Ouchi, *IEEE Trans. Magn.* **15** (1979) 1456-1458.

- [62] G. Choe, M. Zheng, E. N. Abarra, B. G. Demczyk, J. N. Zhou, B. R. Acharya, K. E. Johnson, *J. Magn. Magn. Mater.* **287** (2004) 159-166.
- [63] Hashimoto, S. Saito, M. Takahashi, *J. Appl. Phys.* **99** (2006) 08Q907.
- [64] M. Takahashi, S. Saito, *J. Magn. Mag. Mater* **320** (2008) 2868-2873.
- [65] K. Tanahashi, A. Kikukawa, N. Shimizu, Y. Hosoe, *J. Appl. Phys.* **91** (2002) 8049.
- [66] B. R. Acharya, J. N. Zhou, M. Zheng, G. Choe, E. N. Abarra, K. E. Johnson, *IEEE Trans. Magn.* **40** (2004) 2383.

Chapter 2

Instrumentation and fabrication techniques

2.1 Introduction

This chapter provides a short overview of fabrication techniques, that involve a variety of methods including physical, chemical process, computing design etc and generally involve two main groups called *top-down* and *bottom up*. The top-down nanofabrication includes the conventional lithographic methods (photolithography, electron beam lithography), and focused ion beam (direct-beam-writer lithography) that used to pattern the nanostructure for investigating in the present thesis.

A number of fabrication processes have to be carried out in a specially constructed and environmentally controlled laboratory called a cleanroom. A cleanroom is an environment, typically used in manufacturing or scientific research that has a low level of environmental pollutants such as dust, airborne microbes, aerosol particles and chemical vapors. The cleanliness of a cleanroom is represented by its class. A class 1 area has less than 1 particle/ ft^3 greater than $0.5\mu m$ in size whilst a class 100 area has less than 100 particle/ ft^3 . In addition to cleanliness, cleanrooms are designed to control temperature, humidity, air pressure, vibration, noise and lighting, all of which are factors that greatly affect the fabrication procedures. The main fabrication performed in this thesis was carried out in the James Watt Nanofabrication Centre (JWNC) at the University of Glasgow, a newly built, top of the range facility with rooms ranging from class 10,000 to class 10.

2.2 Substrates for fabrication

A substrate is a medium on which a film is grown. For samples to be imaged in the TEM, electron transparent Si_3N_4 membranes (Fig. 2.1) were used for thin film deposition and lithographic patterning. The selected substrate is a 50 nm thick, $100 \times 100 \mu\text{m}^2$ Si_3N_4 membrane window supported on a 500 μm thick bulk silicon [1]. The thickness 50 nm is to ensure both electron transparency and mechanical hardness of the membrane. These wafers are made in two main sizes: $2 \times 2 \text{ mm}^2$ single membranes for continuous film deposition or patterning with the focused ion beam, and $9 \times 9 \text{ mm}^2$ block of 4 membranes for electron beam lithography. The bulk silicon is wet etched through a Si_3N_4 mask on the back side of the substrate to leave the Si_3N_4 membrane on the opposite site. For lithography, an etched topographic cross and some alignment markers on the membrane are used to direct the electron beam to the transparent regions. Moreover, cleave lines allow the membrane substrate to be separated individually for subsequent measurements.

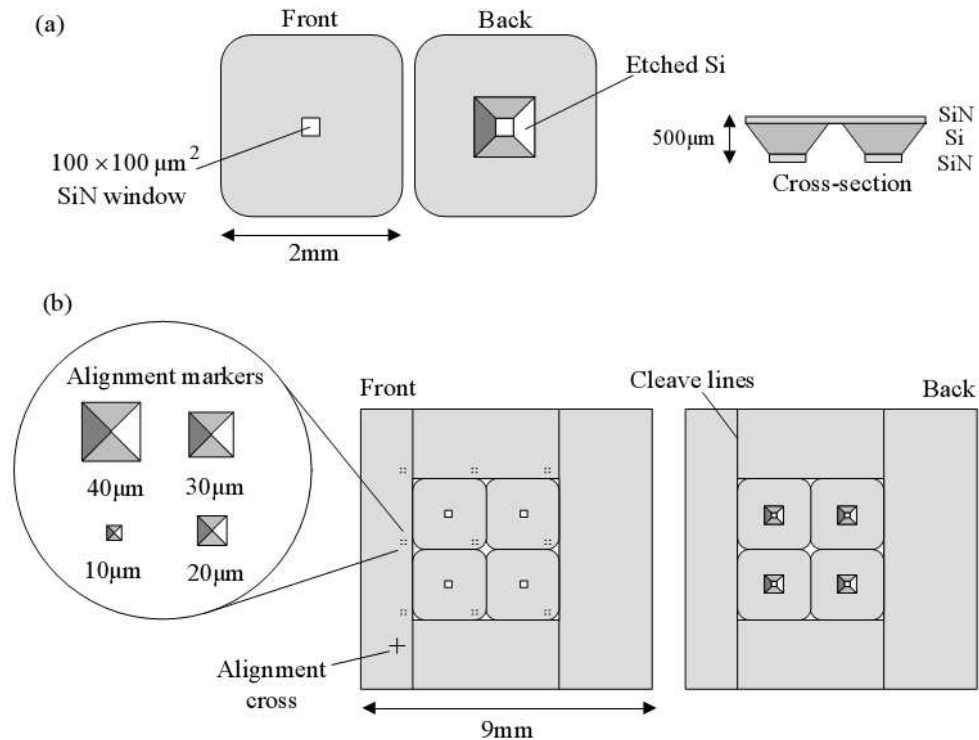


Figure 2.1: Front, back and cross-section (a) schematic diagrams of a single Si_3N_4 membrane, and a block of 2×2 membrane wafer used for thin film deposition and electron beam lithography (b) [2].

2.3 Thin film deposition

2.3.1 Thermal evaporation

Thermal evaporation is a conventional and common deposition technique that is well established. The technique is based on evaporating source material in vacuum by a heating resistor such that the material travels directly to the target substrate, where they will condense back to solid phase. This technique is used in microfabrication to make the thin films with thickness ranging from sub-micrometre scale to micrometre scale [3]. Firstly, a clean substrate is placed on the holder in the chamber. The raw

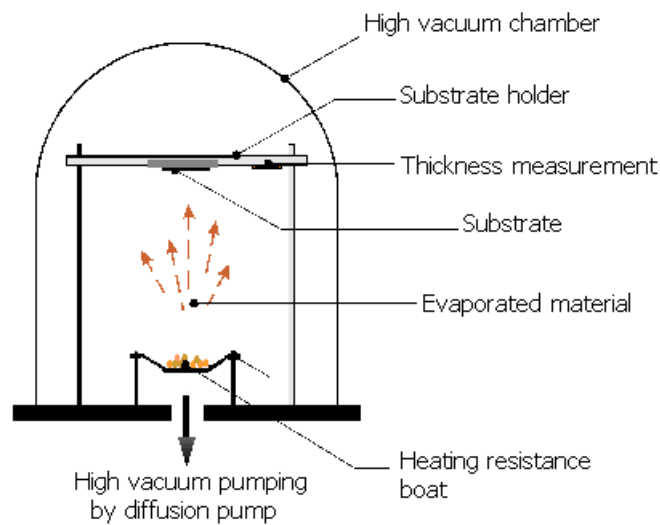


Figure 2.2: Schematic diagram of a resistive thermal evaporation system (redrawn from PhD thesis of Shabbir A. Bashir (1998), King's College London).

material (in this case commercial $\text{Ni}_{80}\text{Fe}_{20}$ alloy) is put on the tungsten heating resistor, then the chamber is evacuated to base pressure up to 2×10^{-6} mbar. The resistor will be heated by a DC current up to 55 A using a tungsten crucible to evaporate the melted material a temperature over 1500°C . The vapour of the material is deposited on the substrate (Fig. 2.2) with a deposition rate of ~ 0.1 nm/s [4]. The thickness of the deposited film is monitored by using a quartz oscillator and is calibrated using an atomic force microscopy (AFM). Thermal evaporation was used to fabricate $\text{Ni}_{80}\text{Fe}_{20}$ film used in chapters 4, 5. A fine structure of NiFe film is obtained with a mean grain size ~ 6 nm without any texture produced.

2.3.2 Sputtering technique

Besides thermal evaporation, thin films (in this thesis the CoIr film) can also be fabricated by sputtering techniques. Vacuum evaporation is based on the evaporating process of the melted materials, in the case of sputtering the deposition of the material is sputtered by the kinetic energy transfer induced by the accelerated ion particles of the inert gas (e. g. He, Ar). Sputtering is a process whereby atoms are ejected from a solid target material due to bombardment of the target by energetic ions [3,5]. The principle of a sputtering system is illustrated as follows Fig. 2.3. The sputtered material is used as a cathode in a system in which a glow discharge is established in an inert gas (e.g. Ar, He) in low vacuum of $10^{-1} - 10^{-2}$ mbar and in a voltage of several kilovolts. The substrate on which the material will be deposited is arranged on the anode, which can be grounded. The positive ions created by the discharge are accelerated toward the target (cathode) with almost the same speed as they gained in the cathode fall region. Under the bombardment of the gas ions, the material is removed from the target and deposited on the substrate. Depending on the voltage, the sputter deposition can be divided into two categories: DC sputtering and AC sputtering. The DC sputtering involves using a DC voltage between target and substrate. However, this only appropriate for conducting material. To overcome this limitation, an AC voltage at radio frequency should be used for non-conducting material, so-called AC sputtering or RF sputtering. Alternatively, in order to increase the density of charge bombarding the target, a magnet can be placed under the target to create a trap of

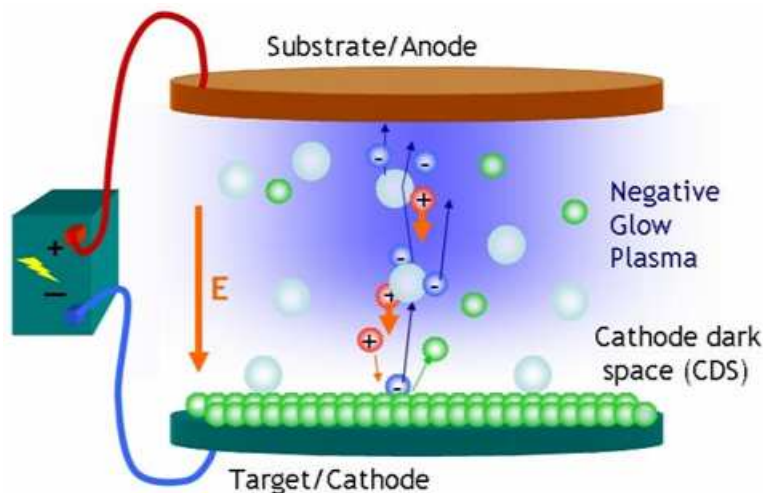


Figure 2.3: Schematic diagram of a DC sputtering system (photo from ETA Film Technology Inc. (Taiwan)).

gas ion. This is called magnetron sputtering.

Sputtering deposition is an effective route for fabricating high quality thin films in nano-size thickness in large scale. The ability to control the deposition rate from few Angstroms per minute to few nanometres per second by changing the sputtering power and to fabricate the film with very small roughness is the main advantages of the sputtering technique. However, a disadvantage of the sputter deposition is that it is harder to control the composition of the film in accordance with the target because of various sputter rates of different elements. DC sputtering was employed to deposit CoIr film (chapter 6) and $\text{Ni}_{81}\text{Fe}_{19}$ film (chapter 5) in collaborations with Tohoku University (Japan) and University of Leeds (UK), respectively.

2.4 Electron beam lithography

According to the Oxford English Dictionary, lithography means "*process of obtaining prints from stone or metal surface so treated that what is to be printed can be inked but the remaining area rejects ink*". It comes from the Greek: *lithos* means stone, *grapho* means to write.

2.4.1 Lithography and electron beam lithography

Nowadays, lithography in material science is a set of photochemical processes used to obtain a pattern on the surface of a wafer by irradiating a resist layer coated on surface using radiation (EM or e-beam). In photolithography, light (UV, X-ray) is used as radiation for creating the pattern on resist. This was used in the semiconductor industry until the 1970s when projection printers started to be used [3,6]. Similar to the optical microscope, the resolution of the photolithography is limited by the wavelength of the light used to expose the resist. The best resolution of the photolithography can be down to hundreds of nanometres.

Electron beam lithography (*EBL*) is similar to photolithography but the light radiation is replaced by an electron beam and the electron beam writer system is a scanning electron microscope. The pattern is formed by scanning an electron beam as a raster on an electron-sensitive resist, of which the chemical properties will be changed after exposing and it can then be removed by a developer (positive resist) or be inert in the

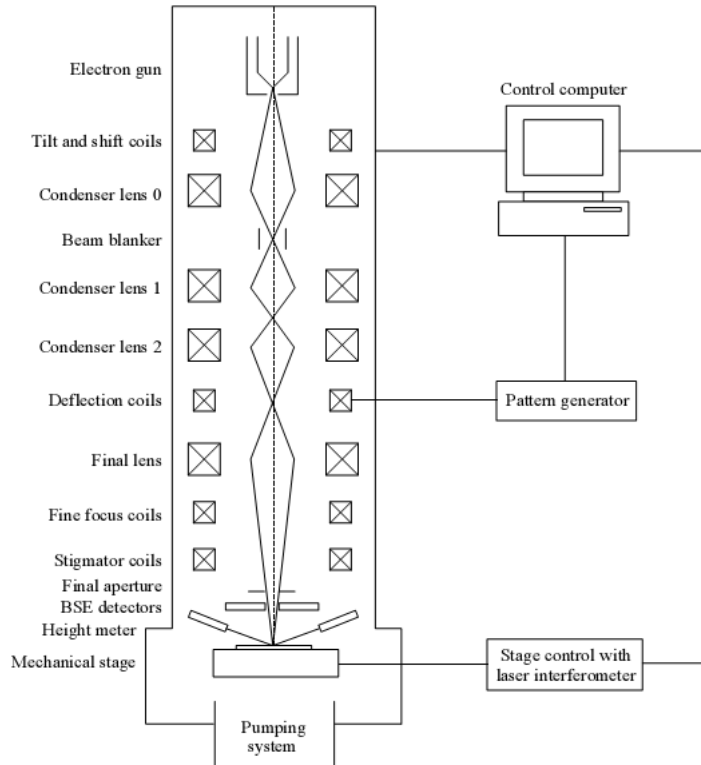


Figure 2.4: Schematic diagram of the Vistec VB6 UHR EWF beamwriter used for electron beam lithography [2].

developer (negative resist).

The beam writer system used for this work is a Vistec VB6 UHR EWF with thermal field emission gun operating at 50 kV and 100 kV voltages. Structure of this system is illustrated in Fig. 2.4. The electrons are generated by an emission gun at the top of the column and directed along the optic axis by tilting and shifting coils. Instead of using a physical mask to define the pattern like photolithography, the beam is controlled by deflection coils via computer and exposed regions as determined by an electronic computer-aided design (CAD) mask. The VB6 system allows a feature size down to 3 nm to be obtained, making very high resolution patterns. Although the ability to create any pattern electronically without the need to fabricate expensive mask plates makes e-beam a highly flexible tool, the exposure process occurs serially, pixel-by-pixel, resulting in a large writing time. This, together with the high equipment and maintenance costs are the main drawbacks of the technique. As well as being able to write single step jobs, electron beamwriters are capable of aligning a substrate (registration) to within ~ 50 nm, allowing users to write multiple lithography steps for more complex samples. This is a further improvement on photolithography which uses

a mask aligner to set the wafer to within $\sim 1 \mu\text{m}$. The duration time of a job in the EBL is much longer than that in photolithography and the EBL is more expensive than photolithography. However, this is offset the superior performance of EBL over photolithography.

2.4.2 Resist and spinning resist

There are two types of resist used for e-beam lithography. One type is called *positive resist*, of which the chemical behaviour is changed by electron exposing so that it will be dissolved by developing solution. One of the first positive resist developed for e-beam lithography was polymethyl methacrylate (*PMMA*). It is the standard positive e beam resist and remains one of the highest resolution resists available [7]. Electron beam exposure breaks the polymer into fragments that can be dissolved in methyl isobutyl ketone (MIBK), while both the exposed and the unexposed PMMA can be dissolved in pirolidone or acetone.

A negative resist is a type of resist in which the portion of the photoresist that is exposed by the electron beam becomes relatively insoluble to the photoresist developer. The unexposed portion of the resist is dissolved by the resist developer. Negative resists

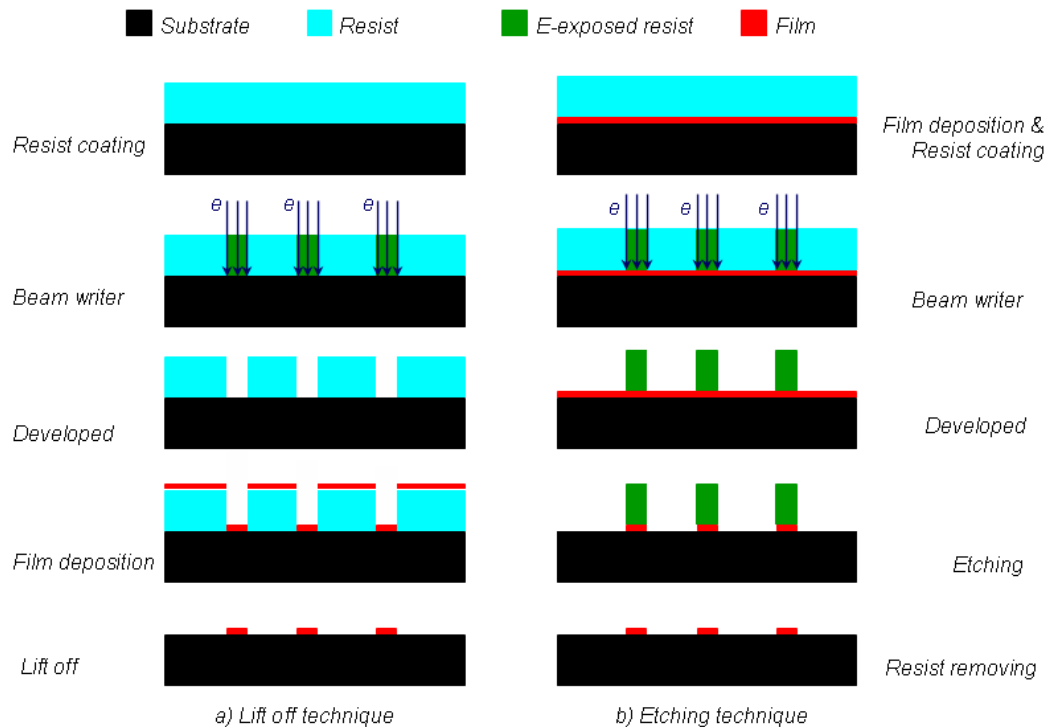


Figure 2.5: Block diagram of two patterning techniques: a) lift off, b) etching techniques.

were popular in the early history of integrated circuit processing, but positive resist gradually became more widely used since they offer better process controllability for small geometry features [8].

Processing in EBL is possible via two procedures (Fig. 2.5): lift-off and etching. In the lift-off technique, the pattern is obtained by removing unwanted areas in organic solvents e.g. acetone (Fig. 2.5(a)). The film is deposited after developing the resist and positive resist is employed. Whilst, in the etching process (Fig. 2.5(b)), the pattern is obtained by dry etching the unwanted areas in highly oxidising plasma gas. The pattern is protected by the resist remaining after developing the resist and the film was deposited on the substrate before coating the resist. The lift-off technique is simpler, quicker and cheaper than the etching but the etching can provide a pattern with better resolution especially in ultra-small patterns [9]. Only lift off is used in the work described in this thesis.

In the present work, a bilayer PMMA resist was used for lift off process: 4% 2010 *ELV* and 4% 2041 *ELV*. In order to coat the resist onto surface of the wafer, a centrifugal spinner was used to obtain a thin and smooth resist covered on the surface. The speed was selected at 5000 *rpm*, and the thicknesses of the resist are 110 nm and 115 nm for 4% 2010 *ELV* and 4% 2041 *ELV* layers, respectively. The wafers coated by resist are rinsed at 180°C for drying to remove solvent and hardening the resist. The bilayer PMMA is employed in order to obtain a clear undercut profile for lift-off process (will be discussed in detail later).

2.4.3 Design, layout and beam writer

In the EBL, the pattern is written on the substrate by a control computer from the design and job layout files as the input. In the present work, the patterns are designed using the program Tanner L-Edit supported by Tanner Research Inc. and produced as the *.gds files. Within the one file, L-Edit allows creating individual cells or structures which can be brought together to make up the final design. In addition, different layers can be specified if multiple lithography steps are required. However, .gds files which are produced by most CAD programs are not compatible with the beam writer system because the machine is only able to handle primitive shapes [2]. Hence, additional processing steps are required to convert the file to a format compatible with the beam

writer.

The L-Edit output (*.gds file) is transferred to a computer (CATS computer) employing a program named CATS (Computer Aided Transcription System). Once a series of input parameters are provided along with the .gds file, CATS fractures the design into trapezia with sides of maximum length $6.4 \mu m$. The .gds file is then converted into a .clib readfile and CATS uses this file to create .cft, .dat, .cinc, .log and .log-long files (Fig. 2.6). These are subsequently combined by the computer to produce a final .iwfl file which is sent to both the beamwriter control computer and the job layout program BELLE (Beamwriter Exposure Layout for Lithographic Engineers) used in the next step of the conversion process. BELLE requires the .iwfl file complete with all of the patterning information to produce a final job layout (.com) file.

Finally, the layout file is sent to the control computer and together with the design file, is used by the beamwriter to pattern the resist. Fig. 2.6 illustrates the processing steps before patterning. During electron exposing, the electron scattering within the resist and substrate is clearly visible and some backscattered electrons can be seen leaving the PMMA surface. It is this scattering which gives rise to a natural undercut in exposed resist. Note that as the electron energy rises, the scattering angle in the resist decreases, assuming the resist is of the same thickness. It means that there is little natural undercut, which may be good or bad depending on the application.

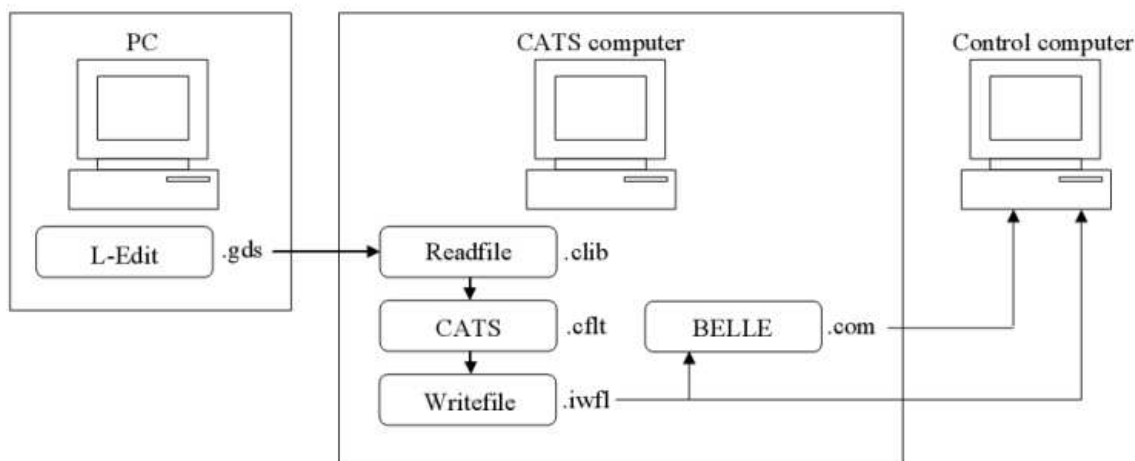


Figure 2.6: File processing required before patterning can begin: designed by L-edit software in PC, transferred to CATS computer for fracturing, and finally sent to control computer for writing the pattern [2].

2.4.4 Resist development

After exposure in beam writer system, the sample will be subject to development. In this thesis, lift-off technique was employed for patterning. For 4% 2010 *ELV* and 4% 2041 *ELV* PMMA bilayer, developer is a mixture of methyl isobutyl ketone (MIBK) and iso-propyl alcohol (IPA) in volume ratio of 1 : 2.5. The temperature was kept at 21°C in 60 seconds. The wafer was then cleaned by the IPA and finalised by plasma cleaner to ensure a clean undercut as seen in Fig. 2.7.

As seen in Fig. 2.7(a), when a single layer PMMA resist is used, a sharp undercut is formed after developing, then some of the metal lands on the sides of the resist. Once the resist is dissolved, this metal falls onto the surface creating regions of thicker material, and is problematic. To prevent this problem, two layers of PMMA resists with different molecular weight and hence various electron sensitivities are used (Figs. 2.7(b,c)). In this case, the bottom resist layer forms a wider mask than the top layer because of more electron sensitivity. The top layer with narrower mask defines the overall dimensions of the structure deposited. Since the underlying mask is hardly in contact with the deposited films, the subsequent lift-off process of the resist is largely facilitated (Fig. 2.7(b,c)).

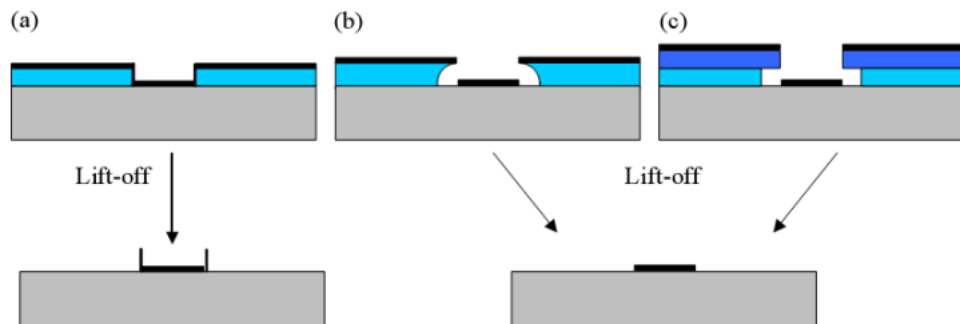


Figure 2.7: The different profiles achieved with (a) a single layer of resist, (b) resist soaked in chlorobenzene and (c) a bilayer of electron sensitive resist [2].

2.5 Focused ion beam

Focused ion beam (*FIB*) microscope was invented in 1979 by Seliger et al. as a scanning ion probe system with a beam of gallium ions focused down to a diameter of 100 nm, with a current density of 1.5 A.cm^2 [10]. After 30 years of development, the FIB has become a technique employed widely in the semiconductor industry and materials

Chapter 2: Instrumentation and fabrication...

science fields for site-specific analysis, deposition, ablation of materials as well as patterning [11, 12]. Besides, FIB is also a strong tool for imaging surface morphology of the solids in a similar manner to a SEM by collecting the secondary electrons produced as the ion beam is rastered across the surface as well as repairing integrated circuit and trimming of write head pole tips. Recently, FIB was exploited to modify the magnetic properties and magnetic structure of the magnetic thin films [13, 14].

A modern FIB involves a liquid metal ion source, commonly gallium (LMIS - Fig. 2.8(a)), consisting of a tungsten reservoir and needle. The ion beam Ga^+ is generated by applying a potential ~ 12 kV like a field emission electron gun (Fig. 2.8(a)) and control by a system of electromagnetic lenses and apertures (Fig. 2.8(b)). The FIB equipment used in this work is an FEI Strata 200XP Dual Beam, which consists of two beams (dual beam): an electron beam column for SEM and an ion column (Fig. 2.8(c)). The gallium LMIS possesses brightness of the order $10^6 \text{ A.cm}^{-2}\text{srad}^{-1}$ and yields a beam with chromatic energy spread approximately 5 eV. The FIB machine was used for patterning the magnetic elements or preparing the cross-sectional specimens for TEM measurements.

The ions from the LMIS enter the ion column which contains two electrostatic lenses

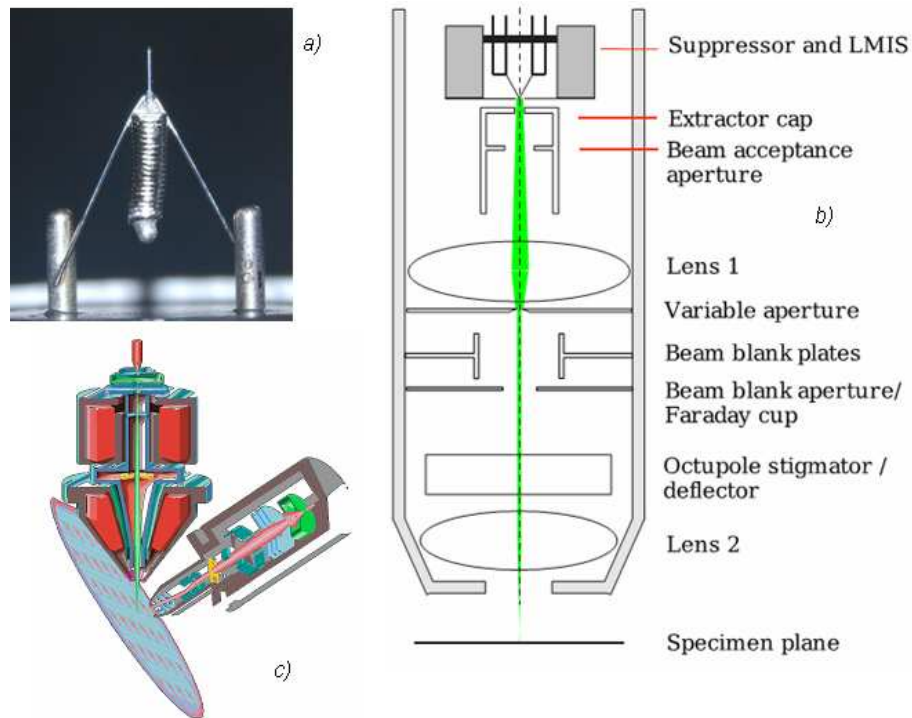


Figure 2.8: Photograph of a gallium liquid metal ion source (a), schematic of ion column in the FIB (b) and dual beam system (c) [11].

that deliver a focused beam of Ga^+ ions with a typical energy of 30 keV, to the surface of the specimen. The first of the lenses operates at predetermined potential settings and acts to accelerate the ions and focus them through the variable lenses and apertures. The second lens controls the convergence of the beam at the specimen surface and its current can be varied by the user. It is commonly adjusted to focus the displayed on-screen image. The octopole stigmator/detector assembly just above the second lens provides control of the scanning, shift and astigmatism of the beam. The ion beam current can be adjusted by varying the apertures with different diameter, which determines the resolution (or the full width half maximum). Beam currents ranging from 1 pA to 20,000 pA are available with probe size from 6 nm to 350 nm, respectively. For patterning jobs, the resolution of the pattern is determined by the probe size.

Moreover, the presence of the electron column (using a field emission gun) allows the processing to be directly observed in real time. The electron column is aligned to the vertical axis, which is perpendicular to the specimen plane, whereas, the ion column is fixed at 52° tilting from the vertical axis (Fig. 2.8(c)). Another capability of the FEI Strata 200 is the Pt, W depositions by gas injection. A retractable gas injection needle, which connected to a cylinder containing either Platinum carbonyl or Tungsten hexacarbonyl gases, is mounted into the specimen chamber, which can be inserted nearby the region of the beam when platinum or tungsten deposition is required. This feature is extremely helpful for the protection of specific areas on the specimen during the milling process. It is also employed for repairing circuits or depositing electrical contacts.

In this thesis, the FEI Strata 200 FIB microscope was exploited to pattern the magnetic thin film elements (in chapters 4, and 5), and in preparing TEM cross-section in chapters 4, 6. Furthermore, the FIB was also used as a SEM for imaging nanostructures.

Bibliography

- [1] B. Khamsehpour, C. D. W. Wilkinson, J. N. Chapman and A. B. Johnston, *J. Vac. Sci. Technol. B* **14** (1996) 3361-3366.
- [2] C. Brownlie, *A TEM Investigation of Controlled Magnetic Behaviour in Thin Ferromagnetic Films*, PhD thesis, University of Glasgow, 2007.
- [3] L. Eckertova, *Physics of thin films*, Plenum Press Publishing, New York and London (1986) ISBN 0-306-41798-7.
- [4] B. Khamsehpour, C. D. W. Wilkinson, J. N. Chapman, *J. Appl. Phys.* **67** (1995) 3194.
- [5] W. D. Westwood, *Sputter deposition* (AVS Education Committee book series), Education Committee, AVS (2003) ISBN-10: 0735401055.
- [6] R. C. Jaeger, *Introduction to Microelectronic Fabrication (Modular Series on Solid State Devices)*, Vol. 5, Prentice Hall; 2nd ed. (13 Nov 2001), ISBN-10: 0201444941.
- [7] M. A. McCord, M. J. Rooks in *Handbook of Microlithography, Micromachining and Microfabrication*, **Vol. 1: Microlithography**, ch. 2, ed. by P. Rai-Choudhury.
- [8] I. Zailer, J. E. F. Frost, V. Chabasseur-Molyneux, C. J. B. Ford, M. Pepper, *Semi. Sci. Tech.* **11** (1996) 1235.
- [9] X. Kong, D. Krása, H.P. Zhou, W. Williams, S. McVitie, J.M.R. Weaver, C.D.W. Wilkinson, *Microelectronic Engineering* **85** (2008) 988-991.
- [10] R. L. Seliger, J. W. Ward, V. Wang, and R. L. Kubena, *Appl. Phys. Lett.* **34** (1979) 310.
- [11] D. R. McGrouther, *Effects of focused ion beam irradiation on thin ferromagnetic films*, PhD thesis (2004) University of Glasgow.

- [12] C. A. Volkert, A. M. Minor, *MRS Bulletin* **32** (2007) 389-399.
- [13] D. McGrouther, J. N. Chapman, F. W. M. Vanhelmont, *J. Appl. Phys.* **95** (2004) 7772.
- [14] D McGrouther, WAP Nicholson, J N Chapman, S McVitie, *J Phys D: Appl Phys* **38** (2005) 3348-3353.

Chapter 3

Instrumentation and characterisation techniques

3.1 Introduction

Transmission electron microscopy (TEM) is the main characterisation technique used in this project, especially for quantitatively determining the micromagnetic structure. The TEM is a powerful tool not only for microstructure observation with atomic resolution but also for magnetic imaging with very high quality images. This chapter will concentrate on reviewing briefly the TEM from physical microstructural analysis to quantitative magnetic imaging in Lorentz TEM.

3.2 Transmission electron microscopy

The optical microscope is a familiar instrument for observing small objects using visible light. However, it is well-known that the resolution of a conventional optical microscope is limited by the wavelength of its illumination, so, the best optical microscopes are only able to resolve features down to few hundred nanometres [2]. Modern materials science and engineering requires a better microscope that can resolve features at a smaller length scale down to the atomic scale. In 1925, Louis de Broglie [1] hypothesised that electrons exhibit wave-like characteristics, with the possibility of wavelengths far shorter than visible light:

$$\lambda = \frac{h}{p} \tag{3.1}$$

with $h = 6.625 \times 10^{-34}$ *J.s* is the Planck's constant, and p is the momentum of the particle. This leads to the idea of designing a microscope using the electron wave

to overcome the resolution limitation of conventional optical microscopes. With an electron moving through an accelerated voltage of 100 kV, the wavelength is about 3.70 pm (3.70×10^{-12} m), which is much shorter than that of the light. It means that if electron waves can be used for imaging, superior resolution may be possible.

3.2.1 Conventional transmission electron microscopy (CTEM)

TEM is a technique whereby an electron beam is transmitted through an ultra thin sample, interacting with the specimen when passing through it. The transmission electron microscope was first built in 1931 by Max Knoll and Ernst Ruska and the first commercial TEM was produced in 1939 [2]. Principally, a TEM is equivalent to an optical microscope but the illumination system is replaced by the electron beam, and the glassy lens (in optical microscope) is substituted by electromagnetic lens in a high-vacuum column. A modern TEM consists of main components: electron source, magnetic lens (for beam converging, focusing, magnifying and projecting), apertures, beam-control coils, image recording and detectors (CCD camera, film, etc.).

In the TEM, the electrons are generated in a filament (either thermionic filament or field emission gun) then accelerated to become a high-energy electron beam by an electric field (a modern TEM often uses an accelerating voltage of few hundred kV). The electron beam is condensed subsequently to a narrow and parallel beam by a condenser lens system. If the electron is accelerated through a voltage of V , the wavelength is given by:

$$\lambda = \frac{h}{\sqrt{2m_e eV}} \quad (3.2)$$

If the accelerating voltage is high enough (above ~ 100 kV), the velocity of the electron will be a significant fraction of the speed of light and the relativistic effect will need to be included, and the wavelength will be re-written as [2]:

$$\lambda = \frac{h}{\sqrt{2m_e eV(1 + \frac{eV}{2m_e c^2})}} \quad (3.3)$$

where m_e , e are the rest mass and the charge of the electron, c is the speed of light in vacuum. With a voltage of 200 kV (value for all TEM equipment used in this thesis), the wavelength is 2.51 pm.

Following electron emission, a condenser system generally consisting of two condenser

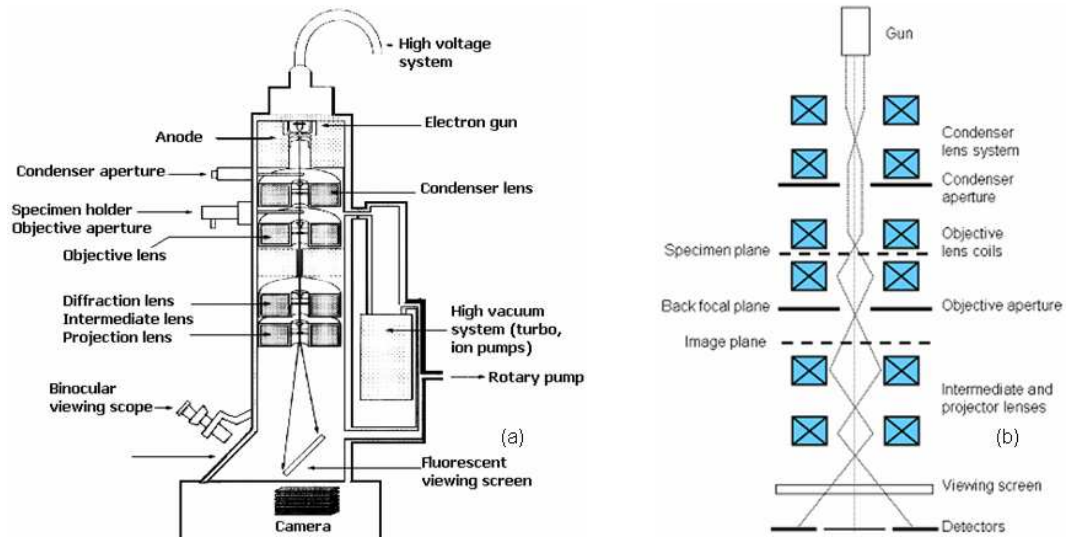


Figure 3.1: (a) The structure of a transmission electron microscope (from University of Delaware, US) and (b) simplified ray diagram for image formation in a CTEM [3].

lenses and an condenser aperture are employed to control the electron intensity, spot size and beam convergence. For TEM analysis the sample must be thin enough for electron transparency. Hence, with 200 kV-accelerated electrons, the maximum thickness of the specimen should not exceed ~ 100 nm. Below the sample, a short focal length objective lens is used to form the image, and to form a diffraction pattern in back focal plane. The image is focused at the image plane by varying the focal length of the lens. A set of intermediate and projector lenses are then used for magnification, producing a final real image on a fluorescent screen or CCD camera. As the electrons travel in the TEM with very high energy, the complete TEM column must possess a high vacuum environment (up to $\sim 10^{-7}$ mbar) to prevent the interaction of the electrons with the air and to avoid contamination of the specimen. Fig. 3.1 illustrates the principle instruction of a TEM and ray diagram of in a TEM. The image is collected at image plane of the microscope by various methods e.g. CCD camera, fluorescent screen, optical film, semiconductor detectors, etc. Moreover, spectroscopies (EDX, EELS) are recording by specific detectors.

As mentioned above, the electron beam in the TEM is focused by electromagnetic lenses [2, 4]. Hence, the resolved power (resolution) of the TEM is not only limited by the diffraction but also by the aberrations, which is an intrinsic artefact of the electromagnetic lenses. The resolution of the microscope is the resolving power, which can be defined as the shortest distance between these points on the object that can still be

distinguished by the observer. Practically, it was found that the resolution in magnetic lens depends on the spherical aberration, C_s , and the wavelength of the electron beam as follows [4]:

$$r_p = 0.91 (C_s \cdot \lambda^3)^{1/4} \quad (3.4)$$

For example, with typical values of λ and C_s of 2.5 pm and 1.2 mm, a point-to-point resolution of 0.34 nm is reached. The C_s of the Lorentz lens in the Phillips CM20 is larger, up to 8000 mm, causing a lower point-to-point resolution of 2.2 nm.

3.2.2 Scanning transmission electron microscopy (STEM)

Scanning transmission electron microscopy (STEM) is a combination of both the TEM and the SEM in which deflection coils are employed to scan a fine focused electron probe across the surface of a thin specimen and is generally used to detect localised signals at a very high resolution [6]. The rastering of the beam across the sample makes these microscopes suitable for analytical techniques such as mapping by energy dispersive X-ray (EDX) spectroscopy, electron energy loss spectroscopy (EELS) and annular dark-field imaging (ADF). Principle of STEM is described in Fig. 3.2.

The STEM was built for the first time in 1938 by Baron Manfred von Ardenne (working

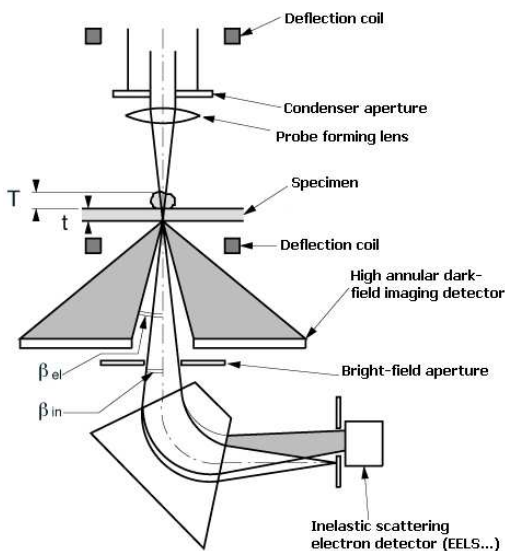


Figure 3.2: Principle schematics of a scanning transmission electron microscope (from M.E. Müller, Imaging nature across dimensions): the electron beam is focused as a fine probe by condenser lens and aperture; and scanned as a raster on the specimen by deflection coil. The transmitted beam is collected by HAADF detector (high angle deflected beam), bright field (BF) detector (low angle deflected beam) and EELS detector for chemical analysis.

for Siemens Berlin) [6] but the technique did not further develop until 1960s because the requirement of a chromatic electron beam to be focused on to a very narrow spot. This technique was again activated with the development of cold field emission gun by Albert Crewe and co-workers in 1969 to build a much better STEM [7], able to visualise single heavy atoms on thin carbon substrates [8]. Atomic-resolution chemical analysis using the STEM was firstly established in 1993 [9]. Nowadays, it is possible to use the STEM to capture atomic resolution images (HAADF image) where the contrast is directly related to the atomic number (Z -contrast) or for nanochemical mapping (EELS, EDX) with resolution down to angstrom scale.

3.3 Physical microstructure characterisation by TEM

3.3.1 Electron-specimens interaction

In the TEM, the electrons travel with very high kinetic energy (up to hundreds keV) and pass through the specimen. There are a number of interactions between the electrons and the specimen, which are summarised in Fig. 3.3(a). When the incident beam travels through the sample, some electrons pass straight through unaffected by the specimen (transparent electron) whereas a fraction are scattered by a variety of processes, affecting both the spatial and angular distribution. These interactions produce

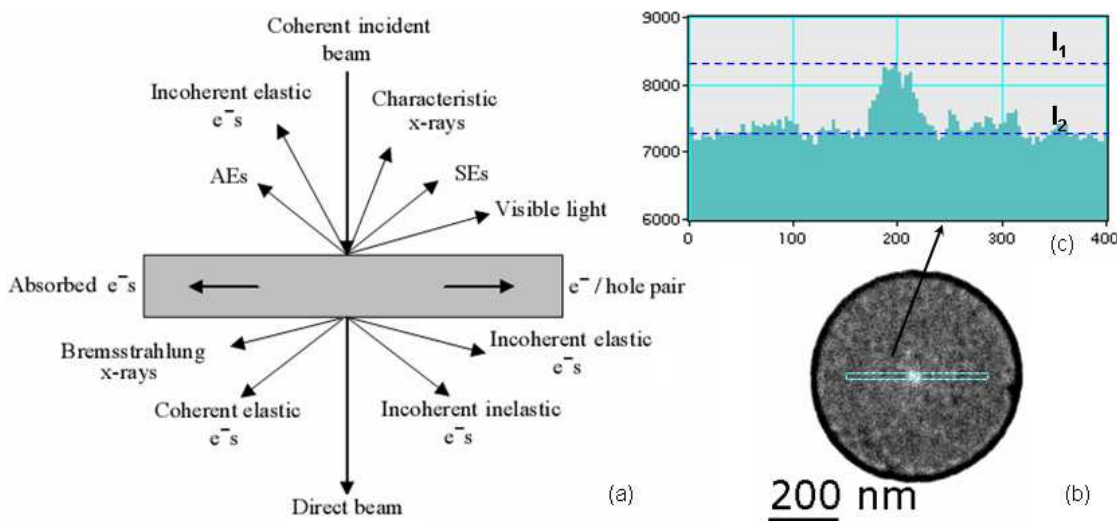


Figure 3.3: Various electron-specimen interactions produce forward and backscattered electrons as well as a large number of secondary signals (a) (copied from William and Carter book [2]), a Fresnel image of a permalloy dot showing contrast of magnetic vortex (b) denoted by the variation of the intensity (c).

forward and backscattered electrons, as well as a large number of secondary signals. In effect, an initial uniform distribution of illumination emerges from the sample with a non-uniform intensity, and this is what allows details of the specimen to be observed. Essentially, the intensity of the TEM image arises from contributions of the direct and scattered beams. The interactions in conjunction with the microscope set up may result in variations of intensity in the image, so-called contrast (Figs. 3.3(b,c)), which is defined as the difference in intensity between two neighbouring areas and is given by the equation:

$$C = \frac{I_1 - I_2}{I_2} = \frac{\Delta I}{I_2} \quad (3.5)$$

where I_1 and I_2 are the intensities of the adjacent areas and $\Delta I = I_1 - I_2$ is the intensity difference (Fig. 3.3(b)). Depending on the interaction, the contrast can be divided into three main types [2]:

- Amplitude contrast, resulting from absorption effect induced by specimen thickness or by chemical composition of the specimen (mass-thickness, and Z-contrast - in STEM etc.);
- Diffraction contrast, contributed by various scattering of the electron due to the elastic scattering by crystal lattice. The diffraction contrast can be seen by dark field and bright field images (detailed in next section);
- Phase contrast, related to the different scattering of the electrons essentially by the interaction with electric and magnetic potentials in the specimen. The phase contrast includes lattice fringes in high-resolution TEM, Moire fringes, and Fresnel contrast (including magnetic imaging).

3.3.2 Electron diffraction

Diffraction is the phenomenon which refers to the scattering of waves when it encounters any obstacle [10]. It occurs with any type of wave and results in the formation of a diffraction pattern behind the scattering object.

In the TEM, the electron waves are elastically scattered by the periodic arrangement of atoms in the crystal lattice with each atom acting as a point source of spherical wavefronts. If the waves are incident at an angle, θ , on a set of lattice planes (hkl),

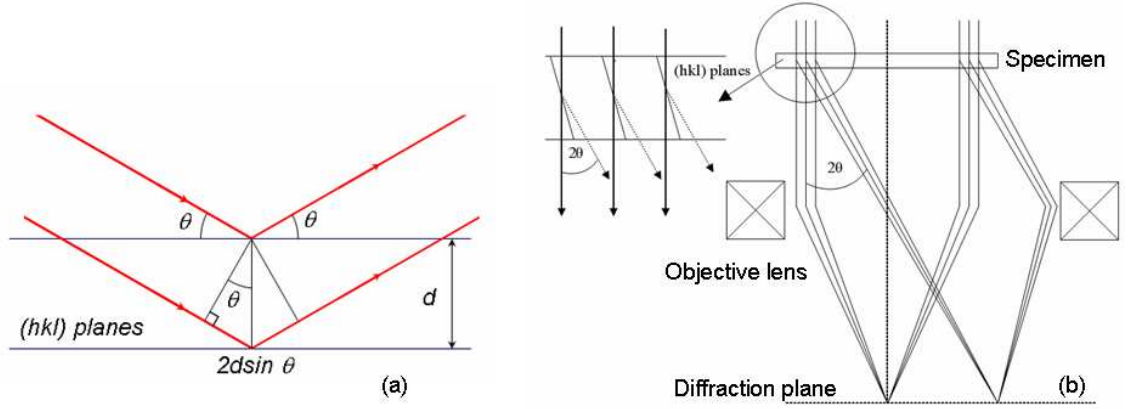


Figure 3.4: Electron diffraction on crystal lattice: (a) two incident waves reflecting on (hkl) planes are in-phase when their path difference is equal to an integer number of wavelengths, and (b) principle of electron diffraction in the TEM.

within the crystal, some of the radiation will be reflected at an equal angle and will interfere with one another (Fig. 3.4(a)). The path difference of two waves is $2d \sin \theta$ (with d is the spacing of the (hkl) planes). To obtain the maximum interference, it must satisfy the Bragg's law [4]:

$$n \cdot \lambda = 2d \cdot \sin \theta \quad (3.6)$$

where n is an integer number which is the interference order. In electron diffraction, $\sin \theta \leq 1$, and hence Bragg reflection can only occur for $\lambda \leq 2d$. Therefore, it is easy to understand why it is not possible to produce diffraction patterns from crystals using visible light.

If we consider the diffraction phenomenon in reciprocal lattice space, the spacing of (hkl) planes is given by:

$$d_{hkl} = \frac{1}{\mathbf{g}_{hkl}} \quad (3.7)$$

with \mathbf{g}_{hkl} the reciprocal vector given by:

$$\mathbf{g}_{hkl} = h\mathbf{a}^* + k\mathbf{b}^* + l\mathbf{c}^* \quad (3.8)$$

where, \mathbf{a}^* , \mathbf{b}^* , \mathbf{c}^* are the unit-cell translation vectors in reciprocal space, which are related to lattice constants a , b , c , and the unit-cell volume, V_c via the relations:

$$\mathbf{a}^* = \frac{\mathbf{b} \times \mathbf{c}}{V_c} \quad (3.9)$$

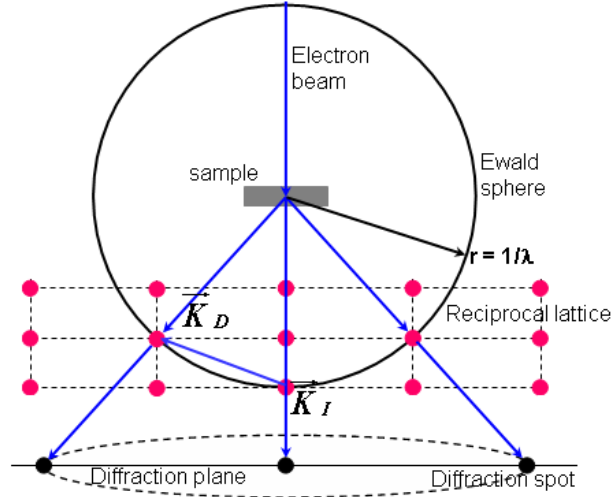


Figure 3.5: The Ewald sphere of reflection to construct the diffraction spot from reciprocal space.

$$\mathbf{b}^* = \frac{\mathbf{c} \times \mathbf{a}}{V_c} \quad (3.10)$$

$$\mathbf{c}^* = \frac{\mathbf{a} \times \mathbf{b}}{V_c} \quad (3.11)$$

If we define difference vector, $\mathbf{K} = \mathbf{K}_D - \mathbf{K}_I$ with \mathbf{K}_I , \mathbf{K}_D are the incident and diffracted wave vectors, respectively. The difference vector will given by:

$$|\mathbf{K}| = \frac{2 \sin \theta}{\lambda} \quad (3.12)$$

As a result, Bragg's law can be rewritten in reciprocal lattice space as:

$$\mathbf{K} = \mathbf{g}_{hkl} \quad (3.13)$$

The equation 3.13 represents the Laue condition for constructive interference. The construction of diffraction spots can be understood using the Ewald sphere representation (see Fig. 3.5). The Ewald sphere is a sphere in reciprocal space of radius of $r = 1/\lambda$. From intersections of the Ewald sphere and reciprocal space (Fig. 3.5), the vectors \mathbf{K}_I , \mathbf{K}_D are shown, and the diffraction spot can be constructed [4]. In the TEM, electrons that pass through the specimen are brought to focus in the back focal plane of the objective lens, the diffraction pattern is produced in this plane.

In a single crystal diffraction experiment, the electron wavelength, beam direction and reciprocal planes which intersect with the Ewald sphere are fixed, resulting in a pattern with bright spots on a dark background (Fig. 3.6(a)). In the case of polycrystalline

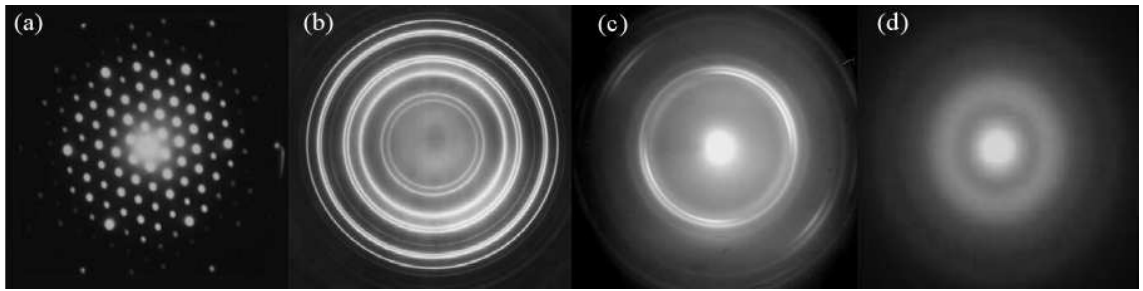


Figure 3.6: Electron diffraction patterns obtained by a) single crystal specimen, b) polycrystalline specimen, c) textured-polycrystalline sample and d) amorphous sample [12].

sample, all possible orientations of crystallites are present and a ring pattern is visible (Fig. 3.6(b)). This pattern appears as a superposition of many single crystal spot patterns, therefore continuous rings are formed. Moreover, in a textured-polycrystalline sample, the pattern will have non-uniform rings due to preferred orientations of the grains. Crystalline texturing is the distribution of crystallographic orientations of the grains in a polycrystalline material, occurring in a polycrystalline sample when some preferred orientation exist [11].

The characteristic feature of the textured specimen can be seen in a pattern by tilting the specimen. If a texturing orientation exists, diffraction rings of some planes will appear and other ones may be disappeared (Fig. 3.6(c)) because some planes deviate from the Bragg condition. Meanwhile, when it is performed on an amorphous sample, a series of fuzzy rings (halo rings) in the pattern is observed (Fig. 3.6(d)).

The TEM diffraction pattern can be of two types: selected area electron diffraction (*SAED*) and convergent beam electron diffraction (*CBED*). The SAED uses a parallel beam passing through the specimen via the area that is selected by selected area aperture in an intermediate image plane. SAED is employed in this project to determine the crystal structure and textured orientation of CoIr/Ru films in chapter 6. Whilst, the CBED uses a convergent beam (focused by condenser system as a probe) therefore allows determining crystallography of smaller crystallites more precisely but was not used in present work.

3.3.3 Dark-field and bright-field imaging

Formation of images and electron diffraction patterns on the viewing screen or CCD camera are fundamental operations of a TEM. In imaging mode, the intermediate lens

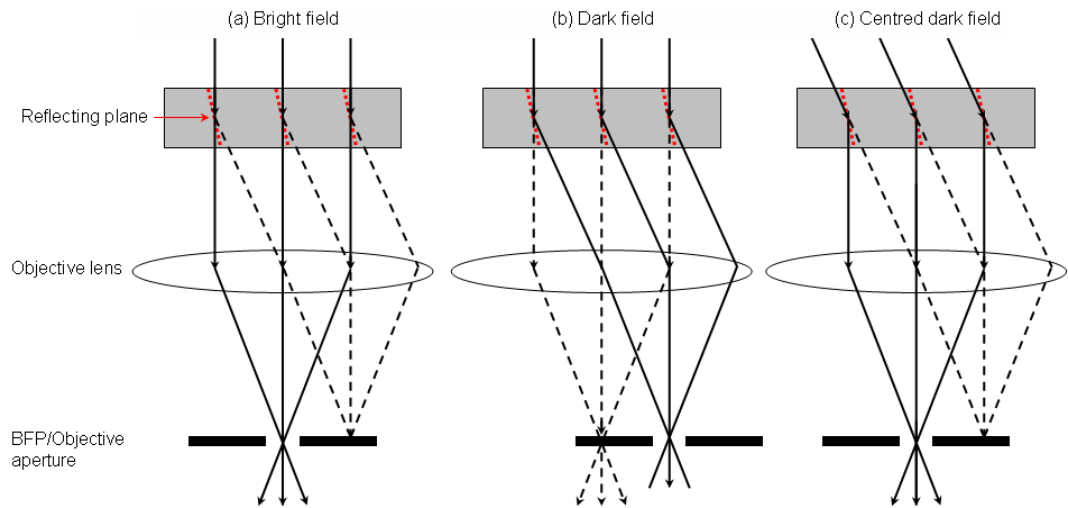


Figure 3.7: Principle of bright-field and dark-field imaging: a) bright-field image, b) dark-field image and c) centred dark-field image.

is set so that the object of this lens is the image of the objective lens produced at the first image plane. On the other hand, in the diffraction mode, the intermediate lens is weakened so that the back focal plane of the objective lens (at which the DP is formed) becomes the object.

The diffraction pattern on the viewing screen contains a bright central spot formed by the direct electrons and several spots or rings produced by the scattered electrons. The diffracted electron beams can be selected using the objective aperture to produce either bright-field (BF) or dark-field (DF) images. In order to capture a BF image, the aperture is centred around the direct beam, allowing only the unscattered electrons to contribute to the image (Fig. 3.7(a)). If this aperture is moved and centred around one (or some) of the diffracted beams, then a DF image is created (Fig. 3.7(b)). However, in common dark-field imaging, the selected electrons travel off-axis and suffer from aberrations. By tilting the incident beam onto the specimen at an angle equal to the Bragg angle the scattered electrons travel down the optic axis and the direct electrons off-axis. The objective aperture is centred around the scattered beam to produce a centred dark-field (Fig. 3.7(c)).

Fig. 3.8 shows an example of bright-field (BF) and dark-field (DF) plan-view images of the $\text{Co}_{80}\text{Ir}_{20}/\text{Ru}$ multilayer film. The BF image has a higher intensity whereas the DF is less intense but with a higher contrast level. However, with digital imaging, lower contrast intensity is much less of a problem than when images were recorded in the pre-digital era. Therefore, the BF image is simple and clear to observe the grain

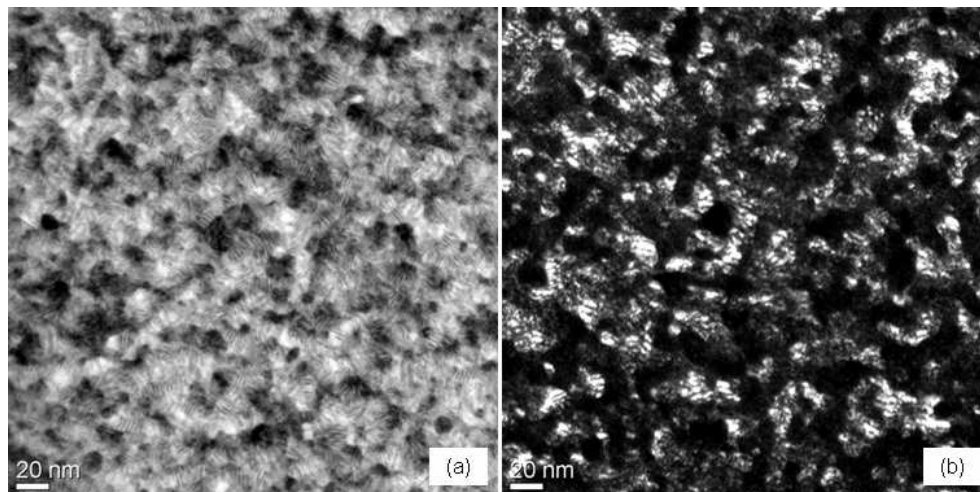


Figure 3.8: An example of bright-field (BF) and dark-field (DF) (by selecting $(10\bar{1}0)$ diffraction ring) plan-view images of the $\text{Co}_{80}\text{Ir}_{20}/\text{Ru}$ multilayer film.

structure but the DF image can provide a high contrast of grain/crystallites.

3.3.4 High-resolution TEM

High-resolution transmission electron microscopy (*HRTEM*) is an imaging mode of the TEM based on phase contrast imaging that allows the imaging of the crystallographic structure of a sample at an atomic scale [13]. Because of its high resolution, it is an invaluable tool to study nanoscale properties of many materials such as semiconductors and ferromagnets.

Contrast arises from the interference in the image plane of the electron wave with itself. Due to the inability to record the phase of these waves, the HRTEM relies on generating intensity from this interference, however the phase of the electron wave still carries the information about the sample and generates contrast in the image, so called phase-contrast imaging for further quantitative analysis. However this is true only if the sample is thin enough that amplitude variations do not slightly affect the image. Fig. 3.9 illustrates an example of a HRTEM image of cross-sectional specimen of $\text{Co}_{80}\text{Ir}_{20}/\text{Ru}$ multilayer film, in which the contrast from lattice fringes is obvious. The HRTEM requires a thin and clean specimen. Normally, the specimen should be thin enough that the weak phase object approximation is valid. In principle the theoretical critical thickness for this approximation is up to 2 nm [27], but in fact the HRTEM can work with sample much thicker than theoretical limit.

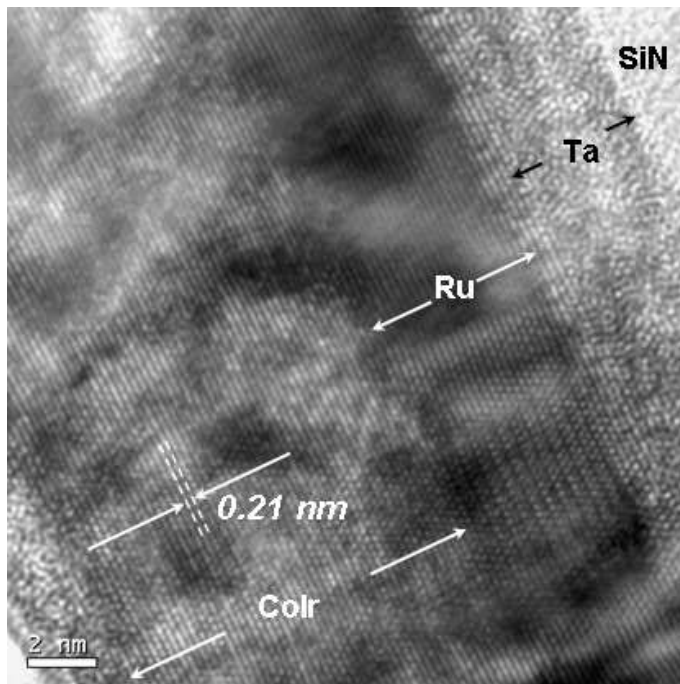


Figure 3.9: An example of HRTEM micrograph of cross-sectional specimen of $\text{Co}_{80}\text{Ir}_{20}/\text{Ru}$ multilayer film.

3.3.5 FEI Tecnai T20 and TF20

All basic TEM measurements (microstructural, diffraction analysis) in this thesis were performed using the FEI Tecnai T20 in the Kelvin Nanocharacterisation Centre. The Tecnai T20 is a standard commercial microscope using a LaB_6 thermionic filament but includes a couple of additional features i.e. Lorentz lens for Fresnel imaging, and a Gatan Image Filter (GIF) for energy filtering and element mapping. The T20 operates with a maximum accelerating voltage of 200 kV, the spherical aberration coefficient of the objective lens $C_s = 1.2 \text{ mm}$ provides a point resolution of 2.4 \AA .

HRTEM images were recorded on a FEI Tecnai TF20. The Tecnai TF20 consists of a field emission gun operating at 200 kV accelerating voltage, which is considered as a state-of-art, nano-analytical transmission electron microscope. The TF20 can provide high quality HRTEM images and can acquire spectra (EELS, EDX). Furthermore, STEM capability is included in the TF20 with Fischione HAADF STEM detector and capability to map the chemical compositions using electron energy loss spectroscopy (EELS) with spatial resolution down to 0.2 nm.

3.4 Magnetic imaging in TEM

Magnetic imaging encompasses the techniques for observing the magnetic structure (magnetic domain pattern) of the ferromagnetic samples. Nowadays, magnetic imaging involves transmission electron microscopy (Lorentz TEM, electron holography), scanning electron microscopy (spin-polarised SEM - SEMPA), optical Kerr microscopy, magnetic force microscopy (MFM), scanning tunneling microscopy (spin-polarised STM), X-ray magnetic circular dichroism (PEEM-XMCD), etc. Among them, Lorentz microscopy is one of the most powerful techniques providing very high spatial resolution.

3.4.1 Lorentz microscopy

The usage of conventional transmission electron microscope (CTEM) to image the magnetic domains started in 1959 by Hale et al. [15]. They used a CTEM and captured images revealing the presence of domain walls by simply defocusing the imaging forming lens. This refers to the Fresnel imaging mode and this branch of CTEM became known as Lorentz microscopy or Lorentz TEM. Since then, Lorentz microscopy has been established and become a strong tool for magnetic imaging with high spatial resolution. The Lorentz TEM involves both CTEM (including Fresnel and Foucault mode) and STEM (differential phase contrast) for imaging as reviewed by Chapman [16]. Recently, the transport-of-intensity (TIE) algorithm [17] has been applied for quantitative analysis of Lorentz TEM, providing a new approach to interpret the information of magnetic induction distribution in thin films from Lorentz microscopy [18–20].

Lorentz microscopy refers to the deflection of the electron beam due to Lorentz force (Fresnel diffraction), F_L which is well-known as:

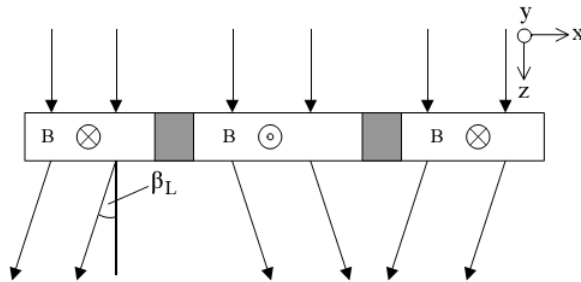


Figure 3.10: Deflection of the electrons due to Lorentz force when passing through a thin magnetic film.

$$\mathbf{F}_L = -e [\mathbf{E} + (\mathbf{v} \times \mathbf{B})] \quad (3.14)$$

with \mathbf{E} , \mathbf{B} are the electric and magnetic field in the specimen, e , \mathbf{v} are the electron charge and velocity. For a parallel beam, which is incident perpendicular to the plane of the specimen (parallel to the z - axis), the deflection angle due to Lorentz force is given by [16]:

$$\beta_L(x) = \frac{e\lambda}{h} \int_{-\infty}^{+\infty} B_{\perp}(x, y) dz \quad (3.15)$$

where $B_{\perp}(x, y)$ is the in-plane component of magnetic induction at point (x, y) , e is the magnitude of the electron charge, λ is the electron wavelength and h is Planck's constant. If stray field effects are ignored, the magnetisation is uniform (M_s) and the specimen is of constant thickness, t , the equation (3.15) can be simply written as:

$$\beta_L = \frac{e\lambda B_s t}{h} \quad (3.16)$$

with $B_s = \mu_0 M_s$ is the saturation magnetic induction. For the electron beam with energy of 200 kV passing through a 20 nm thick film with a saturation induction of $B_s = 1$ T, the deflection angle β_L is 1.2×10^{-5} rad. This means that the magnitude of the electron beam due to Lorentz force is much smaller than the angle of Bragg diffraction in order of 10^{-2} rad.

The above description is based on a classical optical point of view, image calculation for a general magnetisation point of view is very difficult. This can be overcome by taking a quantum mechanical point of view, in which the motion of the electron is considered as a wave and the specimen is a phase object. The image in Lorentz microscopy is

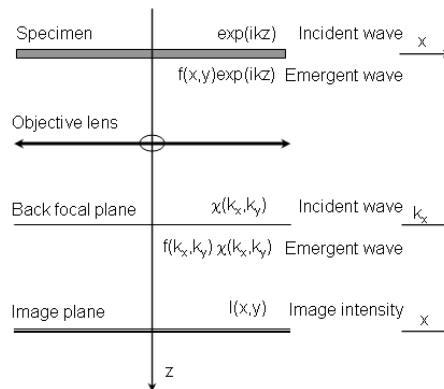


Figure 3.11: Lorentz image formation in CTEM. This picture is re-drawn from Chapman (1984) [16].

constructed by considering the electron wave propagation (Fig. 3.11).

As the electron wave passes through the specimen, any phase shift ϕ needs to be taken into account. The phase shift includes magnetic phase shift, ϕ_m due to the interaction with magnetic vector potential (\mathbf{A}), and electrostatic phase shift, ϕ_e induced by electrostatic potential, V :

$$\phi_m(r) = -\frac{e}{\hbar} \int_{-\infty}^{+\infty} \mathbf{A} d\mathbf{l} = -\frac{e\mu_0}{4\pi\hbar} \otimes \int_{-\infty}^{+\infty} (\nabla \times \mathbf{M}(\mathbf{r})) d\mathbf{l} \quad (3.17)$$

$$\phi_e = \frac{\pi V t}{\lambda E} \quad (3.18)$$

where, t is the thickness of the sample, λ is the wavelength of the electron wave. The exit wave function can be written as:

$$\psi(r) = A(x, y) \cdot e^{i(kz + \phi)} = A(x, y) \exp[i(kz + \phi)] \quad (3.19)$$

Where, $A(x, y)$ is the amplitude function, $k = 2\pi/\lambda$ is the wave number, and $\phi = \phi_m + \phi_e$ is the total phase shift. If we include the microscope term (transfer function, $TF = \chi(K)$ - K is the spatial frequency; aperture function - APF), the complex wave function at the back focal plane of the imaging lens will be given by:

$$\Psi(k_x, k_y) = FT[\psi(r)] \times \exp(i\chi(K)) \times APF \quad (3.20)$$

Here, the FT is the Fourier transform operation. Commonly, the transfer function in Lorentz microscopy is given by:

$$\chi(K) = \pi \Delta f \lambda K^2 + \frac{\pi C_s \cdot \lambda^3 \cdot K^4}{2} \quad (3.21)$$

here, Δf is the defocus value, C_s is spherical aberration, λ is the wavelength of the electron. The APF is a top-hat function having value 1 inside its radius and 0 outside. The wave function at the image plane is given by an inverse Fourier transform of the wavefunction in (3.20):

$$\psi_i(x, y) = FT^{-1}(FT(\psi(x, y)) \exp(\chi(K))) \quad (3.22)$$

The intensity of the image is obtained by calculating the modulus of the wave function:

$$I(x, y, \Delta f) = \psi_i(x, y) * \psi_i^*(x, y) \quad (3.23)$$

Therefore, the intensity of the image formed at the image plane will be a function of defocus, aberration and total phase shift, depending on the mode of the microscopy (Fresnel, Foucault).

3.4.2 Fresnel imaging

Fresnel imaging is a simple and fast imaging mode for observing the domain walls by simply defocusing the imaging lens an amount of Δf (defocus) below or above the object plane (Fig. 3.12(a)). When we change the current through the objective lens, the location of the image plane along the optical axis is effectively altered by an amount called image defocus. In this case, the image plane of the objective lens does not coincide with the objective plane of the imaging system. The transmitted beam travelling at an angle β will arise from an area displayed by a distance $\Delta f \beta$. The distance Δf is known as the defocus. The Fresnel image is formed with domain walls denoted by dark and bright bands on a grey background. Black contrast is formed when the beams are divergent (divergent wall) whereas the white contrast of domain wall is obvious as the beams are convergent (convergent wall). Generally, increasing

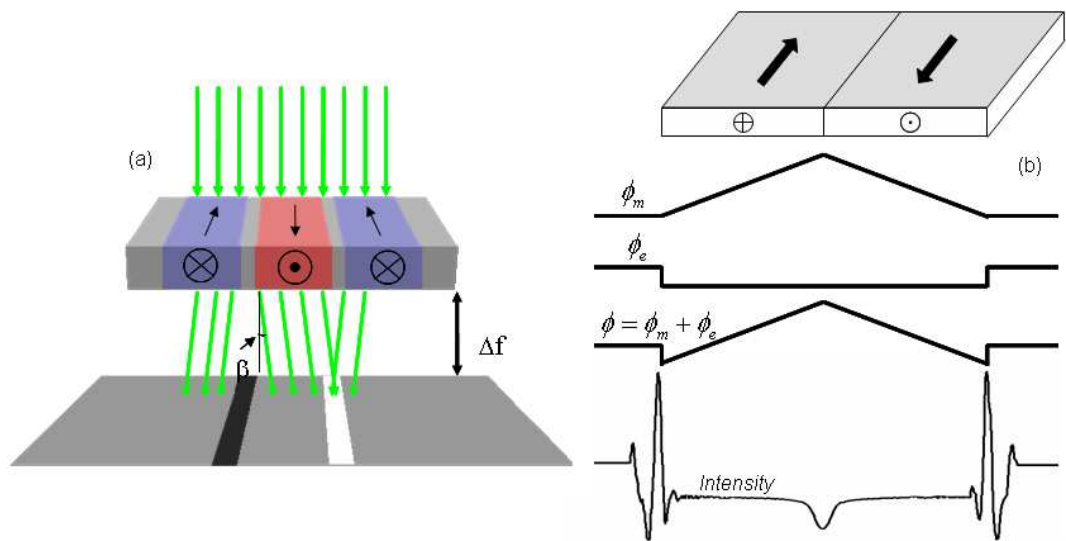


Figure 3.12: Principle of defocused Fresnel image (a) and mechanism of intensity profile in terms of phase shift (b) in a patterned thin film with an inclusion of amplitude contrast.

the defocus gives rise to an increase of the contrast of the Fresnel image. It has been shown that the intensity of the Fresnel image in the low-defocus regime (linear regime, $\Delta f \lambda k^2 \ll 1$) is linearly dependent with defocus and Laplacian of the phase shift [20]:

$$I(\mathbf{r}, \Delta f) = 1 - \frac{\Delta f \lambda}{2\pi} \nabla_{\perp}^2 [\phi(\mathbf{r})] \quad (3.24)$$

However, poorer resolution results from increasing defocus. The Fresnel imaging can provide the best spatial resolution around few tens nanometre.

In Fresnel imaging of the continuous thin films, the Fresnel image provides a pattern of domain walls in a grey background of magnetic ripple (if the film is polycrystalline). Magnetisation ripple is the small wavelike fluctuations of the magnetisation direction that occurs in thin ferromagnetic films. It originates from random orientation of local anisotropies of each crystallite [22]. The magnetisation ripple lies perpendicular to the mean direction of local magnetisation (Figs. 3.13(a)). In continuous films, the electrostatic phase shift is constant and therefore there is no contribution of this component in the contrast of the Fresnel image. High contrast is possible with Fresnel imaging which is sensitive to the variation of the magnetic structure, allowing the in-situ measurements to be performed in real time.

In Fresnel imaging of the patterned films, besides the contrast of magnetic domain walls, strong edge contrast is also visible because of the variation of electrostatic phase at the edge (e.g. Fig. 3.13(b)). Therefore, in a small patterned element, the edge contrast sometimes overlaps the magnetic contrast and makes it harder to interpret. The mechanism of strong edge contrast in patterned films can be understood via fig. 3.12(b).

The advantages of Fresnel imaging for studying magnetic specimens include its ease of operation and the high levels of contrast. It is also well-suited to real-time in-situ imaging, allowing reversal sequences to be recorded during magnetising experiments. Fresnel imaging allows observation of the behaviour of walls under external fields, the domain wall shape, magnetic domain geometry, etc (magnetising experiments). However, Fresnel imaging is very limited for quantification of the magnetic structure of films.

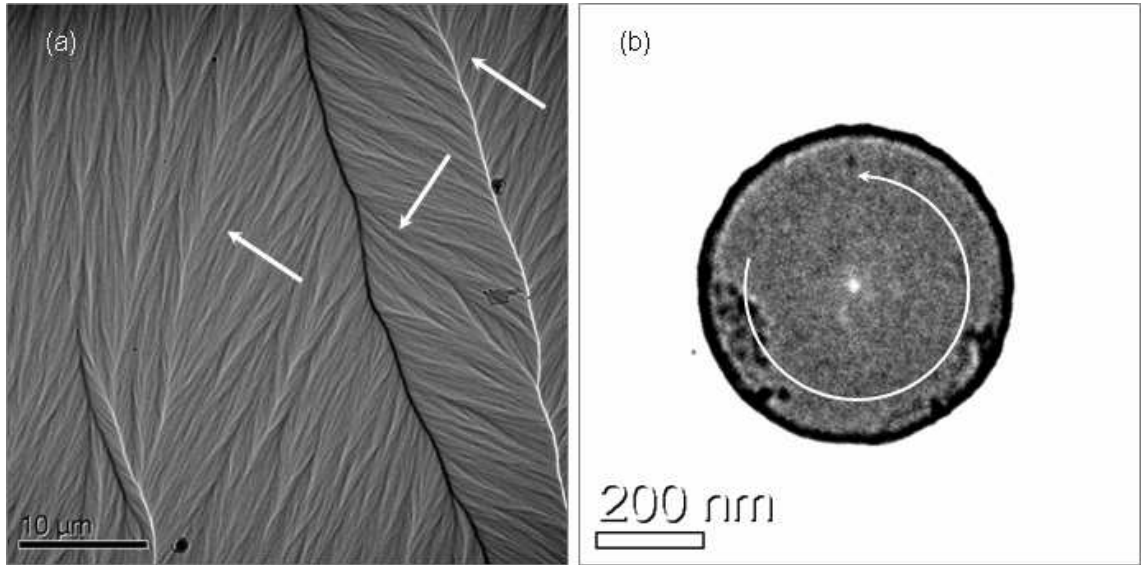


Figure 3.13: Fresnel images of (a) 20 nm thick $Ni_{80}Fe_{20}$ showing the domain walls on magnetic ripple background; (b) a 20 nm thick $Ni_{80}Fe_{20}$ sub-micron dot showing a magnetic vortex at the centre contributed by curling magnetisation and strong edge contrast mainly by electrostatic phase shift.

3.4.3 Differential phase contrast (DPC)

Differential phase contrast (*DPC*) is a technique for visualising the distribution of magnetic induction in thin samples, carried out in a STEM by using a focused electron beam as a probe scanning on the sample as a raster. DPC, which is basically a local low angle diffraction technique, has been developed for magnetic imaging since 1978 [23] from differential phase contrast optics. DPC is one of the leading techniques to image the magnetic structure with very high resolution down to less than ten nanometres [25]. The principle of DPC is illustrated in Fig. 3.14.

DPC imaging allows mapping the magnetic induction in the sample with where the differential phase proportional to the integrated magnetic induction:

$$\nabla\phi(r_{\perp}) = -\frac{e}{\hbar} \int_{-\infty}^{+\infty} (\mathbf{B} \times \mathbf{n}_z) dz = -\frac{e}{\hbar} (\mathbf{B}_{\perp} \times \mathbf{n}_z) \cdot t \quad (3.25)$$

The DPC technique requires the field emission gun to create a very high monochromatic electron beam that is converged as a probe by a probe forming aperture (Fig. 3.14(a)). The probe is controlled to scan across the specimen by scanning coils. After passing through the specimen, the electrons emerge as a cone of illumination which is projected onto a circular quadrant detector (Fig. 3.14(b)). If the sample is non-magnetic, the disc will be centred on the detector. If a magnetic specimen in place, the Lorentz force

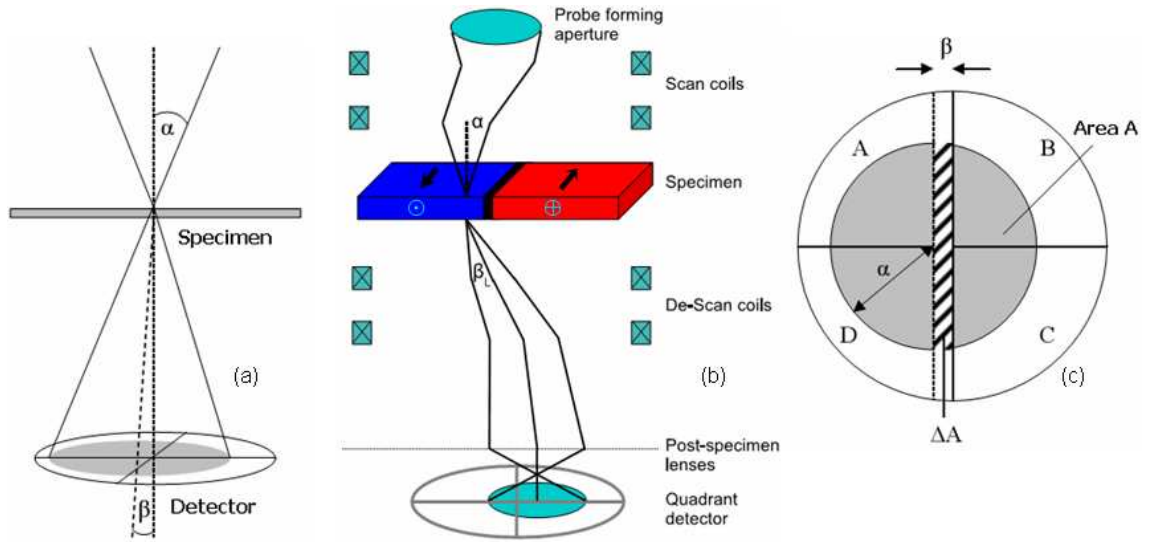


Figure 3.14: Principle of the DPC technique: a) probe scanning on the specimen, b) construction of a DPC system and c) probe image on the detector.

may deflect the electrons and shift the disc to a position that is no longer concentric on the detector (Fig. 3.14(c)). When performing DPC, it is necessary to make sure the beam remains stationary with respect to the detector whilst scanning. This is to ensure that deflections caused by the magnetic induction are the only shifts of the beam from the central position. To achieve this, descan coils are used after the beam has passed through the specimen (Fig. 3.14(b)). Each segment of the detector measures a separate electron signal and the difference signals taken from opposite halves on quadrants will provide information on the induction as two orthogonal components. Additionally, the sum of the signals from the four quadrants also produces a bright field image of the specimen.

The convergent angle of the incident beam is denoted by α and is proportional to the radius of the disc, whereas the deflection angle is denoted by β . When the disc is shifted a distance β on the detector, the area covered on region $B + C$ (Fig. 3.14(c)) decreases by an amount $\sim 2\alpha\beta$. Similarly, a same amount is transferred to the area of the region $A + D$, resulting in an difference of $\Delta A = 4\alpha\beta$ between two regions (Fig. 3.14(c)). The difference signal is written as [24]:

$$S = \frac{I\Delta A}{A} \quad (3.26)$$

where I is the intensity of the electron beam ($I \propto \pi\alpha^2$), A is the total area of the spot on the detector. The (3.26) can be rewritten as:

$$S = \frac{I}{\pi\alpha^2} \left[\left(\frac{\pi\alpha^2}{2} + 2\alpha\beta \right) - \left(\frac{\pi\alpha^2}{2} - 2\alpha\beta \right) \right] = \frac{4I\beta}{\pi\alpha} \quad (3.27)$$

The equation (3.27) indicates that the difference signal produced is linearly proportional to the Lorentz deflection, which is shown in eq. (3.15) to be directly related to integrated magnetic induction. Therefore, the difference signal is proportional to the magnetic induction as follows:

$$S = \frac{4IeB_s\lambda t}{\pi\alpha h} \quad (3.28)$$

It is important to note that the linear relation in (3.28) is only valid when the deflection is small ($\beta < \alpha/10$) at which the $\Delta A = 4\alpha\beta$ is valid.

The DPC mode is in-focus imaging mode and the resolution of the image produced in the DPC mode is determined by the diameter of the probe, which is dependent on demagnification of source and diffraction/aberration effects. The demagnification of the source depends on whether the system is aligned and set in low magnification scanning (LMS) or high magnification scanning (HMS) - Fig. 3.15. In LMS mode, the upper Lorentz lens is turned off, resulting in a larger probe at the specimen due to a smaller demagnification of the optical system and smaller probe angle providing a resolution about $\sim 20 - 30 \text{ nm}$. However, as $\beta \sim \alpha/10$, the DPC signals are very sensitive to the changes of magnetic induction, and therefore producing a high contrast. Whereas, in HMS mode the upper Lorentz lens is switched on to form a finer probe below 10 nm with large probe angle. Therefore, a greater useful magnification is achievable with very high spatial resolution in HMS mode by scanning a smaller area of the sample with a finer probe. The best resolution down to 1.9 nm was demonstrated in VG HB5 STEM at the University of Glasgow [25]. Nevertheless, since $\beta \sim \alpha/1000$, the signal is less sensitive to changes in magnetic induction, and a lower level of contrast is produced. In the Philips CM20 microscope used in this project, the 8-segment quadrant was modified as a two-channel quadrant detector with small inner detector (symbolised as E, F, G, H) for LMS mode and large outer detector (symbolised as A, B, C, D) for HMS mode [24]. Using the 8-segment detector is a modification to the DPC technique (Fig. 3.16a). Briefly, the difference images involving only the outer

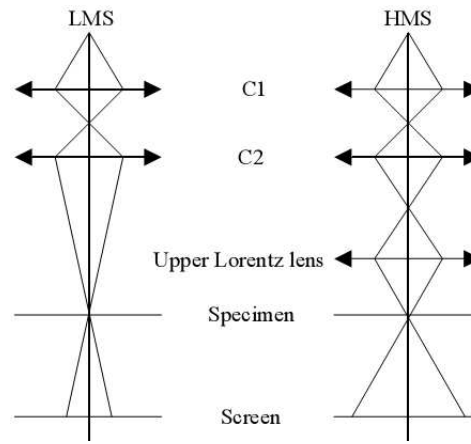


Figure 3.15: Low magnification scanning (LMS) and high magnification scanning (HMS) DPC.

quadrant detector provide information about the position of the bright-field disc and are relatively insensitive to any intensity modulations with it. They are well suited for revealing the low-spatial-frequency component of the signal. Indeed, those electrons in the central part of the BF disc do not contain information about such components and only contribute to the noise in the image of a slowly varying object. Generally, the magnetic structure falls into this category. By contrast, the signal of crystallites is contained in the mid-band or higher-spatial-frequency range of the optical system, and thus it can be efficiently collected using the inner detector. Therefore, using an eight-segment detector allows separating substantially the information into low-spatial-frequency (mainly magnetic) and high-spatial-frequency (mainly non-magnetic) components, which can be displayed in separate images [25].

The advantages of the DPC technique are that it can be used to recover quantitative magnetic information at a very high spatial resolution of below 10 nm with the phase variation is directly proportional to the magnetic induction (equation 3.25). Due to the phase gradient experienced by the electron beam between areas containing the magnetic film and those with only the supporting substrate, however, edge contrast arising from electrostatic phase contribution is also present in DPC images. However, as DPC is an in-focus mode though, these fringing effects are less than in Fresnel images, therefore DPC is the preferred option for the investigation of sub-micron sized thin film elements and structure of domain wall. The main disadvantage is that the instrumental setup is a lengthy procedure, and the DPC operates in scanning mode, so the average DPC experiment requires (field emission gun, special detector, etc.) far

more time to complete than those performed in the Fresnel mode. Moreover, the DPC requires more complex equipments than that the Fresnel imaging.

3.4.4 Philips CM20 TEM/STEM

All magnetic imaging described in this thesis is carried out using a Philips CM20 at the Kelvin Nanocharacterisation Centre which was specifically modified for magnetic imaging from a basic commercial microscope. The CM20 uses a field emission gun for generating the electron beam with an accelerated voltage of 200 kV. The main modification of the CM20 [24] is the addition of twin upper and lower Lorentz lens to enable in-situ measurements in both Fresnel and DPC modes of the Lorentz TEM (see Fig. 3.16(b)). In addition, the gap between the objective lens pole-pieces has been widened to allow a magnetising stage or specialised rods to be used for in-situ experiments. The lower Lorentz lens plays a role of an imaging lens, hence the objective lens can be switched off and imaging is performed with the specimen in field free space. A field emission gun filament produces highly monochromatic electron beam, that allows creation of a fine probe of electron beam for DPC mode.

The ability to be able to perform in-situ experiment [12] is an advantage of the Lorentz TEM, in which an external magnetic field is applied to change the magnetic state of the specimen and the magnetic structure of the specimen is recorded at each state. This is very useful for studying the dynamic behaviour of the ferromagnetic thin films. In the Philips CM20, the external magnetic field is generated by weakly exciting the

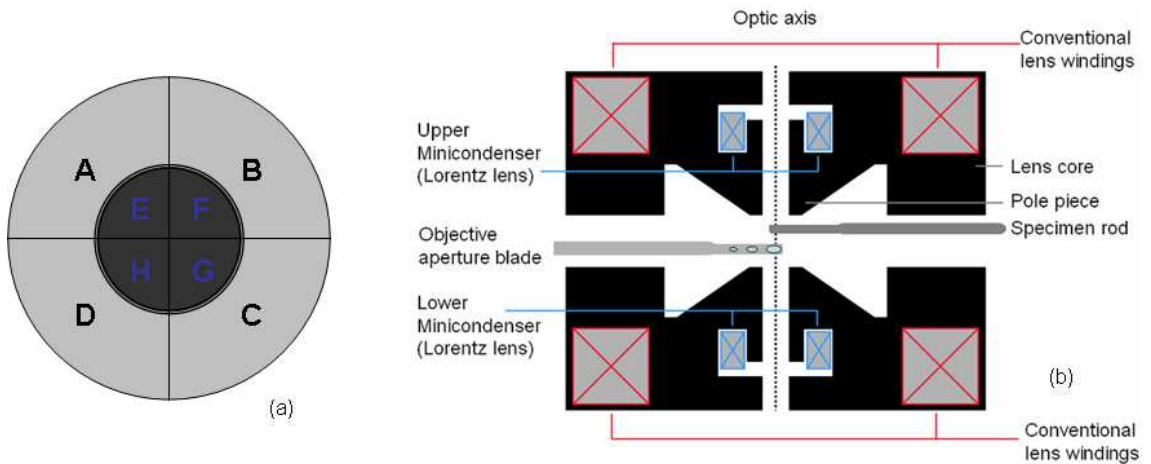


Figure 3.16: Modifications in the Phillips CM20: (a) an eight-segment detector for DPC, (b) modified objective lens.

objective lens and the magnetic structure change can be imaged. When current is passed through the lens coils, a magnetic field, \mathbf{H} which is parallel to the optical axis of the microscope, is produced in the specimen region. The direction of this field (up or down) can be controlled by passing the current through the coils in the forward or reverse directions respectively. The value of the magnetic field is calibrated using a Hall probe [26].

When the specimen is placed in the horizontal position (0° tilt), the field is perpendicular to the specimen plane. A magnetic field component that is parallel to the specimen plane, is created by tilting the specimen at an angle θ (Fig. 3.17). The magnitude of this component is given by:

$$H_{\parallel} = H \sin \theta \quad (3.29)$$

A problem associated with this technique though, is that the component of field perpendicular to the sample can affect the magnetisation. This sensitivity to the perpendicular component lowers the in-plane field necessary to reverse the magnetisation and can allow the formation of magnetic states which would otherwise be difficult to form [12]. This is less of a consideration for continuous films which have a large out-of-plane demagnetising factor.

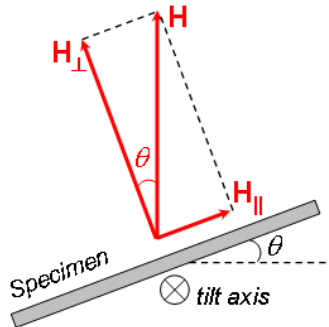


Figure 3.17: Generating a magnetic field parallel to the specimen plane by tilting the specimen.

3.4.5 Magnetisation ripple in Lorentz image

In 1960, Fuller and Hale [15] discovered that the magnetisation direction in a thin film is non-uniform on a microscopic scale and named the phenomenon ‘Magnetisation ripple’ (see Fig. 3.13(a)). Since then, many attempts have been paid in order to discover its origin and its effect on the film behaviour using number of methods, but the tech-

nique of Lorentz microscopy has proved so far the most powerful for this purpose [27]. Magnetisation ripple (also known as dispersion) is the phenomenon in which the magnetisation direction varies locally and quasiperiodically from its mean direction. It is a consequence of the anisotropy of the individual crystal grains and the random (in either two or three dimensions) distribution of the crystallite axes. Hence, the magnetisation ripple is only observed in the Lorentz image of polycrystalline samples. Since experimental works beginning in the 1960's both Hoffmann [22] and Harte [28] developed theories of magnetization ripple. Both agreed that the ripple spectrum is dominated by a longitudinal component and there is reasonable semiquantitative agreement between their predictions and such observable experimental quantities as the predominant ripple wavelength. The main technique used for determining the ripple wavelength was the Fresnel mode of Lorentz microscopy in which changes in magnetisation are related to changes in contrast in defocused images of the magnetic films. Besides, DPC mode of the Lorentz microscopy is also a reasonable tool for characterising the ripple [29]. Fig. 3.18 illustrates the representation of the magnetisation ripple (including longitudinal ripple and transverse ripple) configuration (a) and mechanism of displaying ripple in a magnetised thin film (b) [27]. Since the magnetisation ripple is related to the anisotropy of the film, characterisation of the ripple spectrum would gather fruitful information about the anisotropy of the film e.g. anisotropy field, etc. In the present thesis, characterisation of ripple spectrum in Fresnel images is conducted to understanding the micromagnetic behaviour of the CoIr film (in chapter 5).

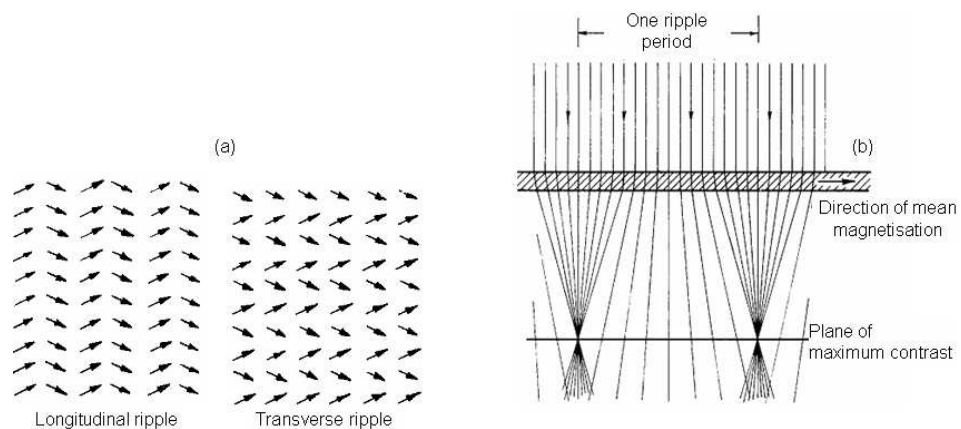


Figure 3.18: (a) Schematic representation of longitudinal and transverse magnetisation ripple configurations; (b) ray diagram of electron traversing a film displaying ripple (b). The pictures are redrawn from Leaver (1968) [27].

3.5 Summary

In this chapter, a brief review of transmission electron microscopy (TEM) was presented begin with basic TEM for analysing physical microstructure, crystal structure and micromagnetic structure. In the Lorentz microscopy section, which is the main method of this thesis, the principle of this microscopy technique including quantum mechanical point of view, the contrast mechanisms of Fresnel imaging, DPC mode of LTEM as well as the modification of the Philip CM20 for magnetic imaging were discussed. Lorentz microscopy is the key technique of the present work and it has been used to quantitatively characterise the micromagnetic structure of the thin films as described in following chapters.

Bibliography

- [1] L. de Broglie, *La nouvelle dynamique des quanta*, Électrons et Photons: Rapports et Discussions du Cinquième Conseil de Physique. Solvay (1928).
- [2] D. B. Williams, C. B. Carter, *Transmission Electron Microscopy: A Textbook for Materials Science*, volume 1: Basic, 2004, Springer, ISBN-10: 030645324X.
- [3] B. R. Craig, *Magnetic and physical characterisation of soft thin films for use in perpendicular recording heads*, PhD thesis, University of Glasgow, 2006.
- [4] M. De Graef, *Introduction to conventional transmission electron microscopy*, Cambridge University Press, 2003, ISBN 0 521 62995 0.
- [5] R. J. Keyse, P. Goodhew, A. J. Garratt-Reed, G. W. Lorimer, *Introduction to Scanning Transmission Electron Microscopy (Microscopy Handbooks)*, Bios Scientific Publisher Ltd., 1st ed. (1998) ISBN-10: 0387915176.
- [6] M. von Ardenne, *Zeitschrift für Physik*, **108** (1938) 553-572.
- [7] A. V. Crewe, M. Isaacson, and D. Johnson, *Rev. Sci. Instrum.* **40** (1969) 241.
- [8] A. V. Crewe, J. Wall, and J. Langmore, *Science* **168** (1970) 1338-1340.
- [9] N. D. Browning, M. F. Chisholm, S. J. Pennycook, *Nature* **366** (1993) 143 - 146.
- [10] J. M. Cowley, *Diffraction physics*, North Holland, 1st ed. (1975) ISBN 0 444 10791 6.
- [11] D. E. Laughlin, B. Y. Wong, *IEEE Trans. Magn.* **27** (1991) 4713-4717.
- [12] C. Brownlie, *A TEM Investigation of Controlled Magnetic Behaviour in Thin Ferromagnetic Films*, PhD thesis, University of Glasgow, 2007.

- [13] H. H. Rose, *Sci. Technol. Adv. Mater.* **9** (2008) 014107-014136.
- [14] D. B. Williams, C. B. Carter, *Transmission Electron Microscopy: A Textbook for Materials Science*, volume 3: Imaging, 2004, Springer, ISBN-10: 030645324X.
- [15] M. E. Hale, H. W. Fuller, and H. Rubinstein, *J. Appl. Phys.* **30** (1959) 789.
- [16] J. N. Chapman, *J. Phys. D: Appl. Phys.* **17** (1984) 623.
- [17] M. R. Teaque, *J. Opt. Soc. Am.* **73** (1983) 1434-1441.
- [18] M. De Graef, *J. Appl. Phys.* **89** (2001) 7177.
- [19] V. V. Volkov, Y. Zhu, *Ultramicroscopy* **98** (2004) 271-281.
- [20] S. McVitie, M. Cushley, *Ultramicroscopy* **106** (2006) 423-431.
- [21] X. Portier, A. K. Petford-Long, *J. Phys. D: Appl. Phys.* **32** (1999) R89.
- [22] H. Hoffman, *IEEE Trans. Magn.* **4** (1968) 32-38.
- [23] J. N. Chapman, P.E. Batson, E. M. Waddel, R. P. Ferrier, *Ultramicroscopy* **3** (1978) 203-214.
- [24] J.N. Chapman, A.B. Johnston, L.J. Heyderman, S. McVitie, W.A.P. Nicholson, B. Bormans, *IEEE Trans. Magn.* **30** (1994) 4479.
- [25] J. N. Chapman, R. Ploessl, D.M. Donnet, *Ultramicroscopy* **47** (1992) 331-338.
- [26] M. F. Gillies, J. N. Chapman, J. C. S. Kools, *J. Appl. Phys.* **78** (1995) 5554.
- [27] K. D. Leaver, *Thin Solid Films* **2** (1968) 149.
- [28] K. J. Harte, *J. Appl. Phys.* **39** (1968) 1503.
- [29] A. Gentils, J. N. Chapman, G. Xiong, R. P. Cowburn, *J. Appl. Phys.* **98** (2005) 053905.

Chapter 4

Fresnel imaging of magnetic vortex in permalloy nanodots

4.1 Objective and motivation

Recently, controlling behaviour of magnetic domain walls has been extensively studied due to potential applications for spintronic devices [1–4]. In particular the vortex domain wall is of considerable interest. The magnetic vortex is a magnetic configuration, which consists of an out-of-plane magnetisation (M_z) at its core and in-plane curling magnetisation (M_x , M_y) around the vortex core. Therefore, a magnetic vortex can be identified as having a chirality of the in-plane flux closure (clockwise or counter-clockwise), and the direction of the out-of-plane component (polarity or polarisation) as seen in Figs. 4.1, 4.2. Vortex state can be transformed to single-domain state when the dimension of the dot (diameter, thickness) changes (see section 1.4.3 in chapter 1).

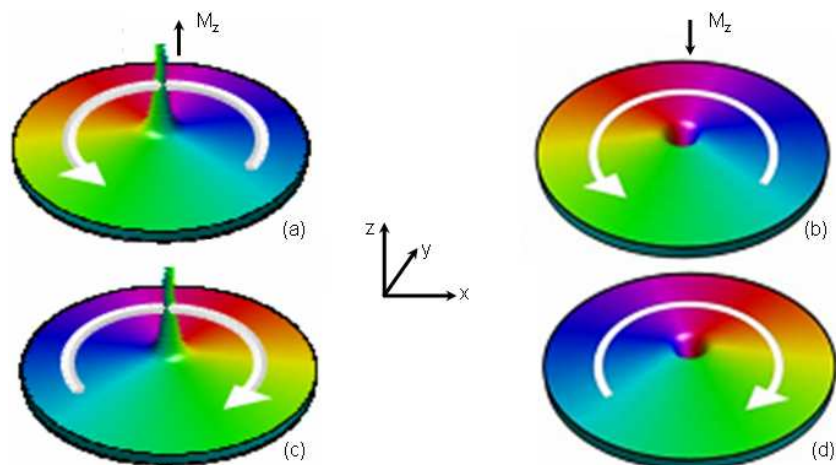


Figure 4.1: Four possible states of a magnetic vortex: (a,b) counter-clockwise chirality with up/down polarities, (b,c) clockwise chirality with up/down polarities.

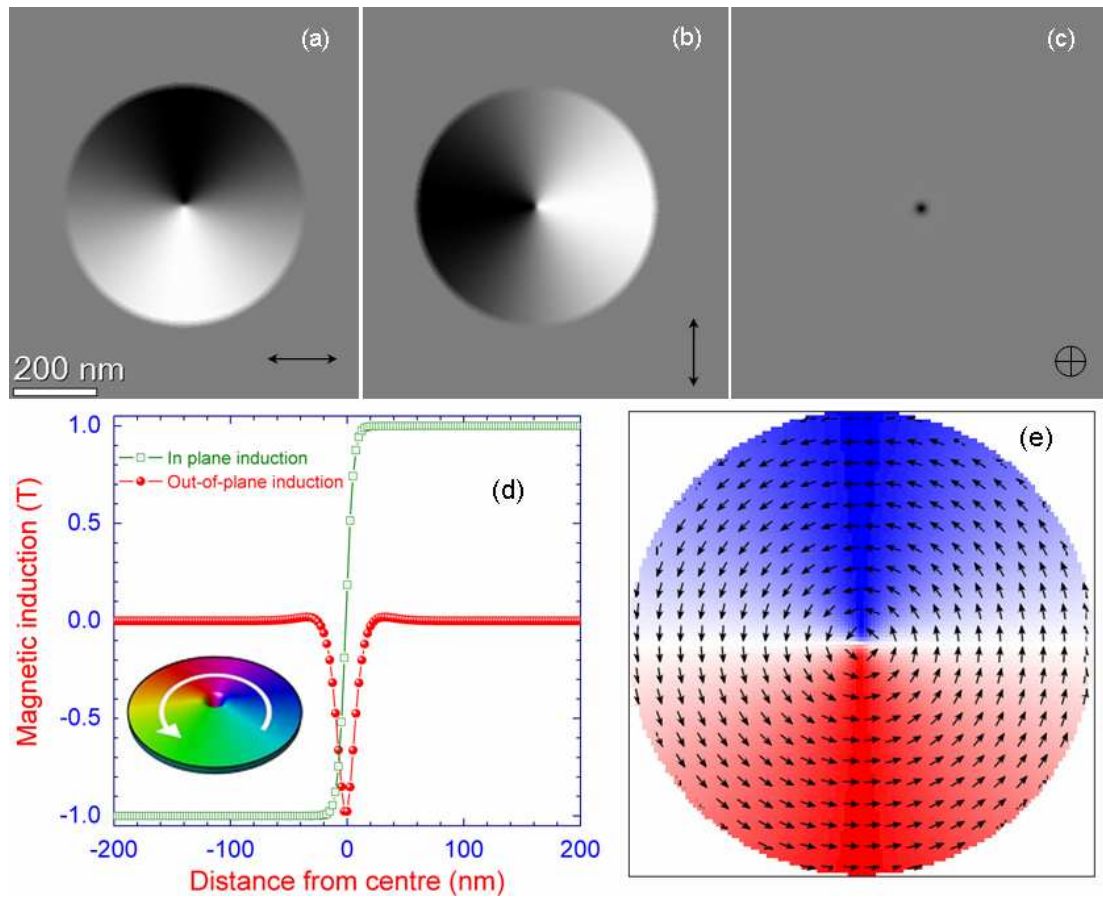


Figure 4.2: Magnetic configuration of the simulated 600 nm - diameter $\text{Ni}_{80}\text{Fe}_{20}$ with thickness of 20 nm: M_x , M_y , M_z components of the vortex core (a,b,c) as the grey scale images, the profiles of the in-plane and out-of-plane component around the vortex core (d) and spin pattern of vortex (e). The colour in frame (e) illustrates the variation of the horizontal component of the in-plane magnetisation.

Recently, much of the work in this field [2,4–7] has indicated that the magnetic vortex could be a promising candidate for the memory cell in near-future non-volatile data-storage. It has been shown that the vortex core gyrates around its equilibrium position as excited by field or current pulses and that it can either be switched by an alternating magnetic field or via the spin-transfer torque mechanism on a nanosecond time scale. Potentially, a magnetic vortex can be used to store two bits of information: the sense of the in-plane flux closure can be employed as an information carrier, and the out-of-plane polarization of the magnetic vortex core can also be regarded as ‘0’ or ‘1’ of a bit element [4]. Other recent interest is arrays of magnetic dipoles which are placed on square lattices. As the dipoles interact with a vortex, they experience different degrees of frustration. If two dipoles point into a vortex and two points out, an ordered array is resulted. This is called the spin-ice rule in analogy to hydrogen bonding in ice crystals. Lateral patterns are presently used for understanding the magnetisation reversal mech-

anism and for analysing interactions and correlation effects, such as magnetic dipoles and magnetic vortices. They are also applied for writing and reading bits and for fabricating logic elements [8]. If the results are demonstrated, they have the potential of being simpler in the design as compared to logic devices based on GMR or TMR spin valves. Therefore, understanding the micromagnetic structure and behaviour of the magnetic vortex will be useful not only from a fundamental scientific point of view but also for technological applications.

The micromagnetic structure of the magnetic vortex has been studied using a number of methods e.g. magnetic force microscopy (MFM), photoemission electron microscopy (PEEM), spin-polarised scanning tunnelling microscopy (SP-STM), or by Lorentz TEM. MFM can characterise the out-of-plane component of the vortex structure, although it has a relatively long imaging time (up to ten minutes) and has a limited spatial resolution [1]. X-ray microscopy can determine the structure of the vortex [9] although this requires a synchrotron source. SP-STM is able to image both components of the magnetic vortex with very high resolution but requires the use of different tips which are sensitive to either the in-plane component or the out-of-plane component [10]. None of these methods is able to characterise simultaneously both the polarity and the in-plane curling magnetisation of the vortex in a single experiment [11]. LTEM which is based on utilising the Lorentz force can obtain magnetic contrast from the magnetisation which is not parallel to the electron beam (chapter 3). Therefore, it is possible to characterise both in-plane curling magnetisation and out-of-plane polarity of the vortex using LTEM in a sample tilted with respect to the electron beam.

The present chapter aims to present a quantitative study of the micromagnetic behaviour and structure of the magnetic vortex in permalloy circular nanodots, with special emphasis given to exploit the Fresnel imaging mode of LTEM to characterise in-plane curling magnetisation and out-of-plane polarity of the magnetic vortex:

- The nucleation and annihilation of a magnetic vortex in the permalloy nanodots is influenced by the edge geometry of the dots. This may be useful for tailoring the behaviour of the magnetic vortex in the nanodots, or other types of nanopatterned elements.

- Determination of the vortex core by Fresnel imaging, providing a quick method to determine the out-of-plane component of the vortex in a single experiment with high resolution. In order to do that, Fresnel images of the vortex are recorded when the specimen is tilted to introduce a contribution of the vortex polarity in the Fresnel images. However, this contribution is relatively small and only visible by obtaining a difference image of two symmetrically tilted Fresnel images to eliminate the contrast from in-plane magnetisation, amplitude and diffraction contrasts. Image tilting, displacement and geometrical distortion may influence the difference image, and hence the difference image must be aligned by cross-correlation. The method will be justified by a study of the observed contrast characteristic due to misalignment.
- Recovery of electron phase using transport-of-intensity equation for quantitatively mapping the magnetic induction in the dots is presented. A study of the contribution of low spatial-frequency on the quality of reconstructed phase will be presented and discussed.

Micromagnetic simulation combined with image calculation and experimental observation in LTEM are presented in this chapter.

4.2 Influence of edge geometry on the micromagnetic behaviour of the vortex in permalloy dots

Results in this section show that the nucleation and annihilation of the magnetic vortex in nanodots is sensitive to the edge slope of nanopatterned elements. We have used the Objective Oriented Micromagnetic Framework (OOMMF) package (see section 1.3.7 in chapter 1) to simulate the magnetic structure and magnetisation reversal of the NiFe nanodots. Furthermore, Fresnel images calculated from the output of the simulation are also used for comparison with experimental Fresnel images.

The simulation was performed for a 20 nm thick circular dot with a diameter of 600 nm. The material is permalloy $\text{Ni}_{80}\text{Fe}_{20}$ with a saturation magnetization of $M_s = 860 \times 10^3 \text{ A/m}$ ($B_s = 1 \text{ T}$), and exchange constant $A = 13 \times 10^{-12} \text{ J/m}$ [12]. The damping coefficient is chosen as 0.5 with a cubic cell size of $2.5 \times 2.5 \times 2.5 \text{ nm}^3$, this

dimension being smaller than the exchange interaction length of the permalloy, which is defined as:

$$L_{ex} = \sqrt{\frac{2A}{\mu_0 M_s^2}} \quad (4.1)$$

In this situation, $L_{ex} = 4.0 \text{ nm}$ for $\text{Ni}_{80}\text{Fe}_{20}$. An external field in range $\pm 300 \text{ Oe}$ is applied along the x-axis with a field step of 6 Oe . In OOMMF, the object is defined by a mask. The OOMMF package works with geometrically perfect elements of constant thickness and straight edges, thus the basic 3D unit cell is rectangular. The structures with sloping edges are constructed by using a multilayer-mesh (Fig. 4.3) in which the slope of the edge is modified by changing the size of layer from bottom layer to the top (Figs. 4.3(b-e)). The bottom layer diameter defines the diameter of the object. For a straight-edge structure, multilayers with the same dimensions were used (Fig. 4.3(a)). For 20 nm thick object, 8 layers of 2.5 nm thickness for each one are used and the resulting edge geometries used in simulation were: 90° (perpendicular edge), and 30° , 45° , 60° , 75° (sloping edges) are shown in Fig. 4.3.

4.2.1 Micromagnetic simulation results

The relaxed stated shows that a vortex state is supported in the dots with various edge slopes and in demagnetised remanent state, the vortex is located at the centre of the dot. Fig. 4.4 illustrates the spin pattern (a) of vortex state formed in demagnetised state and corresponding Fresnel image (b) for the dots with 45° sloping edge as an example. The starting state of the magnetic configuration in the dot is chosen as a vortex with counter-clockwise chirality (Fig. 4.4(a)) for all cases. The same vortex

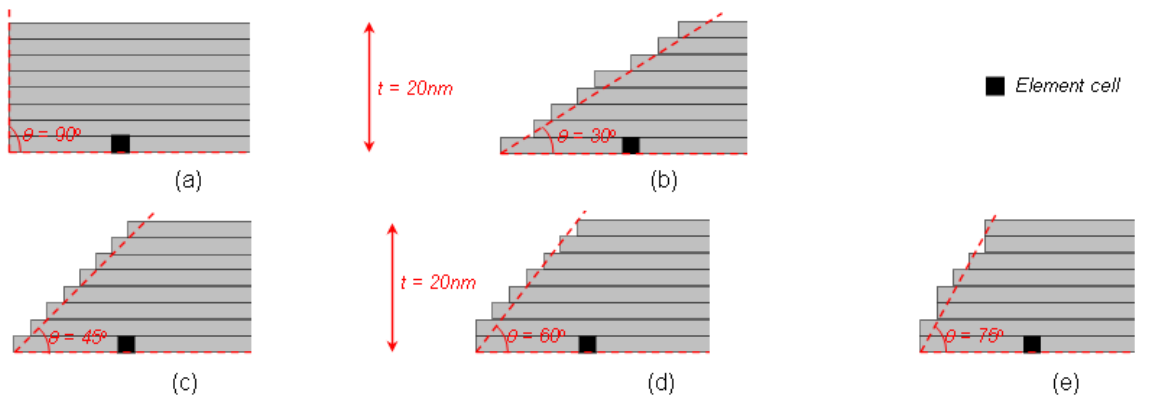


Figure 4.3: Multilayer-mesh is used to define the slope of the edge: (a) perpendicular edge ($\theta = 90^\circ$), (b) $\theta = 30^\circ$, (c) $\theta = 45^\circ$, (d) $\theta = 60^\circ$, (e) $\theta = 75^\circ$.

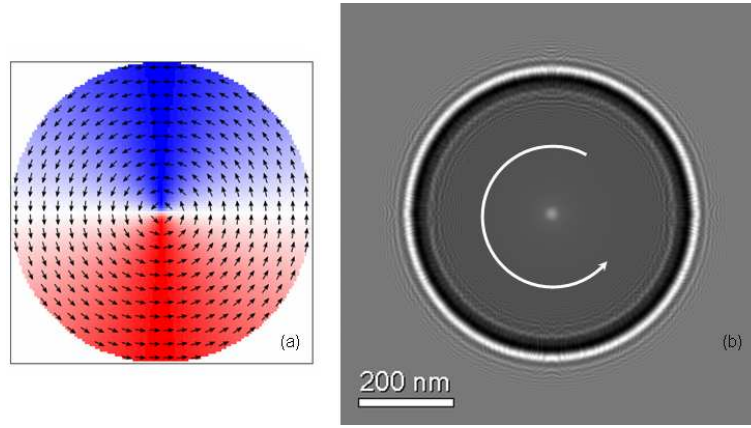


Figure 4.4: OOMMF simulation result of formation of vortex state (a) in 600-nm-diameter and correspondent Fresnel image at $200 \mu m$ defocus (b). Cell size in this case is $2.5 \times 2.5 \times 2.5 \text{ nm}^3$.

core diameter of $14.0 \pm 1.0 \text{ nm}$, which is determined as the full width at half maximum of the M_z profile as shown in Fig. 4.2(c), is found for all dots with various edge geometries. A characteristic feature of the 90° -edge dot can be seen in the Fresnel image (Fig. 4.5(a)) is that increased edge contrast due to the sharp edge is visible more than that of other sloping dots (Figs. 4.5(a,c)). This is caused by effect of the Fourier transform algorithm used to calculate the Fresnel image on the discontinuous variation of the electrostatic phase shift at the edge which is described in (Figs. 4.5(e,f)). The 90° edge dot has a sharp-change electrostatic phase at the edge (Fig. 4.5(e)) whereas the sloping-edge dots induce a smaller gradient change of electrostatic phase at the edge over a number of pixels (Fig. 4.5(f)). It is important to note that the contrast of the vortex in the Fresnel images (bright or dark contrast) is defined by the deflection of the electron after transmitting through the sample. Bright contrast (so-called convergent core) is observed if the beam is convergent whereas a dark contrast is called divergent core when the beam is diverged.

Fig. 4.6 shows the magnetisation and magnetisation reversal sequence of the dot with the perpendicular edge with a hysteresis loop (a) and magnetisation configuration of the dot at various magnetic fields (0-5). In the simulation, the magnetic field is incremented by 6 Oe at each step. Initially, the vortex is located at the centre of the vortex (state - 0). Under an external magnetic field, the vortex core moves perpendicular to the field direction to the top of the dot when the field varies increases. The vortex exists until a field value called *annihilation field*, H_a . Up to this point the magnetisation process is reversible. Above the annihilation field, the vortex is expelled in an irreversible

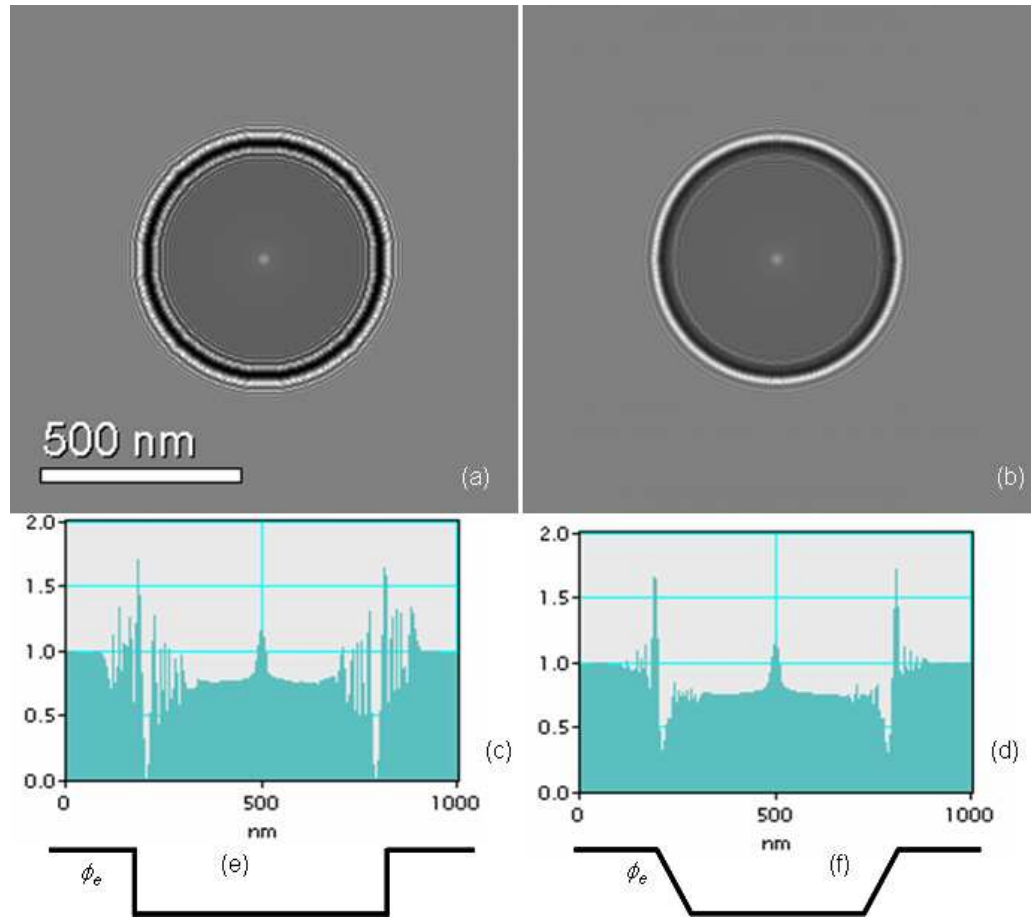


Figure 4.5: Simulated Fresnel images for the dots with 90° edge (a) and 45° edge (b) at demagnetised state; and line profiles of Fresnel images through the vortex (c,d). Frames (e,f) illustrate the electrostatic phases for two cases.

process and the dot approaches a saturation state (Fig. 4.6(2)). A similar initial magnetisation process is also observed for other dots with various edge geometries (see Fig. 4.7) but with different H_a dependent on the edge profiles. Namely, decreasing the edge slope from 90° (perpendicular edge) to 75° , 60° , 45° , the annihilation field increases from 180 Oe, to 210 Oe, 240 Oe and 270 Oe, respectively. This shows that the edge slope significantly affects vortex annihilation in the nanodots.

Significant differences are also observed in the demagnetisation curves (Figs. 4.6, 4.7). The perpendicular dot has a remanent magnetisation with a reduced remanence, $M_r/M_s = 0.8$. The magnetisation in the dot starts to disperse from a C-state at the remanent state (Fig. 4.6(3)). This C-state has a C-shaped magnetisation, and the curvature of the magnetisation becomes larger as the diameter increases [31]. The magnetisation then switches irreversibly with a coercive field, $H_c = 36$ Oe. After nucleation, the vortex moves reversibly until it is annihilated at the annihilation field but the behaviour is different for the dots with sloping edge. In the sloping edge dots, the vortex is nucle-

ated in the reducing positive field (e.g. at +130 Oe for 45°-edge dot - Fig. 4.7(4)). By reducing the magnetic field to zero, the vortex moves back to the centre of the dot in a reversible process and a zero-remenance state is obtained. By reducing the magnetic field from zero to -300 Oe, the vortex moves reversibly to the bottom of the dot, and is annihilated (Fig. 4.7(5)) before approaching saturation in the opposite direction. Zero-remenance is observed for the all the sloping edge structures.

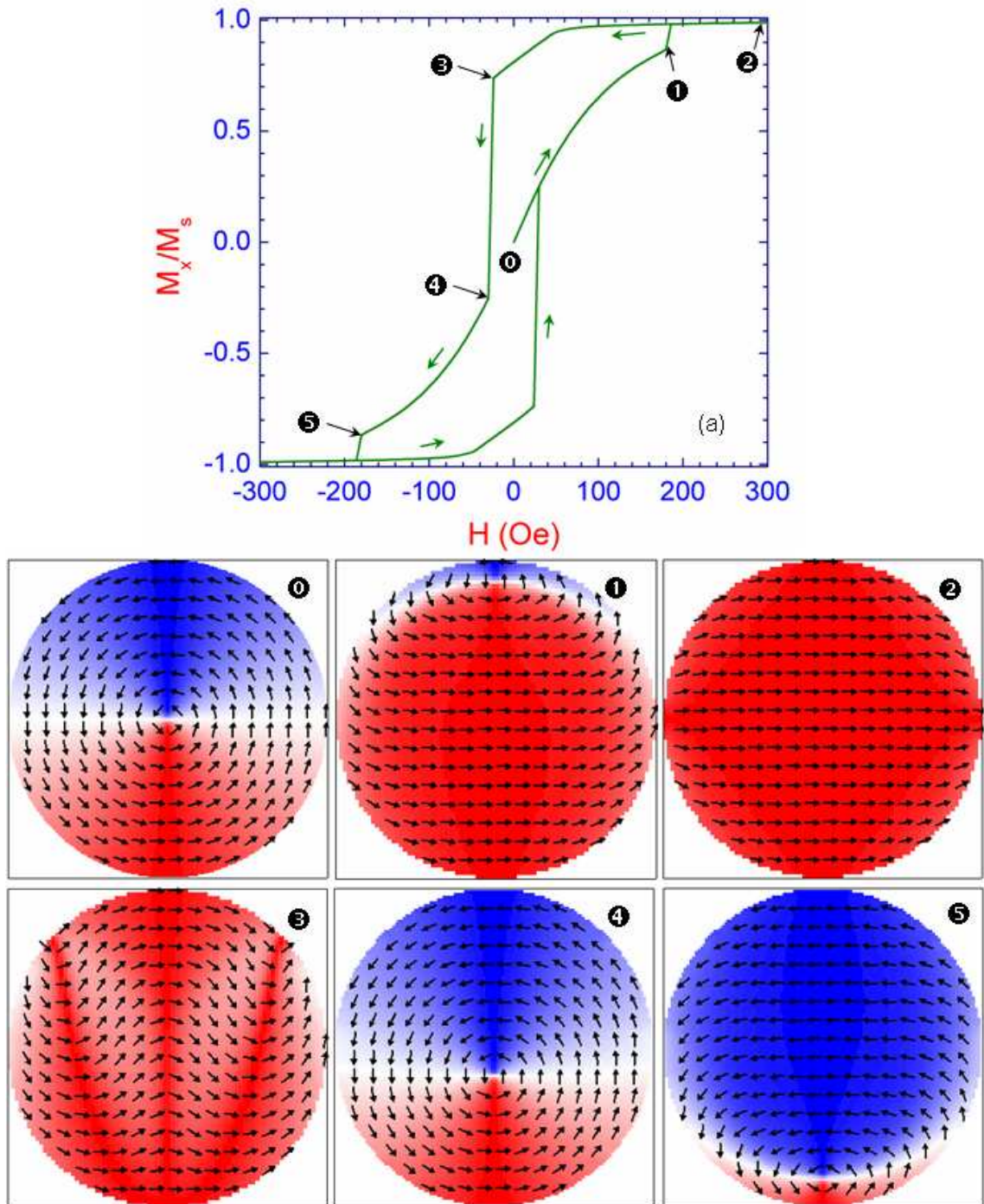


Figure 4.6: Simulated hysteresis loop (a) and magnetisation configuration (0-5) of the 90°-edge dot.

The variation of the edge profile suggests that a sloping edge appears to allow easier generation of the vortex on reducing the field. In the dots, the magnetic configuration is strongly defined by the shape and is very sensitive to the edge geometry as the inhomogeneity of the edge helps to nucleate the edge domain, which is the nucleation for the reversal [14, 15]. Fig. 4.8 illustrates the magnetisation configuration of the 45° -edge dot at the state before nucleating (a,b,c,d,e) the vortex by reducing magnetic

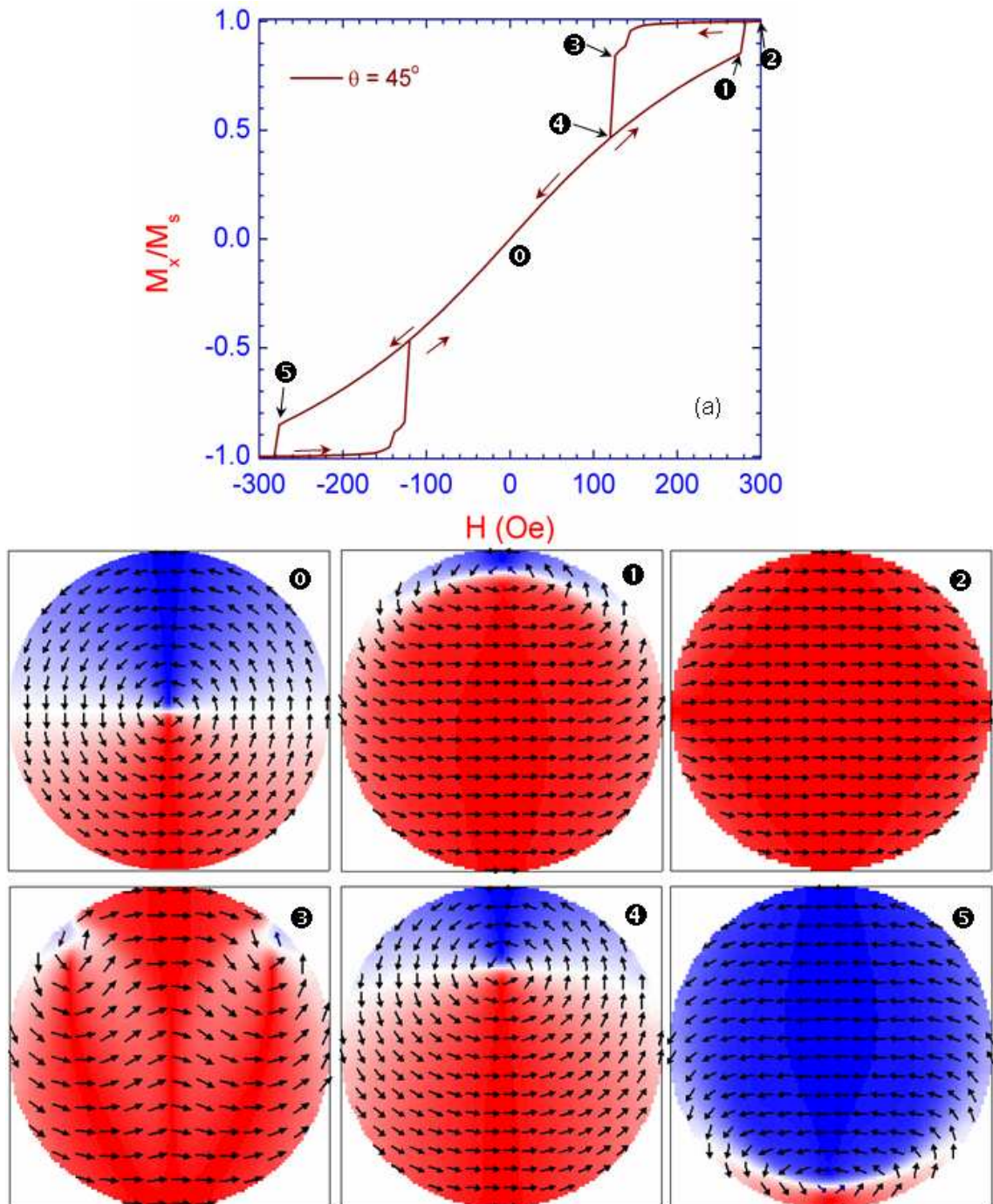


Figure 4.7: Simulated hysteresis loop (a) and magnetisation configuration (0-5) of the 45° -edge dot.

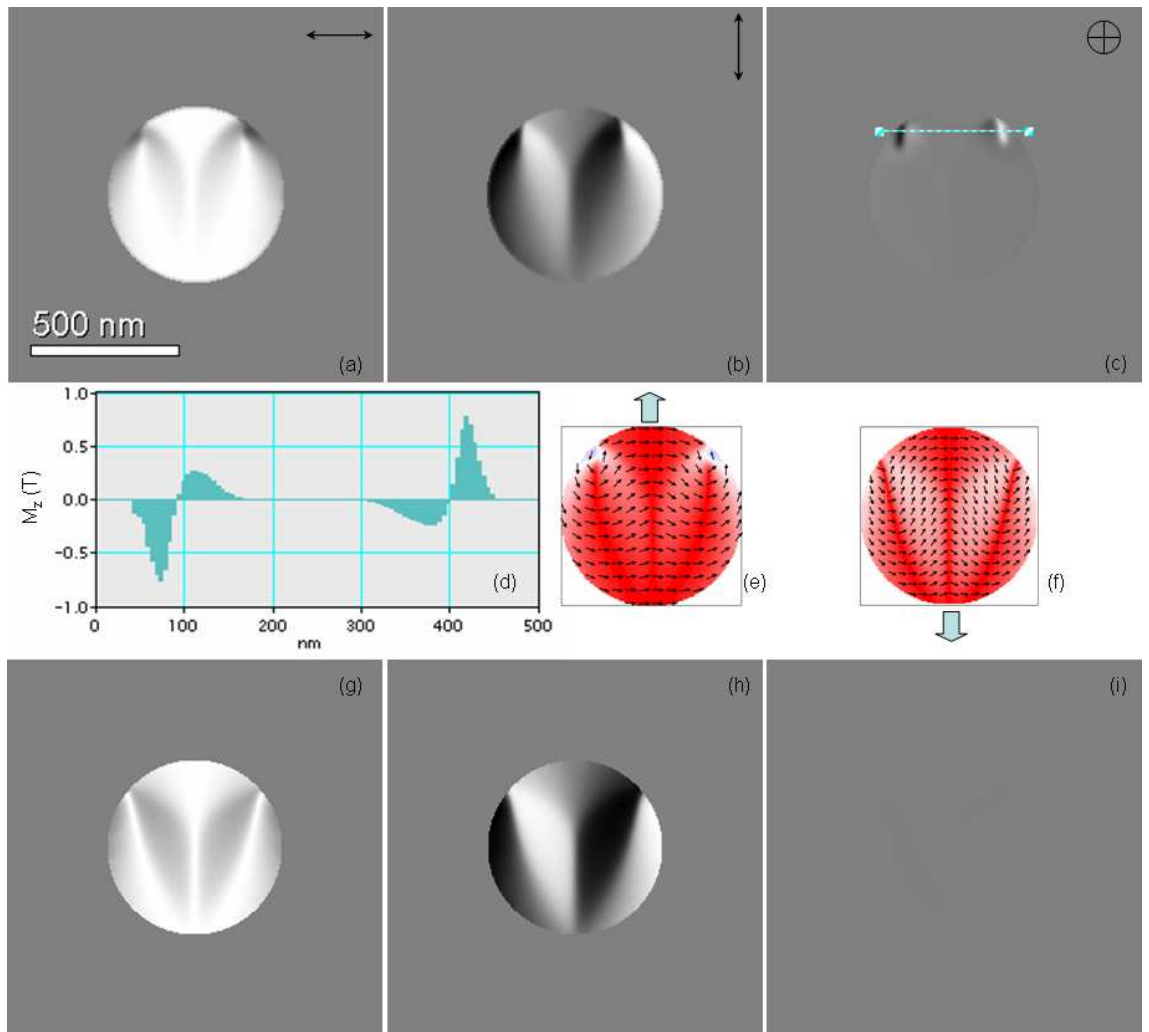


Figure 4.8: Magnetisation components, M_x (a), M_y (b), M_z (c) before vortex nucleation (+136 Oe) as the grey scale images of the 45° -edge dot. Frame (d) shows the line profile of the M_z image measured through the reversed domains, frame (e) shows the spin pattern from OOMMF simulation. Frames (f,g,h,i) show the similar result for the dot with a straight edge at -30 Oe.

field (+136 Oe) comparing with corresponding state for straight edge dot (f,g,h,i) at -30 Oe. In this state, the in-plane magnetisation is dispersed, whereas near the edge of the sloping edge dot, with formation of small domain with a negative component of M_x (Fig. 4.8(a)) and with a significant out-of-plane magnetisation component present as seen in the M_z image (Fig. 4.8(c)). These domains are nucleated near the edge of the dot, and would appear to be the source for the vortex. In the 90° (Fig. 4.8(f,g,h,i)), before nucleating the vortex, the formation of such domains is not observed. Only the dispersion of the magnetisation with an S-state, of which magnetisation deviates as an S-shaped pattern, is observed. The S-state magnetisation pattern is a well-known metastable state in rectangular and elliptical nanostructures [32]. This suggests that

the edge geometry is the origin of such differences in the micromagnetic behaviour of the vortex. The hysteresis loop characteristics as the functions of the edge slope angle are plotted in Fig. 4.9.

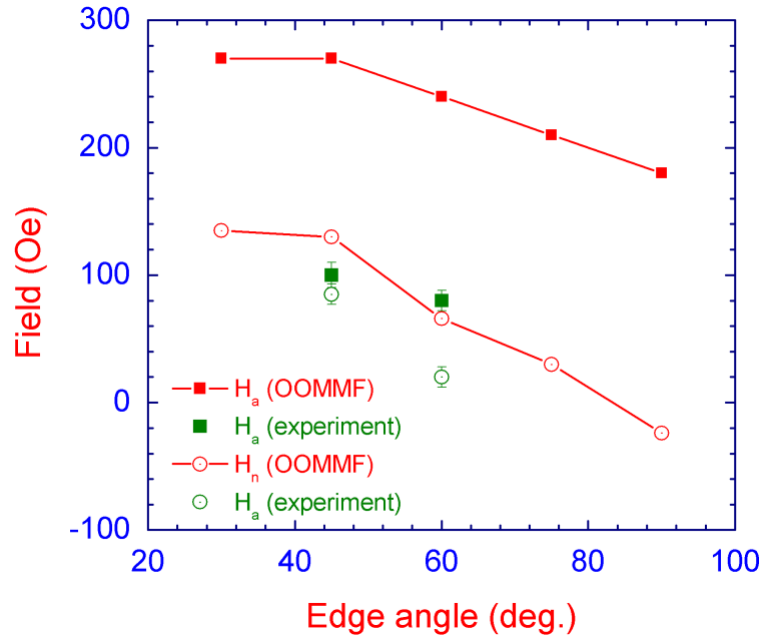


Figure 4.9: Hysteresis loop characteristics (annihilation field, H_a , nucleation field, H_n) of the magnetic vortex as the functions of the edge angle. The discontinuous square and circular dots show experimental results.

4.2.2 Experimental observation

Experimental observation was performed on the Philips CM20 LTEM for lithographically patterned samples. The edge profile of the dots was varied by changing the dose of electron exposure in the lithographic process in order to study the edge geometry affected micromagnetic behaviour. The measurements were repeated many times and the results were averaging out over number of dots on the substrate. Figs. 4.10(I) and 4.10(II) illustrate the experimental Fresnel images of the dots at various magnetic fields in initial magnetisation and demagnetisation processes, respectively. Corresponding states of the vortex in these processes are interpreted by comparing with simulated results which were presented previously. A similar picture to the micromagnetic simulation observed previously with the vortex located the centre of the dot in demagnetised state (Fig. 4.10(a)), and the annihilation of the vortex at the top of the dot at the annihilation field (Fig. 4.10(b,c)): The vortex core moves reversibly perpendicular to the field direction to the top of the dot when the field varies increases and exists below an-

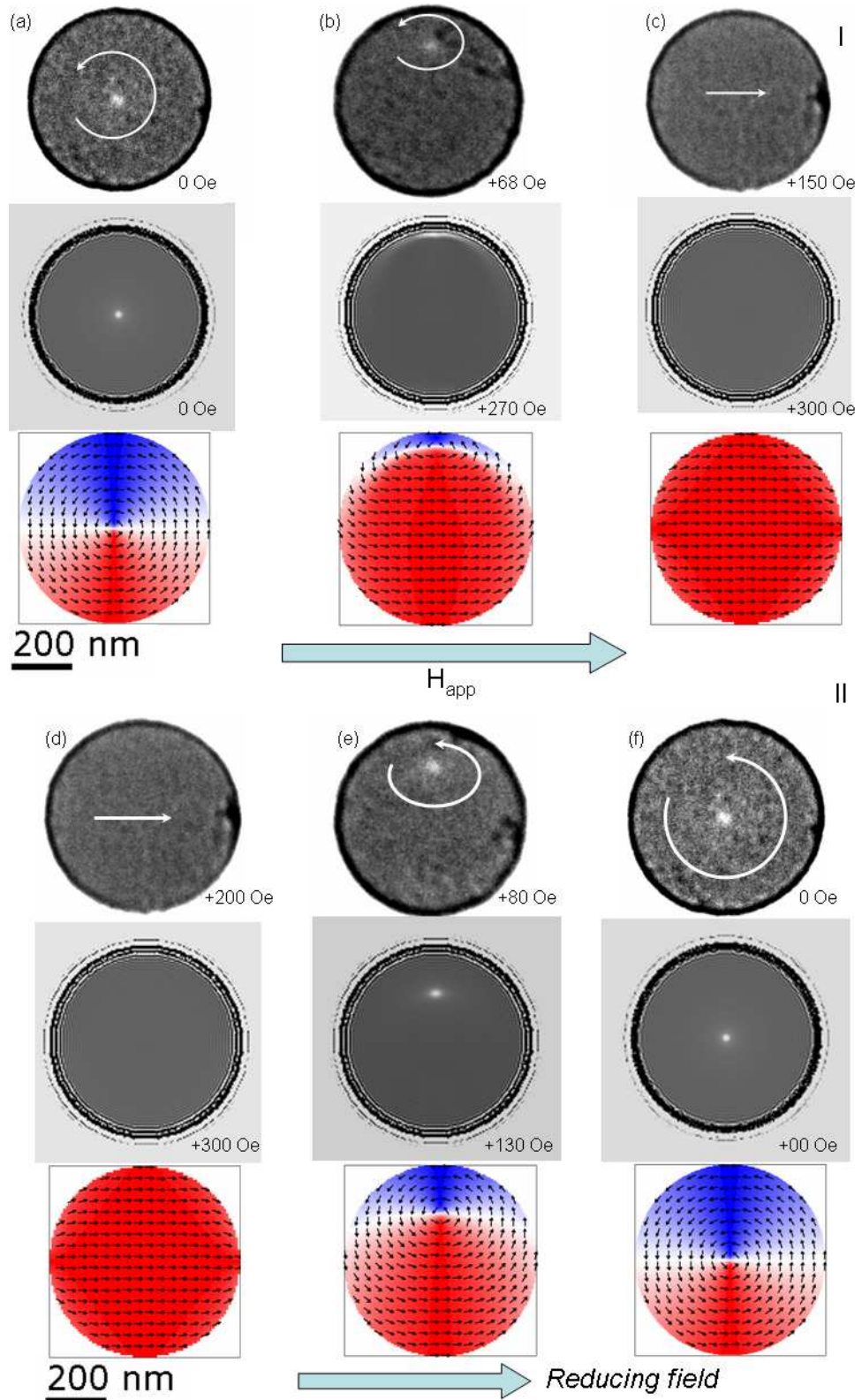


Figure 4.10: (I): Fresnel images of the 600 nm diameter dot in initial magnetisation process: (a) 0 Oe, (b) 68 Oe, (c) 150 Oe compared with Fresnel images and spin patterns obtained by simulation at corresponding states for the dot with 45° edge. (II): Fresnel images of the 600 nm diameter dot demagnetising process: (d) - +200 Oe, (e) - +80 Oe, (f) - 0 Oe compared with Fresnel images and spin patterns obtained by simulation at corresponding states for the dot with 45° edge.

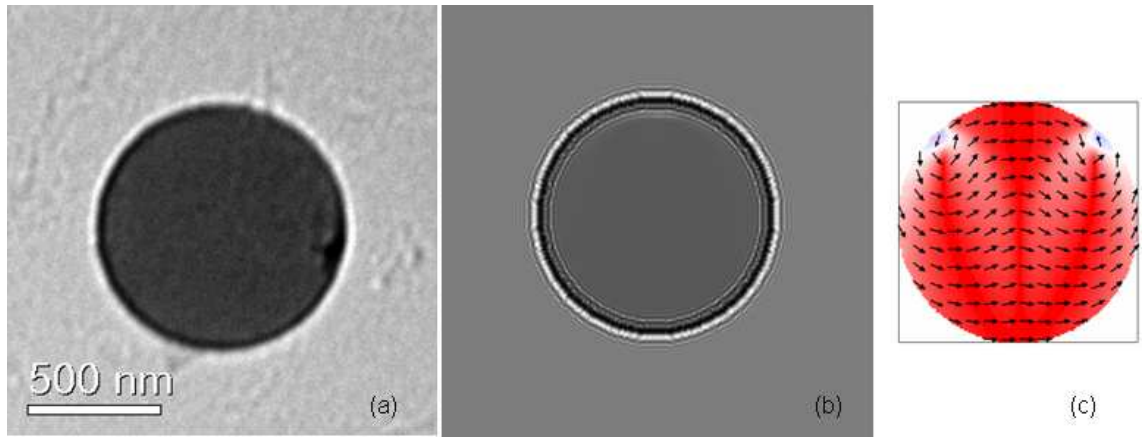


Figure 4.11: Experimental (a) and simulated Fresnel images of the 45° -edge $\text{Ni}_{80}\text{Fe}_{20}$ dot at the state before nucleation of the vortex. Frame (c) shows the simulated spin pattern. The detailed magnetic structure of this state was shown previously in Fig. 4.8

nihilation field, H_a ; above the annihilation field, the vortex is expelled in an irreversible process and the dot approaches a saturation state. In the demagnetisation process, the vortex is nucleated in reducing the magnetic field (at +80 Oe - Fig. 4.10(e)), indicating the behaviour of a sloping edge dot. When the field is relaxed to zero, the vortex moves back to the centre of the dot in a reversible process. It is noted that the state prior to nucleation of the vortex (at +80 Oe) only produces very weak contrast from the simulation and there is little discernable contrast present in the experimental Fresnel image (Fig. 4.11). The edge profiles of the elements were now studied by looking at cross-section samples.

Fig. 4.12 illustrates a SEM micrograph of a dots array used in experiment (a) and TEM cross-sectional images of the dots (b-d). Cross-sectional specimens were prepared using focused ion beam milling. It is found that the edge profile of lithographically patterned dots varies when the dose of the electron exposure is changed. Namely, when the dose changes from $2000 \mu\text{Ccm}^{-2}$ to $2500 \mu\text{Ccm}^{-2}$, the edge slope varies from approximately 60 ± 7 degrees to around 45 ± 5 degrees, although the edges are less uniform than in the simulations. From Figs. 4.12(c,d), it can be seen that the higher dose provides a higher slope angle of the edge however the bottom surface is not completely flat in this case (Fig. 4.12(d)). This observation is consistent with results [17,18] that the edge profile of the lithographically patterned semiconductor and metallic films can be modified by electron beam dose. As a result, the behaviour of the vortex in the dot has been observed to change significantly when the edge geometry is modified. A comparison of

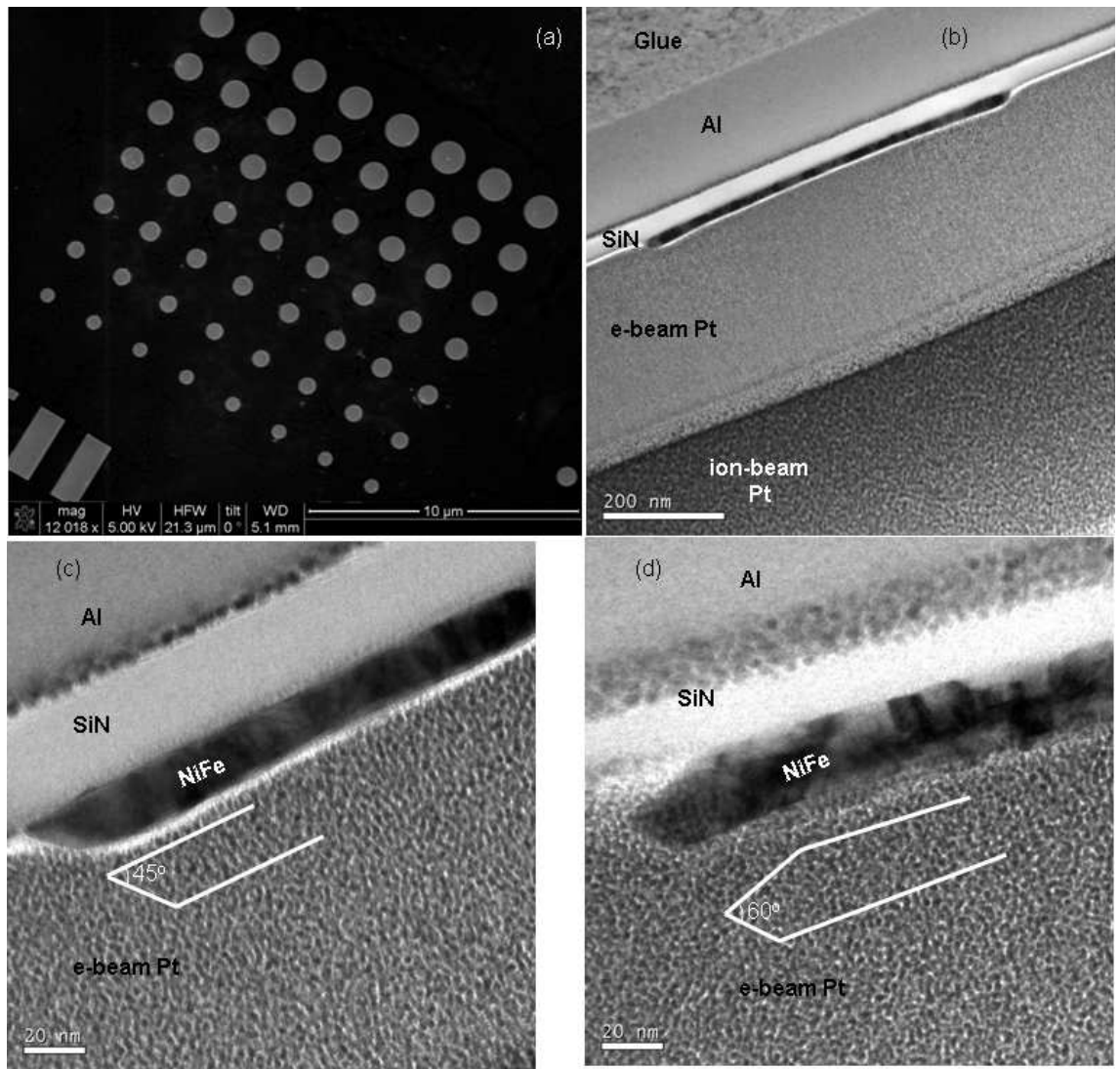


Figure 4.12: SEM image (a) of $\text{Ni}_{80}\text{Fe}_{20}$ dot array for experiment; (b) TEM cross-section image of a dot in specimen series fabricated with the dose of $2500 \mu\text{Ccm}^{-2}$, and (c) TEM images of cross-section showing edge geometries 45° ; and (d) other specimen series fabricated with the dose of $2000 \mu\text{Ccm}^{-2}$ showing a 60° edge slope.

the behaviour of the vortex in the dots with changing edge profile is shown in tab. 4.1 (or in Fig. 4.9). These results experimentally confirm that the behaviour of the vortex in the dots is sensitive to the change of the edge profile. This effect was discussed previously that the magnetic configuration in a patterned film is defined by the shape of the edges and is very sensitive shape fluctuation and edge roughness because of demagnetising field induced by dipole interactions. When the edge is sloped, the shape anisotropy is reduced by the appearance of a magnetostatic energy term called lateral interface roughness anisotropy [19]. As a result, the magnetisation direction will always change close to the borders to form the edge domains [14, 15]. The inhomogeneity in the magnetisation at the edge will dominate the magnetic switching properties, acting

Table 4.1: Hysteresis loop characteristics of experimental patterned dots with various edge slopes modified by changing electron dose. This results were also plotted in Fig. 4.9.

Dose (μCcm^{-2})	Edge slope (deg.)	H_a (Oe)	H_n (Oe)	H_c (Oe)
2000	60 ± 7	$+85\pm 8$	$+20\pm 8$	0 ± 4
2500	45 ± 5	$+100\pm 10$	80 ± 8	0 ± 4

as nucleation sites.

The differences in annihilation field and nucleation field between experimental and OOMMF simulated results are assigned to be the dot structure. In OOMMF, the microstructure of the dots is ignored (considered as single crystal with uniaxial anisotropy), however, the sample in experiment is polycrystalline with not perfectly homogeneous grain structure. Furthermore, in OOMMF, the thermal fluctuation is neglected and the behaviour of the dot seems to be at 0 K. However, in experiment, the measurement was performed at room temperature, and thermal fluctuation leads to a change in the vortex behaviour [20].

4.3 Determination of vortex core polarity using off-axis Fresnel imaging

In this section, an investigation is presented in which out-of-plane component (polarity) of the vortex core in the magnetic nanodots can be determined using tilted Fresnel images. The method is developed from calculation of Fresnel images combined with experimental observations in the TEM.

4.3.1 Method description

Returning to the previous section, the magnetic configuration of a magnetic vortex in 20 nm-thick NiFe dot is illustrated in Fig. 4.2. In this structure, a counter-clockwise chirality is denoted by the spin pattern (Fig. 4.2(e)). The dark contrast at the centre of the M_z -component image (Fig. 4.2(c)) reflects a downward polarity at the core of the vortex with a core diameter of 14.0 ± 1.0 nm. The distribution of the magnetisation components (in-plane and out-of-plane components) is shown in the Fig. 4.2(d).

The Fresnel images of the micromagnetic simulation structure were calculated by using programing script running on the software program Digital MicrographTM [21, 22] from

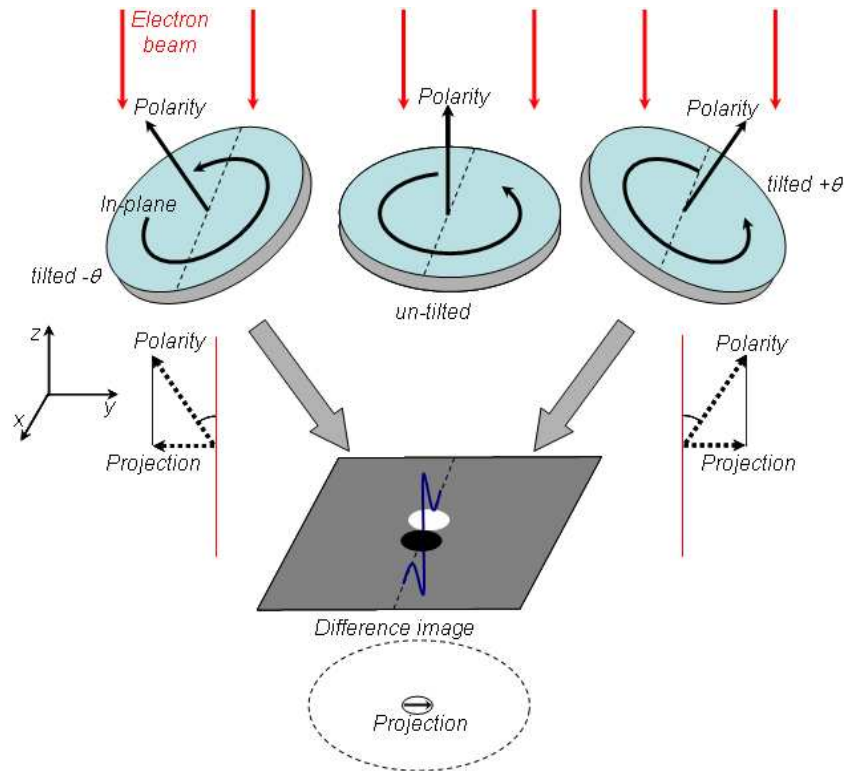


Figure 4.13: Tilted Fresnel images to determine the vortex polarity. Contribution of polarity projection to Fresnel images is enhanced by obtaining a difference image of two symmetrically tilted Fresnel images.

Gatan used for image acquisition and processing. The three orthogonal magnetisation components (as shown in Figs. 4.2(a,b,c)) are used as the inputs for the calculation which incorporates the microscope parameters (defocus Δf , accelerating voltage V , spherical aberration C_s). In the experiment, Fresnel images of the submicron $\text{Ni}_{80}\text{Fe}_{20}$ dot arrays have been acquired using the Philips CM20 microscope. In the simulation, a pixel size of 2.5 nm, which is close to the value of experimental imaging at 15,000 times magnification, was selected with other input parameters equivalent to those of the CM20 microscope ($V = 200$ kV, $C_s = 8000$ mm).

Conventionally, no information of the magnetic induction parallel to the electron beam is provided by the LTEM because no Lorentz force occurs ($\mathbf{F} = q(\mathbf{E} + \mathbf{v} \times \mathbf{B})$). Therefore, there is no contribution of the vortex polarity in the Fresnel images when the sample is perpendicular to the beam (un-tilted). However, by tilting the specimen at an angle to the horizontal plane, the vortex core will be as a result not parallel to electron beam and this creates an in plane component contribution on the horizontal plane (Fig. 4.13). Therefore, in this case the vortex core will contribute to the contrast of the Fresnel image. However, the contribution of the vortex polarity in the tilted

Fresnel image is relatively small compared to a strong contrast of the in-plane curling magnetisation component and is not prominent in a single Fresnel image. However the main contribution to the contrast, which is provided by the curling in-plane components, can be subtracted by calculating a difference image of two Fresnel images produced by symmetrically tilting the specimen (Fig. 4.13). As a result, the contrast of the vortex polarity can be visible in a nearly zero background. However the observed contrast due to the polarity in the difference image is highly dependent on the displacement of the images due to tilting specimen, and the non-magnetic contributions e.g. diffraction contrast and noise. Therefore, alignment of images to subtract the difference image is very important and needs to be taken care.

4.3.2 Evidence of vortex polarity

Fig. 4.14 illustrates two simulated Fresnel images of the dots tilted at $\pm 30^\circ$ angle (a,b). It is apparent that both the tilted Fresnel images (Figs. 4.14(a,b)) and untilted Fresnel image (Figs. 4.4, 4.5 in section 4.2.1) are visually not different from each other. However, the polarity contrast will be characterised in the difference image of these Fresnel images (Fig. 4.14(c)). With this difference image, the contribution from in-plane curling magnetisation and diffraction contrast from crystalline structure is effectively eliminated.

The contribution of the out-of-plane component in tilted images is evidently apparent by the appearance of white-black bipolar contrast in the difference image (Fig. 4.14(c)). A 17% contrast level of the polarity is observed in the difference image (Fig. 4.14(d)). The width of the bipolar contrast, defined as the distance between the peaks of white and black contrasts in the difference image (Fig. 4.14(d)), is measured and shown to be 22.5 nm. In this case, the contrast level was compared to the background level around the vortex in the un-tilted Fresnel image and given by:

$$Ct(\%) = \frac{I_i - I_s}{I_s} \times 100\% \quad (4.2)$$

with I_i , I_s are the intensities of the interested position and standard background level (0.75 in simulation and 8,000 counts in experiment), respectively.

The formation of this white-black contrast is due to the contribution of the vortex

polarity in the tilted Fresnel images. The contribution of the in-plane components is the same for the both images and therefore is cancelled in the difference image. Whereas, the projection of the vortex polarity in the tilted Fresnel images has the same magnitude but in opposite sign (see the diagram in the Fig. 4.13). This causes a bipolar-like white-black in the difference image (Fig. 4.14(c)). When the direction of the out-of-plane polarity changes to the opposite direction, the bipolar contrast is switched to black-white (opposite to white-black contrast of the down polarity).

Fig. 4.15 compares the tilted Fresnel images and difference images for three simulated states based on the simulation in Fig. 4.1: i) normal vortex with in-plane curling magnetisation and vortex core (a,b,c) i.e. using all three magnetisation components; ii) a vortex with no out-of-plane core - only curling magnetisation (d,e,f) i.e. having no z- component of magnetisation; iii) a state with only out-of-plane core (g,h,i) to highlight the contribution of polarity of the vortex core in the tilted Fresnel images.

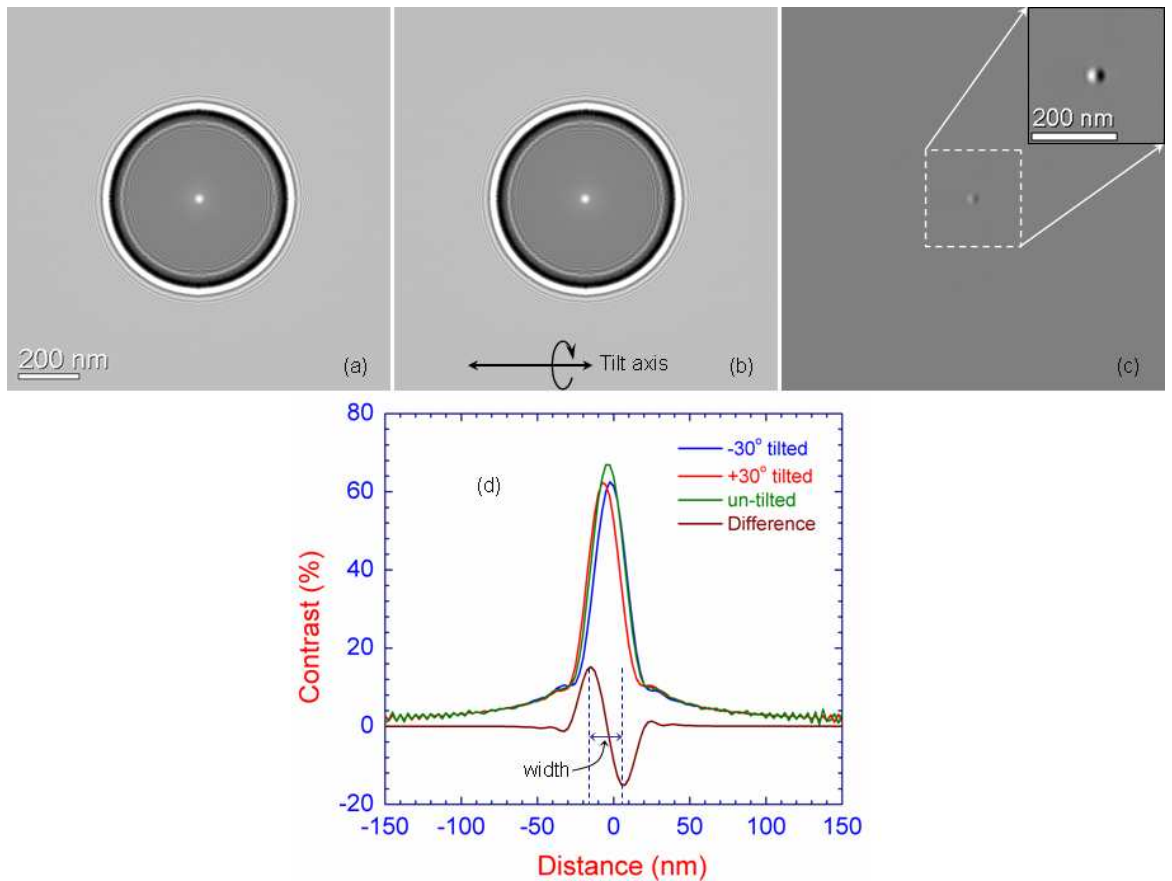


Figure 4.14: Simulated Fresnel images of a 20 nm thick permalloy dot with 600 nm diameter at $\pm 30^\circ$ tilted angles (a,b), and difference image (c) at $250 \mu\text{m}$ defocus. Line profiles of contrast of the images are shown in frame (d) in comparing with contrast of the vortex in untilted Fresnel image. The inset a contrast-enhanced selected area of white-black contrast of difference image.

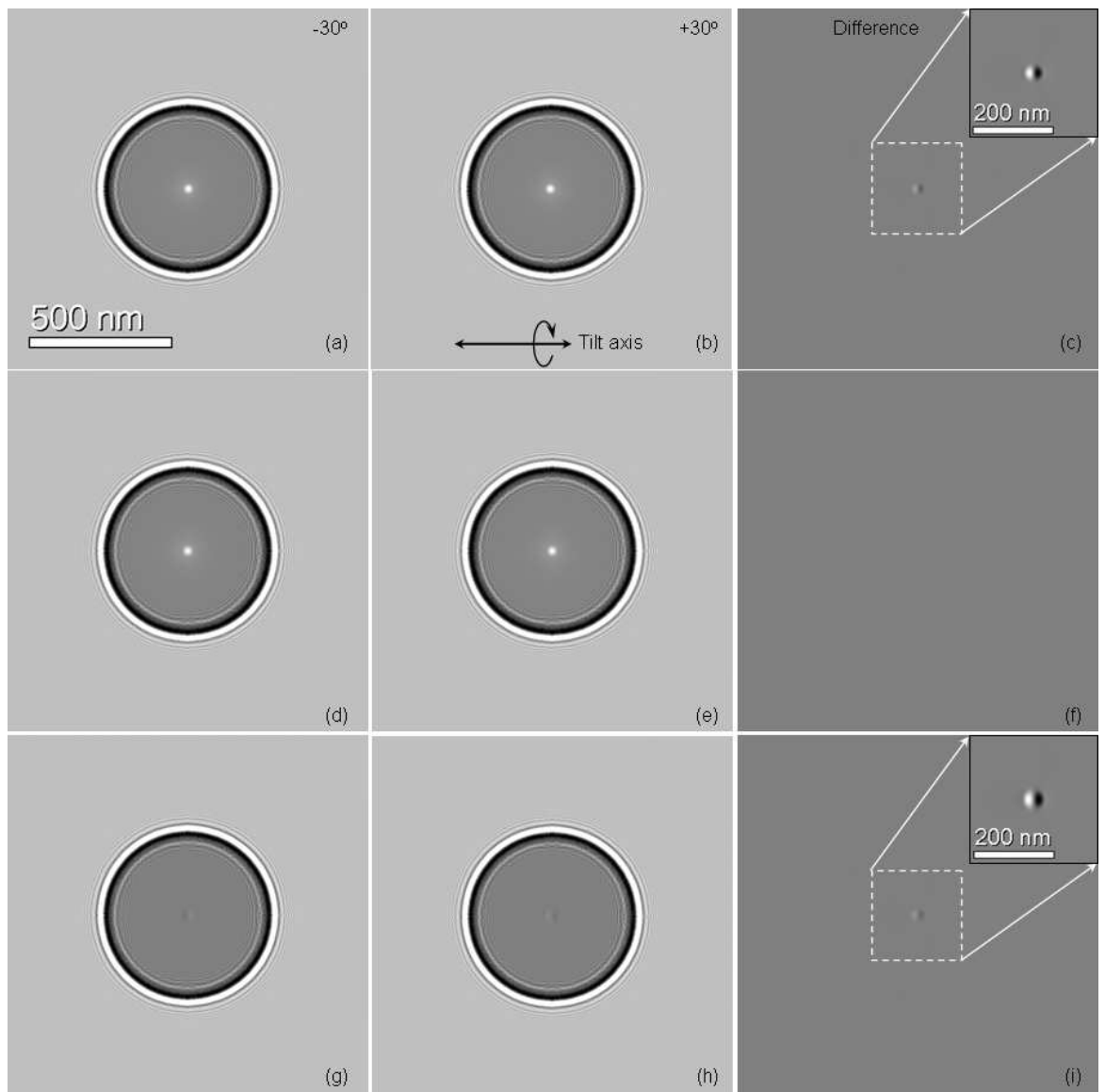


Figure 4.15: A comparison of tilted Fresnel images and difference image in three cases: (a,b,c) a normal magnetic vortex with in-plane curling magnetisation and out-of-plane core; (d,e,f) a curling magnetisation without out-of-plane core; (g,h,i) a structure with only out-of-plane core. Defocus value in this case is $250 \mu m$.

Note that the second and the third states are not physically realistic, they are used here only for a comparison. It is obviously seen that the bright contrast at the centre of the vortex forms arises mainly from the in-plane curling magnetisation (both cases Figs. 4.15 (a,b,c) with out-of-plane core, and Fig. 4.15(d,e,f) without out-of-plane core), confirms that the contrast of the vortex is dominated by the curling magnetisation. In the difference image obtained from the tilted Fresnel images of the structure with only out-of-plane core (Figs. 4.15(g,h,i)), the white-black bipolar contrast contributed by the out-of-plane core is observed, but it is also weaker than the strong edge contrast contributed by electrostatic phase shift. The contribution of the out-of-plane core is

relatively weak and localised on a small scale area around the centre of the dot (see Figs. 4.15(g,h)). The contrast of this contribution is hardly visible in the individual images, but clearly seen in the difference image in which the background is subtracted (Fig. 4.15(i)). Furthermore, in the structure without out-of-plane core, the difference image (Fig. 4.15(f)) is a grey-scale (zero contrast) image because of cancelation of symmetric contribution from curling in-plane magnetisation in two tilted Fresnel images. This suggests that the out-of-plane polarity of the vortex can be detected as the appearance of the bipolar white-black contrast in the difference image. It is important to note that in the simulation, no noise or crystalline structure is included, therefore, any contrast level can be detected in principle. Hence, the reliability of the method needs to be confirmed by experiment, in which the contribution from noise and displacement of the images due to tilting is a challenge.

Experimental images were obtained to demonstrate the viability of the method. Fig. 4.16 illustrates a pair of symmetrically tilted Fresnel images of the vortex selected from difference images recorded at $250 \pm 20 \mu m$. In the experiment, the image is displaced when the specimen is tilted. In order to prevent the influence of this artefact on the accuracy of the difference images, the difference image was obtained from two 2^n -pixel square selected on two tilted Fresnel images around the vortex which were aligned by a cross correlation procedure. Cross-correlation is useful for determining displacement of two images. Here, a 128×128 pixels image (2.46 nm pixel size) of the vortex was selected from a 512×512 pixels Fresnel image of the whole permalloy dot and the cross correlation alignment was corrected. Furthermore, because the sample is polycrystalline, the signal variation from the crystallites can affect on the accuracy of the cross-correlation alignment. In this research, the cross-correlation can detect any displacement up to pixel accuracy which is of the order of mean grain size of the film. The advantage of such a precision is that allows detecting any displacement of the selected frame and the difference image can be correctly subtracted with an error down to 1 pixel.

As seen in Fig. 4.16(c), cross-correlation-aligned difference image shows a well-defined white-black bipolar contrast on the tilt axis in agreement with the simulated difference image. This is interpreted as a downward out-of-plane polarity of the vortex in this case. It is apparent that the contrast level here (19% contrast level, experimentally) is

in good agreement with the value from the simulation (17%). A little higher of polarity contrast is probably due to a thicker dot in experiment (23 ± 3 nm measured by atomic force microscopy). Moreover, the experimental value of the width of the polarity is slightly higher than that of simulation, i.e. 29.5 ± 2.5 nm at 250 ± 20 μm defocus in comparison with 22.5 nm in simulation which is suggested to relate to the difference in thickness.

The evidence of the vortex polarity is clarified experimentally by switching the polarity of the vortex in a magnetic field of 7000 Oe. This field is large enough to switch the polarity in the centre of the vortex and is applied to the specimen by exciting the standard objective lens of the TEM. The difference images are obtained after relaxing the field to zero. For the initial specimen, a down polarity is evident by a white-black contrast of the polarity in the difference image (Fig. 4.16(c)). After applying a

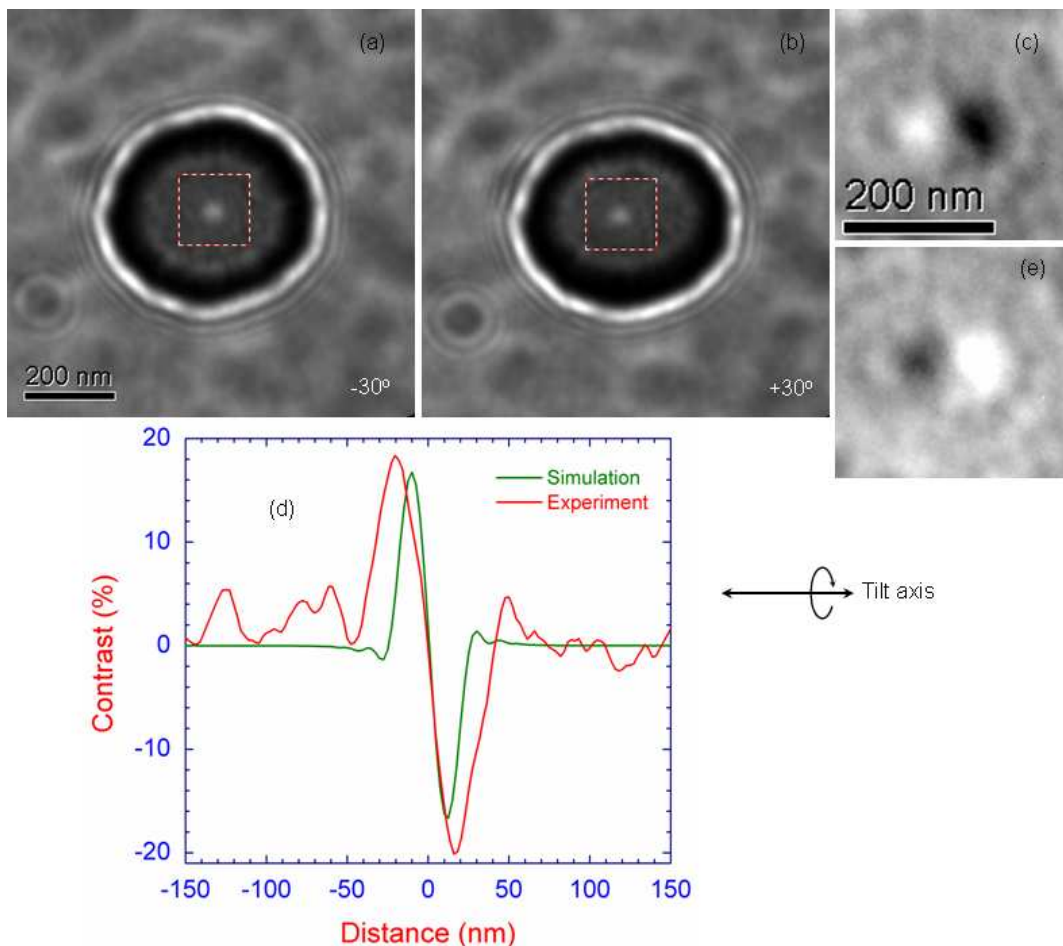


Figure 4.16: Experimental Fresnel images at $\pm 30^\circ$ tilted (a,b) and difference image (c) at 250 ± 20 μm defocus. The plot in frame (d) compares experimental and simulated contrast profiles with 5-lines averaging; frame (e) illustrates another difference image for an opposite polarity.

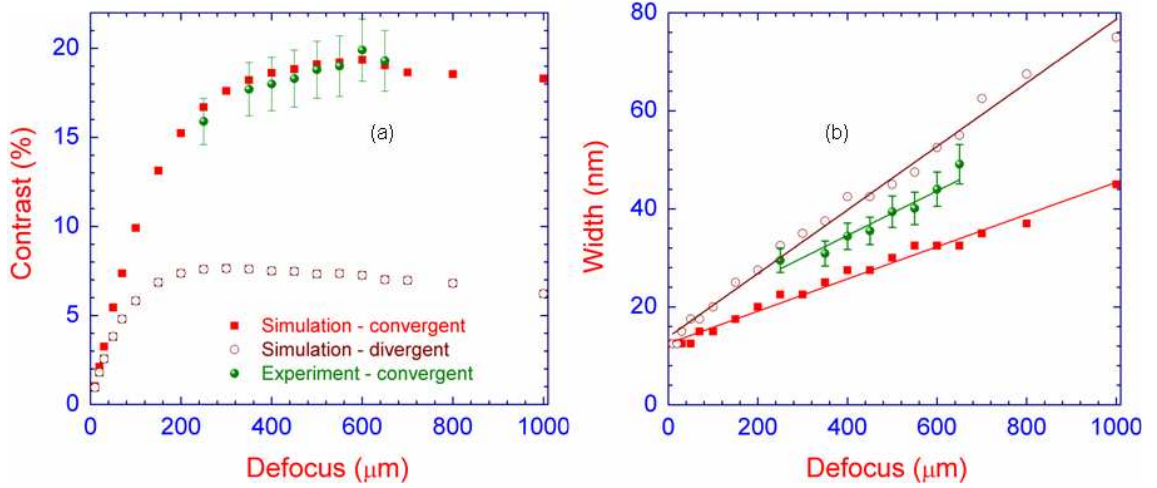


Figure 4.17: The contrast (a) and the width (b) of the polarity as a function of the defocus value. The simulation results are denoted by the red (convergent core), brown (divergent core) dots and the experimental data are denoted by the green dots.

magnetic field of 7000 Oe (the field points up), the out-of-plane magnetisation of the vortex is switched to the opposite direction (up direction), represented by a black-white contrast of the polarity in the difference image (Fig. 4.16(c)). Since then, applying a negative magnetic field pointing down of -7000 Oe leads to switching the polarity to downward direction, therefore, a reverse sign of the contrast in the difference image is again visible. Therefore, states of the polarity are interpreted by comparing with simulation: down (white-black contrast) and up (black-white contrast).

By increasing the defocus value, the contrast arising from the vortex polarity also increases (Fig. 4.17) and an agreement between simulation and experiment is observed. It is also seen from Fig. 4.17(b) that the width of the polarity white-black contrast linearly increases with the defocus value. Extrapolating the linear defocus dependence of the width provides us the width of the vortex core as the intercept of the line. This value is 12.5 ± 2.5 nm and 16.5 ± 2.5 nm for simulation and experiment, respectively. It should be noted from Fig. 4.17(b) that the divergent case in simulation exhibits a large width of bipolar black-white contrast, but also linear dependence on the defocus. However, simulated defocus dependences of the polarity width for both convergent and divergent cases have the same intercept known as the width of vortex core (12.5 ± 1.0 nm). These values are consistent with the diameter of the core given by OOMMF simulation previously (14.0 ± 1.0 nm) but it is notable that this is measuring a different aspect of the vortex.

Fig. 4.17(b) shows that the bipolar contrast in the difference image for the divergent

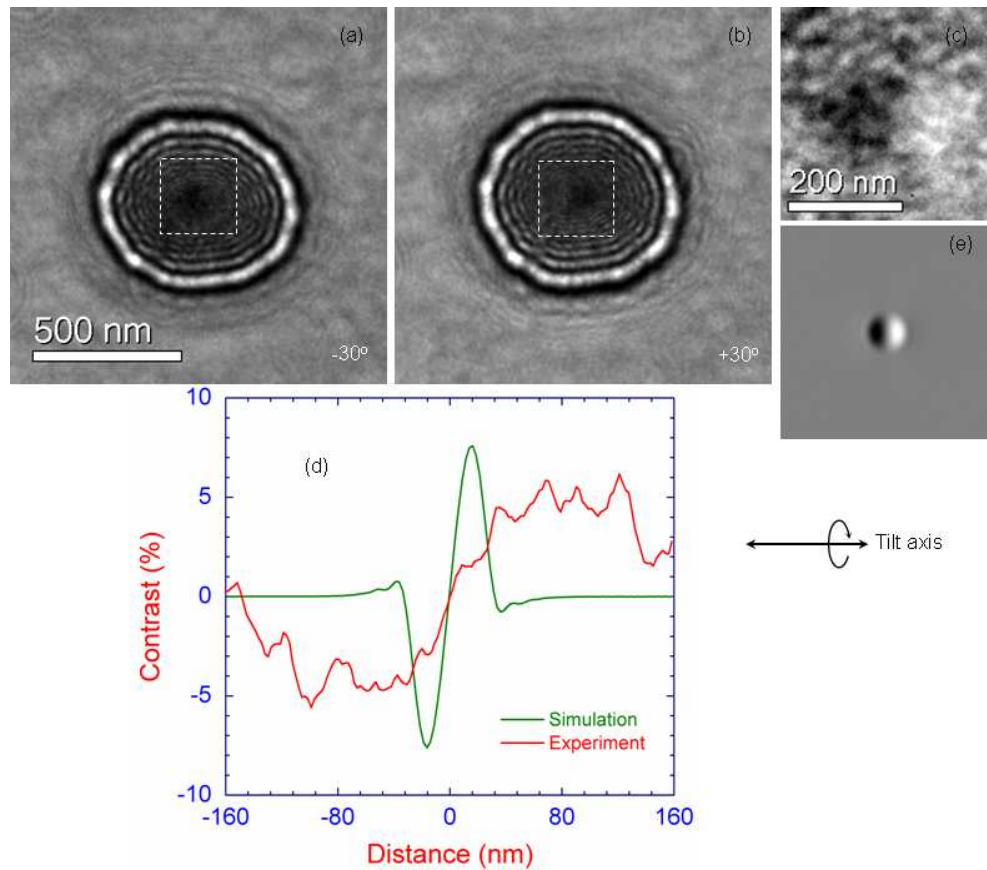


Figure 4.18: Tilted Fresnel images (a,b) and difference image (c) for the case of divergent vortex case. Frame (d) illustrates line-trace profile of contrast and frame (e) shows a simulated difference image in the same condition ($\Delta f = 250 \mu m$).

vortex (dark contrast in the Fresnel images e.g. Figs. 4.18(a,b)) is lower than that of the convergent case. The maximum contrast for the divergent case is 8% at $300 \mu m$ defocus. Fig. 4.18 illustrates the experimental tilted Fresnel images and difference image recorded at $250 \pm 20 \mu m$ compared with simulated difference image in the same condition (for downward polarity case). The bipolar black-white contrast is just about visible (Fig. 4.18(c)) but with a very low level (Fig. 4.18(d)). This weak contrast

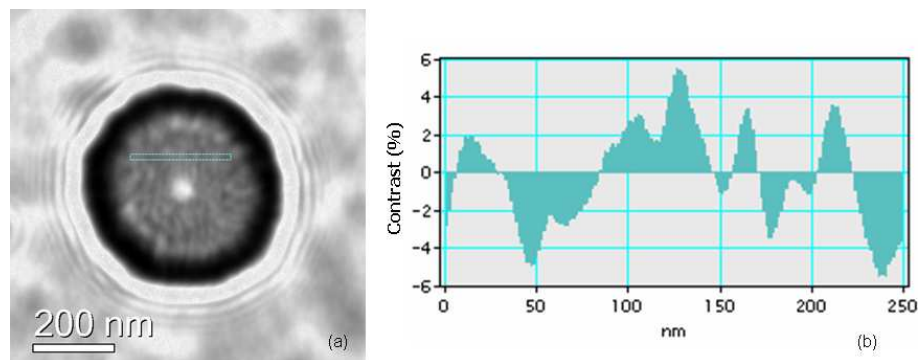


Figure 4.19: Un-tilted Fresnel image (a) of the dot recorded at $\Delta f = 250 \mu m$ and (b) the level of signal variation measured from a 5-line profile near the vortex core.

(Fig. 4.18(d)) is comparable to signal variation of the background - Fig. 4.19. The contributions here are from diffraction from grains etc. Therefore, the divergent core will not be used to characterise the polarity. Further study of the reason for the discrepancy of the predicted value is worth further study, however this was not followed up in this project.

4.3.3 Justification of the method

As mentioned above, when the specimen is tilted, the Fresnel image is displaced, and such a displacement may introduce artefacts into the difference image if not corrected. The cross-correlation procedure is used to align the selected images for subtracting the difference image, and it is expected that this will eliminate error from displacement. However, the accuracy of cross-correlation alignment may be affected by the noise from polycrystalline structure of the film (not an issue in simulated images). The aim of this section is to justify the method by examining the effects of misalignment of the cross-correlation procedure.

This is illustrated by comparing the difference images of two structures: (i) a real magnetic vortex with in-plane curling magnetisation and out-of-plane core; (ii) an unrealistic vortex with only in-plane curling magnetisation (no out-of-plane core). Again it should be noted that the structure without the out-of-plane core is not physically realistic but is included as a comparison. In order to compare, difference images are subtracted from the selected Fresnel images (Fig. 4.20), in which one 2ⁿ selected frame

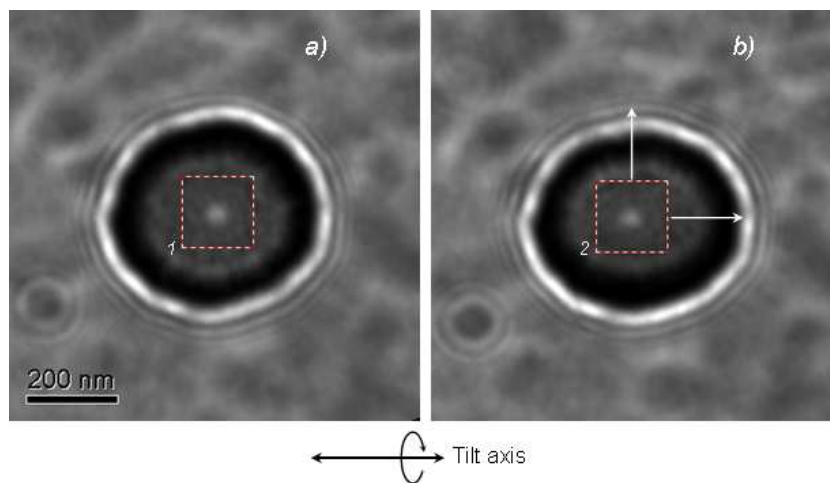


Figure 4.20: Experimental Fresnel images at 250 μm defocus, $\pm 30^\circ$ tilted (a,b). Difference image is obtained when frame (1) is fixed, frame (2) moves out of cross-correlated position a number of pixels on two orthogonal axes.

(frame (2) in Fig. 4.20(b)) is slightly displaced out of cross-correlated position whereas one frame is fixed as a reference (frame (1) in Fig. 4.20(a)). The cross-correlation is also used to check the displacement of the selected frame in both experimental and simulated cases. The results (shown in next paragraphs) will confirm that the structure with an out-of-plane core is identified from the ‘unrealistic structure’ without an out-of-plane core even in the misalignment case. It is important to note that the cross-correlation image of the two selected frames in the tilted Fresnel images exhibits a well-defined maximum bright contrast at the centre of the image when two selected frames are in alignment position.

Fig. 4.21 shows a series of the simulated difference images obtained when the selected frame is displaced a number of pixels from the cross-correlated position (the pixel size here is 2.5 nm). As seen in the difference image series of the structure without an out-of-plane core, no bipolar contrast is observed in the cross-correlated difference image but the bipolar contrast immediately appears as a black-white contrast when the frame is displaced. The sign of bipolar contrast (black-white or white-black) is reversed when the selected frame passes the cross-correlated position. As seen in Fig. 4.21(a,b), when the selected frame is displaced further away from cross-correlated position (0 pixel), the level of bipolar contrast increases.

In the structure with a down polarity, the bipolar contrast goes through a minimum value (nearly zero contrast) when the selected frame is displaced two pixels from the cross-correlated position on the tilt axis and then the contrast increases when the selected frame is continuously moved far away from this position. In the structure with an opposite polarity (up polarity), a similar trend is observed but the compensated contrast (zero contrast) is at the opposite side of the tilt axis (Fig. 4.21(b)).

Actually, when the selected frame was displaced on the tilt axis, the behaviour of the bipolar contrast looks quite similar for both structures. The different behaviour for two structures can be seen much more clearly when the selected frame is displaced on the axis normal to the tilt axis. Fig. 4.22 displays a series of the simulated difference images subtracted from various positions of the selected frame which is displaced on the axis perpendicular to the tilt axis. For the case of the structure without an out-of-plane core, the bipolar contrast is observed with the displacement axis parallel to the tilt axis and continuously changes with number of displacement pixels, as seen in

Fig. 4.21(b). However, for the structure with an out-of-plane core, when the selected frame is displaced perpendicular to the tilt axis, the bipolar contrast rotates relative to the displacement axis as it goes further from the cross-correlation position (Fig. 4.22). This rotation is reversed when the polarity is switched to the opposite direction. A discontinuous change of contrast is observed when the selected frame passes the cross-correlated position. Furthermore, the rotation of the bipolar contrast in the difference images can be characterised in terms of the rotated angle which is defined by the angle between the white-black contrast and the tilt axis. Fig. 4.22(b) shows the dependence of the rotated angle on the number of displaced pixels an arcsine function. This suggests that the rotation of the bipolar white-black contrast from the tilt axis to the displacement axis when the selected frame was displaced out of the cross-correlated

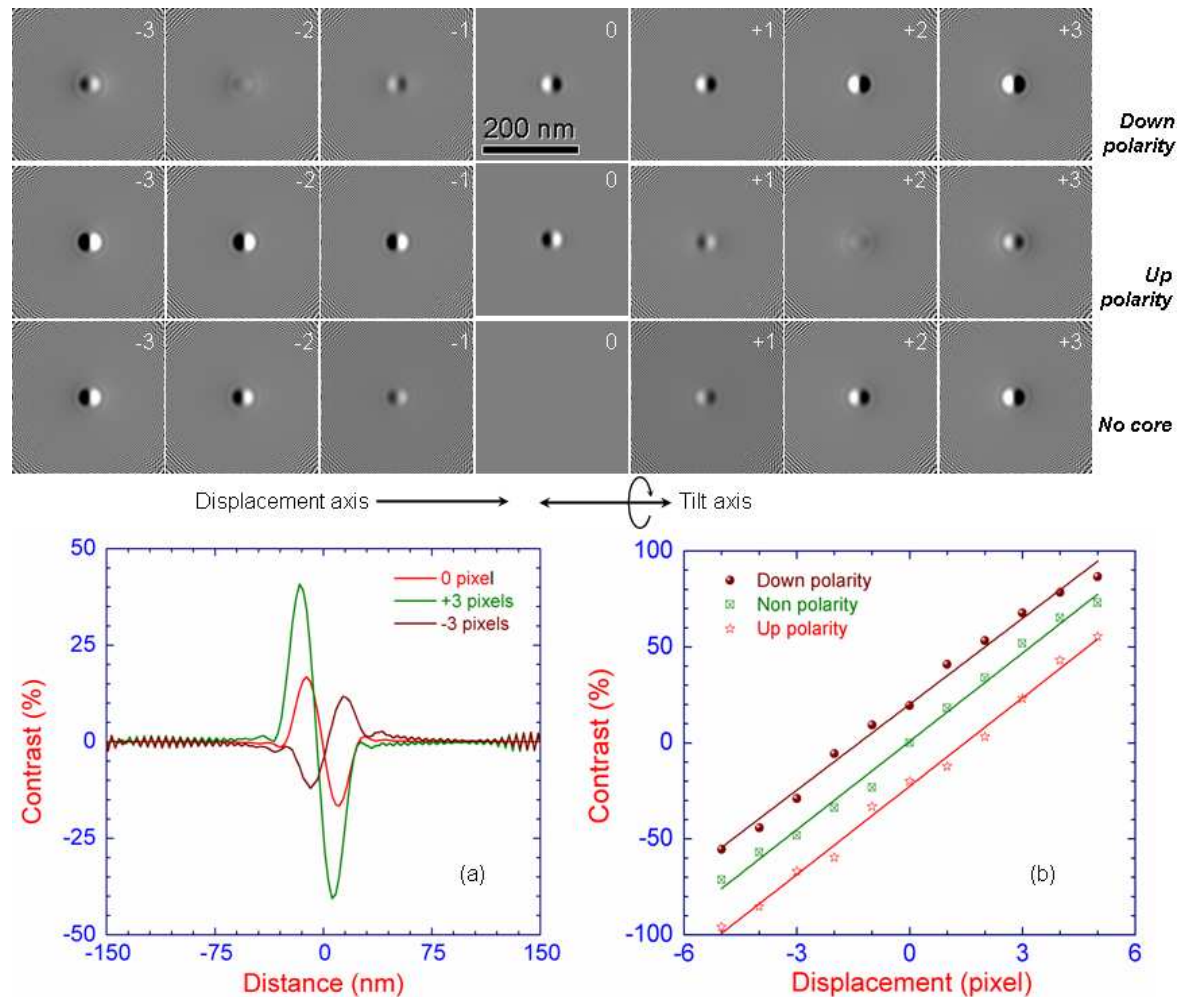


Figure 4.21: Simulated difference images at various positions of selected frame when it is displaced on the tilt axis for the vortex structures with up/down polarity and without an out-of-plane core. Frames (a,b) show the contrast at various displaced positions (a) and the variation of polarity contrast as a function of number of pixels displaced (b). Defocus value in this case is $250 \mu\text{m}$.

position can be considered as the characteristic behaviour of the structure with an out-of-plane polarity.

This validation is also applied to the experimental Fresnel images of the permalloy dots. Fig. 4.23 illustrates a series of the difference image (defocus value here is $250 \pm 20 \mu m$) when the selected frame is displaced on two orthogonal axes: tilt axis (x-axis) and axis normal to the tilt axis (y-axis). A familiar picture, which is consistent with the simulation case (Figs. 4.21,4.22), is obvious in this process. When the selected frame is displaced on the tilt axis, the compensated position (no bipolar contrast on the difference image) is found when the frame is displaced 5 pixels (Fig. 4.23(a)); and a rotation of bipolar contrast is also observed when the selected frame is displaced on the y-axis, which is perpendicular to the tilt axis. This indicates a good agreement

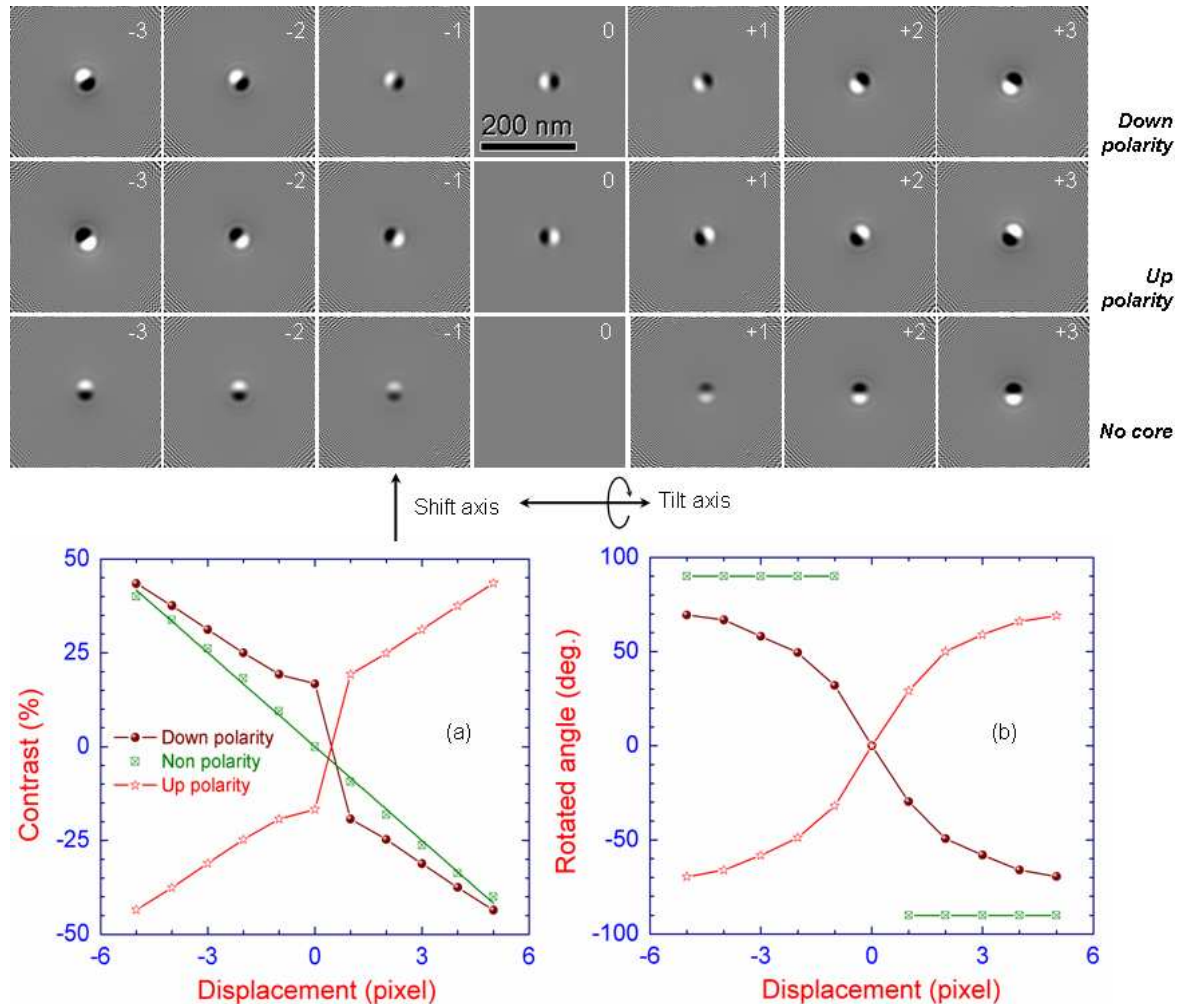


Figure 4.22: Simulated difference images at various positions of selected frame when it is displaced on the axis normal to the tilt axis for the vortex structure with down/up polarity and without out-of-plane polarity. The variation of polarity contrast (a) and rotated angle (b) as a function of displacement position are included. Defocus value in this case is $250 \mu m$.

between simulation and experiment.

Both simulated and experimental observations confirm the reliability of the method to determine the vortex polarity even in aligned or misaligned situations. In experiment, the noise from non-magnetic components (e.g. crystal structure of the film, the electron source, etc.) can cause the misalignment of the cross-correlation. However, the misalignment also results in a characteristic behaviour of bipolar contrast of the polarity (e.g. rotation of the bipolar contrast above). In particular the relative orientation of the tilt axis and the expected directionality of the bipolar contrast is one of the keys factors in assessing the contrast from the difference images.

4.3.4 Discussion

The method suggested here provides a route to determine the out-of-plane polarity of the vortex core by using simple tilted Fresnel images obtained through Lorentz microscopy. Previously, the vortex core polarity has been determined using magnetic force microscopy (MFM) [1], spin-polarised scanning tunnelling microscopy (SP-STM) [10], X-ray dichroism (XMCD) [9], or by electron holography [23]. The SP-STM method provides the best spatial resolution although require a long time for imaging (up to 10 minutes) and a clean flat surface for the specimen. The MFM is a reliable technique but one must be aware that the magnetic field of the tip may affect the magnetic structure of the sample. Of the other techniques XMCD requires a synchrotron source, and electron holography recovers the phase information by applying an algorithm to the interference pattern obtained. An advantage of the method in the present work is its speed and simplicity. Only two Fresnel images are required together with a cross-correlated alignment, so that it is possible to determine quickly the polarity in parallel with determination of the in-plane curling magnetisation. Recently, Phatak et al. [11] has also described the method to determine the vortex polarity in which the same tilted Fresnel image is exploited. In this method, only one tilted Fresnel image is required, although an analytical model is applied to interpret the polarity direction. The method was applied to a relatively thick film (above 50 nm) and the Fresnel image is recorded at very high defocus (above 450 μm). This compares with a much lower thickness (20 nm) in this study together with a smaller defocus (250 μm).

In our method, the non-magnetic contributions to the image contrast are effectively

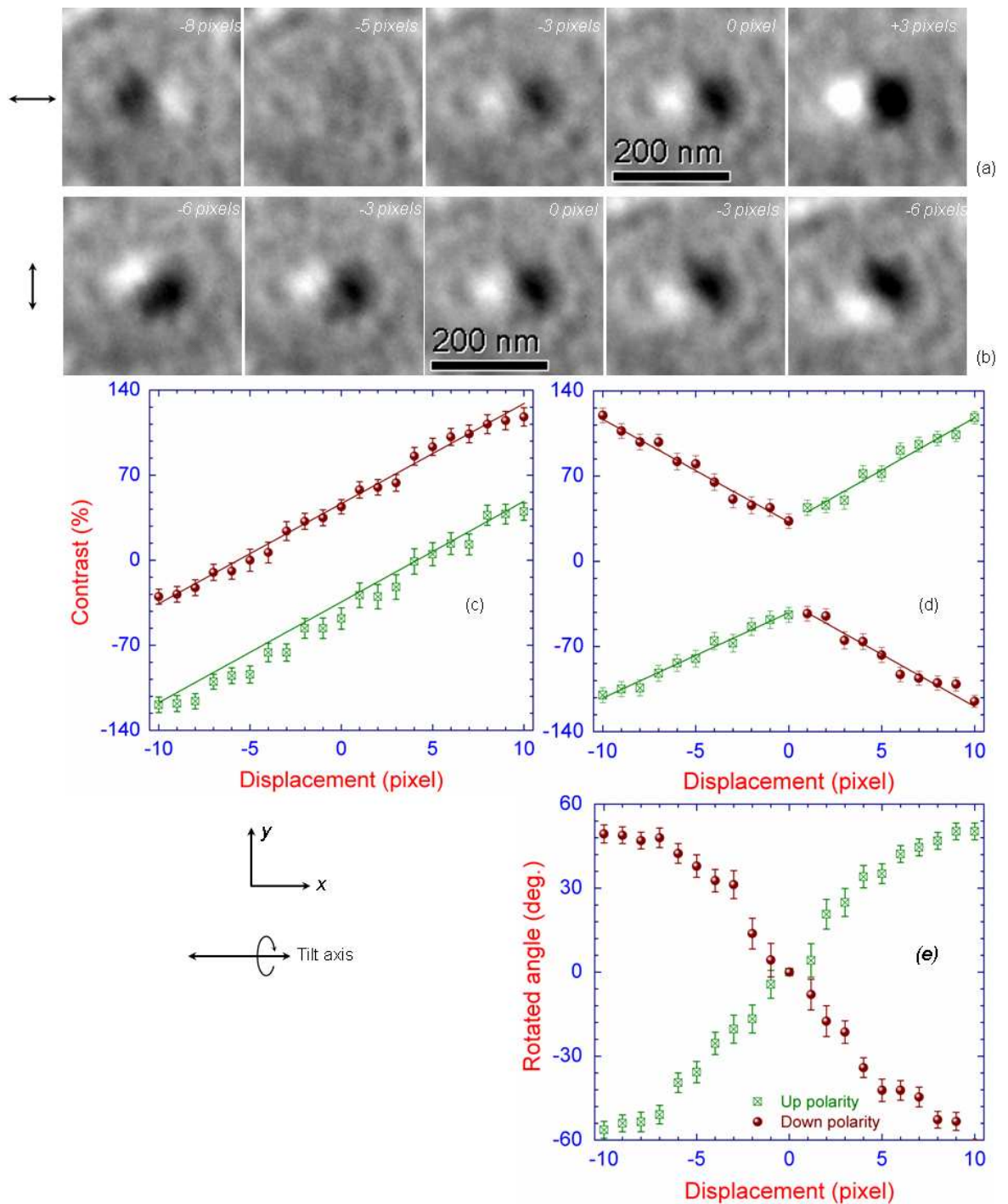


Figure 4.23: Experimental difference images at various positions of selected frame when it is displaced on x axis (a), y axis (b). Plots (c, d) provide the contrast of polarity on the the x and y axes, respectively, plot (e) shows the rotated angle of black-white contrast as a function of pixel number. Defocus value here is $250 \pm 20 \mu m$.

eliminated by using a difference image and the polarity can be detected directly with a white-black bipolar contrast arising from the out-of-plane polarity in the difference image. It is very easy to characterise the behaviour of the bipolar contrast by varying the defocus and the spatial extent of the vortex core can be determined (e.g. 16.5 ± 2.5 in this case) by extrapolation of the Fresnel images. Potentially the method can be

applied for thinner films and possibly at lower focus values, this should be considered in future experiments.

4.4 Mapping magnetic structure in a magnetic vortex by phase reconstruction

4.4.1 Transport-of-intensity equation

In the Fresnel images, it has been indicated in the previous section that the curling in-plane magnetisation is the main contribution to the contrast of the vortex in the image. The out-of-plane core contributes to this contrast only when the sample is tilted, but this contribution is relatively small as shown in the previous section. In order to map quantitatively the in-plane curling magnetisation of the vortex from TEM images alone, an algorithm is required. The transport-of-intensity equation (TIE) [24] can be used to recover the electron phase from TEM images and has been applied successfully in a number of areas e.g. optics, X-ray crystallography, magnetic imaging [31–33]. One such area is magnetic imaging [22, 25–27] when it is used to map the distribution of magnetic induction in thin films. This section will present a study using TIE to map the curling magnetisation in a thin film disk. It will be seen that the TIE method has problems resulting from low spatial frequency signal contributions that limit routine application of this method.

Fig. 4.24 illustrates the principle of the TIE method. Here, the electron beam is considered as a plane wave impinging on the specimen, which distorts both the amplitude and the phase of the incoming wave. For a pure phase object, there is no amplitude variation, and the information concerning the specimen is encoded only in the phase modulation (wave front deformation). Thus, the amplitude of the exit wave is almost constant immediately below the specimen exit surface. However, when the wave propagates through space, the intensity at some places will increase and at other places the intensity will decrease (Fig. 4.24(a)) because the phase modulation induced by the specimen. The transport-of-intensity equation allows us to determine phase information from intensity measurements only (Fig. 4.24(b)). The general wave function can be written as:

$$\psi(x, y, z) = \sqrt{I(x, y, z)} \exp(i\phi(x, y, z)) \exp(ikz) \quad (4.3)$$

where, $I(x, y, z)$ is the intensity of the wave, $\phi(x, y, z)$ is the electron phase due to the sample. The TIE mathematically corresponds to the Schrödinger equation for high-energy electrons in free space. According to [24], the TIE is described as:

$$\nabla \cdot (I(x, y, z_0) \nabla \phi) = -\frac{2\pi}{\lambda} \frac{\partial I(x, y, z_0)}{\partial z} \quad (4.4)$$

where, $I(x, y, z_0)$ and $I(x, y, z)$ are the intensity of the in-focus image and at position (x, y, z) , respectively; λ is the wavelength of the electron wave. The electron phase is obtained by solving the TIE as:

$$\phi(x, y, z) = \frac{-2\pi}{\lambda} \nabla_{xy}^{-2} \nabla_{xy} \left(\frac{1}{I(x, y, z_0)} \nabla_{xy} \nabla_{xy}^{-2} \frac{\partial}{\partial z} I(x, y, z_0) \right) \quad (4.5)$$

where, ∇^{-2} is an inverse Laplacian operation. This equation is the main solution for phase reconstruction. In the equation (4.5), $I_0 = I(x, y, z_0)$ is the intensity of the reference Fresnel image (e.g. in-focus image), $\frac{\partial I(x, y, z_0)}{\partial z} \approx \frac{I(x, y, z_0 + \Delta f) - I(x, y, z_0 - \Delta f)}{2\Delta f}$ ($I(x, y, z_0 + \Delta f)$, $I(x, y, z_0 - \Delta f)$ are the intensities of Fresnel images at positive/negative defocus Δf). Therefore, it can be solved numerically with I_0 and $I(x, y, z_0 \pm \Delta f)$ as the inputs of the algorithm. This assumes that the imaging of the spatial frequency in formation is linear referring to linear Fresnel imaging discussed previously (Chapter 3).

We have developed formulation of the algorithm in the Digital Micrograph scripting environment in which the inverse Laplacian operator in (4.5) can be numerically calculated using a fast Fourier transform (FFT) [28]:

$$\nabla_{\perp}^{-2} (f(x)) = FT^{-1} \left[\frac{FT(f(x))}{|\mathbf{k}_{\perp}|^2} \right] \quad (4.6)$$

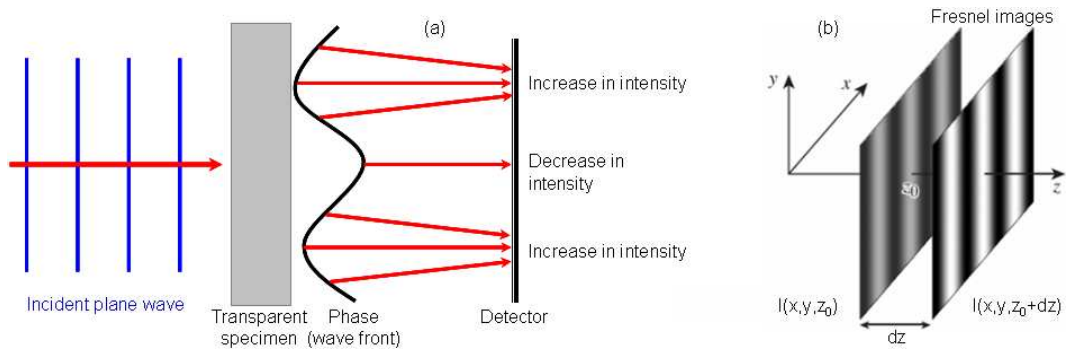


Figure 4.24: Principle of TIE considered as the propagation of the plane wave through a transparent specimen (a) and application of the TIE to recover the phase from the Fresnel images (b).

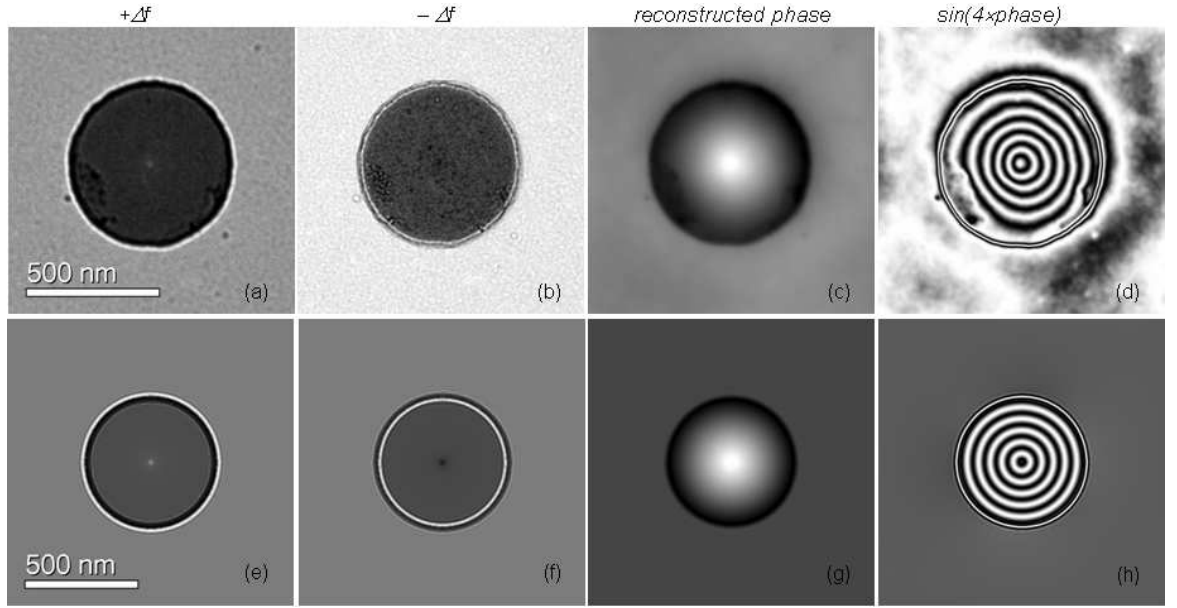


Figure 4.25: An example of phase reconstruction using the TIE from Fresnel images with a comparison between experiment (a-d) and simulation (e-h) for 20 nm thick, 600 nm diameter $\text{Ni}_{80}\text{Fe}_{20}$ nanodot taken at $140 \mu\text{m}$ defocus.

where, FT and FT^{-1} denote the Fourier transform and inverse Fourier transform operators, respectively; \mathbf{k}_{\perp} is the in-plane spatial frequency.

The phase can be reconstructed from three inputs: the intensity image at zero defocus value (in-focus Fresnel image), the Fresnel image at $-\Delta f$ defocus and the Fresnel image at $+\Delta f$ defocus (which in simulations include defocus value, aberration, wavelength etc). The in-focus image is used as the reference image (I_0). An example of the TIE algorithm applied to a $\text{Ni}_{80}\text{Fe}_{20}$ nanodot is illustrated in the Fig. 4.25. Here, Fresnel images were taken at a defocus of $\pm 140 \mu\text{m}$ and the pixel size is 2.5 nm. In the case of the experimental images, great care must be taken to ensure any magnification change due to defocus is corrected in addition to scaling for changes in intensity. The in-plane curling magnetisation of the magnetic vortex is visible as the lines of flux produced by calculating the sine of the reconstructed phase (Figs. 4.25(d,h)). There is a qualitatively good agreement between the reconstructed phase by using simulated Fresnel images and experimental images. Moreover, from the reconstructed phase, it is possible to obtain the integrated induction using the relation (see Chapter 3):

$$\nabla\phi(x, y) = -\frac{e}{\hbar}(\mathbf{B}_{\perp} \times \mathbf{n}_z).t \quad (4.7)$$

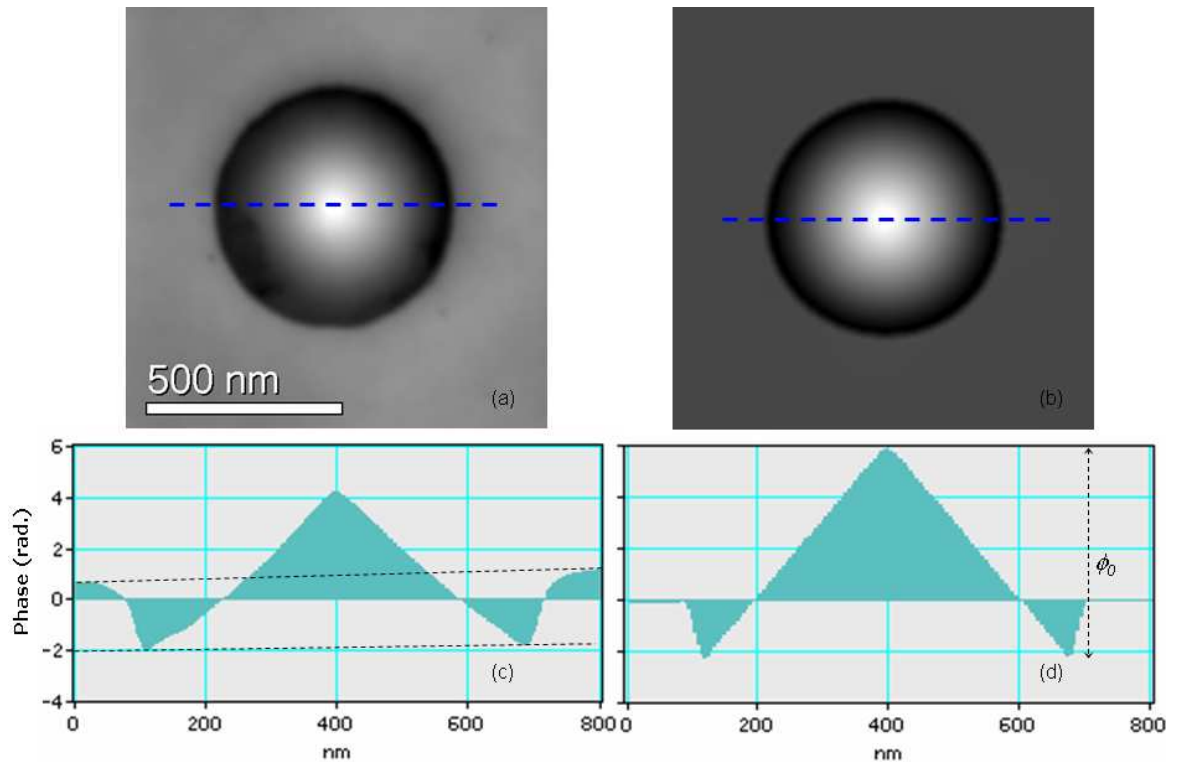


Figure 4.26: The reconstructed phases recovered: from experimental inputs (a), from simulated inputs (b) and their corresponding line profiles (c,d). The blue dash lines denote the lines to measure the profiles.

Fig. 4.26 shows a comparison of the reconstructed phases recovered from experimental and simulated inputs (shown in Figs. 4.25(c,d) and Figs. 4.25(g,h)), respectively and their corresponding line profiles (c,d). As seen in line profiles (Figs. 4.26(c,d)), a quantitative difference between simulation and experiment is observed. The recovered phase reconstructed from experimental Fresnel images (Figs. 4.25(a,c)) shows a lower phase magnitude (ϕ_0) than that from simulated Fresnel images (6.2 rad. and 4.2 rad., respectively) but a higher phase variation from free space to the specimen (2.8 rad. and 2.2 rad., respectively). A zero constant and uniform phase in free space area is observed in the simulated reconstructed phase, whereas the experimental recovered phase shows a variation of phase in the free space region, which was confirmed previously to be related to the non-negligible noise sources [25]. It has been shown that this variation even exists when the specimen is removed. To illustrate the contributions from such noise, consider the difference of two images of free space taken $100 \mu\text{m}$ either side of focus as shown in Fig. 4.27(a) and with the intensity variation shown in Fig. 4.27(c). The signal variation observed has a typical profile representing noise from the source and detector. Applying the TIE algorithm results in a phase image as shown in Fig.

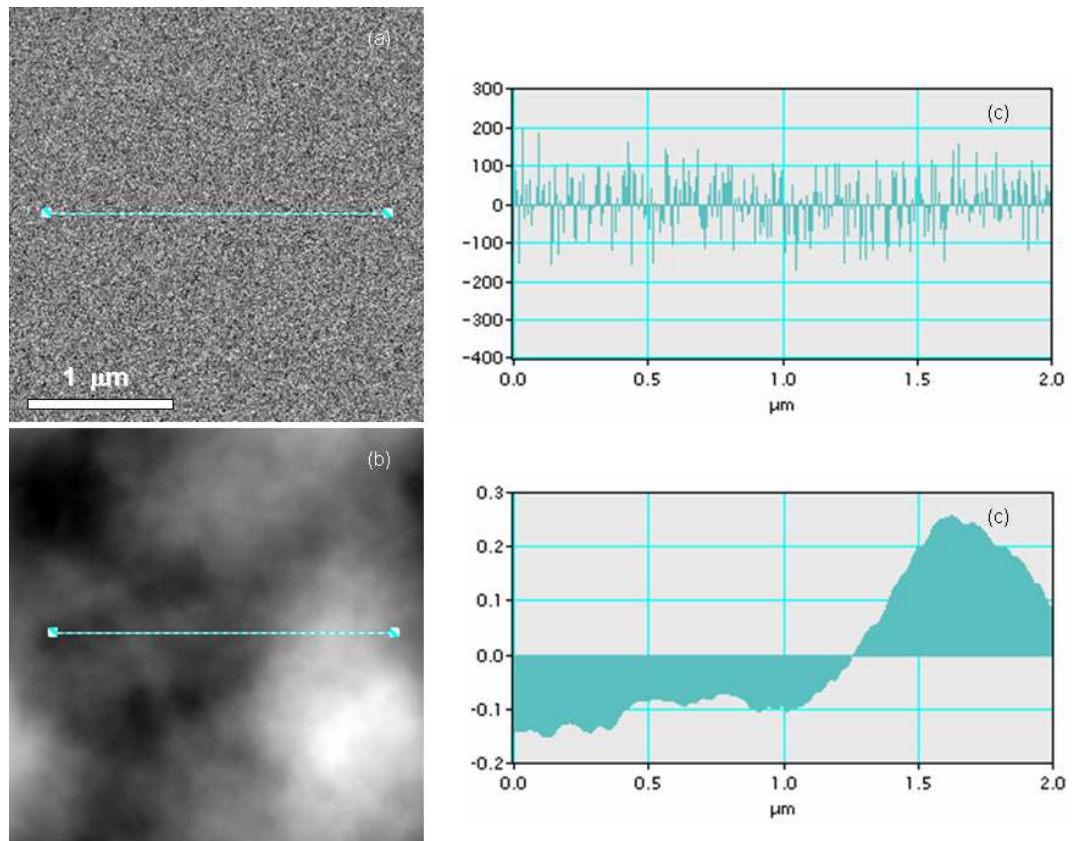


Figure 4.27: Difference image of the free space (a) taken at $\pm 100\mu\text{m}$, corresponding reconstructed (b); and line profiles of the difference image (c) and reconstructed image (d) with vertical scale in radians [29].

4.27(b) with associated line-trace (Fig. 4.27(d)). It is clear that the phase image is dominated by low spatial frequency variations [29]. Therefore, the work in the following section will concentrate on the contribution of the low-spatial frequency noise to the TIE phase reconstruction. In particular, the magnetic phase is neglected in the example studied to highlight the problem by using a non-magnetic sample (in this case, holey carbon film). This problem is particularly an issue if the algorithm is to be used at low defocus values.

4.4.2 Low-spatial frequency noise in reconstructed phase

Reconstruction of the phase of a holey carbon film provides a measurement of electrostatic phase shift. Assuming the carbon film is of constant thickness, the phase (only electrostatic phase) can then be represented by a top-hat function with a finite slope at the edges. For images calculated here the pixel spacing is taken as 2.5 nm and the variation over the edge is assumed to be linear and occurs over 4 pixels (10 nm). The electrostatic phase shift due to inner electrostatic field depends on the thickness of

the film, t , the mean inner potential, V , the wavelength of the electron wave, λ and electron energy, E (chapter 3):

$$\phi_e(x, y) = \frac{\pi V t}{\lambda E} \quad (4.8)$$

In this work, the holey carbon film, supplied by Agar Scientific, is about 20 nm thick as measured by EELS and its mean inner potential is $V = 9.09$ V. This therefore provides a phase jump $\sim \pi/3$ radians between the film and the vacuum. Fig. 4.28 illustrates simulated and experimental Fresnel images of a holey carbon film captured at a defocus value of $+160 \mu\text{m}$ (a,b). The variation of the electrostatic phase at the edge of the hole can be understood in terms of measuring the edge profile of the hole from the in-focus Fresnel images as shown in Figs. 4.28(c,d). It is important to note that the phase jump at the edge is proportional to the edge profile of the hole measured from in-focus images. The TIE algorithm described previously is applied to retrieve the phase of the holey carbon film with both simulated and experimental inputs.

It has been noted that the TIE reconstruction appears to be robust beyond the strict definition of defocus condition [11]. The TIE algorithm can be well applied for lin-

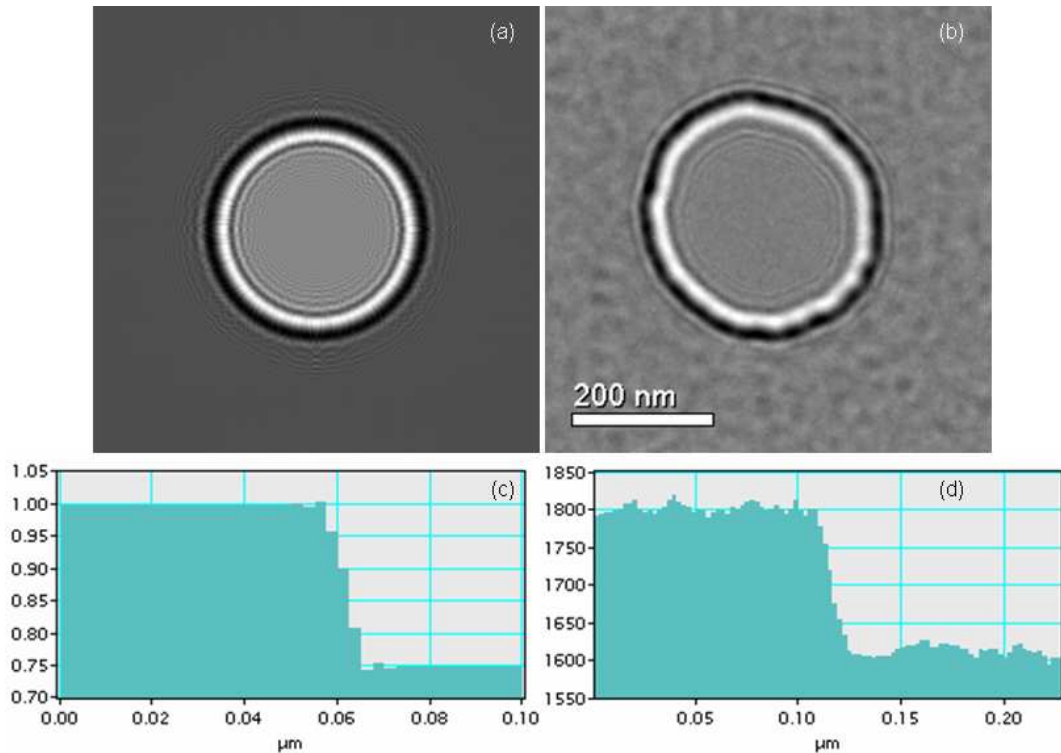


Figure 4.28: Simulated (a) and experimental (b) Fresnel images of a holey carbon film taken at defocus value of $+160 \mu\text{m}$ in field free mode in the TEM. Frames (c,d) shows the edge profiles of the holey carbon film in simulation (c) and experiment (d) measured from in-focus images (un-defocused images).

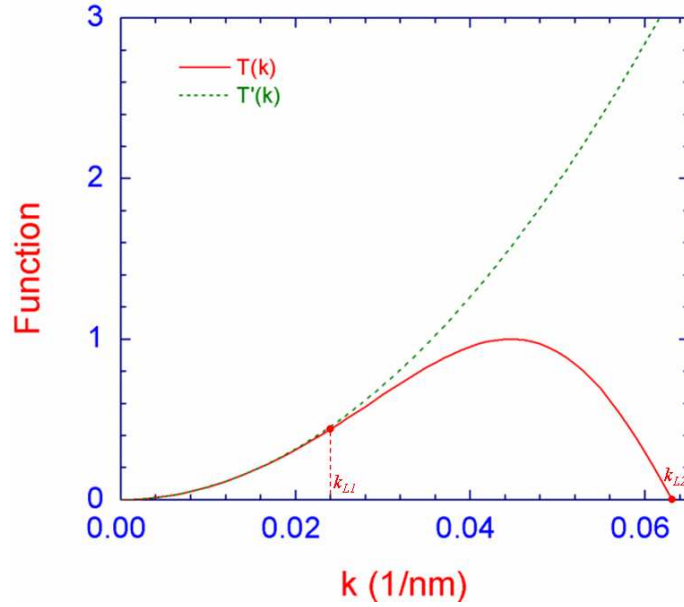


Figure 4.29: Transfer function ($T(k)$) and derivative of the transfer function $T'(k)$ with respect to spatial frequency k . From this plot, the linear limit for the Fresnel image is determined as the point at which two curves start to deviate (k_{L2}).

ear Fresnel imaging in which the condition $\pi\lambda\Delta f k^2 \ll \pi$ [22, 25–28], where Δf is the defocus value and k is the highest spatial frequency of interest. As a result, we can then calculate the maximum defocus allowed for a given spatial frequency for this strict definition. From this condition, we have derived the linear imaging condition is $\Delta f_{L1} = 1/(10\lambda k^2)$ ($\pi\lambda\Delta f k^2 = \pi/10 - k_{L1}$). Using this condition, the images taken in Fig. 4.28 correspond to a spatial frequency limit of $(62.5 \text{ nm})^{-1}$. Looking at the transfer function we can see this corresponds to the linear limit whereas the transfer function goes through the first zero at the limit $\Delta f_{L2} = 1/(\pi\lambda k^2)$ (k_{L2}), [22] (see Fig. 4.29). Clearly the information transfer between (k_{L1} and (k_{L2} is non linear although at least they have the same sign of transfer.

The spatial frequency components present in the images of the holey carbon film is now considered in more detail. The highest possible spatial frequency for the pixel spacing corresponds to $k_{max} = (5 \text{ nm})^{-1}$, which in the strictest interpretation of the linear regime corresponds to defocus values of $\Delta f_{L1} = 1 \mu\text{m}$ and $\Delta f_{L2} = 3.2 \mu\text{m}$. Such small defocus values would be required if an accurate phase reconstruction on the pixel scale is required. In the situation here the spatial extent of the phase variation of the edge of the hole is 10 nm. The defocus values for this dimension is given by $\Delta f_{L1} = 4 \mu\text{m}$ and $\Delta f_{L2} = 12.7 \mu\text{m}$. In the images from the holey carbon film considered the interest is in the lower spatial frequency phase components to be recovered using TIE, therefore,

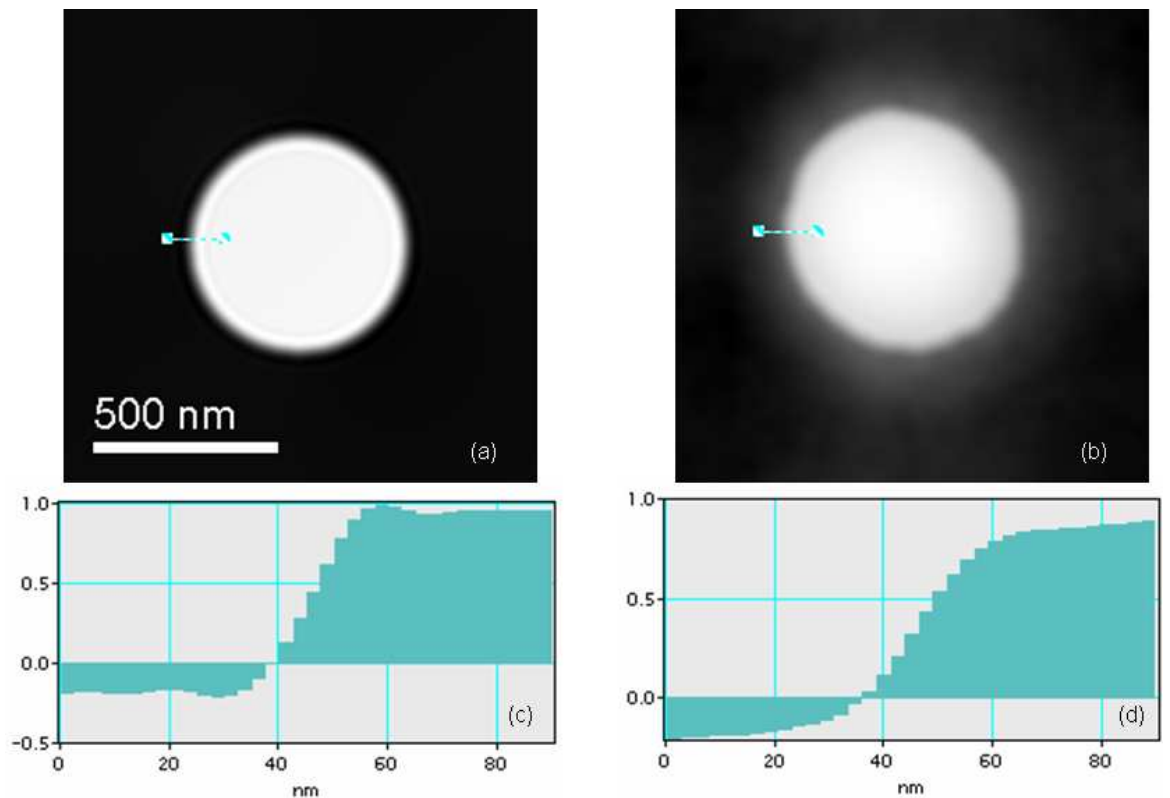


Figure 4.30: Reconstructed phases of the holey carbon film: (a) simulated, (b) experimental results taken at a defocus value of $160 \mu m$, and line profiles measured near the edge of the hole (c,d).

spatial frequency is sacrificed to look at the magnitude of the phase jump at the edge rather than its detailed profile. Therefore larger focus values than those defined above are used.

Fig. 4.30 shows reconstructed phases of the holey carbon film recovered from simulated Fresnel images (a) and experimental Fresnel images (b) taken at a large defocus of $160 \mu m$. A comparison of line profiles measured at the edge of the hole is displayed in Figs. 4.30(c,d). It is found that the edge profile has been broadened as expected (as seen in the edge profiles of the holes in the in-focus Fresnel images shown Figs. 4.28(c,d)) but that the phase jump between inside and outside of the hole has been well preserved. In this case, the limits of spatial frequency from the definitions above are (k_{L1} and k_{L2}) are $(63 \text{ nm})^{-1}$ and $(35 \text{ nm})^{-1}$, respectively. This confirms the ‘robustness’ of the TIE method as long as one is aware of the spatial frequency limitation. There is still some spurious low spatial frequency contribution in the experimental image though it is not significant at this edge.

An example of the low spatial frequency phase problems can be seen from the phase reconstructed from the holey carbon film from the images taken at a lower defocus (80

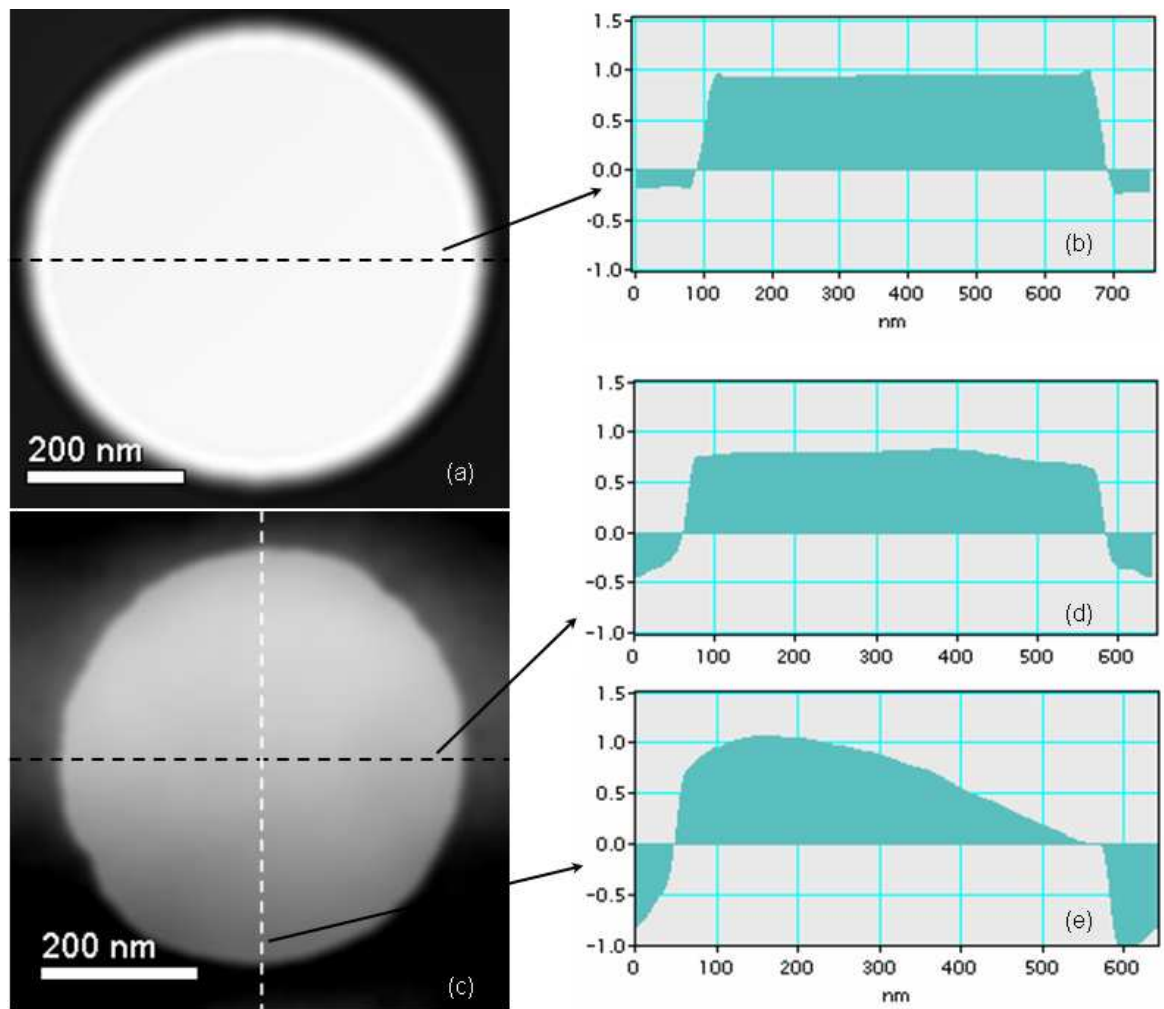


Figure 4.31: Simulated (a) and experimental (c) TIE reconstructed phase of holey carbon film and their line profile (c, d, e), taken at $80 \mu\text{m}$ defocus and image size of 256×256 pixels.

μm) is illustrated in Fig. 4.31. In this case, a significant low spatial frequency signal variation in the TIE phase recovered from the experimental images was found which does not relate to any expected phase variation from this structure (Fig. 4.31(d,e)). This is consistent with previous studies [25,26] which attributes this to noise artefacts. It is now shown that the source of these variations arises from the TIE ‘filtering’ effect. The effect can be further quantified by considering a single spatial frequency component in the difference image. It is assumed that a uniform ‘white noise’ exists in the background from the difference image, (Figs. 4.27(a,c)), the quantised spatial frequency components can be seen to have a strong dependence in the recovered phase from the TIE filter. The reason for this is that the TIE algorithm is to first order an inverse Laplacian of the difference image, in effect this means that the spatial frequency spectrum in k space has a multiplicative factor of $1/k^2$ for each k component.

The white noise spectrum in the Fourier transform of the difference image is shown in (Fig. 4.32). For simplicity consider that in 1-D, the white noise can be written as a Fourier series form $I(k) = \sum_{i=1}^n A_i \sin(2k_i x)$, with spatial frequency components k_i . The spatial frequencies are quantised in the digital image, being multiples of the lowest spatial frequency. The associated phase recovered via the TIE inverse Laplacian will have the form for each component of $\phi_k = (A_k/k^2) \sin(2kx)/(4\pi\lambda\Delta f)$. Each frequency component has effectively been attenuated by a $1/k^2$ factor, at low spatial frequency the weighting will be 1/1, 1/4, 1/9, etc. Therefore the white noise has been heavily filtered such that the low frequencies dominate and the lowest frequency component will have the largest amplitude by a factor of 4 over the next lowest frequency. The effect on a white noise type of signal variation is seen in the image shown in Figs. 4.27(a,c). The white noise is heavily filtered by the TIE method resulting in a spectrum which is dominated by low frequency variations (Fig. 4.32).

From the reconstruction it can also be seen that a smaller defocus gives a larger amplitude component making the problem worse. Therefore at lower defocus values, the low contrast and contributions from noise in the images cause serious problems. In effect the background noise is a function of the imaging conditions and does not change with focus, however the relative effect of the filtering is much worse at low defocus. To high-

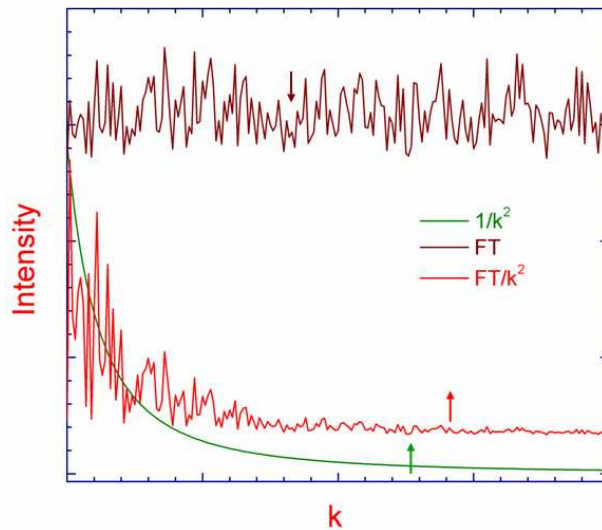


Figure 4.32: Filtering effect in the TIE solution using Fourier transform algorithm. The white noise spectrum from the vacuum is shown in the top trace. The TIE in effect is a filter in k space with a factor of $1/k^2$ as seen in the green linetrace. The resulting filtered white noise spectrum shows that the low frequencies have been significantly enhanced in the red linetrace. The arrows illustrate displacement of the plots.

light this effect we consider the phase reconstructions from a hole in the carbon film using the same images but in one case using an area of 512×512 centred on the hole whilst in the other an area of 256×256 pixels is used, the same pixel spacing is used in each case. These areas were defined from original images of the size 1024×1024 pixels. The main difference here is that the lowest spatial frequency present in the larger image is double that in the smaller image. Intuitively one might expect the phase variation from the background in the reconstructions should be the same, however the filtering effect in experimental images means that the low spatial frequency noise or artefact contribution in the larger area images is considerably greater.

The TIE reconstructions from these areas are shown in Fig. 4.33 from a defocus set of images at $\pm 80 \mu m$. From the smaller area images (Figs. 4.33(a) and (b)) it was found that although the edge profile is again broadened, the phase profile resembles a top hat function with a rather small variation due to the background. The phase jump is

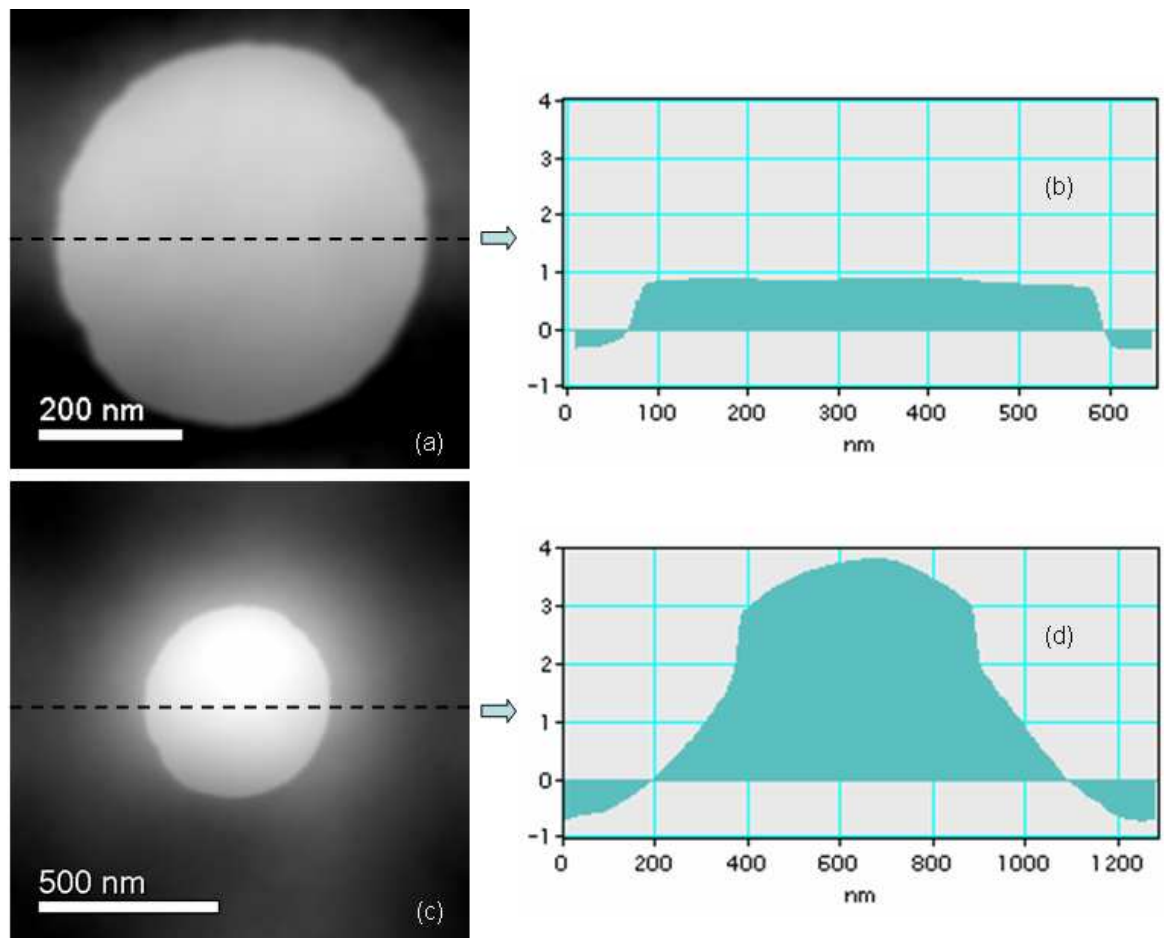


Figure 4.33: Experimental TIE reconstructed phase from holey carbon film taken at defocus value of $80 \mu m$ from images with the size of 256×256 pixels (a) and line profile from phase (b). Frames (c) and (d) are the results for TIE phase reconstructed from images with the size of 512×512 pixels.

well reproduced at about $\pi/3$. From the same image but using a larger surrounding area (Fig. 4.33(c) and (d)) the low spatial frequency artefacts are much more clearly visible. Although the phase jump can still be discerned, the magnitude of the artefact is larger than the phase jump itself. It is evident that the pixel size and image size are factors in how much this artefact is going to be an issue, in addition to the defocus. A generalisation is that higher magnification and higher defocus will be better. However it really depends on the relative value of this effect to the phase variations that are to be measured. Clearly a working in conditions of low noise will be best but the inherent filtering effect of the TIE means that the problem cannot be easily eliminated. This certainly seems to be a major issue in possible routine application of the TIE method.

4.5 Summary

In this chapter, a quantitative investigation of Fresnel imaging of the vortex state in magnetic nanodots has been performed by a comparison of micromagnetic simulations and experimental observations. The nucleation and annihilation of the vortex state in the dots are confirmed to be sensitive to the change in edge profile of the dot. The polarity of the vortex core is also determined using tilted Fresnel imaging. The polarity can be directly detected with visibility of bipolar white-black contrast in the difference image of two symmetrically tilted Fresnel images. Using this method, the vortex core width has been measured to be 16.5 ± 2.0 nm which is in agreement with previous result that the diameter of vortex core in NiFe patterned films typically only 10-25 nm [30]. The method is quick and less influenced by the resolution of the Fresnel images. Phase reconstruction using the transport-of-intensity equation algorithm to quantitatively map the magnetic structure in the vortex was also investigated. In principle the recovered phase allows mapping the in-plane curling magnetisation in the vortex. The results have shown that the TIE method works best for medium resolution, i.e. larger defocus values so that sufficient phase contrast is visible in the Fresnel images. Furthermore low spatial frequency noise artefacts can be reduced by using smaller images sizes and larger defocus, although the latter gain will reduce the resolution of the method. Although it is possible to try and reduce these artefacts, measuring small phase changes with the TIE method remains very challenging.

Bibliography

- [1] T. Shinjo, T. Okuno, R. Hassdorf, K. Shigeto, T. Ono, *Science* **289** (2000) 930-932.
- [2] S.-B. Choe, Y. Acremann, A. Scholl, A. Bauer, A. Doran, J. Stöhr, H. A. Padmore, *Science* **304** (2004) 420-422.
- [3] S. Kasai, Y. Nakatani, K. Kobayashi, H. Kohno, and T. Ono, *Phys. Rev. Lett.* **97** (2006) 107204.
- [4] B. Van Waeyenberge, A. Puzic, H. Stoll, K. W. Chou, T. Tyliczszak, R. Hertel, M. Fähnle, H. Brückl, K. Rott, G. Reiss, I. Neudecker, D. Weiss, C. H. Back and G. Schütz, *Nature* **444** (2006) 461-464.
- [5] S-K. Kim, K-S. Lee, Y-S. Yu, Y-S. Choi, *Appl. Phys. Lett.* **92** (2008) 022509.
- [6] B. C. Choi, Q. F. Xiao, Y. K. Hong, J. Rudge, G. Donohoe, *IEEE Trans. Magn.* **43** (2007) 2926-2928.
- [7] J-G. Caputo, Y. Gaididei, F. G. Mertens, D. D. Sheka, *Phys. Rev. Lett.* **98** (2007) 056604.
- [8] K. Yamada, S. Kasai, Y. Nakatani, K. Kobayashi, H. Kohno, A. Thiaville, T. Ono, *Nature Materials* **6** (2007), 269.
- [9] K. W. Chou, A. Puzic, H. Stoll, D. Dolgos, G. Schültz, B. Van Waeyenberge, A. Vansteenkiste, T. Tyliczszak, G. Woltersdorf, C. H. Back, *Appl. Phys. Lett.* **90** (2005) 202505.
- [10] A. Wachowiak, J. Wiebe, M. Bode, O. Pietzsch, M. Morgenstern, R. Wiesendanger, *Science* **298** (2002) 577-580.

- [11] C. Phatak, M. Tanase, A.K. Petford-Long, M. De Graef, *Ultramicroscopy* **109** (2009) 264-267.
- [12] J. K. Ha, R. Hertel, J. Kirschner, *Phys. Rev. B* **67** (2003) 224432.
- [13] Z-H. Wei, M-F. Lai, C-R. Chang, N. A. Usov, J. C. Wu, J-Y. Lai, *J. Magn. Magn. Mater.* **282** (2004) 11.
- [14] T. Ishida, T. Kimura, Y. Otani, *Phys. Rev. B* **74** (2006) 014424.
- [15] Y. Zheng, J-G. Zhu, *J. Appl. Phys.* **81** (1997) 5471.
- [16] T. Hesjedal, T. Phung, *Appl. Phys. Lett.* **96** (2010) 072501.
- [17] B. D. Cook, S-Y. Lee, *J. Vac. Sci. Technol. B* **15** (1997) 2303.
- [18] Y-M. Ham, C. Lee, S-H. Kim, K. Chun, *J. Vac. Sci. Technol. B* **15** (1997) 2313.
- [19] R. P. Cowburn, D. K. Koltsov, A. O. Adeyeye, and M. E. Welland, *J. Appl. Phys.* **87** (2000) 7067.
- [20] H. Shima, V. Novosad, Y. Otani, K. Fukamichi, N. Kikuchi, O. Kitakamai, and Y. Shimada, *J. Appl. Phys.* **92** (2002) 1473.
- [21] S. McVitie, G. S. White, *J. Phys. D: Appl. Phys.* **37** (2004) 280-288.
- [22] S. McVitie, M. Cushley, *Ultramicroscopy* **106** (2006) 423-431.
- [23] F. Junginger, M. Kläui, D. Backes, S. Krzyk, U. Rdiger, T. Kasama, R. E. Dunin-Borkowski, J.-M. Feinberg, R. J. Harrison, *Appl. Phys. Lett.* **92** (2008) 112502.
- [24] M. R. Teague, *J. Opt. Soc. Am.* **73** (1983) 1434-1441.
- [25] M Beleggia, M.A. Schofield, V.V. Volkov, Y.Zhu, *Ultramicroscopy* **102** (2004) 37.
- [26] A. Kohn, A. K. Petford-Long, T. C. Anthony, *Phys.Rev.B* **72** (2005) 014444.
- [27] K. Ishizuka, B. Allman, *Microscopy Today*, Nov. 2005, pp. 22-24.
- [28] V. V. Volkov, Y. Zhu, D. De Graef, *Micron*, **33** (2002) 411-416.

- [29] S. McVitie, in: *EMC 2008 14th European Microscopy Congress*, (2008) Aachen, Germany, Springer Berlin Heidelberg, ISBN 978-3-540-85156-1, Part I5, pp. 771-772.
- [30] A. Vansteenkiste, K.W. Chou, M. Weigand, M. Curcic, V. Sackmann, H. Stoll, T. Tyliczszak, G. Woltersdorf, C.H. Back, G. Schütz, B. Van Waeyenberge, *Nature Physics* **5** (2009) 332.
- [31] R. P. Millane, *J. Opt. Soc. Am. A* **7** (1990) 394.
- [32] T. E. Gureye, K. A. Nugent, *Opt. Comm.* **133** (1997) 339.
- [33] K. A. Nugent, *Proc. 8th Int. Conf. X-ray Micro.: IPAP Conf. Series* **7** (2006) 339.

Chapter 5

Magnetic configuration in nanoconstrictions

5.1 Objective and Motivation

When a conducting electron traverses a magnetic domain wall (DW), it is scattered due to the magnetic moments in the DW rotating from one domain to another. This scattering contributes to the resistance of the system, and the contribution is called domain wall magnetoresistance [1]. When the DW is located in a geometrically constrained structure, this contribution may result in a significant change of magnetoresistance, which can be detected by anisotropic magnetoresistance (AMR) [2]. Furthermore, because of the geometrical constraint effect, the structure of the DW may be changed in comparison with the DW in a continuous film. In this situation, the structure of the wall is dependent on the geometrical dimension of the constriction in addition to the material parameters [3].

In this chapter we present an investigation in which the aim is to observe directly the confinement of DWs in permalloy nanostructures using Lorentz microscopy and to compare these results with AMR measurements. Furthermore, the nature of the DW confined in the structures is studied using STEM Lorentz microscopy in an attempt to confirm the compression of the DW in the constrained structure. The research is a part of an EPSRC-funded project called the Spin@RT consortium. This work described here involves two of the other partners in the network: Stoner Laboratory, University of Leeds, and Condensed Matter Physics group, Durham University (United Kingdom).

5.2 Structure for research

The lithographically defined structure studied in this chapter consist of two pads of magnetic thin film (an elliptical pad and an elongated pad), connected to each other by a small bridging constriction (Fig. 5.1) - called an ‘H-shape structure’. The pads of different shapes and sizes result in different switching fields, which in turn allows for the possible nucleation of a domain wall in the constriction when one pad’s magnetisation is reversed. The easy-switched pad was designed as a two-dimensional ellipsoid, whilst the hard-switching pad was elongated and given triangular ends in order to suppress propagating domain wall formation [4].

The structures were fabricated by electron beam lithography and lift-off technique described in chapter 2. A 7 nm thick $\text{Ni}_{81}\text{Fe}_{19}$ was grown on substrates by DC sputtering at the Stoner Laboratory, University of Leeds. The width of the constriction (w) was selected as 200 and 300 nm, and the height (h) varied from 280 nm to 900 nm (Fig. 5.1(b)). For TEM measurements, the structures were patterned on electron transparent SiN membrane (see chapter 2, section 2.2). A 2 nm thick Al layer was deposited on the top of the NiFe film for protection and a 10 nm thick Au layer was deposited on the back side of the membrane to prevent electrostatic charging. Structures were also fabricated on a bulk Si substrate for transport and magneto-optic measurements. The structures were contacted with two Au electrodes on either side of the nanoconstriction for electrical transport measurements. The hysteresis loops of the structures were measured by micron scale magneto-optic Kerr effect (MOKE) magnetometer at the

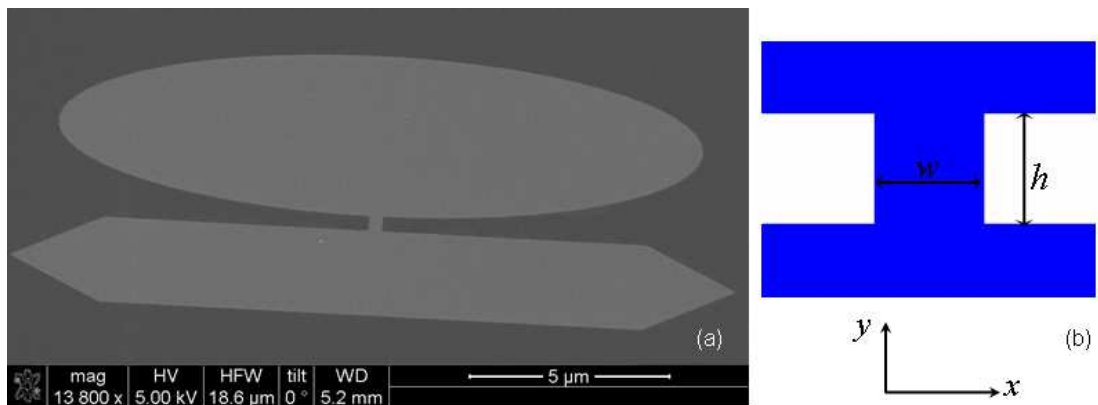


Figure 5.1: SEM micrograph of a ‘H-shape’ structure with two micrometer size pads (an elliptical pad and an elongated pad), connected by a $200 \times 280 \text{ nm}^2$ constriction (a). Frame (b) defines the geometrical dimension of the constriction with the width, w and the height, h .

Durham University. A $5\ \mu\text{m}$ -laser spot can be focused on either pads or on the constriction [2].

Micromagnetic simulations using OOMMF were performed to interpret the magnetic structure.

5.3 Micromagnetic behaviour of the structures

Fresnel imaging of the Lorentz microscopy was employed to observe the micromagnetic behaviour of the patterned structures. A magnetic field ranging from $+20\ \text{Oe}$ to $-20\ \text{Oe}$ was applied parallel to the long axis of the pads by weakly exciting standard objective lens of the microscope and introducing a planar component of the field by tilting the specimen as described in chapter 3 (section 3.4.4). Fig. 5.2 shows an example of a reversal process in a structure with a $200 \times 280\ \text{nm}^2$ nanoconstriction.

Initially, the two pads are nearly saturated at a magnetic field of $+20\ \text{Oe}$ (Fig. 5.2(a)). The magnetic contrast arising from weak magnetisation ripple and thick dark fringes at the bottom edges of the two pads indicate that they are both magnetised in the same direction. When the magnetic field is reduced to zero (Fig. 5.2(b)), the magnetisation ripple increases in dispersion, but the magnetisation remains parallel to the easy axis as indicated by the thick dark fringes at the bottom edges of the two pads. It can be seen that the ripple in the elongated pad has less dispersion than the elliptical one due to shape anisotropy.

Applying the field along the negative direction leads initially to the start of the magnetisation reversal of the elliptical pad with the formation of a multi-domain state (Fig. 5.2(c)) at $-3.6\ \text{Oe}$. Simple schematics of the magnetisation configuration in such a state can be interpreted as shown in Fig. 5.3(a). Increasing the strength of the negative field to $-4.1\ \text{Oe}$ results in a single DW nucleating and moving to the bottom of the elliptical pad, and one end of the wall appears to be pinned at the constriction (see Fig. 5.2(d)). The switching of the elliptical pad is clearly demonstrated by a reduction of the ripple dispersion and changing the contrast at the edge (the top edge now appears dark). Further increase of the applied field, to $-9.0\ \text{Oe}$, results in the wall being driven to the edge of the pad, and eliminated. The reversal of the elliptical pad is now completed and the anti-parallel state of the structure is established (Fig. 5.2(e)). In this state,

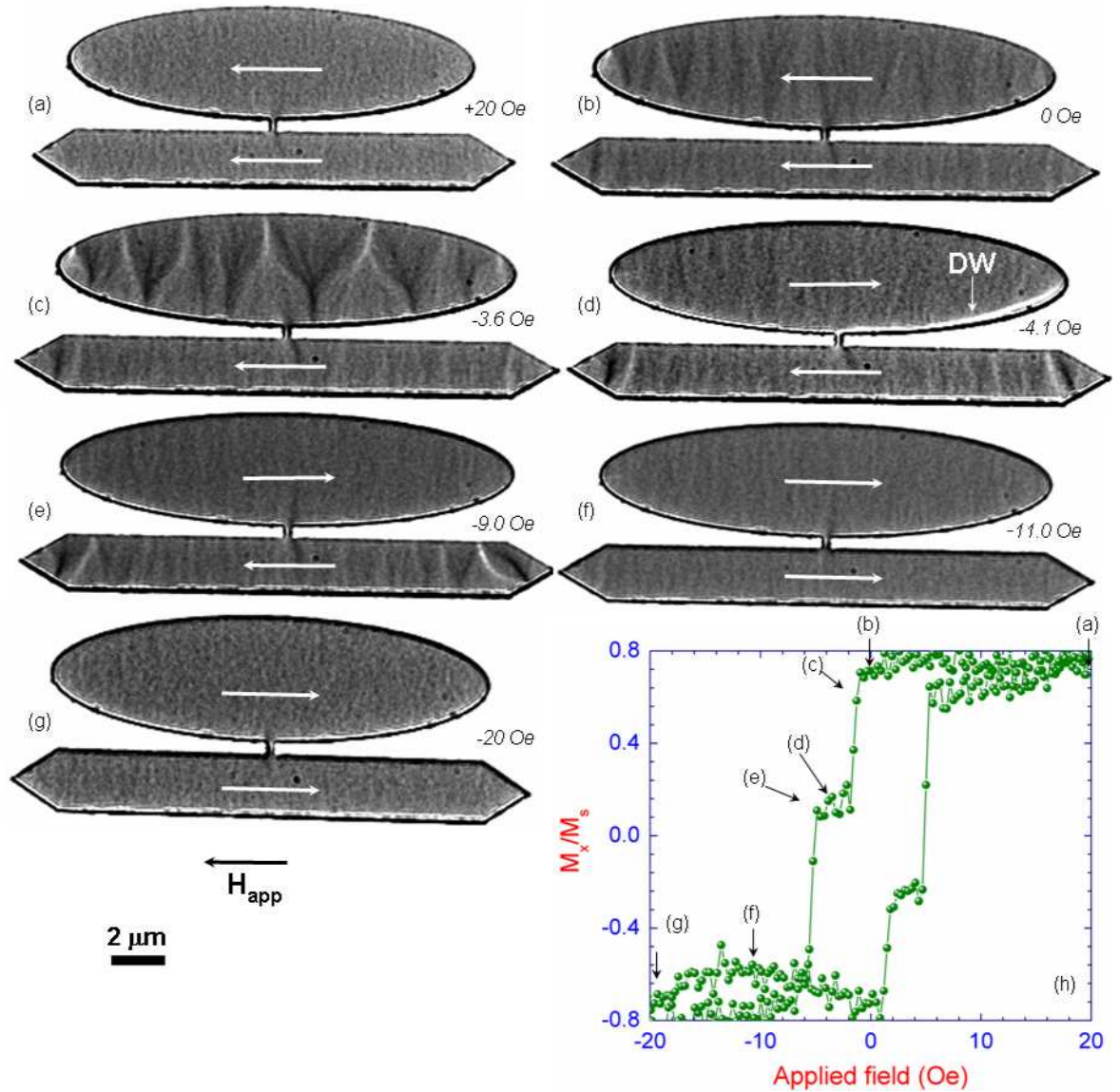


Figure 5.2: Fresnel images of the structure with a $200 \times 280 \text{ nm}^2$ nanoconstriction during demagnetisation at various magnetic field: (a): +20 Oe, (b): 0.0 Oe, (c): -3.6 Oe, (d): -4.1 Oe, (e): -9.0 Oe, (f): -11.0 Oe, (g): -20 Oe, and corresponding hysteresis loop measured by MOKE at the Durham University [2].

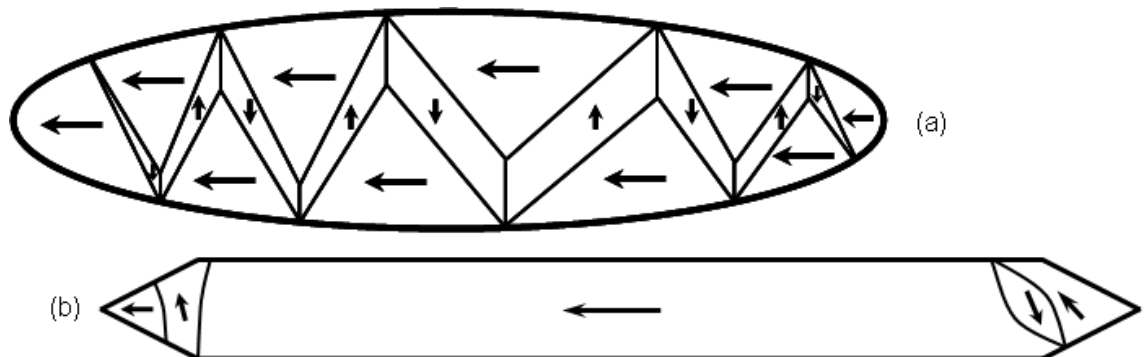


Figure 5.3: Schematic diagrams of the magnetisation configuration in the pads shown in Fig. 5.2: (a) corresponds to elliptical pad in Fig. 5.2(c), and (b) elongated pad in Fig. 5.2(e), respectively.

the magnetisation at the ends of elongated pad shows transverse components (magnetisation configuration of the pad can be interpreted in Fig. 5.3(b)). Further increase of the field strength results in reversal of the elongated pad. Presumably this is due to domain wall nucleation and rapid movement, however the switching is too rapid to observe in the TEM. The parallel state is again observed in the structure but with opposite magnetisation to the original state (see Figs. 5.2(f, g)).

The same process is also observed for return path of the hysteresis sequence. Such a magnetisation reversal process of the structure corresponds to a two-step hysteresis loop (Fig. 5.2(h)) which was previously observed using MOKE [2]. Such a reversal trend is well-defined and reproducible for all structures with various constriction sizes. It is apparent that the domain wall can be reproducibly created and pinned at the constriction during the reversal process for all structures (see an example in Fig. 5.2(d)). It is also apparent that Fresnel imaging has successfully imaged the magnetisation reversal of the pads, and shown the formation of the wall and its location at the constriction. However, for quantitative imaging of magnetic induction distribution, DPC mode of LTEM is required. In DPC mode, two images showing contrast due to orthogonal components of magnetic induction are collected (see chapter 3).

Figs. 5.4(a,b) illustrate a pair of DPC images mapping two orthogonal directions of induction in the state which was found in Fig. 5.2(d). This illustrates the presence of the

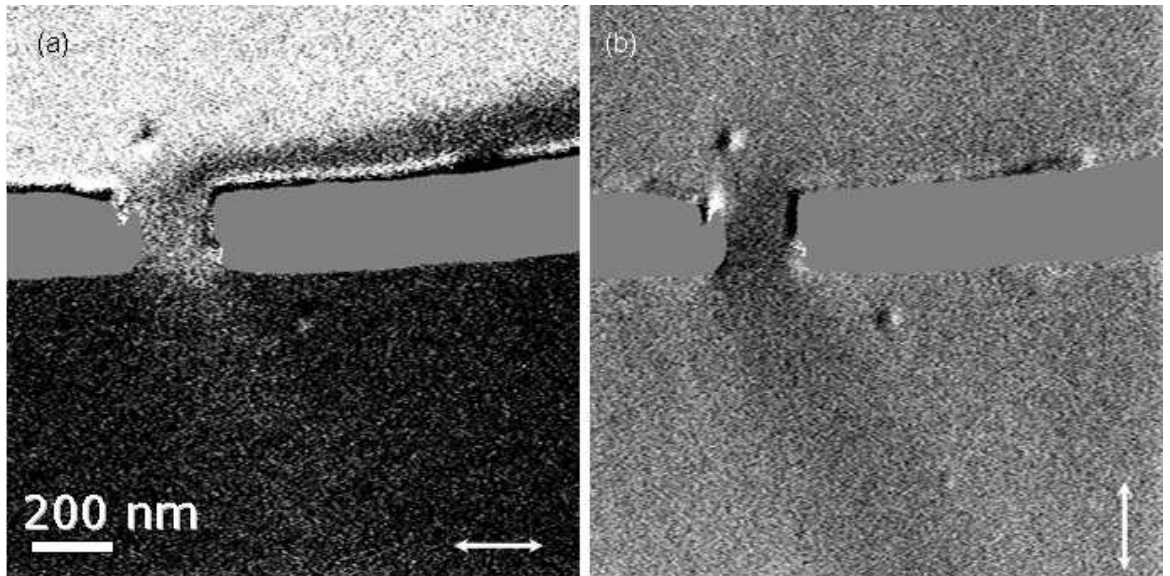


Figure 5.4: A pair of DPC images (a,) of the structure with a constriction size $200 \times 280 \text{ nm}^2$ at domain wall nucleation state (Fig. 5.2(d)) mapped along two orthogonal directions. White arrows denote the mapping directions.

wall near the edge of the elliptical pad with part of the wall located at the constriction. Further DPC analysis with combined interpretation from micromagnetic simulation in the next section shows that this wall is important in defining the magnetic structure around the constriction however the rotation of magnetisation from the pad regions is equally important and the whole structure is considered in the next section.

The Fresnel imaging process was repeated for all the structures with various sizes of the constriction, it was found that the field required to nucleate the single DW (nucleation field - H_N) in the elliptical pad shows appeared to be fairly constant with a weak dependence on the height of the constriction (Fig. 5.5). This can be understood that the nucleation of the wall is a consequence of the magnetisation reversal process in the elliptical pad, it can be seen that low angle DWs formed over whole of the elliptical pad (Figs. 5.2(c,d)) and their nucleation appeared not to be strongly influenced by the constriction or the elongated pad. The field at which the structure switches to the antiparallel state -AP (reversal process in elliptical pad being completed), H_{AP} increases with constriction height (Fig. 5.5). It is apparent that the AP state is established when the wall is eliminated at the bottom of the elliptical pad after it has been pinned at the constriction. As a result, the constriction acts as a pinning site, and elimination

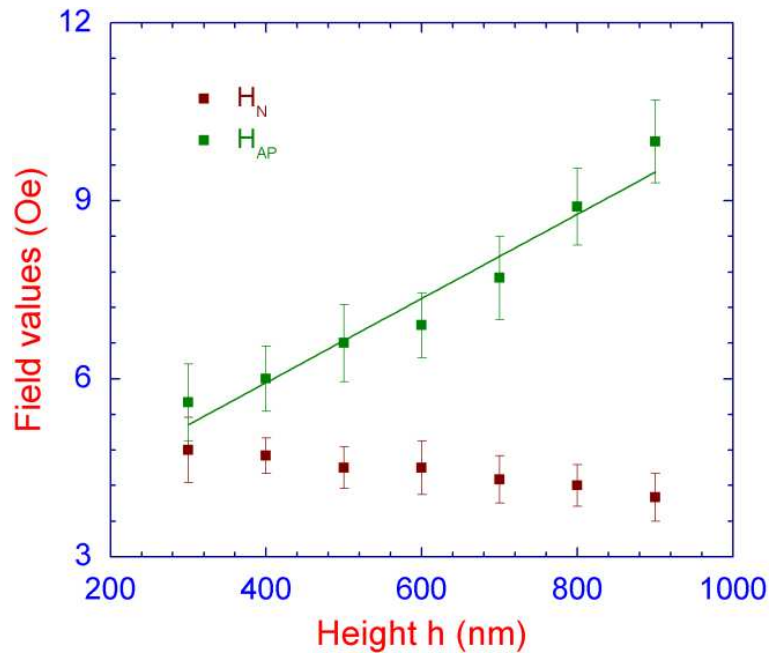


Figure 5.5: Constriction height dependence of field characteristics of the structures with constriction dimension $300 \times h \text{ nm}^2$ ($h = 300 \div 900 \text{ nm}$): H_N : magnetic field to nucleate a single DW in the elliptical pad, H_{AP-P} field for propagating DW from the constriction at which the structure was switched to antiparallel state.

of the wall is influenced by the geometry of the constriction, which is a commonly observed in magnetic systems. Therefore, in this situation, the geometry of the constriction does appear to affect the elimination of the wall, or on the field at which the structure is switched to the antiparallel state. The results in following sections show that in this case the pinning of the domain wall in the constriction forms a complex magnetic structure confined in the constriction. The dimension of this magnetic structure is independent on the height of the constriction (Tab. 5.1). The antiparallel state is established when the Zeeman energy is high enough to break the structure up. A longer constriction, a higher energy is required, resulting in an increasing of the H_{AP} .

5.4 Magnetic configuration in the nanoconstrictions

In this section the aim is to present a quantitative investigation of the magnetic configuration in the constriction. DPC imaging combined with OOMMF simulation is employed to interpret the magnetic structure in the constriction. A series of DPC images were recorded at key points in the reversal process. With antiparallel alignment of the induction in the two pads a reference signal is provided for the integrated induction (300 ± 30 counts $\sim \pm 2B_s t - B_s$: saturation induction, t : film thickness).

Fig. 5.6 illustrates the DPC images of the structure with $200 \times 280 \text{ nm}^2$ constriction in which a domain wall is present in the elliptical pad (experiment - (a) and micromagnetic simulation - (b)). Line profiles of the magnetic induction in Fig. 5.6(c) confirm consistency between the micromagnetic simulation and the experiment. The line profiles are consistent with a hyperbolic tangent function given by [5, 6]:

$$B_x(y) = B_s \tanh\left(\frac{y}{\Lambda}\right) \quad (5.1)$$

where, B_s is the saturation induction, Λ is the domain wall parameter. The width of the domain wall in this case is determined as the full width at half maximum (FWHM) of the first-order derivative of the induction profile function above [6] (Fig. 5.6(d)).

In this situation, the wall width, δ , is 115 ± 10 nm. This wall width is consistent with other experimentally observed value for 7 nm thick $\text{Ni}_{81}\text{Fe}_{19}$ film (110 nm [7]) and theoretical prediction (110 [6]). The wall in the elliptical pad is effectively that of a continuous film, and independent on the constriction geometry. The width of such

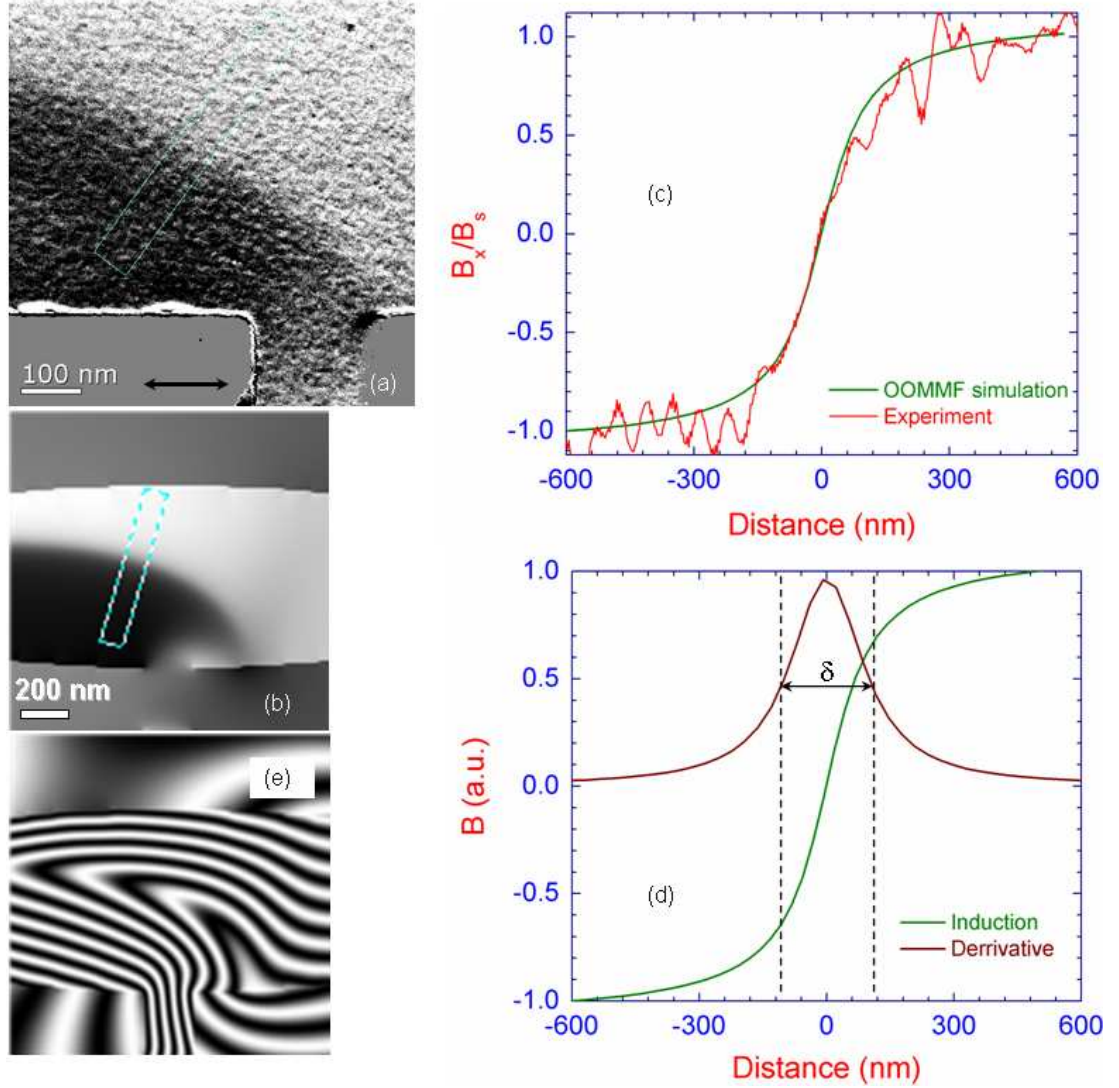


Figure 5.6: DPC images for the structure with $200 \times 280 \text{ nm}^2$ showing a domain wall nucleating in the elliptical pad: (a) experiment, (b) simulation, (c) 20-lines profiles of induction measured normal to the wall, (d) induction profile and its derivative to determine the wall width. Flux lines of the magnetic induction in the sample are shown in frame (e). The black arrow denotes the mapping direction.

a wall can be referred to $\delta \simeq 2\Lambda$ (in this case, $\Lambda = 58 \pm 5 \text{ nm}$), this is a standard definition for such a profile e.g. [5]. Hence, the widths in the following paragraphs will be defined as following this definition $\delta = 2\Lambda$. Note that the error here comes from least square fitting routine and it should be noted that the geometries of the pads in the simulation are smaller than that of experimental structure to reduce computational time but the constriction dimension (both width and height) is kept as in experiment. The distribution of the magnetic induction in the simulated state with the domain wall can be seen clearly via the flux lines of the induction calculated from the electron phase and shown Fig. 5.6(e).

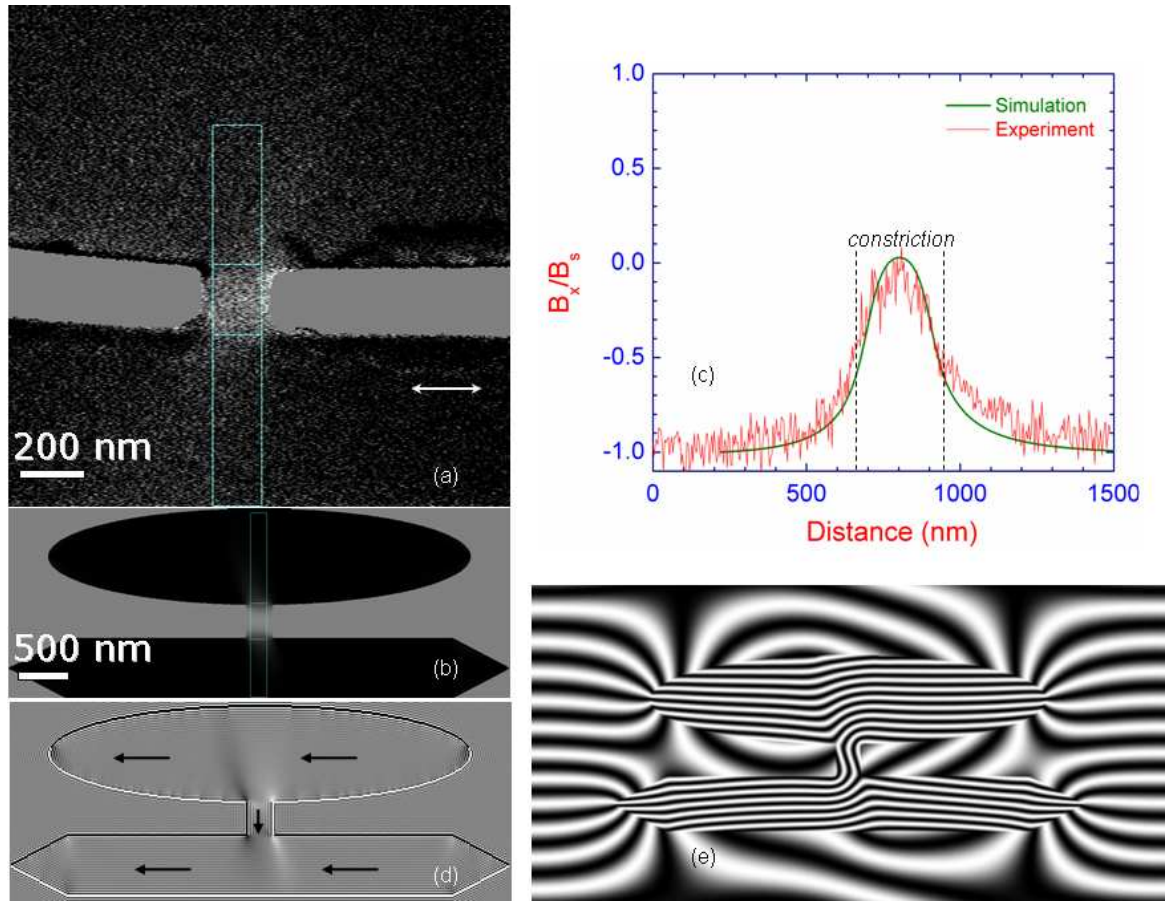


Figure 5.7: DPC images for the structure with $200 \times 280 \text{ nm}^2$ constriction at remanent state: experiment (a) and simulation (b); (c) 20-lines induction profiles in the structure, (d) out-of-plane magnetisation curl component; and (e) simulated induction flux. The black arrow denotes the mapping direction; the region between the dash lines in frame (d) is the constriction area.

Figs. 5.7(a,b) show an experimental and simulated DPC images of the remanent state for the structure with a constriction size $200 \times 280 \text{ nm}^2$. Corresponding 20-line averaged line profiles measured along the constriction are shown in Fig. 5.7(d). It is important to note that the line profile is averaging out over 20 pixels (in all experimental cases), that is over mean grain size of the film ($\sim 10 \text{ nm}$), to reduce the noise from non-magnetic components. A comparison of induction profiles of experiment and simulation measured along the constriction displayed in Fig. 5.7(d) again indicates an agreement between simulation and experiment. The flux lines of the magnetic induction in the structure can be determined by taking the sine of calculated magnetic phase of the structure Fig. 5.7(e) ($\sin n \times \phi$, the integer number $n = 10$ denotes the density of the flux lines). Interpreting this shows that the magnetisations in two pads are aligned parallel each other, whereas magnetisation in the constriction is aligned to the vertical axis. Continuous flux lines from the elliptical pad to the constriction,

and from the constriction to the elongated pad show a configuration which effectively has ‘two-90°-walls’ between each pad and the constriction. However the ‘walls’ look more like regions of rotation than a well defined rotation between two domains. Fig. 5.7(d) shows the out-of-plane magnetisation curl which normally shows the locations of domain walls [8,9], however in this case diffuse white and dark areas are visible around the constriction rather than well defined walls. To try and quantify this configuration we compare the induction profiles shown in Fig. 5.7(c) with a double hyperbolic-tangent function model given by:

$$B_x(y) = B_1 \tanh\left(\frac{y - y_1}{\Lambda_1}\right) + B_2 \tanh\left(\frac{y - y_2}{\Lambda_2}\right) \quad (5.2)$$

Where, B_1 , B_2 are induction coefficients, y_1 , y_2 are geometrical parameters, Λ_1 , Λ_2 are DW parameters, respectively. The first term of (5.2) corresponds to the induction profile from the elongated pad to the constriction, and the second is the profile from the constriction to the elliptical pad.

By fitting the induction profiles (Fig. 5.7(c)) with the analytical model in (5.2), two DW parameters, Λ_1 , Λ_2 , are determined to be 67.5 ± 5 nm ($\Lambda_1 = \Lambda_2$). These correspond to two ‘wall width’ of $\delta_1 = \delta_2 = 135 \pm 10$ nm (using above definition $\delta = 2\Lambda$). Note that the wall width definition in this case expresses the width of 90° variation of the magnetic induction (from the pads to the constriction). The width of the 90°-variations here is much narrower than that predicted for a one dimensional 90°-wall in a continuous permalloy film with the same thickness (where the width is expected to be ~ 250 nm [6]). However it must be remembered that in the experiment we are dealing with a continuous magnetisation rotation from the pad to the constriction rather than a well defined domain wall. This variation is on a quite different length-scale from that of 90° domain walls in continuous films. Furthermore the width of these 90°-variations were found to have the same width (135 ± 10 nm) for the structures with different size of the constriction.

Fig. 5.8 shows experimental DPC images (a,b) compared to a simulated images (c,d) for the state where a DW is pinned in the elliptical pad at the constriction (200×280 nm²). The 20-line-averaged induction profiles shown in Fig. 5.8(e,f) indicate a state similar to the ‘two-wall’ state described previously (Fig. 5.7(c)) but with two different

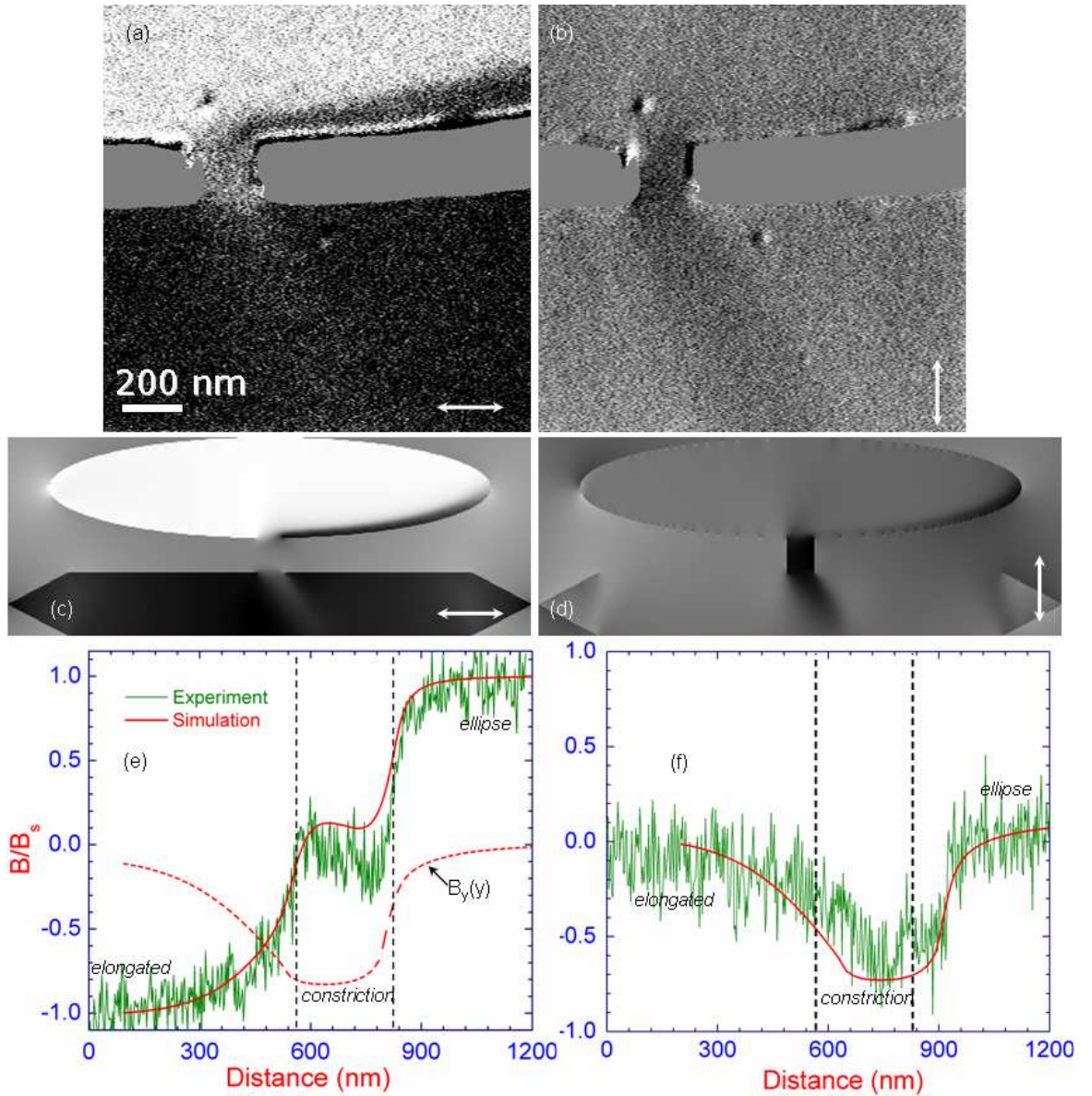


Figure 5.8: DPC images for the structure with $200 \times 280 \text{ nm}^2$ constriction at domain wall nucleation state: experiment (a,b) and simulation (c,d). Frames (e,f) show the induction profiles measured along the constriction height from DPC images that was averaging out over 20 pixels: (e) horizontal mapping, (f) vertical mapping. The white arrows denote the mapping directions.

profiles. In order to understand analytically this configuration, the double-hyperbolic tangent function described in equation 5.2 is again applied to the induction profiles shown in Fig. 5.7(e) and Fig. 5.9; and the magnetic configuration in this case can be explained as:

- The variation of the magnetic induction from the elongated pad to the constriction is consistent with the 90° variation shown previously, and in this case, the width of the 90° variation is determined to be $\delta_1 = 135 \pm 10 \text{ nm}$, which is the same to the width of the 90° variation obtained at the remanent state;

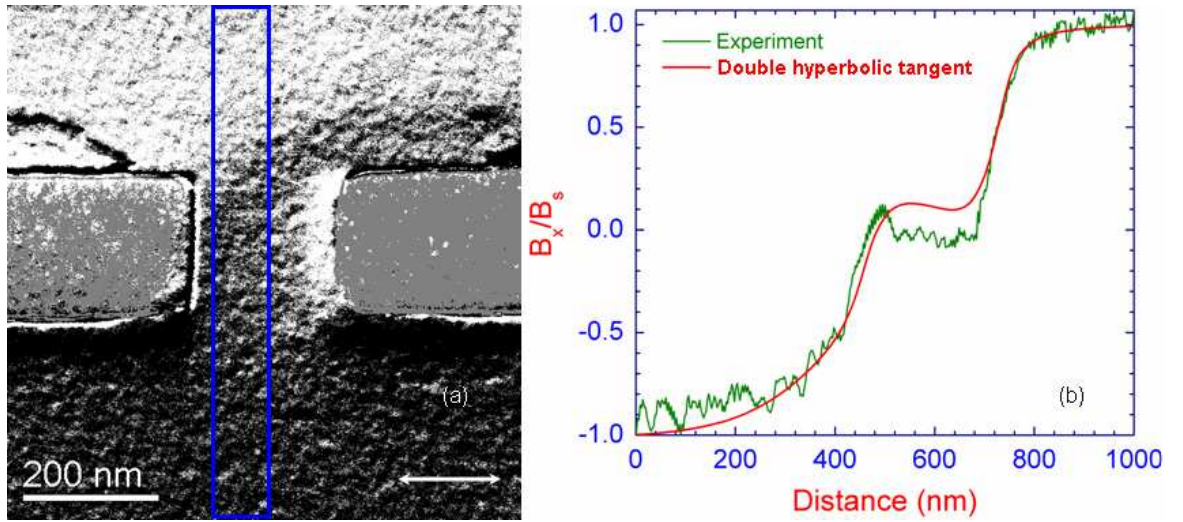


Figure 5.9: (a) High-mag. scanning DPC image and (b) 20-line profiles of the induction measured along the constriction for the structure with a $200 \times 280 \text{ nm}^2$ constriction at domain wall nucleation state. The blue line and the white arrows show the line to measure the profile and the mapping direction, respectively.

- The induction profile from the constriction to the elliptical pad shows a much narrower wall than that of the 90° variation from the elongated pad to the constriction. The width of this variation is measured to be $\delta_2 = 80 \pm 7 \text{ nm}$. The overall profile appears to be a combination of narrow wall and a 90° variation as seen in the previous state, for the induction variation from the elliptical pad to the constriction. However this narrower wall, in effect, also has a 90° rotation variation, although the presence of the DW clearly gives this variation a different character. Furthermore the width of this variation is narrower than that of the

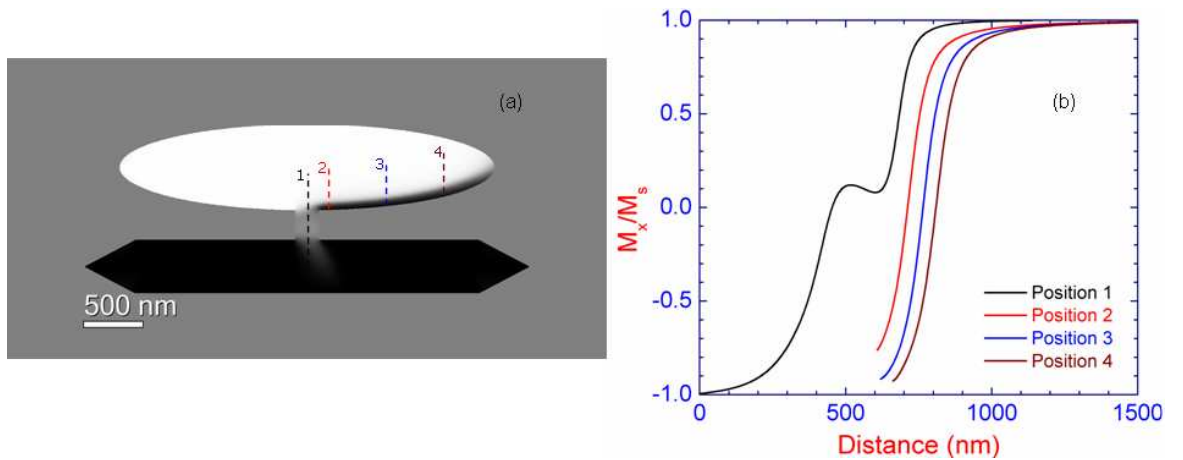


Figure 5.10: (a) Simulated DPC image and (b) 20-line profiles of the induction measured at various positions for the structure with $200 \times 280 \text{ nm}^2$ constriction at domain wall nucleation state: (1) along the constriction, (2-4) various positions cross the wall in the elliptical pad.

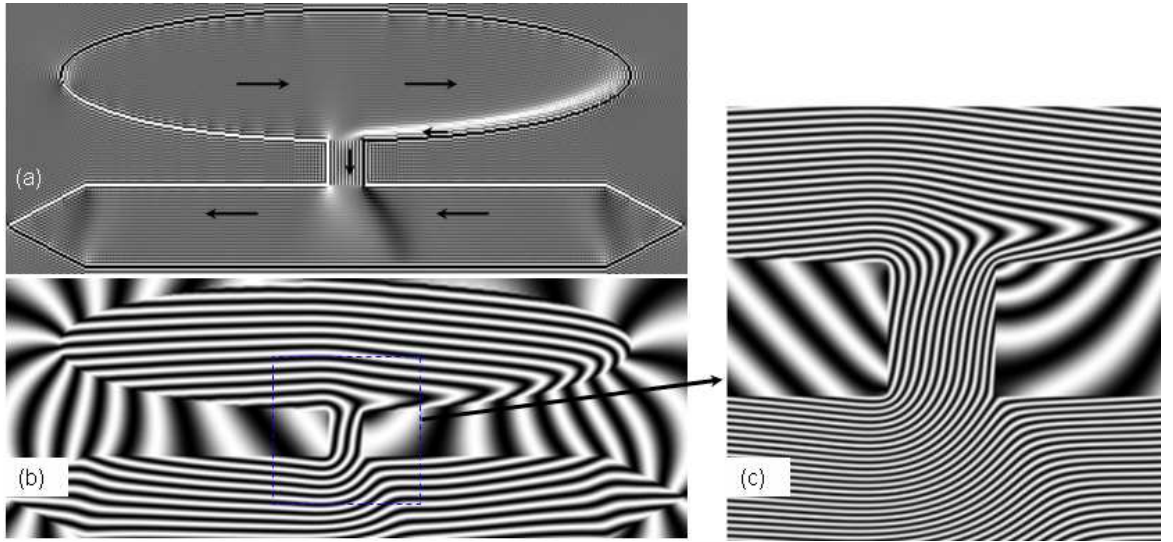


Figure 5.11: The out-of-plane magnetisation curl (a) simulated induction flux calculated from electron phase (b) and (c) magnetisation configuration at domain wall nucleation state for the structure with a $200 \times 280 \text{ nm}^2$ constriction. Frame (c) illustrates a higher density of the flux lines around the constriction.

high-angle wall width measured in the elliptical pad previously ($115 \pm 10 \text{ nm}$);

- Induction profiles in simulation case measured at various positions across the wall shown in Fig. 5.10 indicate that the width of the wall in the elliptical pad hardly changes from the region near the constriction to positions along the length of the domain wall (all have a width around $\delta = 115 \pm 15 \text{ nm}$). It appears that the part of the wall pinned at the constriction can be considered to be compressed though the magnetisation around this region is not really described by a simple one dimensional wall;
- The calculation of flux lines of the induction and out-of-plane magnetisation curl shown in Fig. 5.11 illustrates how the simulated magnetisation varies from the pads to the constriction (Fig. 5.11(b,c)). The magnetisation rotates very smoothly from the elliptical pad to the constriction and to the elongated pad on the left half of the structure but not the right half.

Wall compression is also found in the other structures with different geometrical dimensions of the constriction. Table 5.1 lists the width of the induction variation, δ_2 measured at various constriction dimensions. It appears that the width of the variation increases slightly with the height of the constriction, from $80 \pm 7 \text{ nm}$ for a 280 nm high constriction, to $105 \pm 7 \text{ nm}$ for the constriction with a height of 900 nm (Table 5.1).

Table 5.1: The width of induction variation, δ_{90} at remanent state; δ_2 at the domain wall nucleation state in various geometries of the constriction.

Constriction geometry	δ_{90} (nm)	δ_2	δ_2 (simulation) (nm)
$200 \times 280 \text{ nm}^2$	135 ± 10	$80 \pm 7 \pm 0.07$	80 ± 5
$300 \times 300 \text{ nm}^2$	137 ± 10	$85 \pm 7 \pm 0.08$	87 ± 5
$300 \times 500 \text{ nm}^2$	132 ± 7	$90 \pm 7 \pm 0.08$	90 ± 5
$300 \times 600 \text{ nm}^2$	135 ± 7	$95 \pm 7 \pm 0.08$	100 ± 5
$300 \times 900 \text{ nm}^2$	133 ± 10	$105 \pm 7 \pm 0.08$	107 ± 5

The change of the width appears to be similar to the change of the width of the domain wall confined in geometrically constrained structure as predicted previously [3]. Furthermore this result is also consistent with previous results obtained by SEMPA from a similar structure [10] as described in Fig. 5.12. In a H-shape patterned $\text{Ni}_{80}\text{Fe}_{20}$ with a $500 \times 250 \text{ nm}^2$ constriction (Fig. 5.12(a)), the induction profile measured along the vertical axis of the constriction shows a two-wall 90° profile (Fig. 5.12(c)) similar to the picture described previously in Fig. 5.7(c). In antiparallel state, the induction profile displayed in (Fig. 5.12(d)) was suggested to be the one of a single 180° Néel-type wall with the constriction plays a role of the core of the wall [10]. The wall width was determined to be a function of constriction dimension. Under the application of the external field, the 180° wall was broken into two 90° walls as shown in Fig. 5.12(d).

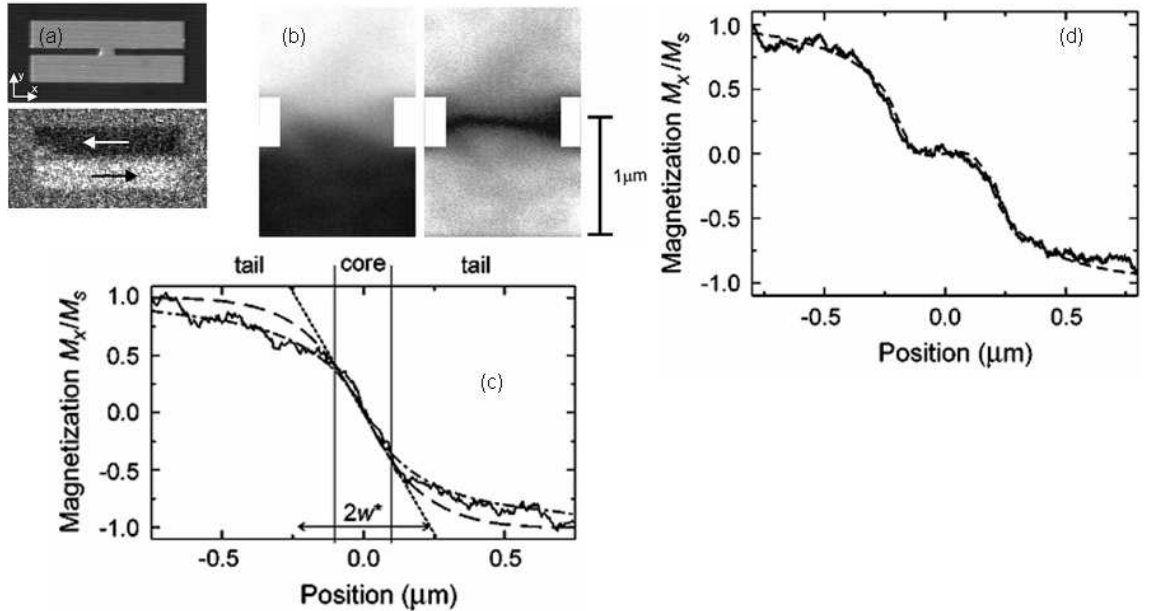


Figure 5.12: (a) SEM micrograph of the H-shape patterned structure, (b) SEMPA images of induction distribution measured in the constriction, (c) induction profile measured in antiparallel state and (d) two-wall profile. These results are redrawn from ref. [10] as a comparison.

Chapter 5: Magnetic configuration in nanoconstrictions

The results given in our case have provided a more detailed analysis of the magnetic configuration which is partly due to the DW in the structure and also the rotation of the magnetisation between the constriction and the pads. Labelling such a variation as a single domain wall, is a little oversimplified although in essence the difference in the states considered here is really due to the domain wall nucleated in the elliptical pad. The magnetisation variation observed around the constriction has similarities to the curling magnetisation seen in the magnetic vortex in the circular disk (see chapter 4).

The DPC images of the structure with $200 \times 280 \text{ nm}^2$ constriction (simulation and experiment) in the fully antiparallel state after the elimination of the DW are illustrated in Fig. 5.13. A comparison of the experimental and simulated data is indicated by the induction profiles measured along the constriction Fig. 5.13(e). These profiles are also consistent with that of ‘two-wall-like’ configuration at the remanent state described

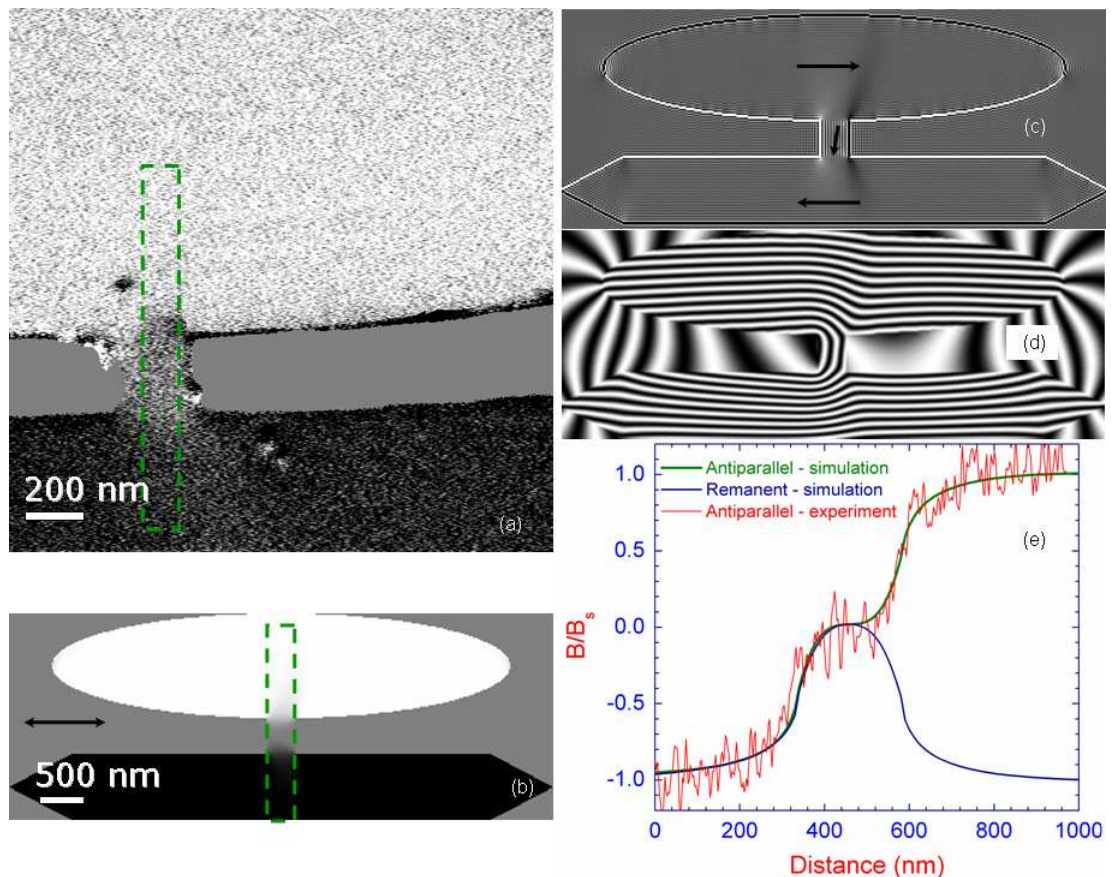


Figure 5.13: DPC images for the structure with $200 \times 280 \text{ nm}^2$ constriction at antiparallel state: experiment (a) and simulation (b); simulated magnetisation curl in the structure (c), flux lines of the induction (d) and 20-line profiles measured along the constriction (e) with a comparison with profile in remanent state. The black arrow denotes the mapping direction.

previously via the double hyperbolic-tangent function given by 5.2. A comparison of the profiles shown in Fig. 5.13(e) with a double hyperbolic-tangent function described previously gives widths of the magnetisation variations as $\delta_1 = \delta_2 = 135 \pm 15$ nm, which are reasonably consistent with that in the remanent state (Fig. 5.13(e)). This confirmation is supported by comparing with the induction profile measured in remanent state as shown in Fig. 5.13(d). This state resembles the ‘two-90°-wall-like’ structure, although the rotation of the magnetic induction from the elliptical pad to the elongated pad is a little different. This is visible through the magnetisation curl (Fig. 5.13(c)) and the flux lines of the magnetic induction calculated from the electron phase (Fig. 5.13(d)). The flux lines shown in Fig. 5.13(c) illustrate a smooth rotation of the induction from the elliptical pad to the constriction via the left side of the structure. As a result, the magnetic rotation configuration between the pads in the structures during the reversal can be interpreted as shown in Fig. 5.14. The continuous flux path varies from a C-type configuration in the remanent/parallel states to an S-type state in the antiparallel configurations.

The magneto-transport result, which is shown detail in section 5.6, indicates that the nucleation of the domain wall in the elliptical pad (and pinned at the constriction) causes a large change of the magnetoresistance denoted by a well-defined peak in AMR curve. This is due to the strong scattering of the spin-polarised electrons on the vari-

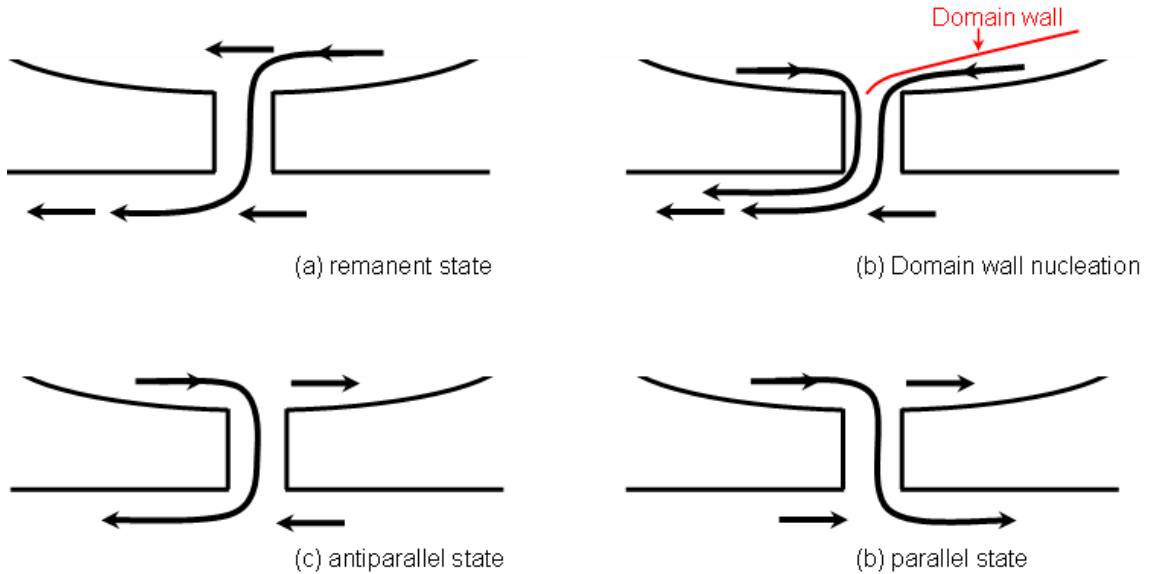


Figure 5.14: Schematics of magnetic configuration in the structures during the magnetisation reversal at various states: (a) parallel-remnant state, (b) antiparallel with domain wall nucleation state, (c) antiparallel state, and (d) switched-parallel state.

ation of the magnetic moment created by the domain wall pinned at the constriction. This is effectively the domain wall resistance contribution. Furthermore, the continuous change of the magnetoresistance during the magnetisation reversal shows that the measured AMR has contributions other than this domain wall resistance which show a more continuous variation. However the domain wall being pinned in the constriction causes a discontinuous change in the magnetoresistance [12]. The investigation of direction of the magnetic induction in the constriction reveals that there is a contribution from the rotation of the magnetic induction in the constriction.

5.5 Rotation of the magnetic induction

In this section, the DPC mode of LTEM is exploited to analyse the rotation of the magnetic induction in the constriction, that is expected to affect the AMR of the structure because the AMR depends on the angle between the magnetic induction and the electrical current density [13]:

$$\rho(\theta) = \rho_{\perp} + (\rho_{\parallel} - \rho_{\perp}) \cos^2 \theta \quad (5.3)$$

where, ρ_{\parallel} , ρ_{\perp} are the resistivity when the current is parallel or perpendicular to the induction, respectively.

The direction of the induction is defined as the angle, θ , between the y-axis - direction of the current density (Fig. 5.15). Magnitude of the θ is determined from the orthogonal components of the magnetic induction with the tangent of the θ is given by:

$$\tan \theta = \frac{B_x}{B_y} \quad (5.4)$$

here, B_x , B_y are two orthogonal components of the magnetic induction, which are averaged over the constriction.

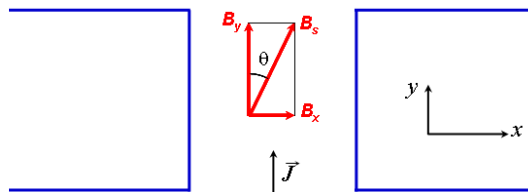


Figure 5.15: The angle of magnetic induction in the constriction is defined as the angle θ with the cosine of θ can be determined from DPC images.

Chapter 5: Magnetic configuration in nanoconstrictions

It is well-known that the DPC mode provides two difference images mapping orthogonal components of magnetic induction with the intensities proportional to integrated induction, $\int B dz$. Therefore, DPC images of the B_x and B_y in the constriction region were analysed. The mean intensities in the constriction region for the two images, C_x and C_y , will be directly proportional to B_x , B_y if the signals are correctly balanced. As a result, the equation (5.4) will be measured as:

$$\tan \theta = \frac{B_x}{B_y} = \frac{C_x}{C_y} \quad (5.5)$$

The antiparallel state is selected as a reference to signal. In this state, the magnetic induction in the two pads point along the x-axis but in opposite directions, resulting in a well-defined symmetry in the intensity of x-component DPC image between two pads as arctangent function. The magnetic induction in the two pads in this state will be $B_{pad-1} = B_x = B_s$, and $B_{pad-2} = -B_x = -B_s$, respectively (Fig. 5.16).

Fig. 5.17 illustrates the magnetic induction angle for the structure with a constriction of $200 \times 280 \text{ nm}^2$ as a function of applied magnetic field. In the remanent state, the

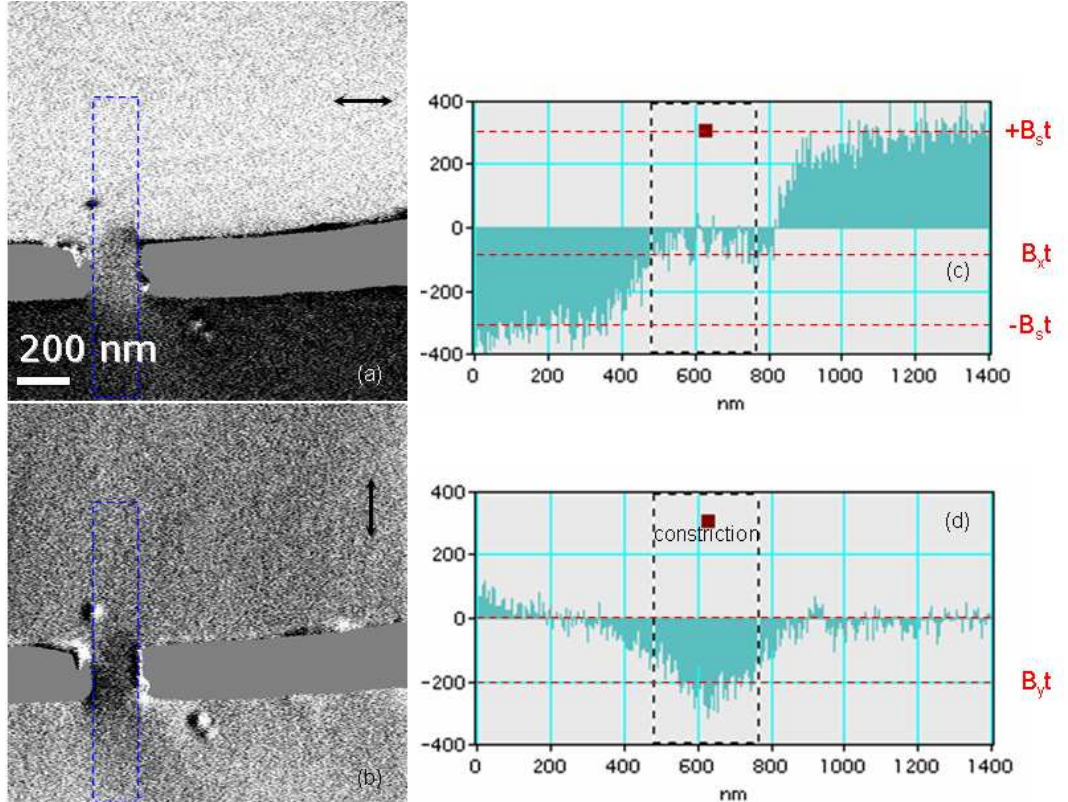


Figure 5.16: An example of determination of the induction angle, θ from two DPC image (a,b). The blue lines denote the 30-line-averaging profile of the induction shown in frames (c,d). The arrows show the mapping directions.

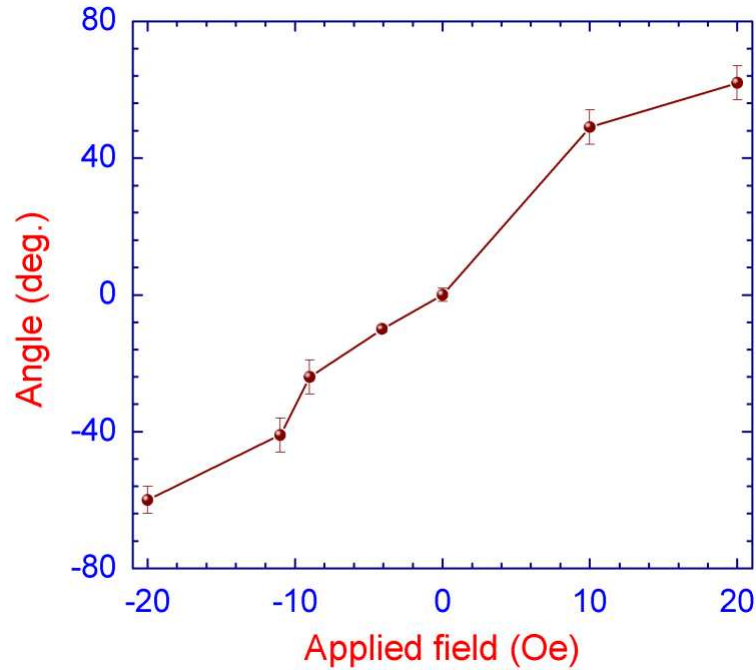


Figure 5.17: Induction angle as a function of applied field during reversal process calculated for the structure with a constriction of $200 \times 280 \text{ nm}^2$.

angle is measured as zero within error, showing that the magnetisation is aligned along the height axis of the constriction due to the shape anisotropy. Increasing the magnetic field causes the magnetic induction to be tilted away from the height axis, denoted by an increase of induction angle. This indicates that during the magnetisation reversal, the angle between the density current and the magnetic induction in the constriction increases. The rotation of the magnetic induction in the constriction in reversal process can be understood with an aid of the schematic shown in Fig. 5.18. When the magnetic field varies from maximum positive field to maximum negative field, the magnetic induction in the constriction is smoothly rotated which is denoted by the variation of the magnetic induction angle θ . At maximum applied field (+20 Oe), the magnetic induction tilts away from the vertical axis, resulting in a low magnetoresistance. The resistivity increases when the magnetic induction rotates from the easy axis to the vertical axis of the constriction.

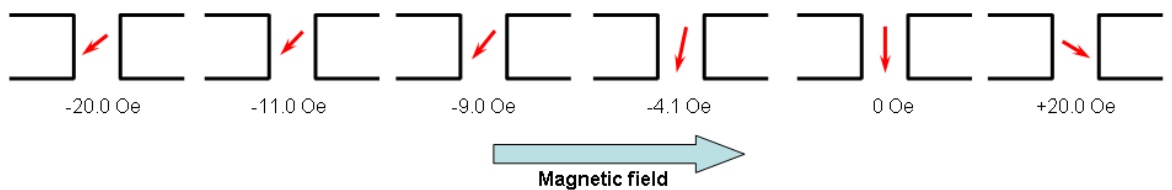


Figure 5.18: Rotation of the magnetic induction in the constriction during reversal process. The magnetic induction is denoted by the red arrows.

Table 5.2: Comparison of induction angle (in degree) for the structures with the smallest ($200 \times 280 \text{ nm}^2$) and largest ($300 \times 900 \text{ nm}^2$) constrictions at certain states. The number in \pm here shows the variation of the magnetic induction direction rather than error.

State	$200 \times 280 \text{ nm}^2$		$300 \times 900 \text{ nm}^2$	
	Simulation	Experiment	Simulation	Experiment
Positive maximum field	62 ± 5	59 ± 7	55 ± 4	48 ± 10
Remanent	0 ± 2	-2 ± 5	0 ± 2	2 ± 6
DW nucleation	-10 ± 1	-12 ± 6	-10 ± 3	-6 ± 5
Antiparallel	-24 ± 5	-39 ± 9	-14 ± 6	-18 ± 6
Parallel	-41 ± 5	-44 ± 10	-34 ± 5	-39 ± 9
Negative maximum field	-60 ± 4	-52 ± 7	-50 ± 5	-44 ± 9

Table 5.2 shows a series of the induction angle calculated for the structures with the smallest ($200 \times 280 \text{ nm}^2$) and largest ($300 \times 900 \text{ nm}^2$) constrictions at various states: remanent, with domain wall nucleation, antiparallel state and parallel state (the field values for the states are different for each structure). Simulated results are calculated from OOMMF simulation. It is notable that the symbol \pm in the Tab. 5.2 shows the variation of the magnetic induction direction rather than error. For the larger constriction height, the smaller induction angle at maximum applied field is observed. A higher field is required to rotate the magnetic induction from easy axis (y -axis) to the hard axis due to the shape anisotropy. However the same variation of the magnetic induction during the reversal is also observed in the structure with a larger constriction ($300 \times 900 \text{ nm}^2$) as described in Fig. 5.18.

5.6 Electrical transport in the structures

The magnetoresistance measurements were carried out at the University of Leeds by Dr. Mark Hickey. The AMR hysteresis curves for the structure with $200 \times 280 \text{ nm}^2$ constriction are displayed in Fig. 5.19. A low value of resistance is observed when the sample is nearly saturated in a positive field, and then it gradually increases when the magnetic field varies from positive maximum applied field. This increase is mainly contributed by the rotation of the magnetic induction in the constriction as mentioned in previous section. The AMR is enhanced to a well-defined peak when the high-angle DW is nucleated in the elliptical pad, and pinned at the constriction to form the complex configuration of ‘domain-wall-confined-like’ state. The elliptical pad then becomes completely switched, leaving an antiparallel state of two pads. Finally, the resistance

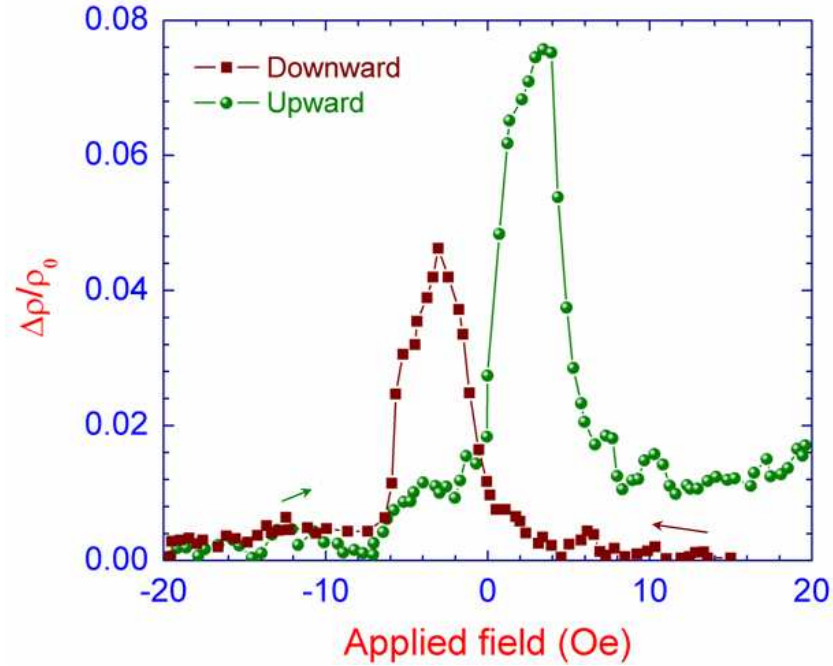


Figure 5.19: The AMR hysteresis loops for the structure with $200 \times 280 \text{ nm}^2$ constriction. The arrows illustrate the direction of the magnetic field variation.

is quickly decreased when the elongated pad reversed and low resistance state is established when uniform magnetisation of two pads is observed.

The magnetoresistance contribution of the induction rotation (as presented in previous section) causes a maximum value at zero field, at which the current is perpendicular to the field, in accordance to the equation (5.3). The contribution from the domain wall nucleation is drastically maximal at the field when the domain wall was nucleated. Domain wall resistance is the main contribution in this case, that can see obviously via the maximum value of the AMR ratio around the nucleation field value. It is also seen from Fig. 5.19 that the two peaks in the AMR hysteresis loop do not have the same magnitude. It is expected that this would be due to scattering differences from the magnetisation configuration around the constriction during the nucleation of the wall in two cycles of the demagnetising process. This suggests that the domain wall did not have the symmetrical behaviour observed in the Lorentz study, as the transport and TEM measurement were performed on nominally identical samples small differences in the physical structure may be responsible for such a difference. Small variations around the constriction where the wall is pinned are the most likely reason for this, any small asymmetry in the fabrication process could produce such an effect.

Further measurements of the magnetotransport for the patterned structures are essen-

tial to better understand the relation between the magnetic structure in the constriction and the magnetotransport behaviour, particularly for spin-transfer torque effect, etc. Simulations of the transport measurements are also expected to provide an insight into this effect.

5.7 Summary

The micromagnetic behaviour of the permalloy patterned thin film containing nanoconstrictions is investigated by means of LTEM. The confinement of the complex structure of wall-like-state induced by the nucleation of the high-angle wall in the elliptical pad is observed. Using two pads as the sources to nucleate DW, the DW can be controlled by magnetic field to be pinned at the constriction in order to form such a complex configuration. The width of this variation of the induction from the elliptical pad to the constriction is dependent on the dimension of the constriction, increases from 80 ± 7 nm in 280 nm height constriction to 105 ± 7 nm in 900 nm height constriction, and narrower than the width of the high-angle wall present in the elliptical pad (115 ± 10 nm). Such a complex state seems to be like the curling magnetisation in a magnetic vortex rather than a conventional linear wall as suggested by the other authors [10]. At the other states of the reversal, the configuration of two-90°-wall-like structures is observed.

The presence of such a complex configuration in the constriction introduces a DW resistance contribution to the magnetoresistance of the structure, which is observed as a well-defined peak in the AMR loop at the field when the wall is confined in the constriction. Analysing the magnetisation reversal process of the constriction by TEM showed that domain wall pinning and additionally the rotation of the magnetic induction in the constriction during the reversal are expected to contribute to the magnetoresistance of the device. The domain wall pinning and compression suggest qualitative agreement with the AMR however the asymmetry in the latter does not appear to be observed in the TEM experiments and therefore further investigation together with simulations is suggested.

Bibliography

- [1] P. M. Levy, S. Zhang, *Phys. Rev. Lett.* **79** (1997) 5110.
- [2] M. C. Hickey, A. Atkinson, C. H. Marrows, B. J. Hickey, *J. Appl. Phys.* **103** (2008) 07D518.
- [3] P. Bruno, *Phys. Rev. Lett.* **83** (1999) 2425.
- [4] K. J. Kirk, J. N. Chapman, C. D. W. Wilkinson, *Appl. Phys. Lett.* **71** (1997) 539.
- [5] A. Hubert, R. Schäfer, *Magnetic Domains*, Chapter 3, Springer Berlin Heidelberg (1998), ISBN 978-3-540-64108-7.
- [6] A. Hubert, *Phys. Stat. Sol.* **38** (1971) 699.
- [7] T. Trunk, M. Redjda, A. Kákay, M. F. Ruane, F. B. Humphrey, *J. Appl. Phys.* **89** (2001) 7606.
- [8] I.E. Beardsley, *IEEE Trans. Magn.* **25** (1989) 671-677.
- [9] S. McVite, G. S. White, *J. Phys. D: Appl. Phys.* **37** (2004) 280.
- [10] P.-O. Jubert, R. Allenspach, A. Bischof, *Phys. Rev. B* **69** (2004) 220410.
- [11] Michael R. Scheinfein, <http://llgmicro.home.mindspring.com/index.htm>
- [12] S. Lepadatu, Y. B. Xu, *IEEE Trans. Magn.* **40** (2004) 2688.
- [13] T. R. McGuire, R. I. Potter, *IEEE Trans. Magn.* **11** (1975) 1018-1038.

Chapter 6

Microstructure and magnetisation reversals of CoIr/Ru multilayer film for SUL

6.1 Objective and motivation

The aim of this chapter is to present a study of the micromagnetic behaviour of CoIr/Ru multilayer film as a soft underlayer (SUL) in perpendicular magnetic recording media. The SUL is a crucial part in the writing process, as well as the reading process in perpendicular magnetic recording. During the write process, the SUL guides the magnetic flux from the write pole to the collector pole with low reluctance. Therefore, the materials for SUL should have high permeability, high saturation magnetisation and low coercivity [1]. Even though high saturation magnetisation materials are used, the thickness of the SUL conventionally ranges between 100 and 400 nm. However it should be noted that a thick SUL may increase significantly the layer roughness, this prohibiting the head flying close to the recording media. Some typical SULs involve NiFe, CoFe, FeAlN, CoNbB, CoFeB, FeTaN, etc. [1].

Litvinov et al. [2,3] confirmed that a SUL with relatively high anisotropy field (from several tens Oe to hundred Oe) also needs to be utilised to optimise the performance of the recording system. This is because the anisotropy of the SUL governs the limit of characteristic bit size, which is limited by the characteristic in-plane length, Δ (often referred to the domain wall width) given by [2,3]:

$$\Delta \sim \sqrt{A/K_u} = \sqrt{\frac{2A}{2\pi H_k M_s^2}} \quad (6.1)$$

where, K_u and A are the uniaxial magnetocrystalline anisotropy and exchange stiffness constant, respectively; H_k and M_s are the anisotropy field and saturation magnetisation ($H_k = 2K_u/\mu_0 M_s$), respectively.

In the absence of a magnetic field, the SUL form domains, e.g. stripe domains or 180° domains with Bloch-type domain walls. However, the formation of such domain walls generate strong magnetic fields, which contribute strongly to noise during the reading process, named spike noise [3]. Furthermore, thick SULs cause another technical problem called wide adjacent track erasure (WATE). The WATE occurs over a range of several micrometers in the off-track direction [4]. However, a thin SUL is unreliable because of the reduction of writability. To suppress the spike noise, the formation of the single domain structure over the whole disk-shaped SUL stacked on or under an antiferromagnetic layer has been suggested in order to prevent the formation of Bloch walls [5]. To reduce the WATE, a multilayer SUL with magnetic moments aligned antiparallel by Ruderman-Kittel-Kasuya-Yoshida (RKKY) coupling is known to be effective [6]. However, it remains a challenge to suppress both artefacts. Hence, the suppression of spike noise and WATE are important technical issues for the development of perpendicular recording technology [2].

Recently, CoIr film with out-of-plane negative anisotropy has been suggested to be employed as a SUL in order to suppress both WATE and spike noise [7]. The WATE can be suppressed by realising a wide distribution of magnetic flux around the return yoke, which can be achieved by reducing the local susceptibility of the SUL in the direction normal to the film plane, χ_\perp . The χ_\perp can be controlled by changing the perpendicular uniaxial anisotropy, $K_{u\perp}$ as [7]:

$$\chi_\perp \sim \frac{M_s}{2(2\pi M_s^2 - K_{u\perp})} \quad (6.2)$$

Generally, the origin of spike noise has been considered as the leakage flux from Bloch walls toward the reading head. A Néel wall effectively reduces the leakage flux [7]. Therefore, the spike noise is reduced by forming Néel walls instead of Bloch wall. Normally, Bloch walls are formed in a thick SUL. But Néel wall formation is favoured by the introduction of a negative perpendicular uniaxial anisotropy $K_{u\perp}$. Using a SUL with a negative $K_{u\perp}$, increases the critical thickness at which Néel walls are formed.

In case of CoIr films this can extend to thicknesses above 100 nm. CoIr films with various content of Ir have been employed to test the spike noise and WATE and have confirmed significant suppression of these problems [7, 8].

In the present chapter, the physical microstructure and micromagnetic behaviour of $\text{Co}_{80}\text{Ir}_{20}$ film grown on a Ru seed layer are systematically investigated using transmission electron microscopy. The CoIr film with nominal composition of $\text{Co}_{80}\text{Ir}_{20}$ was chosen because it has a large negative anisotropy of $K_{u\perp} = -6.10^5 \text{ J/m}^3$, and a saturation magnetisation of $M_s = 0.94T$ (9400 G).

6.2 Physical microstructure of CoIr/Ru film

The negative-anisotropy CoIr film selected in our research has a composition of $\text{Co}_{80}\text{Ir}_{20}$. A 4 nm Ta layer was deposited first as a seed layer followed by a 5 nm Ru layer for texture nucleation. A $\text{Co}_{80}\text{Ir}_{20}$ layer with a thickness of 10 nm was grown on the Ru layer and then two 1 nm cap layers of Ru and Ta respectively were finally deposited on the top of the $\text{Co}_{80}\text{Ir}_{20}$ layer (Fig. 6.1). For TEM measurements, the film was grown on a Si_3N_4 membrane window supported on a bulk Si substrate (see chapter 2, section 2.2). The deposition was performed using C3010-P7 UHV disk sputtering system at the Department of Electronic Engineering, Tohoku University (Japan).



Figure 6.1: Cross-section stacks of the multilayer film system used in the research.

6.2.1 Crystal structure

The crystal structure of the film was determined by means of selected area electron diffraction (SAED) in the TEM. Fig. 6.2(a) illustrates the SAED patterns of plan-view specimen. The uniform circular diffraction rings obtained from the un-tilted specimen

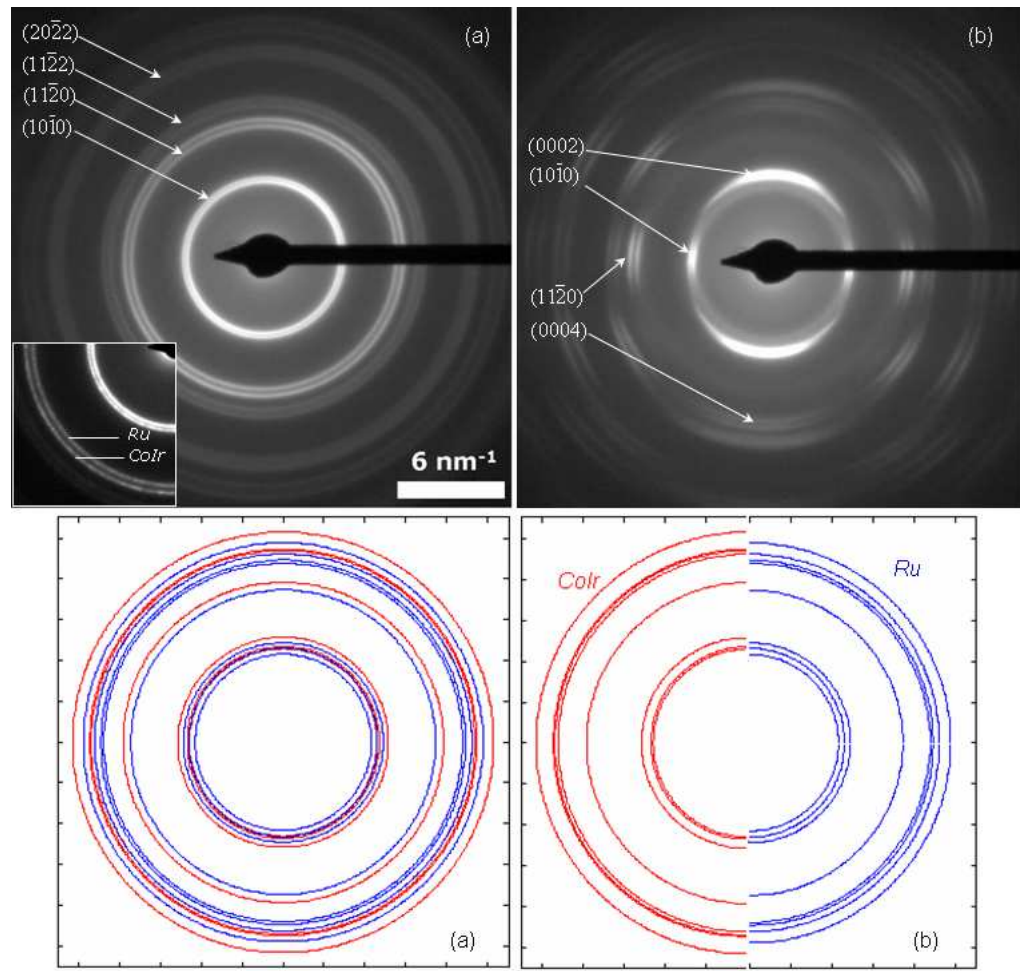


Figure 6.2: SAED patterns of plane-view specimen: (a) un-tilted sample (beam normal to the film) and (b) 30° tilted sample. The inset shows a doublet ring resulted from two crystals. Frames (c,d) shows calculated diffraction rings of CoIr (red rings) and Ru (blue rings) layers (a).

indicate that the film is polycrystalline. Double-ring patterns, highlighted in the inset of Fig. 6.2(a)) confirm that the film consists of two crystal systems with the same symmetry.

It is also seen from Fig. 6.2(b) that the diffraction pattern changes significantly when the specimen is tilted (in this case 30°). By tilting the specimen, the diffraction rings are broken into arcs and the intensity of some rings is either enhanced or reduced. This indicates that the crystallites in the film are not randomly distributed in 3D instead there is a preferred orientation of the crystallites, or texture.

The CoIr is a Co-based alloy [9] which has the *hcp* structure, based on the primitive hexagonal lattice and falling in the $P6_3/mmc$ space group. Our results (Figs. 6.2 and 6.3) indicate that the SAED patterns from the film are well indexed with the hexagonal structure. The structure factors for the *hcp* crystals satisfy [10]:

Table 6.1: Comparison of magnetic characteristics of the $\text{Co}_{80}\text{Ir}_{20}$ film with other magnetic thin films for SUL.

$h + 2k$	l	$ F ^2$
$3m$	<i>odd</i>	0
$3m$	<i>even</i>	$4f^2$
$3m \pm 1$	<i>odd</i>	$3f^2$
$3m \pm 1$	<i>even</i>	f^2

here, h , k , l are Miller indexes, f is scattering factor, and m is the integer number. The lattice spacing for a hexagonal crystal in reciprocal space is given by [10]:

$$d_{hkl}^{-1} = \sqrt{\frac{4}{3a^2}(h^2 + k^2 + hk) + \frac{l^2}{c^2}} \quad (6.3)$$

with, a , c being the lattice constants of the crystal structure. In transmission electron diffraction, because the wavelength of the electron wave is much smaller than the

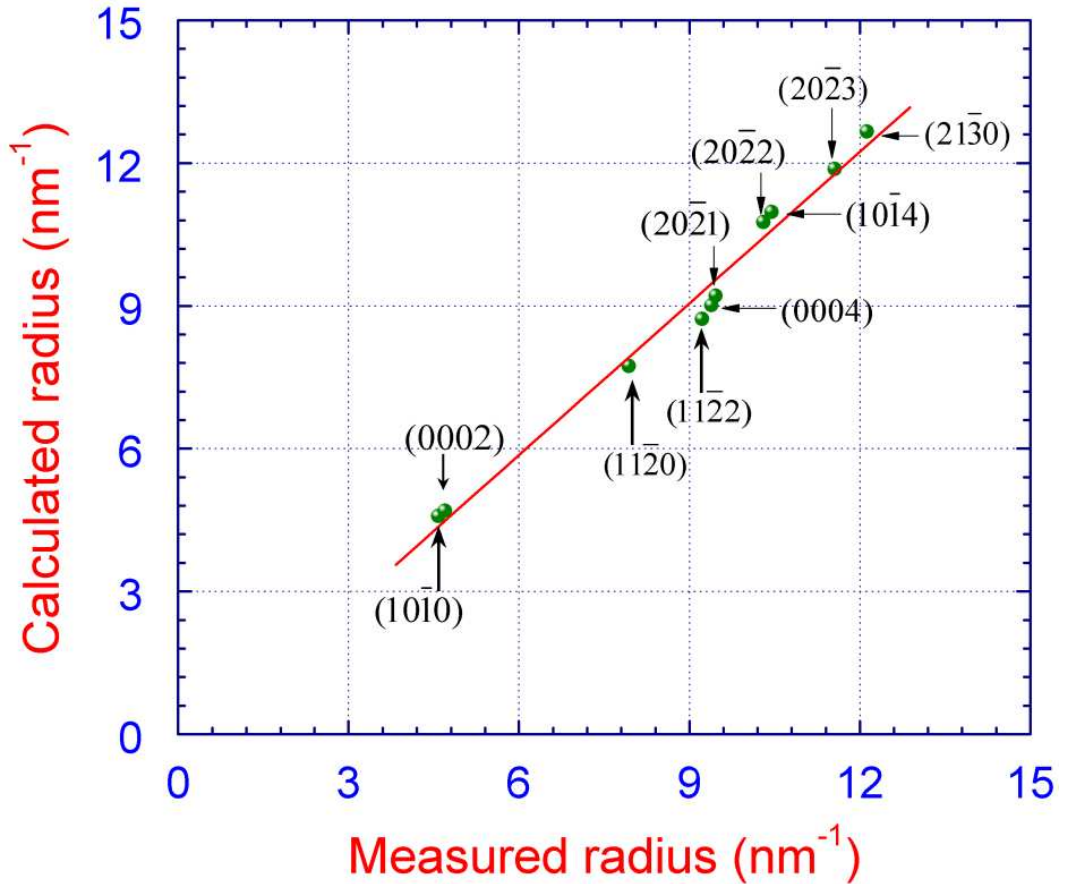


Figure 6.3: Indexing the diffraction rings from SAED patterns for outer rings system (CoIr).

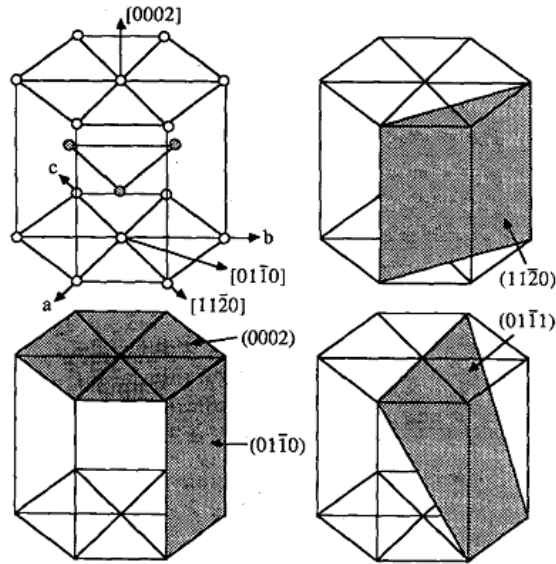


Figure 6.4: Crystallography plane of hexagonal crystal structure [11].

lattice spacing of the crystal planes, the planes which diffract are nearly perpendicular to the plane of the film. So, the planes which appear on a SAED pattern in order of increasing d-spacing are $(10\bar{1}0)$, (0002) , $(10\bar{1}1)$, $(11\bar{2}0)$, $(11\bar{2}2)$, (0004) , $(20\bar{2}1)$, $(20\bar{2}2)$, $(10\bar{1}4)$, $(11\bar{2}0)$, $(20\bar{2}3)$, $(21\bar{3}0)$, etc. HRTEM of a cross-section of this sample (shown in next section) confirmed that the (0002) planes are parallel to the film plane, resulting in a disappearance of the diffraction ring of the (0002) plane in un-tilted diffraction pattern of plan-view specimen [11]. It is also seen that the diffraction spot of the (0002) planes is visible in the SAED pattern of the cross-sectional specimen in which the electron beam is parallel to the film plane or perpendicular to the (0002) planes (see Fig. 6.8). This allows indexing the SAED patterns of the sample and confirms that the sample consists two hexagonal films (CoIr and Ru). The lattice constants are $a = 0.252 \pm 0.008$ nm, $c = 0.426 \pm 0.013$ nm for CoIr (which is consistent with the results in [9] with $a = 0.2585$ nm, and $c = 0.4175$ nm); and $a = 0.268 \pm 0.008$ nm, $c = 0.434 \pm 0.013$ nm for Ru crystal - ($a = 0.270$ nm, $c = 0.428$ nm [12]). It is noted that the error in the lattice constant values was evaluated from the error of the least square fitting algorithm used in indexing the rings.

6.2.2 Plan view grain structure

Bright-field and dark-field imaging (see section 3.3.3, chapter 3) are used to analyse the grain size distribution of the film. DF images are useful in determining useful aspects

Chapter 6: Microstructure and magnetisation reversals...

of the physical structure, e.g., about planar defects, stacking faults or particle size. Firstly DF images were used to determine the distribution of the grain size in the film. For this purpose, an $(10\bar{1}0)$ dark field image was recorded (Fig. 6.5(a)). A threshold image is generated by selecting the limits of minimum and maximum grey-levels to calculate grain size automatically (Fig. 6.5(b)). As a result, over 2000 measurements of the grain diameter are made using the particle sizing feature in the imaging software package Digital Micrograph and the distribution of the grain size is determined and shown in (Fig. 6.5(c)).

The mean grain size is determined to be 24.0 ± 4.2 nm, the grain size distribution is consistent with a log-normal function, which is commonly observed in sputtered films

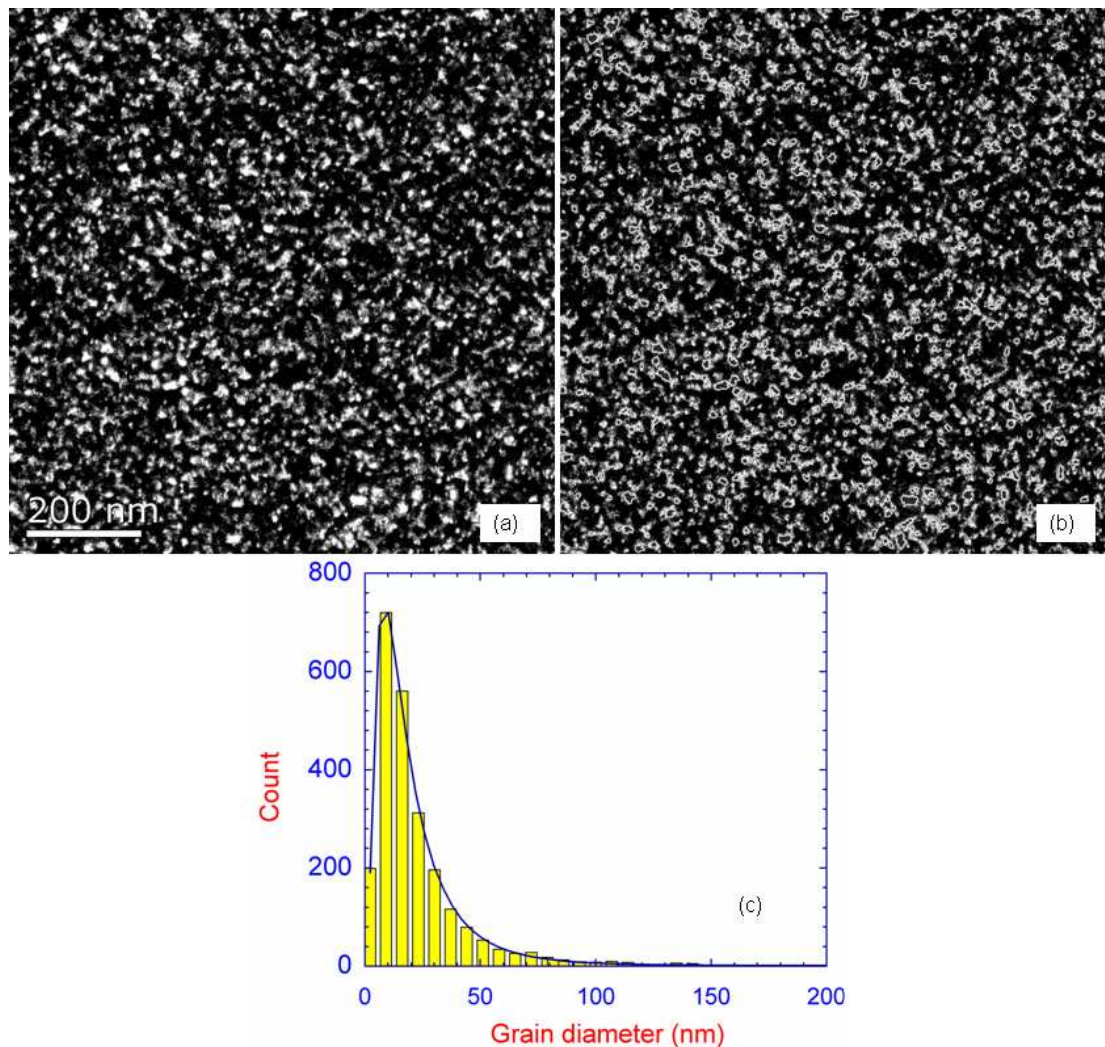


Figure 6.5: (a) A $(10\bar{1}0)$ dark field image, (b) respect threshold image for counting the grains and (c) grain distribution of the plan-view film.

and written as a probability function [13]:

$$P(D) = \frac{1}{\sqrt{2\pi}\sigma D} \exp\left[-\frac{(\ln(D) - \mu)^2}{2\sigma^2}\right] \quad (6.4)$$

where D is the grain size, μ is the mean value of $\ln(D)$, and σ is the standard deviation of $\ln(D)$. The grain size has a peak value of 15.7 ± 1.1 nm with a standard deviation of 2.0 nm. The narrow distribution of grains confirms homogeneity of nano-grains existing in the film.

High-magnification TEM micrographs (Fig. 6.6(a)) reveal a system of Moiré fringes located in the film, confirming two crystalline layers overlapping together (Fig. 6.6(b)). Quantitative analysis shows that the overlap of *hcp*-CoIr and Ru results in the formation of the Moiré fringes in TEM images. The spacing of the Moiré fringes is determined by measuring the intensity distribution on the image using DM software. The average width of Moiré fringes is 2.40 ± 0.07 nm. If the lattice spacings are d_1 and d_2 , the spacing of the fringes is given by the relation [10]:

$$\Delta D = \frac{d_1 \cdot d_2}{|d_1 - d_2|} \quad (6.5)$$

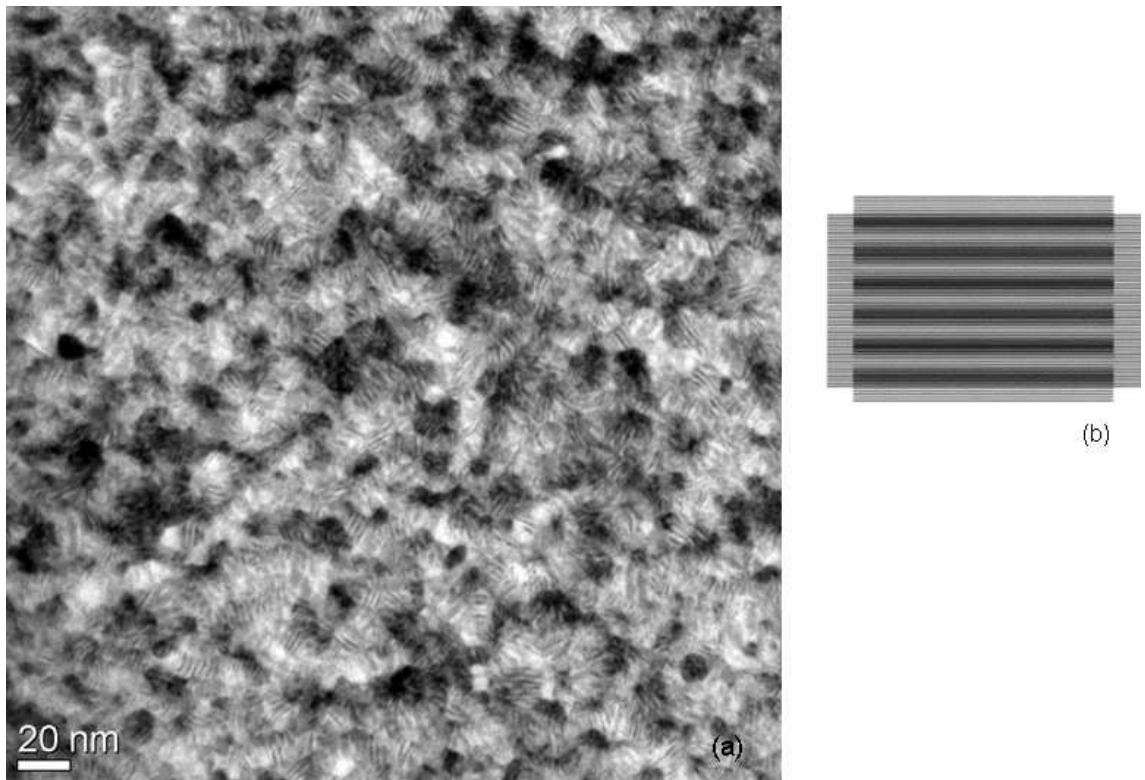


Figure 6.6: (a) Plan-view bright-field TEM micrograph reveal nanostructure of the film and a system of Moiré fringes and (b) mechanism of Moiré fringes formation [10].

Using the ratio $d_2/d_1 = 1.05$ (from diffraction patterns in previous section), the values of d_1 and d_2 are 0.136 ± 0.007 nm and 0.122 ± 0.006 nm. Indexing the diffraction pattern (section 6.2.1) indicates that these values belong to the $(11\bar{2}0)$ planes. This suggests that the planes $(11\bar{2}0)$ are perpendicular to the film plane (Fig. 6.4).

6.2.3 Cross-sectional microstructure

TEM cross-sectional imaging provides useful information about layer structure as well as the interface between the layers. From a multilayer film on a membrane, cross-section specimens are prepared using conventional mechanical process followed by low energy Ar ion milling (see Fig. 6.7). The membrane substrates are firstly cleaved into two halves and ground until both pieces are the same length and width (Fig. 6.7(a)). The $500 \mu\text{m}$ thick pieces are then placed onto a glass slide and thinned to $200 \mu\text{m}$ using

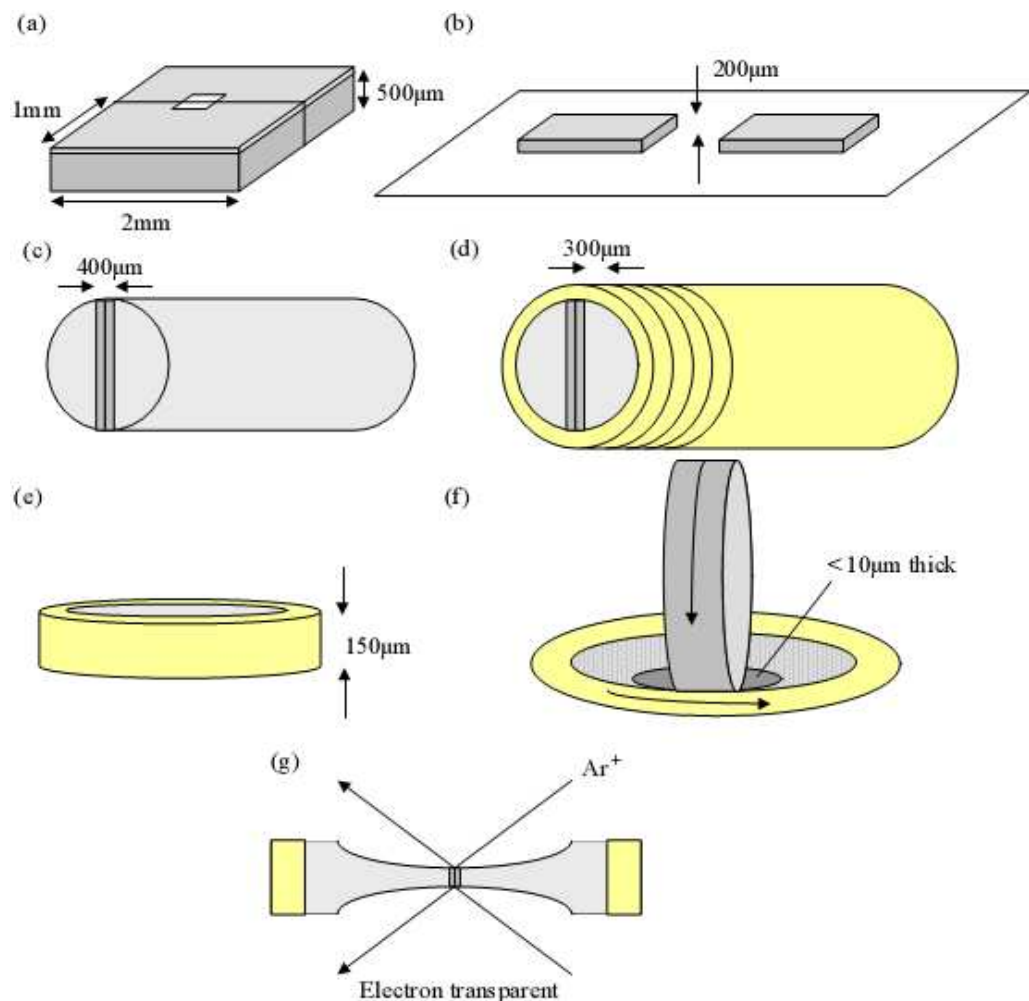


Figure 6.7: Schematic of TEM cross-section sample preparation by conventional method (from Craig Brownlie PhD thesis [14]): (a-e): mechanical process to obtain thin 3 mm discs, (f) mechanical polishing, (g) ion milling to obtained thin-foil specimen.

Chapter 6: Microstructure and magnetisation reversals...

a hand grinder (Fig. 6.7(b)) before being glued face-to-face with an epoxy resin and held together in a slot cut from a molybdenum rod (Fig. 6.7(c)). This assembly is then coated in epoxy, slid into a brass tube and cured at 130°C to set the glue. The $300\ \mu\text{m}$ thick discs are cut from the tube and ground on both sides until a total thickness of $150\ \mu\text{m}$ is achieved (Fig. 6.7(d-e)). The specimen is continuously polished to reach electron transparency by a dimple grinder (Fig. 6.7(f)) and a precision ion polishing system (PIPS) (Fig. 6.7(f)). Finally, a thin specimen is obtained using a gentle ion milling system. Details of the process may be found in ref. [14]. The process was performed by a technician, Mr Brian Miller, in Department of Physics and Astronomy,

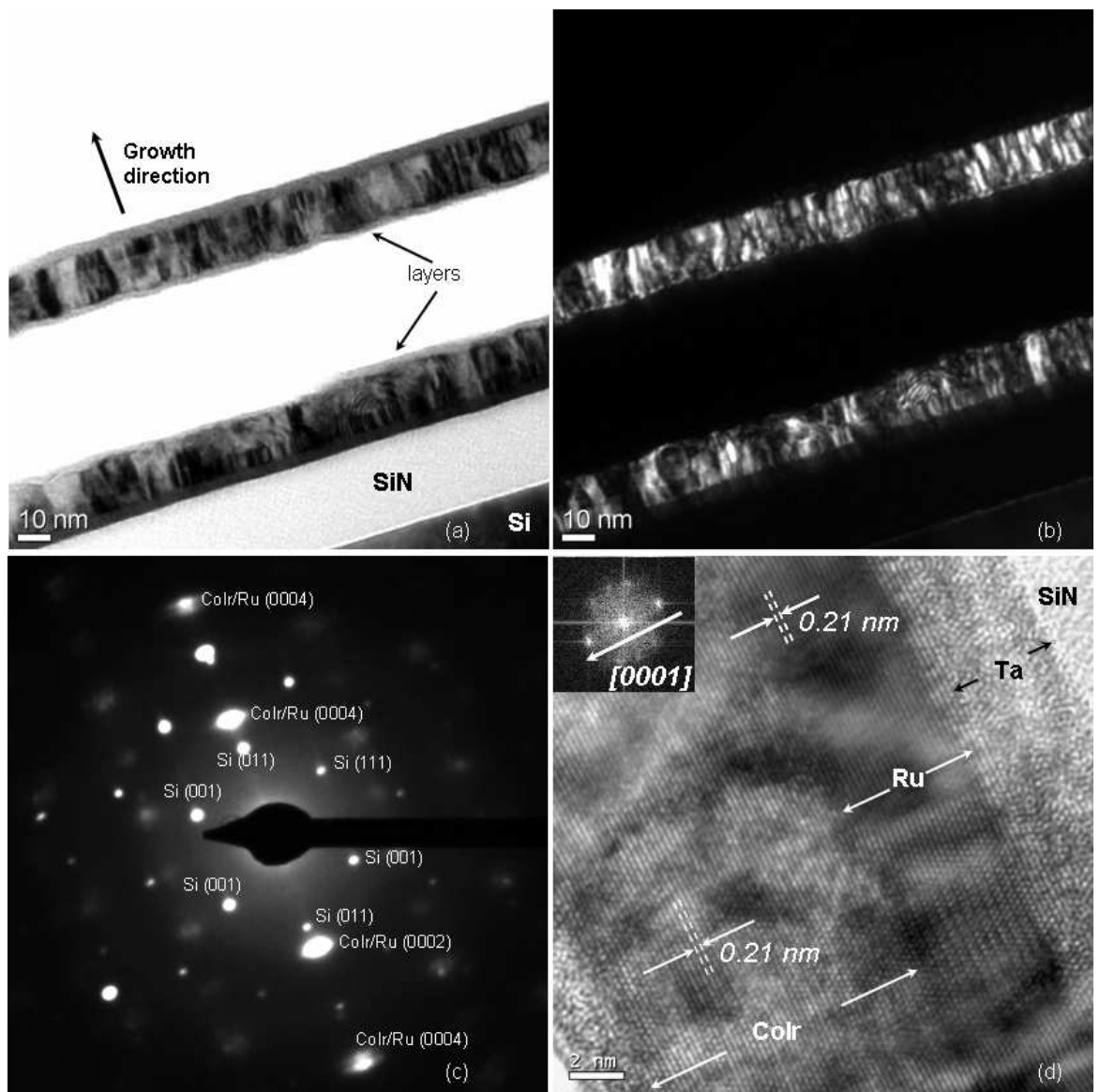


Figure 6.8: Bright-field (a), dark-field (b) TEM micrographs and SAED pattern (c) of two cross-sections of the CoIr/Ru film. Frame (d) shows HRTEM micrograph of cross-section. The inset shows Fourier transform of cross-sectional specimen.

University of Glasgow.

The cross-section TEM images (Figs. 6.8(a,b)) reveal that grains in the film were grown perpendicularly to the film plane. From HRTEM images (Fig. 6.8(d)), the contrast from lattice fringes of crystalline layers (CoIr and Ru), which are parallel to the film plane, are visible whereas no lattice fringes are observed in Ta layer confirming the buffer layer Ta is amorphous. It is possible to see the crystal plane of CoIr/Ru layers parallel to the film plane. A Fourier transform (inset of Fig. 6.8(b)) displays the diffractogram of [0001]-oriented of hexagonal crystal in which the [0001] direction is normal to the film plane. This means that the (0002) planes of the hexagonal layers are parallel to the film plane. Confirmation of the (0002) planes parallel to the film plane is also supported by the SAED pattern of the cross-section (Fig. 6.8(c)) with the appearance of the spots of the (0002) and (0004) planes on diffraction spots from single crystal Si, and a weak diffused patterns of the Ta, SiN amorphous layers.

From the HRTEM image (Fig. 6.8(d)), the CoIr-Ru interface is also revealed. It is apparent that a very sharp and smooth interface between Ru and CoIr layers is visible. This is due to the excellent deposition process. First of all, the hcp-Ru layer is grown on the Ta buffer layer with very slow rate induced by ultra-high vacuum DC sputtering. With the similar hcp structure, the Ru layer acts as a nucleation layer for the CoIr layer to be grown.

6.2.4 Texture determination

In section 6.2.1, the film was confirmed to be textured. From Moiré fringes in the bright-field image (Fig. 6.6), the d-spacing ($d_{CoIr} = 0.136 \pm 0.007 \text{ nm}$) belongs to the $(11\bar{2}0)$ planes, which contain the [0001] direction, and are perpendicular to the film plane. As the (0002) planes were found to be parallel to the film plane, these results suggest that there is a [0001] texture existing in the film, and the texture direction is normal to the film plane. For the zero order Laue zone (ZOLZ), the electron beam direction $[uvw]$ and the allowed Bragg reflection (hkl) satisfy the Weiss zone law [10]:

$$hu + kv + lw = 0 \tag{6.6}$$

Chapter 6: Microstructure and magnetisation reversals...

It is noted that in a hexagonal structure, the plane index with three Miller indexes (hkl) is written as four numbers (hkil) with $i = -(h+k)$, so, the $[uvw]$ can be re-written in a similar four number form $[uvyw]$ with $y = -(u+v)$. Assuming the beam is incident along $[0001]$ direction, the planes which satisfy the equation 6.6 are the set $(10\bar{1}0)$, $(10\bar{1}1)$, $(11\bar{2}0)$, etc. Hence, if the sample is textured along the $[0001]$ direction, the diffraction rings from these planes will be visible from un-tilted SAED pattern. Furthermore, examining the diffraction pattern of the cross-sectional specimen (Fig. 6.8(c)), the beam in this case will be incident along the $[11\bar{2}0]$ direction, therefore, only (0002) planes satisfy the equation 6.6 and indeed, only diffraction ring of the (0002) planes appear on the SAED pattern. This evidence confirms that the sample is highly textured along the $[0001]$ direction, which is normal to the plane of the film.

Further evidence of texture in the sample is found in Fig. 6.9. As a result of the $[0001]$ -texture, the (0002) planes are perpendicular to the beam when the sample is un-tilted, therefore they do not appear in the diffraction pattern. Whereas, other planes e.g. $(10\bar{1}0)$, $(10\bar{1}1)$, $(11\bar{2}0)$ are nearly parallel to the beam (Fig. 6.9(a)), and as a result, their diffraction rings appear in the SAED pattern (Fig. 6.9(c)). When the sample is

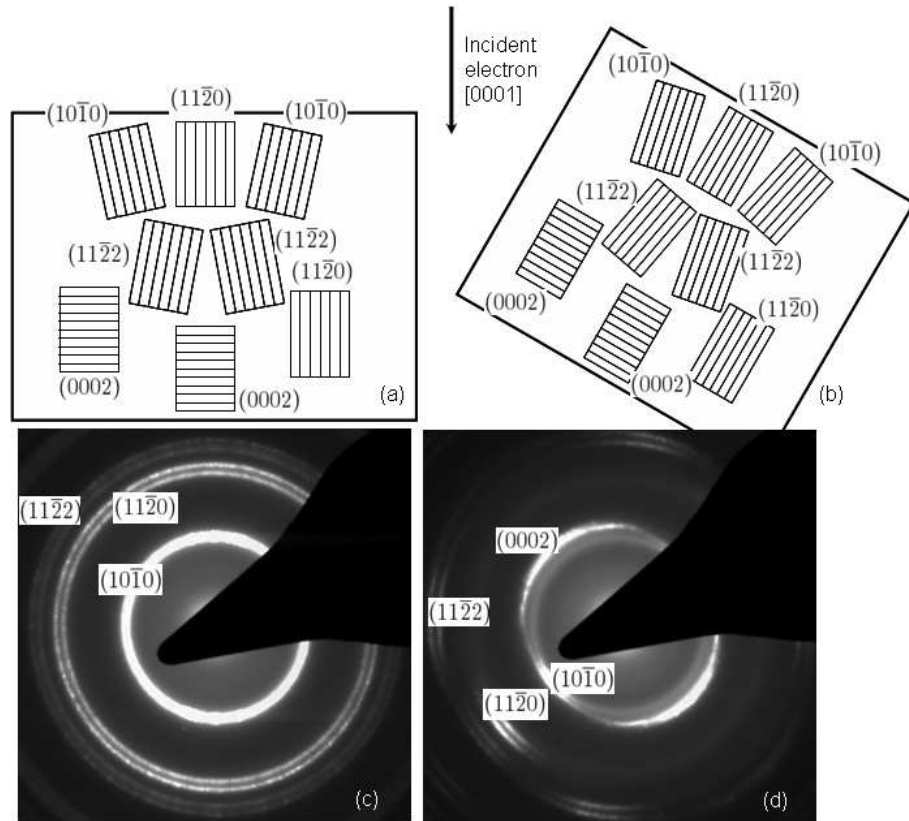


Figure 6.9: Schematic of SAED pattern formation in textured sample with un-tilted sample (a), 30° tilted sample (b) and correspondent SAED patterns (c,d).

tilted, the (0002) planes are not perpendicular to the beam (Fig. 6.9(b)), and their diffraction ring do appear in the SAED pattern (Fig. 6.9(d)).

6.3 Micromagnetic behaviour

As mentioned in section 6.1, the CoIr film in the present work has a negative anisotropy ($K_{u\perp} = -6.10^5 \text{ J/m}^3$), and a saturation magnetisation of $M_s = 9400 \text{ G}$, which was determined from magnetometry on a bulk sample. The aim of this section is to provide an understanding of the micromagnetic behaviour of the CoIr film. In order to understand the micromagnetic structure and magnetisation reversal processes of the film, the Fresnel mode of Lorentz microscopy was employed for magnetic imaging. In-situ measurements were carried out by applying a magnetic field using the objective lens in the TEM. The magnetising experiments involved easy and hard axis field application using a tilt rotate rod in the TEM. In-plane field were applied up to 100 Oe to a nearly saturated state, then the reversal process was recorded by varying the field from maximum positive field to negative field to observe the hysteretic behaviour.

6.3.1 Reversal process on easy axis

Fig. 6.10 shows a hysteresis sequence of Fresnel images of the sample along the easy axis in a magnetic field ranging from $+100 \text{ Oe}$ to -100 Oe . In each frame, the inset shows the fast Fourier transform image (FFT) from which the degree of dispersion of the ripple can be determined. The ripple effect is seen as the fine scale contrast present in the image. Although the ripple contrast is present the magnetisation is generally uniform apart from this. However, the Fresnel contrast from the dispersion allows the average diversion of the magnetisation to be measured. As discussed in chapter 3 (section 3.4.2), the magnetisation ripple is the small wavelike fluctuations of the magnetisation direction that occurs in thin ferromagnetic films. It originates from random orientation of local anisotropy of each crystallite.

Initially the film is magnetised parallel to the easy axis in an applied field of $+100 \text{ Oe}$ to a nearly saturated state. Magnetisation ripple contrast can be observed which is perpendicular to direction of the magnetisation. When the field is relaxed to zero (remanent state), it can be seen from Fig. 6.10 that whilst the dispersion of the ripple

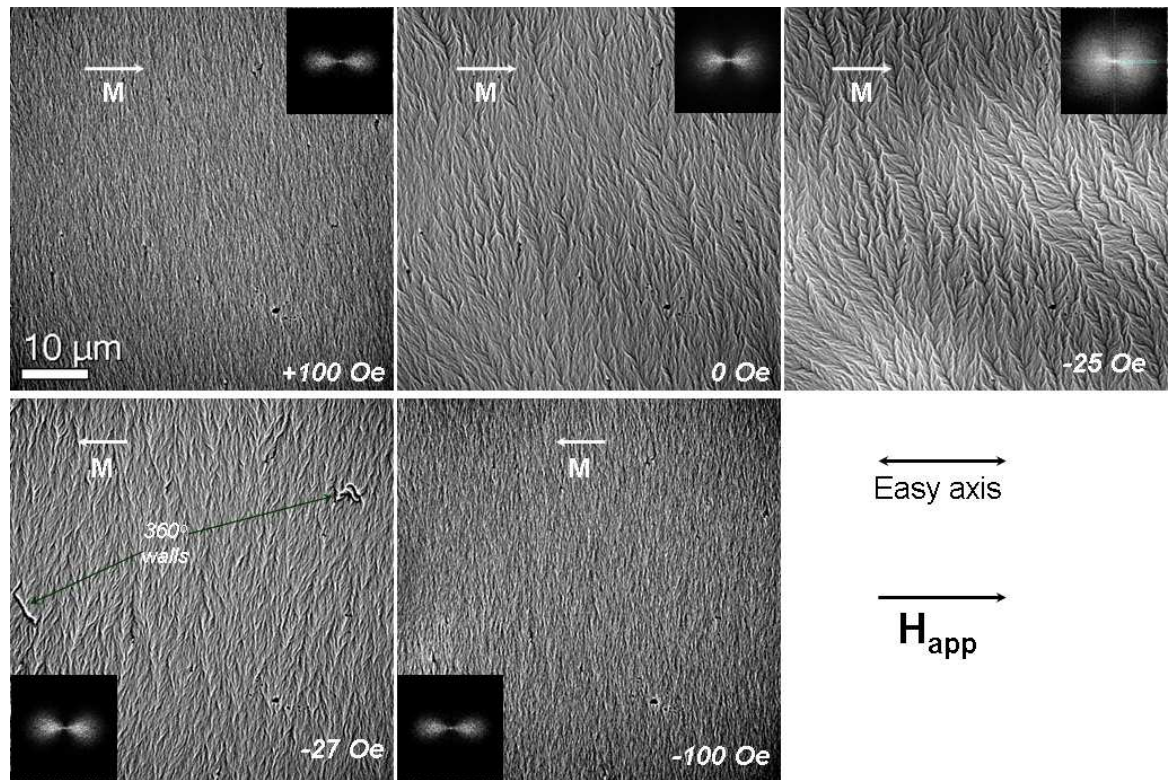


Figure 6.10: Fresnel images in a hysteresis sequence on the easy axis in plane of the film. The insets show the Fourier transform of Fresnel images.

is increased, the magnetisation still remains predominantly parallel to the easy axis. Further increase in the dispersion of the magnetisation is observed when the field is reversed up to a value of -25 Oe. A very small change of magnetic field to -27 Oe leads to a considerable reduction of the ripple dispersion. The reason for this reduction is that a domain wall was seen to rapidly sweep through the film effecting reversal leaving a nearly uniform but oppositely directed magnetisation. The switching field was therefore measured to be 27 Oe for this film. Further field application indicated that the return path is entirely consistent with the outward demagnetisation path. A mean switching field of 27 ± 2 Oe is measured for this process and a hysteresis loop which is quite square in shape is deduced.

It can be concluded that the reversal mechanism along the nominal easy axis is essentially governed by the nucleation and movement of domain walls. The magnetic moments align along the easy axis, and it is expected that the reversal was initialised by nucleating a reversed domain with an associated domain wall sweep through the film. This wall swept so quickly that the CCD camera could not capture, instead it was only visible as a sudden movement on the viewing screen of the microscope.

6.3.2 Reversal process on hard axis

A sequence of Fresnel images during the reversal cycle along the hard axis of the film is displayed in Fig. 6.11. Uniform magnetisation with a small dispersion of the ripple is again observed at the maximum applied field +100 Oe.

The reversal along the hard axis progresses initially with a large amount of dispersion present at 10 Oe, the dispersion is noted to be non-uniform. At 0 Oe the dispersion has further increased and some low angle domain walls are visible. As seen from Fig. 6.11 that the reversal process is started immediately on reducing the magnetic field. When the field is reduced from maximum field (+100 Oe) to the remanent state, low angle domain walls are formed in which the magnetisation in some domains is predominantly pointing along the easy axis, creating low-angle walls structure. Upon increasing the field in the negative direction, a complex structure of domain walls due to the non-coherent rotation of the magnetisation from easy axis to the hard axis is observed. A coercivity of around -18 Oe is estimated from this image sequence with maximum

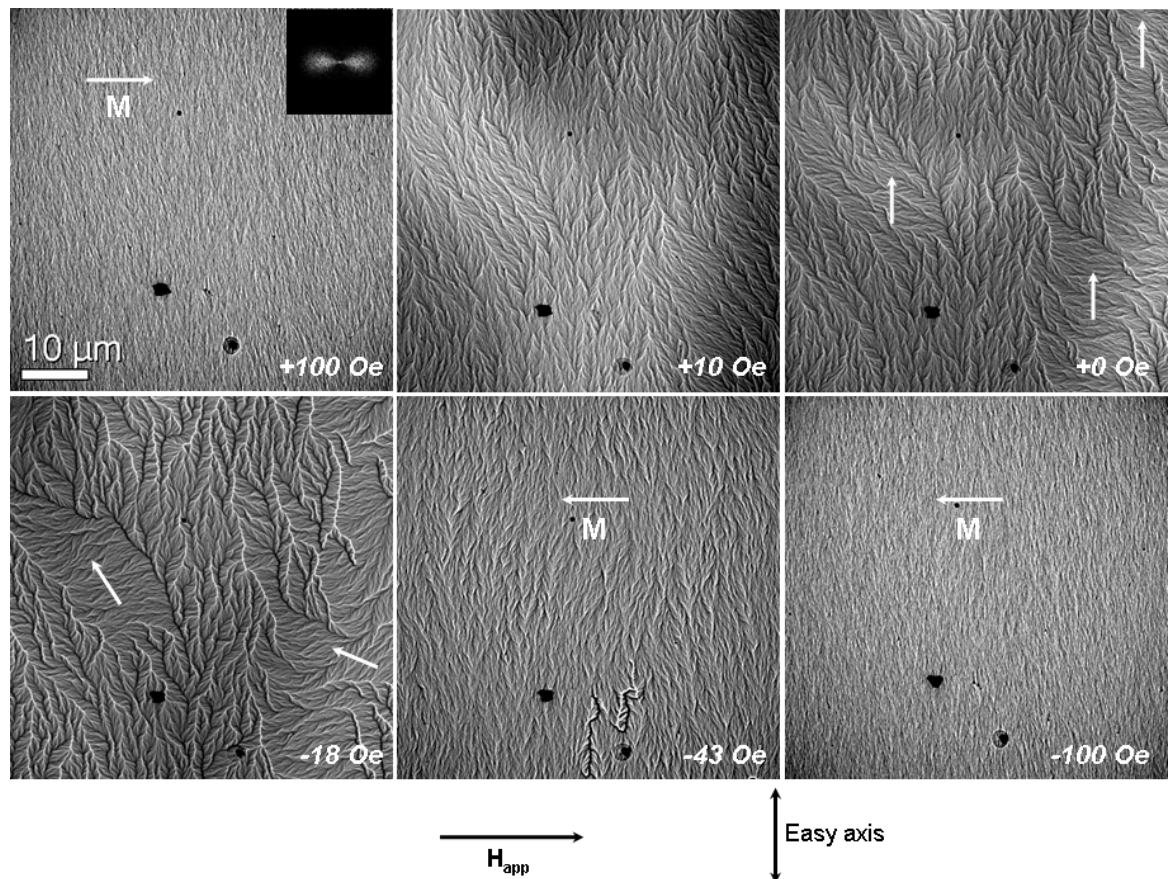


Figure 6.11: Fresnel images in a hysteresis sequence on the hard axis in plane of the film. The inset shows a Fourier transform of the Fresnel image at maximum applied field.

density of low-angle walls. Further rotation and domain wall displacement result in the film being magnetised along the hard direction (-43 Oe). Increasing the field further up to -100 Oe shows a decrease of the magnetisation dispersion.

It is apparent that the reversal process on the hard axis can be identified by gradual formation and movement of low-angle domain walls (Néel-type wall) in a decreasing field resulting from magnetisation rotation. This is clearly a different from reversal mechanism from the easy axis where the wall was nucleated and swept very quickly at a well defined field. The reversal mechanism in the hard axis case is essentially governed by the non-coherent rotation of the magnetisation. This is a little different from ‘classical’ hard-axis reversal that is commonly a coherent rotation to form uniform ripple spectrum or low-angle wall structure. When the field was relaxed to zero field, the magnetisation was relaxed to the easy axis direction by non-coherent rotation of the magnetic moments. Increasing the applied field to the opposite direction, the magnetic moments were rotated from the easy axis to the hard axis. The low-angle walls were formed during such a non-coherent rotation. The hard axis is also identified by a smaller coercivity (18 Oe) than for the easy axis, this state being identified by the maximum density of the walls.

From the hysteresis sequence measurements, it is important to note that the film exhibits typical soft magnetic properties with coercivities on the easy and hard axis of 26 Oe and 18 Oe, respectively.

6.3.3 Formation and suppression of 360° walls

The other notable observation of the reversal experiments is the presence of 360° walls, which occurred in the film during the reversal processes on both easy and hard axes (for example in Fig. 6.10 at -27 Oe and also in Fig. 6.11 at -43 Oe or Fig. 6.12(a)).

The formation of such a magnetic structure, which is energetically unfavourable, was considered to be a result of the singularities in 180° walls (Bloch or Néel lines), which are trapped at an inclusion in a magnetising axis [17]. For example point defects or layer roughness in multilayer films can be responsible for the presence of such walls which pin the movement of two 180° Néel walls and merges them into a single composite wall [18]. It should be noted that the formation of the 360° walls is on a small scale with respect to the continuous film and therefore would not shown up in bulk

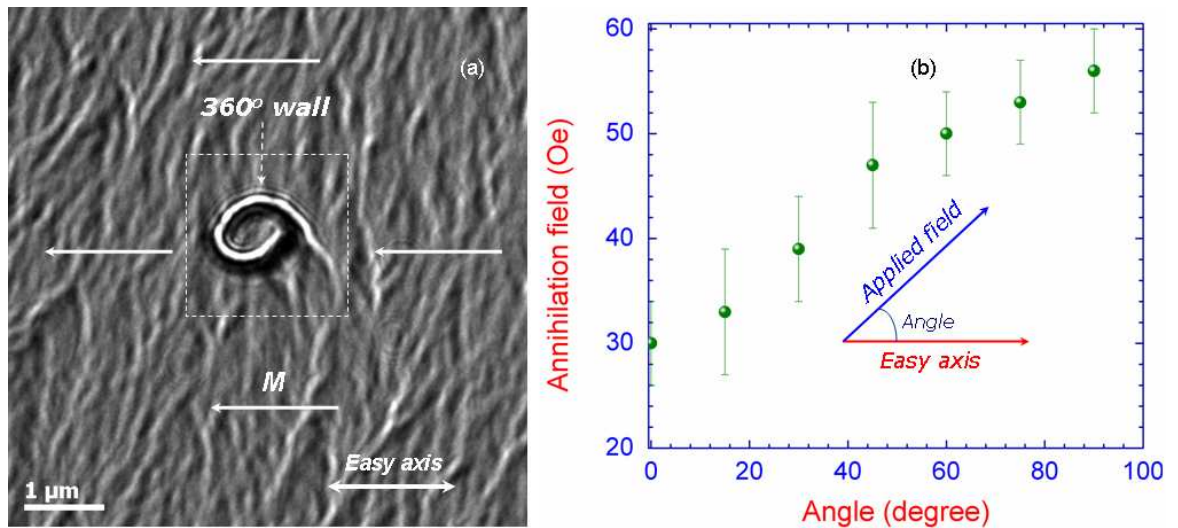


Figure 6.12: Fresnel image of CoIr film as magnetised on the easy axis at negative field of -28 Oe in which a 360° wall is observed (a) and the 360° walls annihilation field as a function of angle between applied field and the easy axis (b).

measurement e.g. magnetometry measurements.

The formation of energetically unfavourable 360° walls results in incomplete magnetisation reversal. These walls can only be removed in higher magnetic field and it was found that the magnetic field to annihilate the 360° walls, H_{an} , is dependent on the direction of the magnetic field or the angle between the magnetic field and the easy axis, θ . Namely, H_{an} is minimum when magnetising on the easy axis ($\theta = 0$, $H_{an} = 30$ Oe) and gradually increases as the direction of the field varies from easy axis to the hard axis (Fig. 6.12(b)). The field dependence for the removal of the 360° wall is similar to recent theoretical predictions [19] which suggest that the 360° wall can be stabilised by applying the field with respect to the easy axis of the film. When the field is applied in the direction along the magnetisation direction in the periphery of the 360° domain wall, then the wall is further stabilised as a sequence of the topology of the magnetisation in the film. In this situation, a critical field strength is required to break the wall up. The strength of this field is independent on the direction of the magnetisation in the periphery of the wall, which may relate to the direction of the applied field.

6.4 Magnetic ripple characterisation

In the previous section, it was seen that much of the contrast in the Fresnel images is due to the magnetic ripple. Interpreting the information from the magnetic ripple of the Fresnel image is helpful to understand the micromagnetic behaviour of the film.

As mentioned above, in a Fresnel image of a polycrystalline magnetic thin film, the contrast of wave-like magnetic ripple is visible. The magnetic ripple can be characterised in terms of the mean wavelength and the mean angle of deviation of the local magnetisation. Principally, it is possible to measure the mean wavelength of the ripple manually. These can be measured by an analysis of the Lorentz images (in this case the Fresnel images) in Fourier space. In this section an analysis is made of the ripple wavelength and how its behaviour is consistent with the classical ripple theory [18, 20–23]. In order to do that, a Fresnel image with homogeneous ripple is firstly recorded. A fast Fourier transform image (FFT) of the Fresnel image is calculated (Fig. 6.13(b)), providing a qualitative aspect of the angular dispersion of the ripple. The mean wavelength value is measured from a line profile of the FFT image modulus (Fig. 6.13(c)) along the magnetisation direction (the axis of the triangle) as the distance between two peaks in the profile, this value can be converted into a real space number.

The dispersion of magnetic ripple varies during the magnetisation process and a typical result is depicted in Fig. 6.14. As discussed in the previous section, the reversal process in the easy axis reveals uniform ripple structure in the Fresnel images, therefore, it allows simple characterisation of the ripple spectrum. Fig. 6.14(a) shows the ripple wavelength as a function of magnetic field during the reversal process on the easy axis.

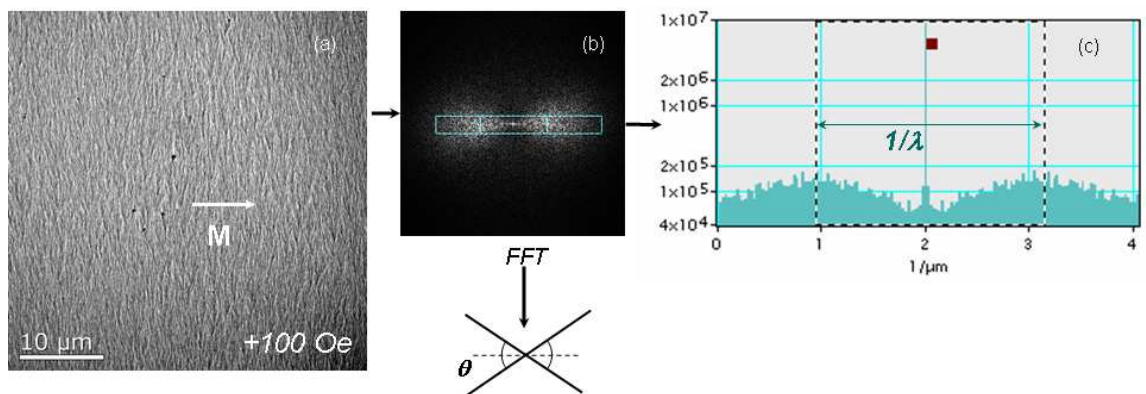


Figure 6.13: Calculation of ripple wavelength from Fresnel image using Fourier transform.

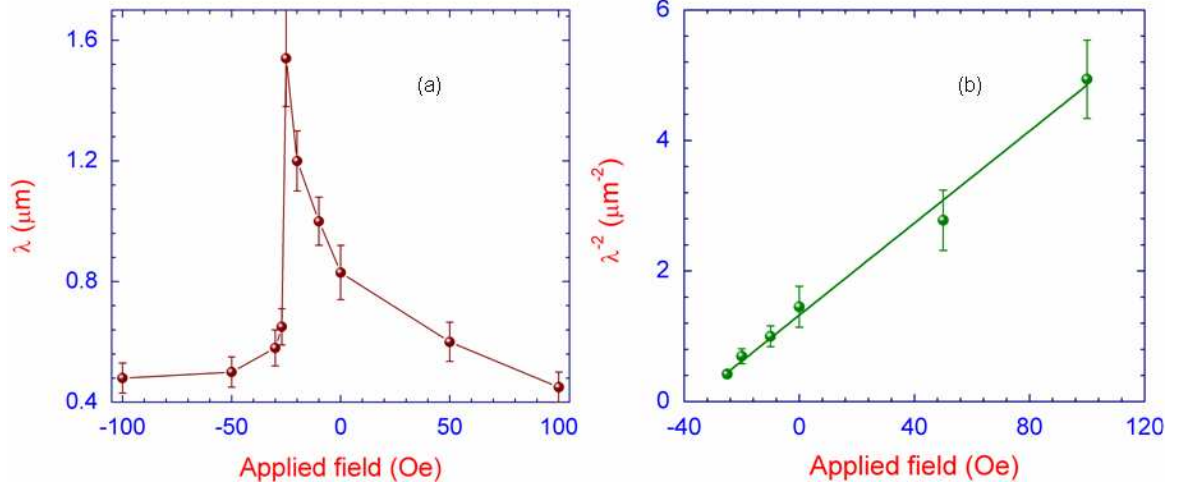


Figure 6.14: The magnetisation ripple wavelength, λ (a) and inverse wavelength square (λ^{-2}) (b) as the function of applied field during reversal process on the easy axis.

At the maximum applied field, the dispersion angle is minimised and the associated shortest wavelength of $\lambda = 0.45 \pm 0.05 \mu\text{m}$ is measured. When the field is relaxed to zero, the ripple shows increasing dispersion, with a wavelength of $\lambda = 0.83 \pm 0.09 \mu\text{m}$ at remanence. The maximum ripple wavelength, $\lambda = 1.54 \pm 0.13 \mu\text{m}$, is observed just before the switching field (-25 Oe). When the magnetisation has switched at -27 Oe, the wavelength dramatically decreases to a value of $\lambda = 0.65 \pm 0.06 \mu\text{m}$, and then further reduces when the film is magnetised close to saturation in opposite direction. According to the ripple theory [21, 22], the mean wavelength is expected to vary as a function of the applied field in the form:

$$\lambda(h) = 2\pi (A/K_u)^{1/2} (h + 1)^{-1/2} \quad (6.7)$$

where, K_u is the uniaxial anisotropy constant, and $h = H/H_k$ is the reduced magnetic field (H_k being the anisotropy field). The magnetic field dependence of ripple wavelength for the easy axis magnetisation process is in good agreement with the ripple theory as seen in 6.14(b). Note that the error of wavelength is essentially caused by the inhomogeneous ripple spectrum. On the other hand, from (6.7), it allows the anisotropy field H_k to be determined from the gradient of the linear dependence:

$$\lambda(h)^{-2} = \left(2\pi (A/K_u)^{1/2}\right)^{-2} \left(\frac{H}{H_k} + 1\right) \quad (6.8)$$

Using this equation (6.8) (Fig. 6.14(b)), an anisotropic field of $H_k = 40 \pm 3 \text{ Oe}$ is obtained from calculation of the gradient and intercept of the linear plot. This value

is consistent with the one deduced from in-situ measurements (43 ± 2 Oe) on the hard axis at which the reversal process was almost completed and tended to saturation state (see Fig. 6.12, -43 Oe frame).

6.5 Discussions

The $\text{Co}_{80}\text{Ir}_{20}/\text{Ru}$ film studied here was found to have a hexagonal structure with highly-textured orientation [0001] normal to the film plane, which is expected to induce a perpendicular negative anisotropy. The perpendicular negative anisotropy is one of the main features required to suppress the WATE and spike noise by forming Néel-type wall even in thicker films. The character of the magnetisation reversal on the easy axis is similar to other soft magnetic thin films e.g. NiFe/CoFe [18] however a complex hard-axis reversal due to non-coherent rotation of the magnetic moments is a characteristic micromagnetic behaviour of the studied film. This micromagnetic characteristic is the formation of Néel-type domain wall even in thicker films [7], rather than Bloch-type walls as seen in conventional SULs. The 27 Oe coercive field in this case is larger than that of NiFe [4, 24], or CoFeNiB [25] but less than other magnetic thin films for soft underlayer e.g. FeCoC [26], or other CoIr film [27]. However, the anisotropy field, H_k , of the studied CoIr film here is higher than other typical soft underlayers [4] e.g. CoTaZr (20 Oe), CoNiZr (25 Oe), $\text{Ni}_{81}\text{Fe}_{19}$ (5 Oe), FeCoN (20 Oe), FeAlSi (15 Oe), etc. The higher anisotropy field gives a better signal - noise ratio (SNR) as revealed in another study [28]. A comparison of the magnetic characteristics of the $\text{Co}_{80}\text{Ir}_{20}$ film with other SULs can be summarised in Tab. 6.2. Magnetisation reversal of the studied $\text{Co}_{80}\text{Ir}_{20}$ film on the hard axis is similar to other SULs that the reversal

Table 6.2: Comparison of magnetic characteristics of the $\text{Co}_{80}\text{Ir}_{20}$ film with other magnetic thin films for SUL.

Materials	$B_s(T)$	H_c (Oe)	H_k (Oe)	Ref.
CoTaZr	1.4	-	20	[4]
CoNiZr	1.2	-	25	[4]
$\text{Ni}_{81}\text{Fe}_{19}$	1.0	1-5	5	[3]
FeAlN	2.0	-	15	[3]
CoFeC	1.5	100	-	[26]
$\text{Fe}_{65}\text{Co}_{35}$	2.4	12	100	[3]
$\text{Co}_{83}\text{Ir}_{17}$	1.1	100	-	[27]
$\text{Co}_{80}\text{Ir}_{20}$	1.34	25-27	40	this study

is essentially governed by the nucleation and movement of the domain walls due to the rotation of the magnetic moments from easy axis to the hard axis [27,29]. However, the reversal on the hard axis of the other conventional SULs was normally observed with the formation of the micrometer size domains due to coherent rotation of the magnetic moments [29], and a uniform reversal was established. In the studied $\text{Co}_{80}\text{Ir}_{20}$ film, complex magnetisation reversal due to incoherent rotation of the magnetic moments is observed that should be an identical feature of the film. Such an incoherent rotation causes a non-uniform reversal, and formation of some special magnetic structures at nanoscale e.g. tiny domains, or 360° walls. Further experimental observation combined with micromagnetic simulation should be carried out to understand the origin of the incoherent rotation and non-uniform reversal on the hard axis.

6.6 Summary

In this chapter, an investigation of physical microstructure and magnetic structure of CoIr with soft magnetic properties has been carried out. Diffraction analysis confirms the existence of a strongly [0001]-oriented texture normal to the film plane with polycrystalline hexagonal CoIr/Ru layers. The crystal structure of the film was determined from diffraction patterns and is consistent with previous measurements on bulk alloys: $a = 0.252 \pm 0.008$ nm, $c = 0.426 \pm 0.013$ nm for CoIr; and $a = 0.268 \pm 0.008$ nm, $c = 0.434 \pm 0.013$ nm for Ru. The film showed uniaxial anisotropic behaviour with nucleation of domain walls on the easy axis and non-coherent rotation yielding formation of low-angle walls in reduced field on the hard axis. The magnetisation reversal of the film is identified by a complex reversal on the hard axis due to incoherent rotation of the magnetisation. Moreover, the formation of 360° walls is observed in the reversal process, which suggests the presence of local defects and/or layer roughness. The dispersion of magnetisation ripple on the Fresnel images is consistent with classical ripple theory, allowing the anisotropy field to be determined and shown to be 40 Oe which suggests that the film is a good candidate for a SULs with small critical bit size limit (estimated down to 25 nm).

Bibliography

- [1] A. Moser, K. Takano, D. T. Margulies, M. Albrecht, Y. Sonobe, Y. Ikeda, S. Sun, E. E. Fullerton, *J. Phys. D: Appl. Phys.* **35** (2002) R157-R167.
- [2] D. Litvinov, R. M. Chomko, L. Abelmann, K. Ramstöck, G. Chen, S. Khizroev, *IEEE Trans. Magn.* **36** (2000) 2483-2485.
- [3] D. Litvinov, M. H. Kryder, S. Khizroev, *J. Magn. Magn. Mater.* **232** (2001) 84-90.
- [4] S. N. Piramanayagam, *J. Appl. Phys.* **102** (2007) 011301.
- [5] K. Tanahashi, A. Kikukwa, N. Shimizu, Y. Hosoe, *J. Appl. Phys.* **91** (2002) 8049.
- [6] B. R. Acharya, J. N. Zhou, M. Zheng, G. Choe, E. N. Abarra, K. E. Johnson, *IEEE Trans. Magn.* **40** (2004) 2383.
- [7] Hashimoto, S. Saito, M. Takahashi, *J. Appl. Phys.* **99** (2006) 08Q907.
- [8] M. Takahashi, S. Saito, *J. Magn. Magn. Mater.* **320** (2008) 2868-2873.
- [9] K. H. J. Buschow, P. G. van Engen, R. Jongebreur, *J. Magn. Magn. Mater.* **38** (1983) 1.
- [10] M. De Graef, *Introduction to conventional transmission electron microscopy*, Cambridge University Press, 2003, ISBN-10: 0521629950.
- [11] D.E. Laughlin, B.Y. Wong, *IEEE Trans. Magn.* **27** (1991) 4713.
- [12] David R. Lide, *CRC Handbook of Chemistry and Physics*, 83rd ed., ISBN-10: 0849304830.
- [13] D.T. Carpenter, J.M. Rickman, K.Barmak, *J. Appl. Phys.* **84** (1998) 5843.

Chapter 6: Microstructure and magnetisation reversals...

- [14] C. Brownlie, *A TEM Investigation of Controlled Magnetic Behaviour in Thin Ferromagnetic Films*, PhD thesis, University of Glasgow, 2007.
- [15] L.Reimer, *Transmission Electron Microscopy: Physics of Image Formation and Microanalysis* (Springer Series in Optical Sciences), Springer; 4th edition (May 16, 1997), ISBN-10: 3540625682.
- [16] S. J. LLoyd, J. C. Joudon, P. A. Midgley, *J. Micros.* **207** (2002) 118-128.
- [17] M. Hehn, D. Lacour, F. Montaigne, J. Briones, R. Belkhou, S. El Moussaoui, F. Maccherozzi, N. Rougemaille, *Appl. Phys. Lett.* **92** (2008) 072501.
- [18] C. R. Craig, S. McVitie, J. N. Chapman, A. B. Johnston, and D. O. O'Donnell, *J. Appl. Phys.* **100** (2006) 053915.
- [19] C. B. Muratov, V. V. Osipov, *J. Appl. Phys.* **104** (2008) 053908.
- [20] M. F. Gillies, J. N. Chapman, J. C. S. Kools, *J. Magn. Magn. Mater.* **140-144** (1995) 721.
- [21] J. Th.M. De Hosson, N.G. Chechenin, D-H. Alsem, T. Vystavel, B.J. Kooi, A.R. Chezan, D.O. Boerma, *Microsc. Microanal.* **8** (2002) 274-287.
- [22] H. Hoffman, *IEEE Trans. Magn.* **4** (1968) 32-38.
- [23] A. Gentils, J. N. Chapman, G. Xiong, R. P. Cowburn, *J. Appl. Phys.* **98** (2005) 053905.
- [24] H. Gong, B. Lu, D. E. Laughlin, D. N. Lambeth, *J. Appl. Phys.* **87** (2000) 6355.
- [25] W. X. Xia, J. J. Kim, T. Yogo, D. Shindo, M. Ito, K. Ohashi, *J. Magn. Magn. Mater.* **320** (2008) 3011.
- [26] E. W. Soo, T. J. Zhou, J. P. Wang, *J. Appl. Phys.* **91** (2002) 8019.
- [27] S. Park, J-G. Zhu, D. E. Laughlin, *J. Appl. Phys.* **105** (2009) 07B723.
- [28] C.K. Lim, E.S. Kim, S.Y. Yoon, S.H. Kong, H.S. Lee, H.S. Oh and Y.S. Kim, *J. Magn. Magn. Mater.* **310** (2006) 2680.
- [29] A. Perumal, Y. K. Takahashi, K. Hono, *J. Appl. Phys.* **105** (2009) 07A304.

Chapter 7

Conclusions and Future works

7.1 Conclusions

This thesis is a set of researches based on exploiting the transmission electron microscopy, namely, LTEM as a powerful tool to understand the micromagnetic structure and micromagnetic behaviours of magnetic thin films and patterned thin films. The main scientific contributions of my research can be described as:

1. Indicating that the behaviour of the magnetic vortex in permalloy nanodots (e.g. annihilation of the vortex, nucleation, etc.) is very sensitive to the change of edge profile. The result is confirmed in terms of micromagnetic simulation and experimental observation on Lorentz microscopy. This result is crucial for tailoring the micromagnetic behaviour of the magnetic patterned thin films.
2. Suggesting a new method in which the out-of-plane polarity of the vortex core can be determined using Fresnel imaging of the LTEM. The method is validated from simulated Fresnel image to experimental images. The advantage of the method in comparison with other methods (e.g. MFM, XMCD, electron holography, etc.) is that no phase reconstruction is required, good resolution and especially quick imaging process to determine precisely the polarity. Furthermore, using two symmetrically tilted Fresnel images, the polarity of the vortex is directly detected and less influenced by the resolution of the Fresnel images. The method is more accurate than a similar method published recently by Phatak et al. using only one tilted Fresnel image and requiring an analytical model to interpretation.
3. Using Fourier transform, we applied successfully the transport-of-intensity equa-

tion (TIE) algorithm to recover the phase of the electron wave with intent to quantitatively visualise the distribution of magnetic induction in the magnetic thin film elements and therefore understand more precisely the magnetic structure. Applying the TIE algorithm will provide a simple route to qualify the magnetic structure of the magnetic thin films. A study of phase reconstruction with non-magnetic sample shows that the TIE acts like a frequency filtering effect, in which the low spatial-frequency noise needs to be cared to optimise the reconstruction. The low-spatial frequency noise can be effectively reduced by using smaller image size.

4. Directly observing the controllable nucleation of a 180° wall in structure with two micro-sized pads connecting to each other by a constriction by magnetically switching. The domain wall is nucleated in an elliptical pad, and pinned at the constriction to form a structure of smooth rotation of the magnetisation from the elliptical pad to the constriction. Such a magnetic configuration was previously suggested to be a single domain wall in similar patterned structure; however, the simulated and experimental evidences shown in the present work confirm that it seems to be like the smooth rotation in the magnetic vortex rather than conventional linear wall. The width of this magnetisation rotation is dependent on the geometrical dimension of the constriction, varies from 80 ± 7 nm for 280 nm height constriction, to 105 ± 7 nm in a constriction with the height of 900 nm. The confinement of such a magnetic configuration in the constriction causes a domain wall resistance, which is suggested to be the main contribution to the measured magnetoresistance in the structure. Besides, the anisotropic magnetoresistance of the structures is predominantly contributed by the rotation of the magnetic induction in the constriction under an application of the external field. At the other state of the magnetisation reversal, the configuration of two 90° rotation ('two- 90° -wall-like' states) from the elliptical pad to the constriction, and from the constriction to other pad (an elongated pad) is also illustrated.
5. Precisely determining the physical microstructure and magnetic structure of soft magnetic film $\text{Co}_{80}\text{Ir}_{20}$ grown on a Ru buffer layer. The film is in hexagonal symmetry with a [0001]-textured orientation normal to the film plane induced

by a seed hexagonal-Ru layer. The c-plane texture results in a negative perpendicular anisotropy, that is an important factor to prevent both spike noise and WATE. Magnetisation ripple contrast was observed in Fresnel images. The theory of ripple dispersion was successfully applied for characterising the ripple. An anisotropy field of $H_k = 40 \pm 3$ Oe was obtained from this analysis. Complex magnetisation reversal with incoherent rotation of the magnetic moments is observed, and a weak anisotropy is indicated with an easy-axis reversal identified by the nucleation of the DW. The coercive fields for easy and hard axes reversal were determined to be 26 ± 2 Oe and 18 ± 2 Oe, respectively, which are consistent with results from magnetometric measurement, confirming a typical magnetic softness of the film. The formation of 360° walls was observed in reversal process and suggested to be incorporated with layer roughness of the multilayer film system and the presence of the defects.

7.2 Future works

There are a number of unfinished works for my research, that can be performed in further career as follows:

1. The research of using tilted Fresnel images to determine the polarity of vortex core still leaves some blanks for further studies. The current method can be realised using large defocus, in which the resolution of the Fresnel images is reduced; and the defocus is out of linear regime of the Fresnel image. So, quantitative determination of out-of-plane magnetisation distribution in the vortex core is a challenge. Hence, further development of the method should be focused on linear regime of the Fresnel image, in which all quantitative imaging can be exploited.
2. Further application of the TIE algorithm should be performed for some other lithographically patterned structure and magnetic thin films to quantitatively analyse the micromagnetic structure of the films. Further investigation of spatial-frequency noise in the TIE should be developed to optimise the TIE.
3. It is necessary to carry out further physical microstructure, magnetic structure and magnetic properties of $Co_{100-x}Ir_x$ films with various x content. Further test

of spike noise and WATE suppression should be performed in collaborating with Japan group. Micromagnetic simulation of magnetic structure of the films using polycrystalline OOMMF code should be carried out to interpret the magnetic structure as well as the micromagnetic behaviour of the films. Influence of the 360° walls in the film on the spike noise and WATE should be analysed further.

4. Electrical transport measurement for structure with nanoconstriction should be carried out systematically to associate with LTEM measurement of domain wall in the constriction by in-situ measurement of the AMR in the TEM. The spin-transfer-torque measurements are expected to be carried out by means of measuring the AMR at various current densities. This work is being conducted in collaboration with University of Leeds. It is expected to observe the flipping of the magnetisation in the constriction and breaking magnetic configuration due to the spin torque transfer from the spin-polarised current with high electrical current density.